A Thermal Model for Rapid Hyperthermia Therapy Planning and Evaluation

by

Gregory Thomas Martin

S.B., Massachusetts Institute of Technology (1988)
S.M., Massachusetts Institute of Technology (1991)

Submitted to the Department of Mechanical Engineering
in partial fulfillment of the requirements for the degree of

Doctor of Philosophy

at the

MASSACHUSETTS INSTITUTE OF TECHNOLOGY

June 1995

Author _____
Department of Mechanical Engineering
May 18, 1995

Certified by _____
Dr. H. Frederick Bowman
Director, Hyperthermia Program, Harvard-MIT Division of HST
Thesis Supervisor

Certified by _____
Dr. William H. Newman
Research Scientist, Harvard-MIT Division of HST
Research Supervisor

Accepted by _____
Professor Ain A. Sonin
Chairman, Departmental Committee on Graduate Students

A Thermal Model for Rapid Hyperthermia Therapy Planning and Evaluation

by

Gregory Thomas Martin

Submitted to the Department of Mechanical Engineeringon May 18, 1995,
in partial fulfillment of the requirements for the degree of
Doctor of Philosophy

Abstract

The effectiveness of local hyperthermia for the treatment of solid tumors is limited by a lack of quantitative modeling tools for therapy planning and evaluation. A new method that permits the rapid calculation of the hyperthermic temperature field is presented. This approach, called the Basis Element Method (BEM), uses a superposition of finite heat sources to solve the bioheat transfer equation for a general heating pattern, non-homogeneous boundary conditions, variable thermal properties and blood perfusion and complex patient geometries. The algorithm speed is increased by decreasing the volume in which sources are integrated, recognizing that thermal perturbations at a distance are exponentially attenuated in a length scale inversely proportional to perfusion. Comparisons to exact solutions of problems with simple geometries show that the BEM approaches the exact solution as the size of the finite sources is decreased and the integration volume is increased. Comparisons of the BEM to finite element solutions of problems with irregular geometry show an RMS temperature difference of less than 0.09 °C. Experimental validation is performed with simulated hyperthermia treatments in a porcine model. The target tissue is instrumented with 101 invasive temperature sensors and 12 invasive perfusion sensors. Hyperthermic energy is delivered by the multi-element FSUM ultrasonic applicator. The steady-state temperature is computed by the BEM using the measured power deposition (SAR) and perfusion values as inputs, and the results are compared to the discrete measurements. Over all the sensors, the RMS temperature error is 0.7 °C. Clinical utility is demonstrated by using the BEM to perform reconstructions of the hyperthermic temperature field from patient treatments. The patients were instrumented with several invasive multi-sensor temperature probes and hyperthermia was induced with the FSUM applicator. The BEM computed the temperature in the tissue from the measured SAR and a mesh automatically generated from patient CT scans. The RMS error between the measured and calculated temperatures is 0.9 °C.

The use of the BEM in clinical hyperthermia will allow the computation of more accurate local thermal dose statistics based on the entire tumor volume instead of discrete temperature measurements. Ultimately, these statistics will help establish thermal dose - tumor response relations which will serve to guide therapy planning.

Thesis Supervisor: Dr. H. Frederick Bowman
Title: Director, Hyperthermia Program, Harvard-MIT Division of HST

Acknowledgments

This thesis has been under development in some form or another for the past four and a half years. Throughout that time, I have relied on many, many people for help, support, and encouragement - technical, moral, social and mental. I hope to distinguish many of these people here. I hope I don't forget anyone, but I probably will. First and foremost thanks and gratitude is extended to my perennial thesis advisor Dr. H. Frederick Bowman who has supervised my Bachelors, Masters, and Doctoral theses. I first sought out Dr. Bowman's mentorship in January of 1987 and have worked continuously with him since. I have found our interaction to be stimulating and intellectually challenging - on topics ranging from heat transfer to religion and theology. My other thesis committee members also deserve much gratitue: Dr. William H. Newman, Professor Borivoje Mikić, Professor Padmakar P. Lele, and Dr. Goran K. Svensson: Dr. Newman for his conception of the project, his guidance (and for paying my stipend for the past three years), Professor Mikić for his heat transfer insight and inspiration, Professor Lele for his guidance and wisdom and Dr. Svensson for providing focus on the clinical application. In my day-to-day activities, I owe the most appreciation to my colleague *Dr.* Kenneth S. Szajda (formerly Graduation Student Peon Szajda). Like Dr. Bowman, Ken has been my companion since my days as a UROP in the lab. His instruction has ranged from analog circuit design to what font will look best in my thesis. He never seemed to tire or be annoyed at my endless questions about C, latex, UNIX, matlab, or cooking (he really is a great cook). To my colleague Daniel A. Sidney, my office-mate and project-mate, I owe much for his help in generating the pretty pictures of the patient anatomy, for his knowledge of obscure vocabulary and for the daily supply of Trident Surgarless Gum. And to Jeff Breedlove, my under-study, I owe gratitude for his help with the Basis Element packing. Other people who deserve honorable mention are Keiko Oh for always making sure my appointment was renewed, among other things, Dr. Steve Burns for the many instances of late-night help with the computers, Jørgen Hansen of the Dana-Farber Cancer Institute for his vital help with the animal and human experiments, and Christopher Newell for always reminding Fred of our meetings. For maintaining my mental stability and supporting me (well, not financially though), I owe much to my friends and family who took pity on me for having spent so many years in graduate school.

Contents

List of Figures

List of Tables

List of Variables

a	Basis Element radius [m]
A	Fourier-Bessel integral coefficients
E	weight function
Bi	Biot number - h L / k_m
C	speed of sound [m s^{-1}]
c_b	blood specific heat [J kg^{-1} $^oC^{-1}$]
h	heat transfer coefficient [W m^{-2} $^oC^{-1}$]
k	wave number
k_m	tissue thermal conductivity [W m^{-1} $^oC^{-1}$]
L	length scale [m]
L_p	perfusion length [m]
$\hat{n}$	unit normal vector
$\vec{n}$	normal vector [m]
N_p	number of perfusion lengths in integration volume radius
p	ultrasonic pressure [N m^{-2}]
P_f	local integration volume packing factor
Pe	Péclèt number - $\omega c_b \rho_b L^2 / k_m$
q	heat flux [W m^{-2}]
Q	internal heat generation [W m^{-3}]
Q_o	maximum internal heat generation [W m^{-3}]
Q_j	internal heat generation magnitude of a uniform finite source [W m^{-3}]
r	dimensionless radial coordinate
r'	radial coordinate [m]
$\vec{r}$	position vector [m]
$\vec{r}_j$	Basis Element position vector [m]
$\vec{r}_p$	position vector of a source center [m]
R'	Basis Element coordinate [m]
R'_+	matching functions coordinate [m]
R	dimensionless Basis Element coordinate

R_+	dimensionless matching function coordinate
R_c	radius of curvature [m]
S	integration surface [m^2]
t	time [s]
T	tissue temperature elevation above the baseline [^oC]
T_h	homogeneous temperature elevation component [^oC]
T_{nh}	non-homogeneous temperature elevation component [^oC]
T_B	boundary temperature [^oC]
u	Green's function [m^{-1}]
u_o	Piston velocity [m s^{-1}]
v	matching function [m^{-1}]
V	heated volume [m^3]
V_{int}	integration volume [m^3]
V_j	local integration volume [m^3]
w	free space Green's functions [m^{-1}]
W	perfusion [ml min^{-1} $100g^{-1}$] = $\omega/\rho \times 60$ s/min $\times 100$
x	Cartesian coordinate [m]
y	Cartesian coordinate [m]
z	Cartesian coordinate [m]

α	absorption coefficient [m^{-1}]
α_m	tissue thermal diffusivity [m^2s^{-1}]
κ	dimensionless thermal conductivity
Λ	wavelength [m]
λ	$\sqrt{\omega\, c_b\, \rho_b / k_m}$ [m^{-1}]
μ	$\cos(\phi)$
ρ_b	blood density [kg m^{-3}]
θ	dimensionless temperature rise
θ_j	dimensionless Basis Element

Θ_j Basis Element [°C]

ϕ angle in spherical coordinates

ω local perfusion rate [s^{-1}]

Chapter 1

Introduction

1.1 Hyperthermia Treatment

In the United States, over one million new cases of cancer are diagnosed each year and more than one half million people die each year from cancer. The current methods of cancer treatment include surgery, radiotherapy, chemotherapy, and immunotherapy. Local hyperthermia therapy, used in conjunction with radiation therapy, has received much attention in the medical research community during the past decade as an additional method for treating neoplastic (tumor) tissue [1]. The effectiveness and safety of hyperthermia depend on the preferential elevation of tumor tissue temperature to therapeutic levels, typically 42 °C, [2], with minimal perturbation to the surrounding, normal tissue.

Local hyperthermia has been induced using a variety of methods with the most common using electromagnetic (radiofrequency and microwaves) and ultrasound energy. Delivery of hyperthermic energy can be non-invasive, as is typically done with ultrasound applicators, [3], intracavitally, as with transrectal microwave applicators, [4], or interstitially as with electrically resistive probes, [5]. The effectiveness of the treatment delivery is typically assessed by a limited number of invasive temperature sensors placed in the tumor region. Issues concerning patient safety and comfort determine the exact placement of the temperature sensor probes, rather than the desire to maximize information from the acquired data.

The ideal delivery of hyperthermia therapy would parallel the current delivery paradigm

of radiotherapy where treatment administration is quick and open loop - utilizing an "aim and shoot" approach. Radiation dosimetry is sufficiently well understood such that no measurement during treatment is necessary for treatment assessment. Hyperthermia delivery and control, however, presently depend on invasive thermometry to measure the thermal dose at the sensor sites with the assumption that these sites are representative of the dose received by the entire target volume. Further, the concept of thermal dose - the temperature-time history necessary to achieve a certain tumor response - is not well enough understood to predict the tumor response from the true dose.

In order to permit a more accurate and realistic assessment of the treatment delivery, more quantitative tools are necessary. These tools ideally would aid in the treatment planning to determine the optimal treatment parameters (transducer power, transducer excitation pattern, and applicator-patient orientation), identify difficult to heat regions and suggest temperature probe placement. After treatment, these tools would quantitatively reconstruct the temperature field based on *in vivo* temperature, power deposition and perfusion measurements and determine the volumetric thermal dose statistics.

Central to the quantitative tools outlined above is a **thermal model** of the tissue hyperthermia treatment. Such a model would solve the three dimensional (3-D) temperature field from the patient geometry, power deposition, thermal properties and perfusion. To obtain the necessary inputs, the model would have to work in concert with patient imaging systems, applicator characterization studies, thermal property and perfusion measurements and the patient thermometry system. To be efficiently used by a clinician, the model would have to interface to an interactive visualization system, capable of integrating the anatomic surfaces with 3-D temperature, power deposition and thermal dose fields into a common coordinate system. The thermal model would have to be able to solve the temperature field with sufficient speed to permit interactive treatment planning. Ultimately, the most benefit from thermal modeling would be obtained by solving the temperature field, in real-time, during therapy to provide the clinician with timely feedback information to guide treatment protocol.

1.2 Tissue Thermal Models

In the hyperthermia therapy literature, the term *thermal modeling* actually consists of two steps:

1. Determination of the significant mechanisms of tissue heat transfer (tissue conduction, internal heat generation, blood convection, and boundary conditions) and the formulation of a set of approximate system equations.

2. Solution of the system of equations.

As with many engineering tasks, the demands of Step 1 - the model formulation - are typically the most difficult and it is especially challenging when applied to the complex heat and mass transfer of physiologic systems. The two steps, however, go hand-in-hand and model formulation is generally performed such that the system of equations is solvable given the application constraints and the *a priori* information about the physiologic system.

Tissue heat transfer is greatly dependent on the convection due to local blood flow. Complete knowledge of the convection heat transfer requires that the blood flow vector field is first characterized and modeled. This alone is a monumental task. The flow vector field is determined from the coupled Navier-Stokes and continuity equations both of which are 3-D, time dependent, partial differential equations applied to the irregular geometry of the vasculature. The convection heat transfer is solved by applying the energy equation, which is also a 3-D, time dependent partial differential equation, and Fourier heat conduction to the vector flow field. Therefore, any model formulation of the tissue heat transfer requires some simplifying assumptions.

Most simplifications employed in tissue heat transfer reduce the flow field to zero or one-dimension which then converts the energy equation to a form solvable by standard techniques. In the literature, the model formulation of the blood convection has been the subject of much discussion and debate. There are two major and divisive schools of thought. The first is grounded in the theoretical foundations of heat and mass transfer in the tissue and seeks a comprehensive theory of transport. Major proponents of this school include Chen and Holmes, [6] and Jiji *et al*, [7, 8] who have proposed models which apply

the conservation laws to a detailed description of the exact vascular morphology. These vascular models have been applied to anatomical locations with a regular vasculature such as a limb, (Song *et al* [9]), and a renal cortex, (Xu *et al* [10]). While these models are useful for the parametric exploration of tissue heat and mass transfer to determine the functional form of various transport characteristics, they are impractical for application to predict the tissue temperature in organs without a regularly arranged vasculature.

The other school of thought advocates the use of empirical expressions to model tissue heat transfer. A prominent continuum model has been developed by Pennes, [11], from invasive temperature measurements made in the human forearm. In this model, the heat and mass transport due to blood flow are lumped together into a single term in the system energy equation. The model neglects the total effect of the vascular morphology and assumes that the net blood flow has no directionality. Thus, the flow field is a scalar quantity that "perfuses" through the tissue. Blood flows into a tissue bed at the arterial temperature and exists in thermal equilibrium with the tissue. If it is assumed that the arterial temperature is equal to the initial and uniform baseline temperature, the Pennes bioheat transfer equation becomes:

$$\frac{1}{\alpha_m}\frac{\partial T}{\partial t} = \nabla^2 T - \frac{\omega \rho_b c_b}{k_m} T + \frac{Q}{k_m} \tag{1.1}$$

where T is the tissue temperature elevation above the baseline; Q is the applied heating; k_m is the tissue intrinsic thermal conductivity; α_m is the tissue intrinsic thermal diffusivity; ω is the local perfusion rate; ρ_b is the blood density; and c_b is the blood specific heat. The major limitations of the Pennes bioheat equation are that mass conservation is not satisfied and the equation fails to predict the temperature near vessels whose diameter is on the order of the characteristic thermal length scale. Otherwise, the model is extremely useful for the prediction of temperature in tissue. There is a wealth of experimental and theoretical analysis that shows the bioheat transfer equation to be a very useful and effective tool for thermal modeling [12], [13], [10], [14].

1.3 Hyperthermia Thermal Models

Thermal modeling for hyperthermia therapy plays many different roles depending on the particular application. Models have been used to aid in applicator design, applicator characterization, treatment optimization, treatment planning, post-treatment temperature reconstruction, and real-time treatment evaluation. The model choice and formulation depends greatly on the needs of the particular application in terms of model simplicity, accuracy, calculation speed, available hardware, and accuracy and availability of the model inputs. For example, the evaluation of an applicator design would most likely require a model with high accuracy and need powerful hardware with a slower calculation speed to achieve the modeling goals. On the other hand, a real-time model would most likely require a simple estimation for the temperature which can be computed quickly on a modest computer. The thermal models are solved by various means, such as analytical techniques using integral transforms, finite element, finite difference, and boundary element methods and hybrid or custom solution schemes. The use of these schemes depends on the model formulation and the ultimate application.

Abdelazim and Hashish, [15], used a Padé approximation to solve the transient, 1-D cylindrical bioheat equation. Jafaria and Higgins, [16], proposed a 2-D, cylindrical model with an analytical solution to the bioheat transfer equation for use in treatment planning. Edelstein-Keshet *et al*, [17], used spherical and cylindrical analytical solutions to the bioheat equation to define treatment descriptors such as the volume fraction above a certain temperature and the weighted average temperature. These analytical models and solutions require simple geometries and homogeneous properties and their usefulness is limited to providing insight into the parametric dependence of the bioheat equation.

Bowman, [18], used the finite element method to investigate the effect of inhomogeneous tumor perfusion on the temperature profiles achieved during scanned, focused ultrasound. Van Den Berg *et al*, [19] used the finite element method in space and the finite difference method in time to solve the bioheat equation in a 2-D patient geometric representation derived from patient CT scans of the pelvic region. Strohbehn *et al*, [20], applied the finite element method to investigate 2-D pelvic hyperthermia by induction coil devices and

radio frequency (RF) annular phased arrays. While the 2-D numerical models are able to account for varying thermal properties, irregular patient geometries and unsymmetric heating patterns, full 3-D modeling is necessary to accurately predict the temperature field in patients.

Spiegel *et al*, [21], described a 3-D finite difference solution to determine the temperature rise in an animal hyperthermia model. Panjehpour *et al*, [22], simulated the interstitial hyperthermia using a 3-D solution to the bioheat equation. They compared steady-state computed temperatures with those measured in an anesthetized dog and found that the difference of 85% of the 80 temperature comparisons were less than 1.0 °C. Charny and Levin, [23, 24], developed a 3-D finite element hyperthermia model of the lower leg from CT scans. Their purpose was to characterize the heating from a mini-annular phased array applicator. Lin *et al*, [25], used a finite difference solution of the bioheat equation to determine the treatment parameters in a scanned, focused ultrasound system which optimize the steady-state tumor temperature distribution. The authors demonstrate that the simulated, optimized treatment parameters result in better temperature distributions, however they also note that in clinical application, such an approach is limited due to patient-to-patient variability in blood flow and tumor geometry. Martin *et al*, [4], used a 3-D finite element solution of the bioheat equation to model transrectal, microwave hyperthermia of the prostate and compared temperature calculations to an *in vivo* canine experiment. Moros *et al*, [26], used a finite difference solution to the bioheat and the Chen-Holmes equations, [6], to compare the results of these two model formulations to *in vivo* hyperthermia induced by scanned-focused ultrasound. They found that the bioheat equation produced better qualitative and quantitative comparisons with the experimental data. O'Brien and Mekkaoui, [27], used an implicit finite difference method to solve for the transient 3-D temperature fields for a simulated tumor near a bone or artery. Their purpose is to model the tissue heating from a dual-beam microwave applicator. DeFord *et al*, [5], used a finite difference algorithm of conductively heated interstitial hyperthermia needles to identify the minimum temperature occurring between needles. A polynomial was fit to the minimum temperatures as a function of power deposition and this fit was used for the on-line and real-time control of the applicator power.

Clegg and Roemer, [28, 29, 30], have used a finite difference solution of the bioheat equation to reconstruct the entire 3-D temperature field from a limited number of temperature measurements taken during hyperthermia therapy. They define a number of zones in the tissue and iteratively solve the model, varying the perfusion in each zone to minimize the error between *in vivo* measurements and the finite difference calculation. When some measurements are not used in the reconstruction, in order to validate the technique, the error between the calculations and the majority of the unused measurements is less than 0.5 °C. However the reconstruction, as such, is an ill-posed state and parameter problem for which the solution uniqueness is not guaranteed, the validity has yet to be demonstrated and the reconstruction requires vast computational resources. Liauh *et al*, [31], compare two different methods for computing the inverse solution for perfusion in temperature reconstruction for the purpose of reducing the required computational time. Liauh and Roemer, [32] demonstrated that multiple minima exist for the inverse solution of perfusion. Liauh and Roemer, [33], describe an improved algorithm for the inverse solution of perfusion which approximates the Jacobian matrix by assuming temperature to be a linear function of perfusion.

The literature also contains references for 3-D thermal modeling using numerical techniques other than finite element or finite difference. Potocki and Tharp, [34], used a full-order extended Kalman filter to estimate the unknown perfusion and temperature from discrete measurements to reconstruct the 3-D temperature field. Mooibroek and Lagendijik, [35], formulated a 3-D solution algorithm from a modified finite difference scheme, which expressly considers the effects of vessels. Martin *et al*, [36, 37, 38], developed the Basis Element Method for the rapid 3-D temperature solution during hyperthermia treatment planning.

1.4 Design of a Thermal Model for Therapy Planning

The successful application of thermal modeling to hyperthermia therapy planning requires the model to work in conjunction with the necessary and available input parameters. The planning system needs to be based on a geometric representation of patient anatomy de-

rived from 3-D imaging such as CT scans. The therapist, during planning, identifies a treatment portal to access the tumor with a given ultrasonic applicator. The ultrasound power deposition field can be calculated in the tissue for the planned transducer excitation configuration either from theoretical considerations, such as the Rayleigh diffraction integral, from empirical relations determined from phantom experiments, or from a combination of theoretical and empirical relations. Tissue thermal properties and perfusion can be taken from a database which contains the cumulative clinical experience of their measurement. Patient geometry, power deposition, thermal properties and perfusion would then be communicated to the thermal model for the 3-D temperature field calculation. The thermal field would then be available to the therapist to determine if a change in the treatment plan is warranted. In particular, the therapist would take care not to over-heated critical organs and not under-heat the tumor volume.

The context in which the thermal model is used places certain requirements and constraints on the model formulation and solution. For instance the model must be able to solve for the 3-D temperature field allowing for inhomogeneous thermal properties and perfusion and be able to consider boundary conditions of specified surface temperature, surface heat flux and surface convection. The solution should be sufficiently accurate to safely plan the treatment and the calculations should be available as fast as possible, ideally in real-time.

Of the thermal models reviewed above, the analytical models assume homogeneous properties and perfusion and the 2-D models are unable to give sufficient accuracy for planning. The 3-D finite element and finite difference solutions allow inhomogeneous properties and perfusion and also provide potentially high accuracy (less than 0.05 ^{o}C). This level of accuracy is usually attained with a nodal spacing of 2-5 mm in a tissue domain of about 30x30x30 cm, for instance in a patient abdomen. Thus the total nodes required number about 10^5-10^6. The computer resources and processor time necessary to solve a mesh of this dimension are great. Usually investigators have used multiprocessor supercomputer facilities to achieve the solution. In addition, these methods depend heavily on an adequate transformation of the continuous problem to the discrete representation. Improper discretization (mesh generation) leads to inaccurate results and solution divergence. Often, the methods must be solved multiple times to demonstrate convergence.

For clinical therapy planning, the use of supercomputer facilities is not practical. At best, an engineering workstation is available in the clinic. Further, the concept of solution "accuracy" is not the most important criterion to judge a hyperthermia thermal model. The inputs to any model - patient geometry, power deposition, thermal properties and perfusion - are not generally known to an accuracy greater than 10%. Thus, attempts to seek a high level of accuracy are fundamentally limited by the precision of the inputs.

Given the special needs of therapy planning, it should be possible to formulate a thermal model which optimally balances accuracy with minimal solution and mesh generation time. The accuracy should be about 0.3 °C (about 1%) and the computation time should take on the order of 1 minute for the full 3-D field calculation. Further, the model should be packaged in a robust software implementation which can be used by a clinician without the assistance of an expert in numerical heat transfer.

This thesis describes the formulation, development and validation of a thermal model, called the Basis Element Method (BEM), expressly designed for hyperthermia therapy planning. The method is grounded in mathematical rigor, and is developed from insight into tissue heat transfer. The model is based on the bioheat transfer equation and the solution algorithm is derived from local and approximate solutions of the tissue heat transfer. This algorithm has enormously simplified and speeded the calculations, while also considering irregular geometries, complex heating patterns, and spatially varying perfusion and thermal properties.

The thesis is divided into six chapters. Chapter 2 examines the determination of the inputs available to the model - thermal properties, perfusion, and power deposition. Chapter 3 describes the algorithm formulation and development. Chapter 4 presents the current implementation of the algorithm. Chapter 5 demonstrates the algorithm validity with comparisons to exact analytical solutions and approximate finite element solutions. Chapter 6 compares the results from large animal and human hyperthermia experiments to the model. Finally in Chapter 7, the conclusions are drawn.

Chapter 2

Assessment of Treatment Parameters

The successful use of thermal modeling in hyperthermia depends greatly on the quantity and quality of data furnished in the form of "inputs" to the model. These inputs are quantitative descriptions of the patient specific treatment parameters which affect the temperature reached during hyperthermia. In particular, these parameters include the patient geometry and anatomy, the tissue thermal properties, the tissue perfusion, and the power deposition in the tissue, often called the Specific Absorption Rate (SAR).

2.1 Patient Geometry and Anatomy

Quantitative information on the patient geometry and anatomy for the purposes of treatment planning and evaluation are obtained from CT scans. In general, the construction of a 3-D model of patient anatomy involves several steps.

1. The collection of 32 to 64 CT image scans in a bit-mapped form, usually with a resolution of 256x256 pixels.

2. The segmentation of the images which identifies and groups entities together from the bit-mapped images.

3. The interpolation of successive image segmentations to group the entities into tissue-organ structures.

4. The identification of the tissue-organ structures.

Piket-May *et al*, [39], describe a highly automated technique for the production of accurate patient models from CT scans. They used the geometry of the patient-specific models to solve for the SAR fields due to electromagnetic hyperthermia. James and Sullivan, [40], also implemented a patient-specific model derived from CT scans, and they used the scanned images to determine the tissue electromagnetic properties for use in the solution of the SAR. Sullivan *et al*, [41], used patient-specific models from CT scans to compute the power deposition fields and they reported the use of their system in clinical hyperthermia treatment planning. Hansen *et al*, [42], have developed a treatment planning system, called HYPER/Plan that uses CT derived patient models in conjunction with ultrasound SAR and temperature calculations.

HYPER/Plan, developed at the Joint Center for Radiation Therapy (JCRT) and the Dana-Farber Cancer Institute (DFCI) in Boston, MA, is the treatment planning system designed to work in conjunction with the thermal model developed in this thesis. HYPER/Plan consists of a set of modules built on a commercially available 3-D visualization software package (AVS) from Advanced Visual Systems, Inc., Waltham, MA. AVS handles all the lower level visual processing such as object lighting, shading, coloring, translation, and rotation. HYPER/Plan contains routines which semi-automatically perform the segmentation, interpolation and organ identification from the CT images. Further, HYPER/Plan contains geometric models of the standard hyperthermia applicators used at the DFCI.

Figure 2-1 shows a picture of a patient-specific model generated by HYPER/Plan from CT scans. The region of interest includes the tumor and the critical organs near the tumor. In particular, the left lung, the ribs and the humerus could potentially be damaged by the ultrasound during therapy. Therefore these organs are an important part of the patient model while their right side counterparts are not.

The thermal model presented in this thesis is designed to interact with the information from the patient and applicator geometry and the transducer excitation pattern contained in HYPER/Plan to allow planning based on predicted temperatures rather than simply the geometric configuration. To realize this goal, the other necessary inputs, thermal properties, perfusion and the power deposition must also be incorporated into the HYPER/Plan

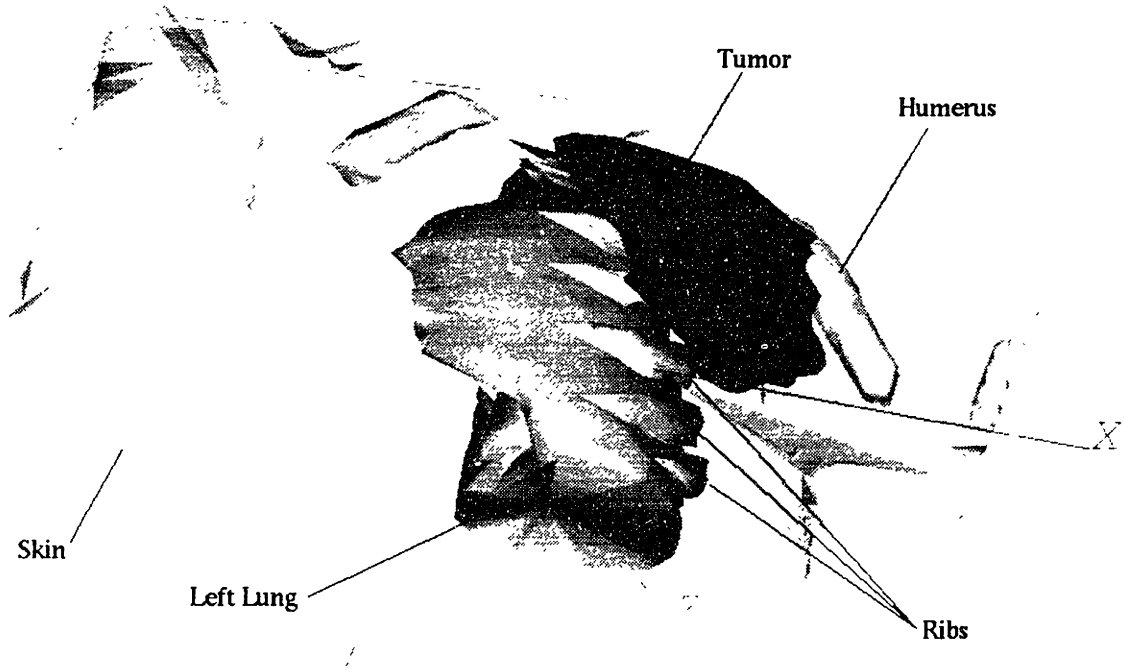

Figure 2-1: A patient specific model generated by HYPER/Plan from CT scans

coordinate base.

2.2 Thermal Properties and Perfusion

The use of the Pennes bioheat transfer equation as the theoretical basis for the thermal model dictates the definition of the thermal properties: intrinsic diffusivity, α_m; intrinsic thermal conductivity, k_m; and the tissue perfusion, ω. These parameters must be quantified and placed in a thermal property database for use in the thermal model. The database should include the values of these parameters for the various tissues relevant to hyperthermia. A comprehensive database would also include the effects of various stimuli such as temperature and sedatives, on the tissue perfusion. Ideally, the database should contain perfusion and thermal property values taken from measurements made in the patient during any previous hyperthermia sessions.

Bowman *et al*, [43], compiled in a review article an extensive tabulation of thermal conductivity and thermal diffusivity values of various animal and human tissues. Chato, [44], has also assembled together human and animal thermal properties. In general, thermal

conductivity of tissue varies from a low of 0.2 W/m-°C for fat tissue with a low water content to 0.6 W/m-°C for tissue with a high water content.

The measurement of perfusion, by various techniques, is widely reported in the literature. Such techniques include: radioactive tracer washout techniques; positron emission tomography (PET); magnetic resonance imaging (MRI); radioactive microspheres; and laser-Doppler flowmetry (LDF). The quality of perfusion data depends greatly on the measurement technique employed. PET uses short half-life isotopes, requiring a special facility; while MRI, due to its numerous other medical applications, may hold future promise. In any case, both of these techniques are complex, expensive and do not permit routine monitoring. Both PET and MRI imaging are able to discern fluid motion, however it is not yet possible to distinguish fluid diffusion from convection using these techniques. Radioactive microspheres are suitable for perfusion validation studies in animal models, but are not used for human measurements. LDF can provide continuous perfusion monitoring, however, the signal depends on a number of factors, such as hematocrit, red blood cell velocity, vascular geometry, and tissue optical properties which vary according to tissue type [45]. Thus, it is not currently possible to apply the LDF calibration and measurements from one tissue type to another. Further, it is unlikely that LDF units can be converted to absolute blood flow in all tissues. LDF is useful, however, in validating the relative perfusion variation for comparison to other measurement techniques.

2.2.1 Perfusion Measurement During Hyperthermia Therapy

In this section the perfusion and the intrinsic thermal conductivity of tumor tissue are measured before, after and when possible during treatment. The purpose is to determine values of the transport parameters and the variation of these parameters during actual hyperthermia treatments. The limited number of measurements reported here are not sufficient to create a perfusion database, but these measurements illustrate many of the factors which influence perfusion level and variation.

Data are gathered using the thermal dilution technique [46], which in this case uses a self-heated thermistor to step the thermistor temperature to a prescribed level using a closed loop feedback circuit. The power dissipated in the thermistor as a function of time along

with the temperature step and the calibration constants are analyzed to quantify the tissue thermal properties. The employment of a far-field, passive "temperature sense thermistor" allows continuous monitoring of perfusion even during changes in baseline temperature. The data sets are analyzed with a special data analysis routine specially developed for these experiments.

Hyperthermia Therapy Procedure

Tissue perfusion and tissue thermal property measurements were made on patients undergoing hyperthermia therapy at the Department of Radiation Therapy in the Dana-Farber Cancer Institute, Boston, Massachusetts (Bowman *et al*, [47]).

Perfusion measurements reported here were made on two patients. In conjunction with the hyperthermia treatments, all patients received radiation treatment and chemotherapy (bleomycine). Patient A received a total of six hyperthermia treatments and patient B received a total of ten treatments. Patients A and B suffered from a recurring metastatic tumor in the left axillary region.

Before the treatment, patients were given the chemotherapeutic drug, lorazepam (tranquilizing agent) and prochloroperazine (sedative and anti-emetic) intravenously. The tumor was injected with Novocaine (local anesthetic) and two invasive probes, each with 2 thermocouples, were inserted into the tumor to monitor temperature. The tumor surface was instrumented with 12 thermocouples taped to the skin surface. The thermocouple temperatures were monitored with a 16 channel thermometry system Model LT-100 (*Labthermics*, Champaign, Illinois) and the temperatures were recorded with a PDP 1153 computer (*Digital Equipment Corporation*, Maynard, MA).

Local hyperthermia was induced with a segmented, plane wave ultrasound applicator, the Sonotherm 1000 (*Labthermics*). The ultrasound power was computer controlled by the PDP 1153. Prior to the instant of power on, the patients were given 50 mg of Demerol (meperidine hydrochloride) as a sedative. Oftentimes, the patients were given another dose of Demerol during the treatment. The ultrasound power was increased gradually and the frequency was adjusted between 1 MHz and 3 MHz to maximize the temperature and minimize patient discomfort. Throughout the treatment EKG was monitored with a Lifepak

8 Cardiac Monitor (*Physio Control*) and blood pressure and pulse were monitored with a Vital Signs Monitor (*Critikon Dinamap*).

Tissue Perfusion Measurement Procedure

A Thermal Diffusion Probe (TDP) Model TDP-100, serial number 25 (*Thermal Technologies*, Cambridge, MA) was used to measure tissue perfusion and thermal properties. A continuous TDP probe was used for all the measurements. The probe was inserted into the tumor through the sheath of a 16 gauge angiocatheter after the inner needle was first removed. The sheath was then removed and the probe alone was taped in place. The probe was usually placed in the growing margin of the tumor, outside the necrosis at a depth of about 2 cm.

The data were recorded with an IBM compatible 286 PC laptop computer (*Zenith*) running Version 2.86 of the TDP *JCONTROL* software. Data were taken before treatment, after treatment and when possible, during treatment. The intrinsic tissue thermal properties, thermal conductivity and thermal diffusivity were computed from the data using a post-process data analysis routine.

Tissue Perfusion Measurement Results

Patient A was a male treated for metastatic lung cancer of the lymph nodes in the left axillary region. Perfusion was measured at the approximate geometric center of a tumor with dimensions 4 x 6 cm and 3 cm in depth. Perfusion measurements were made in 5 of the 6 treatment sessions. The treatment on day 3 was not instrumented. Figure 2-2 shows a summary of the perfusion measurements. Baseline pre-treatment perfusion increased from day 1 to day 11 and decreased from day 11 to day 25. These single point measurements also indicate that tumor blood flow increased after each treatment session relative to the pre-treatment perfusion, in some cases by up to 200 percent. Thus it is expected that the delivery of drugs to the tumor region would be enhanced by hyperthermia treatment. The increase in pre-treatment baseline perfusion from day 1 to day 11 may be due to an increase in tumor vascular compliance and/or tumor regression due to hyperthermia acting with radiation to kill hypoxic cells distant from the vasculature, resulting in a relative increase

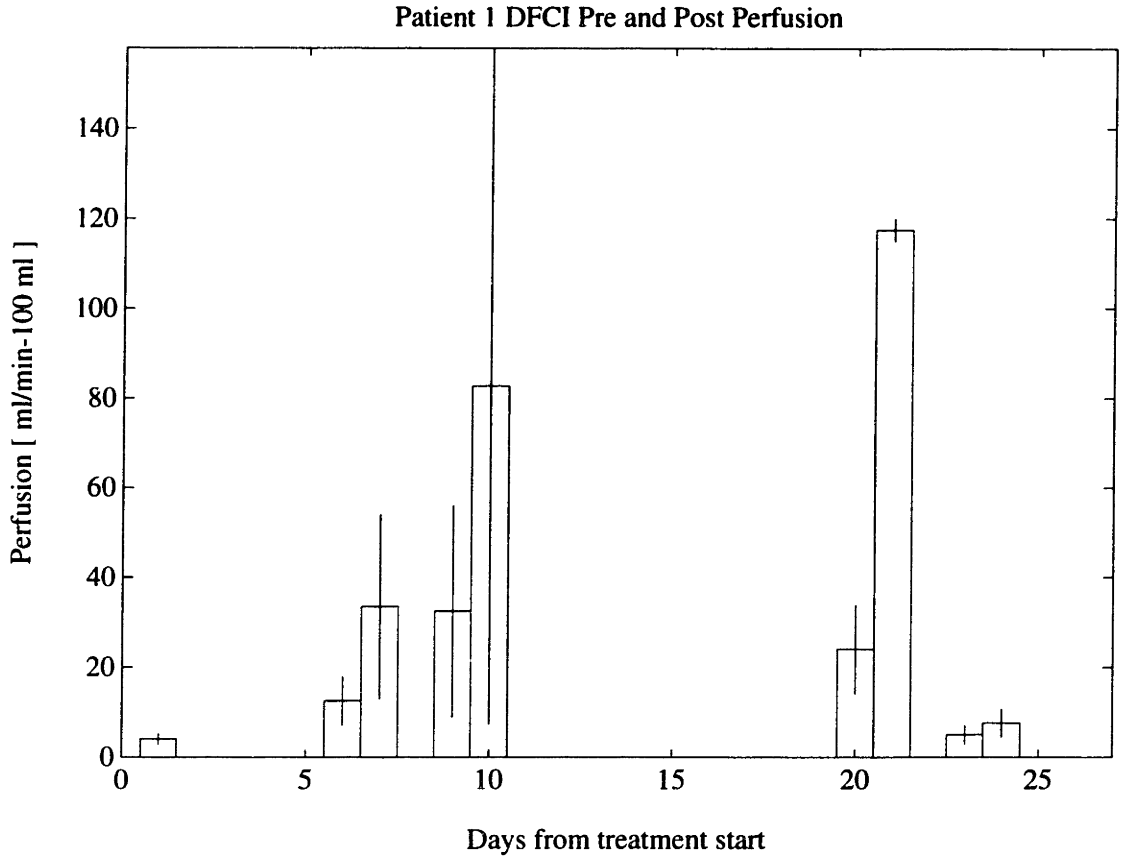

Figure 2-2: Patient A Summary of pre- and post-treatment perfusion measurements

in vascular density. The decrease in pre-treatment baseline perfusion from day 11 to day 25 may be due to direct damage to the vasculature, since the endothelium is thought to be a target of hyperthermia therapy.

Patient B was a 41 year old female with metastatic breast cancer to the lymph nodes in the left axillary region. Perfusion was measured near the geometric center of the central tumor mass. Measurements were made in 7 of the 10 hyperthermia sessions. Figure 2-3 shows of summary of the results. The measurements in patient B correlated in general with the observations from patient A in that the post-treatment perfusions were elevated relative to the pre-treatment perfusions. However, the baseline changes in pre-treatment perfusion observed in patient B were not as well ordered as those observed in patient A. It is interesting to note that the administration of Demerol in 4 recorded observations gave a characteristic transient increase in perfusion of approximately 30 percent, lasting 400-500

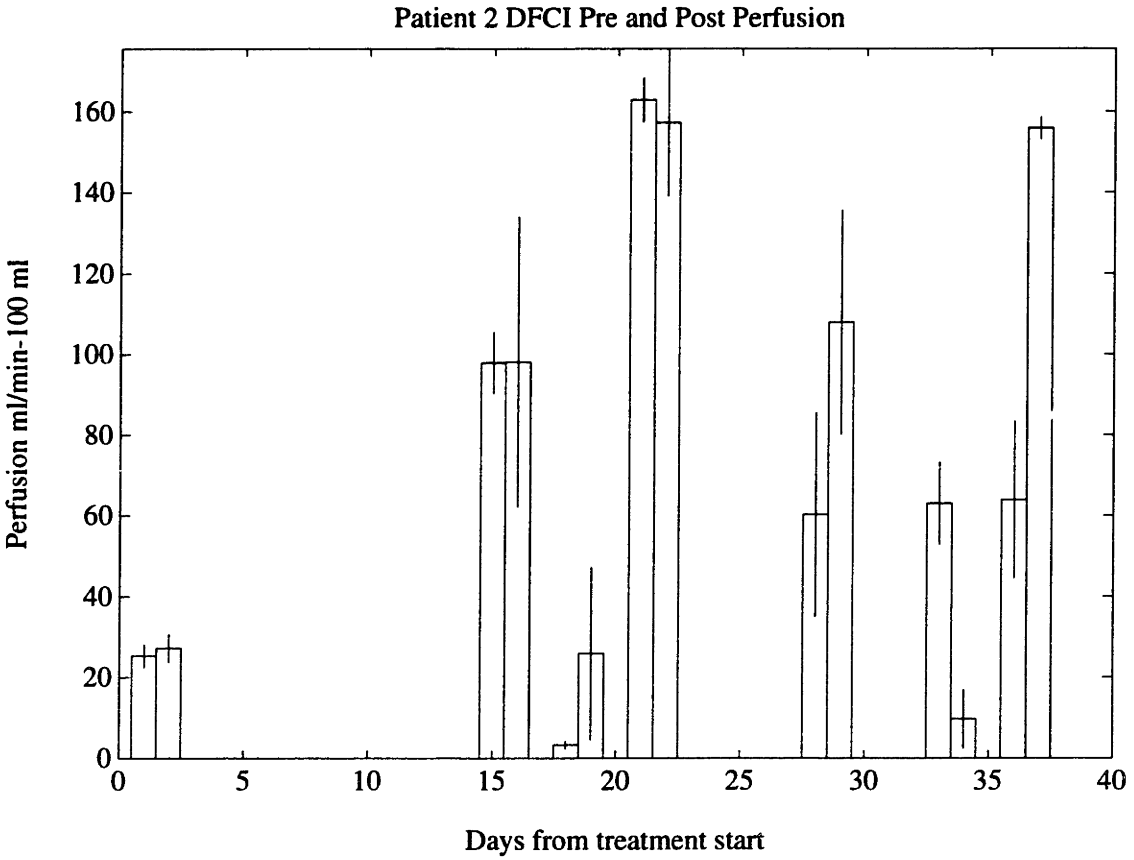

Figure 2-3: Patient B summary of pre- and post-treatment perfusion measurements.

seconds.

2.2.2 Discussion of the Clinical Perfusion Measurement

The clinical, tumor perfusion measurements reveal a most striking feature of tissue blood flow: the variability. This variability in flow is seen at all levels and time windows of the data collection and is clearly depicted in Figure 2-4. It is apparent that perfusion changes from second-to-second with a variation of about 5% without the application of external stimuli. This variation is thought to be a direct result of vasomotor activity in the precapillary arterioles. The transient effect of Demerol on the perfusion is to increase flow by about 30%, but the basic mechanism which causes this change is not known. Changing patient position, with the arm extension, caused a dramatic drop in perfusion by about 60%. This may have been due to shunting of flow by some vessels and a blocking of the flow in

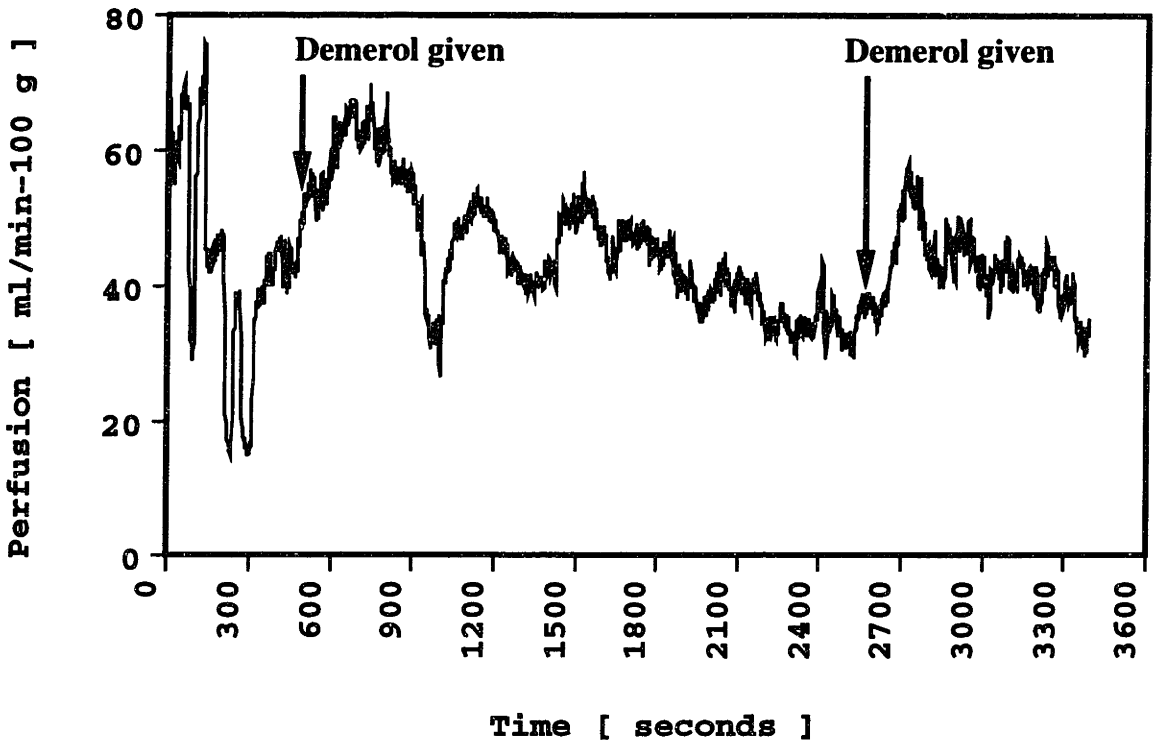

Figure 2-4: Patient 2: Continuous perfusion measurements made before and during treatment.

other vessels in the position change.

The pre- and post-treatment measures of perfusion in Figure 2-2 show a series of hyperthermia induced increases in flow. The line bars indicate not measurement error, but variation in instantaneous flow averaged over several data runs. Further, the pre-treatment flow level varies as a function of the course of therapy. Figure 2-3 shows similar variations, but in a more disordered fashion. These variations in perfusion - as a function of drugs, hyperthermia, course of therapy, and patient position - have grave implications for thermal models of hyperthermia. The transfer of heat during therapy is almost always perfusion dominated. Thus the accuracy of temperature predictions is directly related to the accuracy of perfusion quantification. Since large perfusion variations during therapy are not only possible, but normal and expected, perfusion needs to be monitored before, after and if possible during therapy. These measurements need to be made as accurately and as densely

as possible.

2.3 Power Deposition

Accurate thermal modeling in hyperthermia is directly dependent on the faithful representation of the power deposition in the tissue. Whether the heating method is by ultrasound, microwaves, electromagnetic induction or capacitance heating, the power deposition distribution must be predicted for use in treatment planning and reconstructed for use in post-treatment evaluation. Each of these heating modes uses waves of energy which are directed toward and/or focused on the tissue target volume. The wave energy is converted to heat energy througn the process of absorption by the tissue where certain vibrational states of molecules are excited by the incident energy. Theoretically, knowledge of the wave energy applicator, the tissue geometry, and the tissue properties when used with the solution of the wave equation should predict the power deposition. In practice, various simplifications must be made in order to arrive at a usable solution in a timely fashion.

Currently under evaluation at the DFCI, is a Focused Segmented Ultrasound Machine (FSUM) which consists of 56 plane wave, non-phased square transducers mounted in a hemispherical shaped applicator. To distribute, preferentially, the energy deposition over a large tissue volume, the hemispherical shell of the FSUM undergoes a precessional motion. Here, the analysis of power deposition is confined to ultrasonic sources, however the thermal model presented in this thesis is completely independent of the type of heating device used.

2.3.1 Background

Ocheltree and Frizzell, [48], developed an efficient method for the numerical solution of the sound field from a rectangular transducer insonating a homogeneous and absorbing medium. Their method approximates the pressure at a point in the field by discretizing the transducer into a number of small rectangular sources each of which makes a contribution to the pressure field. The size of each rectangular source depends on the distance of the point from the transducer. The algorithm is made efficient by finding the optimal discrete source size for a given distance from the transducer. Their work is an important step in

being able to predict the power deposited by the FSUM device, however several practical and theoretical limitations exist.

Harrison, [49], notes that in ceramic transducers, the mechanical and thermal stresses of normal operation can change the efficiency and the spatial distribution of the radiated energy over time. Further, the exact mounting configuration of the transducer can significantly affect the radiation distribution. Hansen *et al*, [50], have noted efficiency and energy distribution differences among the 56 identical transducers in the FSUM applicator. These practical considerations all contribute to complicate the effort to predict the FSUM power distribution.

Fan and Hynynen, [51], have shown that the existence of planar boundaries between soft tissues of different ultrasonic properties generally has a negligible effect on altering the power deposition pattern of focused ultrasound. Fan and Hynynen, [52], also showed that curved boundaries between soft tissues of different ultrasonic properties may have an effect when the radius of curvature is small enough. Bone tissue, however, which has an absorption 10 times greater than that of most soft tissue, significantly distorts the ultrasound field. Further the wave velocity in bone is about twice that of soft tissue. The large difference in acoustic impedance between bone and soft tissue is known to cause undesirable heating at the bone interface. Davis, [53], reports measurements that indicate the presence of bone increases tissue temperature elevation by 50 percent. Air cavities in tissue, such as those created by bowel gas and the lungs, are known to cause similar overheating effects. These complexities make the accurate solution of power deposition a task at least as difficult as the computation of the resulting temperature field.

2.3.2 Ultrasound Model

A rudimentary algorithm for the calculation of the ultrasound pressure and intensity fields for the FSUM has been implemented based on the work of Ocheltree and Frizzell. Their algorithm uses the Rayleigh integral which expresses the sound pressure at a given point by:

$$p = \frac{j\rho C}{\Lambda} \int_S u_o \frac{e^{-(\alpha+jk)r}}{r} dS \tag{2.1}$$

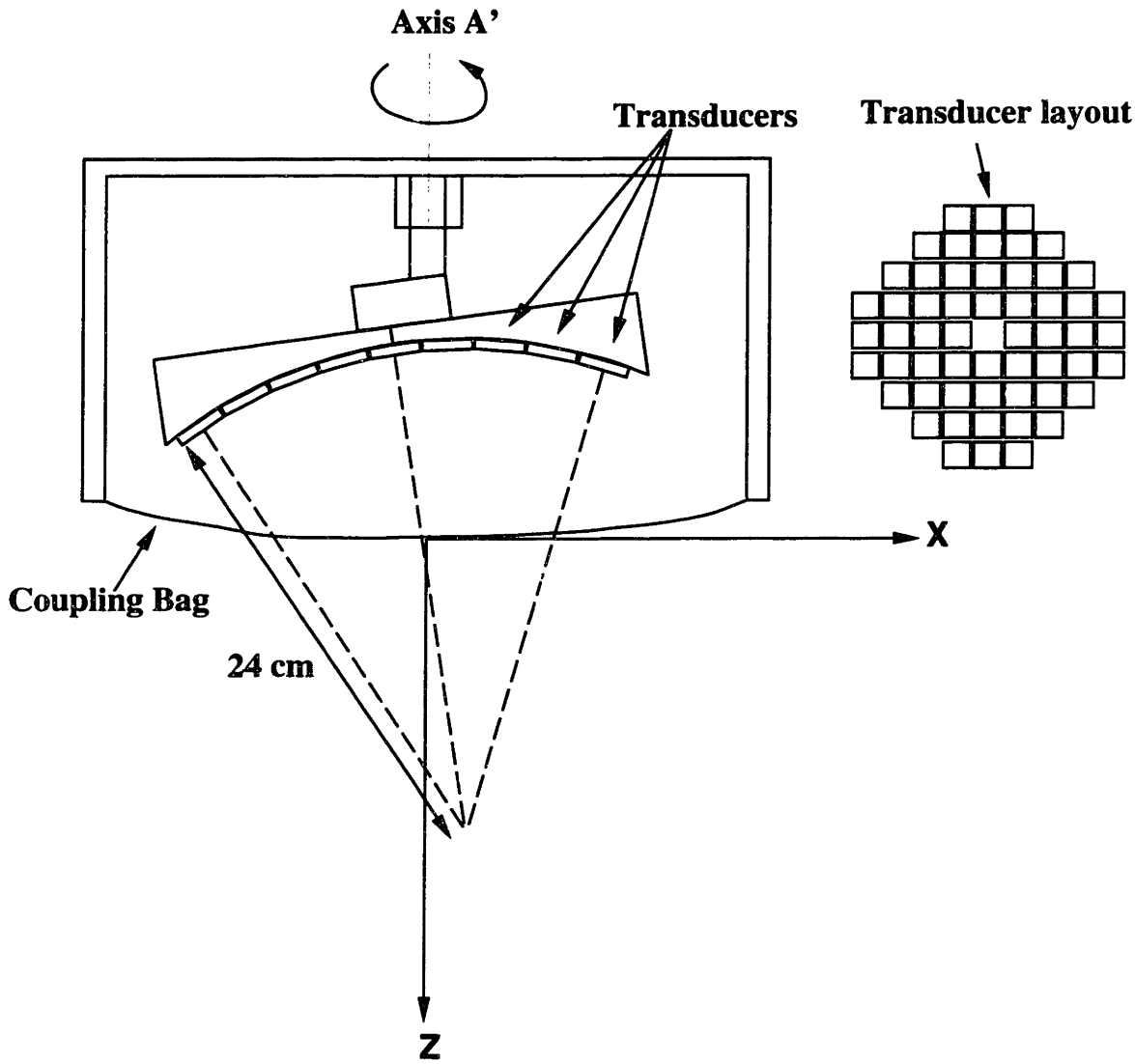

Figure 2-5: Schematic diagram of the FSUM ultrasound applicator.

where ρ is the medium density, C is the phase velocity of the sound waves, u_o is the velocity amplitude of the piston, Λ is the wavelength, k is the wave number, α is the absorption coefficient, r is the distance between the field point and an elemental area of the transducer, and S is the surface area of the transducer. Figure 2-5 shows a 2-D cut away representation of the FSUM applicator. Fifty six square transducers are mounted on the underside of the hemispherical shell according to the transducer layout in Figure 2-5. The applicator housing is filled with degassed water to couple the ultrasound energy to the patient surface.

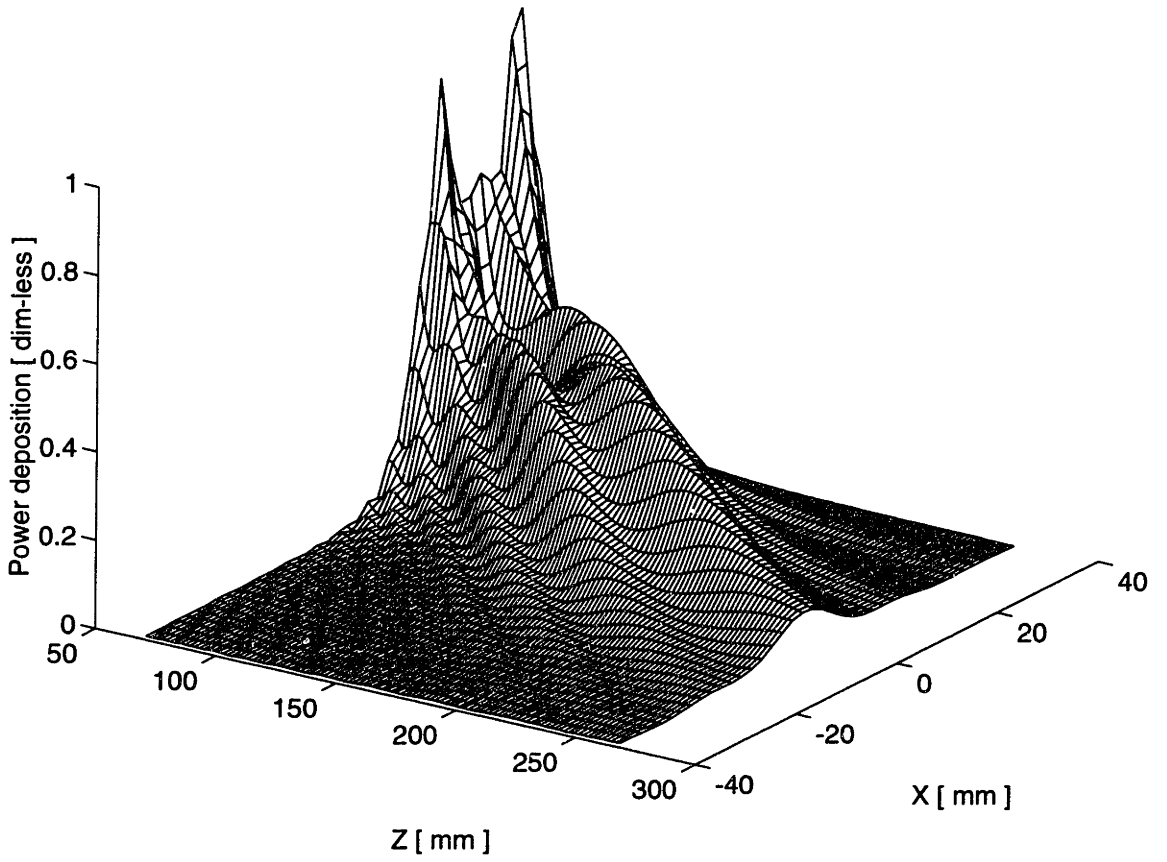

Figure 2-6: Normalized power deposition for a single FSUM transducer.

In order to demonstrate the use of Ocheltree and Frizzell algorithm with the FSUM applicator, some example power depositions were simulated without allowing the precessional motion of the applicator. Figure 2-6 shows the ultrasound power deposition computed for a single FSUM transducer insonating an absorbing medium. The absorption coefficient is 0.35 Nepers/cm at the operating frequency of 1 MHz, which is a representative value of many soft tissues. The power deposition is computed in the plane of the applicator center. A limitation of the algorithm in application to the FSUM is that the degassed water in the housing does not absorb ultrasound energy, but the tissue does. The algorithm, however, assumes the absorption coefficient to be uniform over the entire domain. Thus the predicted ultrasound field is more damped than the actual field. Further, the boundary between the non-absorbing water and the absorbing tissue will, in practice, reflect some energy.

Figures 2-7 and 2-8 show the normalized power deposition from all the FSUM transduc-

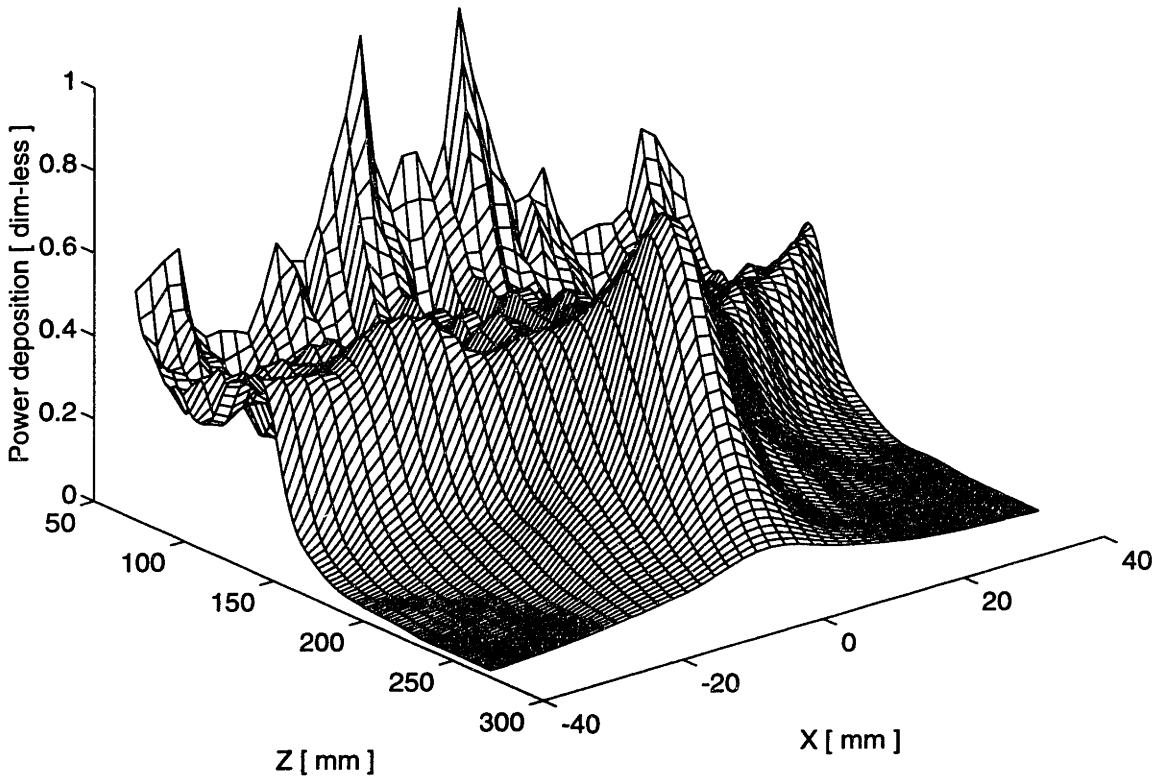

Figure 2-7: Normalized power deposition for all the FSUM transducers.

ers insonating an absorbing medium with an absorption coefficient of 0.35 Nepers/cm for a plane that passes through the applicator center at Y=0 mm and where the Z coordinate is taken from the transducer surface. In this computation, it has been assumed that the power deposition at each field point is the sum of the power deposition from each transducer. Strictly speaking, the computation should sum not the power deposition, but rather the field pressures resulting from each transducer. Further, the ability of the FSUM applicator to precess has not been taken into account in this analysis. It is possible to translate the power deposition field in the manner of the FSUM precession in order to compute a time averaged power deposition.

Based on the experience gained in implementing and using a computational model for the ultrasound power deposition, it is clear that further analysis, both numerical and experimental, is necessary before many issues relevant to routine treatment planning of

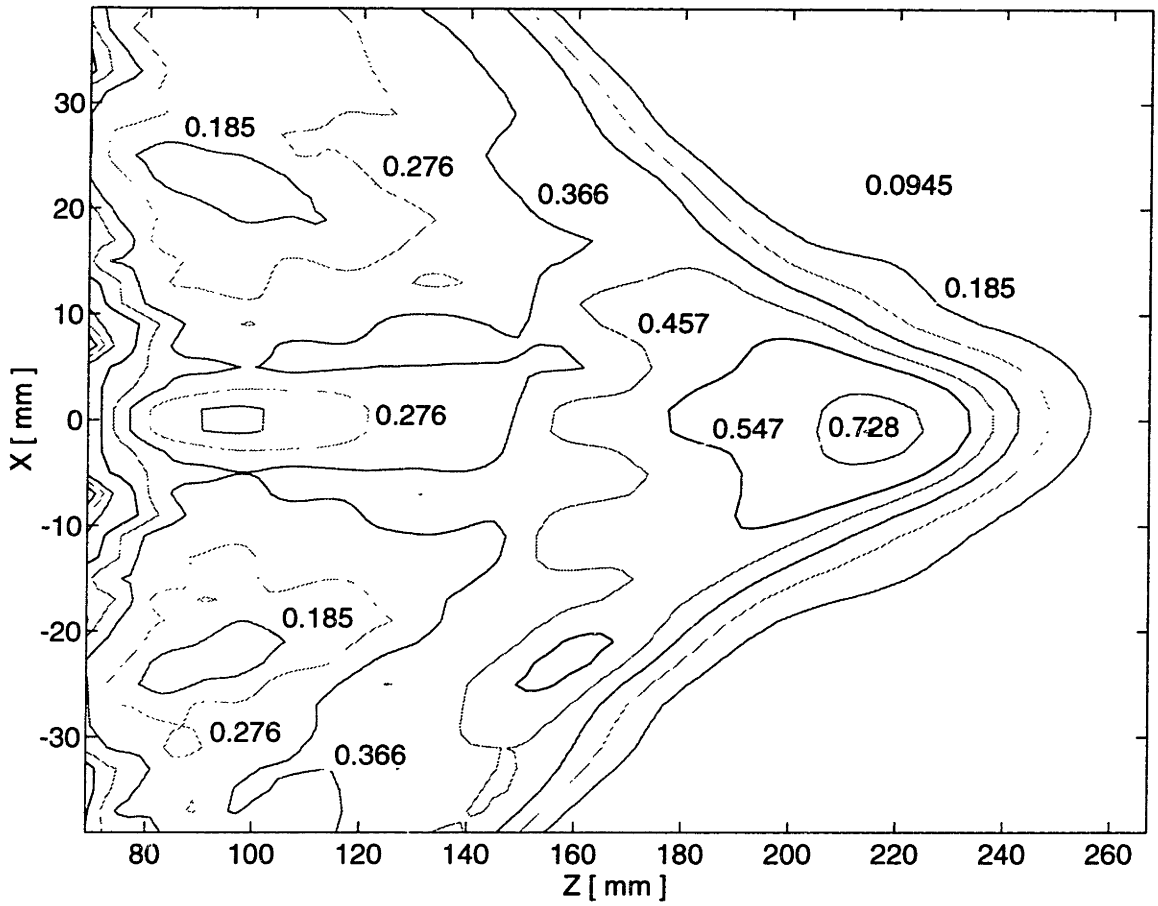

Figure 2-8: Contour plot of the normalized power deposition for all the FSUM transducers.

ultrasound power deposition are resolved. An important issue is the CPU time necessary to compute the ultrasound fields using the Ocheltree and Frizzell routine. It may be possible to circumvent this routine by using a parametric representation of the field from each individual ultrasound transducer. Davis, [53], has approximated the intensity profile from a single transducer as a Gaussian function. It may be possible to use such a functional form to characterize an intensity field from an individual transducer and compute the entire FSUM field from the sum of the transducer parametric functions. As mentioned before, an issue in ultrasound modeling is the intensity distribution near bone and soft tissue interfaces. Breedlove, [54], has modeled this intensity increase at bone surfaces with a one dimensional functional approximation. Using parametric representations, it should be possible to develop a treatment planning ultrasound model that accounts for absorption and reflection characteristics of the various tissue in human anatomy and includes the motion of

the FSUM applicator and the multiple overlapping transducer beams. The development of such a model is beyond the scope of this thesis. However, the development of the thermal model has been guided in general by the observation that the inputs to the thermal model - patient geometry, thermal properties, perfusion, and power deposition - are not usually known to an accuracy greater than 10 percent. Thus the accuracy of the thermal calculations is limited by the accuracy of the inputs.

Chapter 3

Formulation of the Basis Element Algorithm

The solution methodology of the algorithm described in this chapter can be considered a subset of the "source domain methods", [55]. However for the sake of clarity, this method is denoted as the Basis Element Method (BEM). This chapter describes the theoretical background and the algorithm formulation. The theoretical basis for the method is the Green's theorem as applied to the bioheat equation where the temperature at any point in the domain is computed as the convolution integral of the Green's function over the domain volume with internal heat generation. It is noted that the effect of blood flow acts to damp thermal disturbances with an exponential space constant. This damping warrants the separation of the volume integral into two parts: the volume thermally close to the point in the domain where temperature is being computed (the observation point) and the volume thermally distant from this domain point. In the algorithm formulation, the volume integral of the Green's function is further separated into a finite sum of local volume integrals. Exact and approximate analytical expressions for the local volume integrals are derived. These expressions are the Basis Elements and they represent the temperature increment resulting from a source of finite dimension. This is in contrast to the infinitesimal sources of the Green's function.

3.1 Theoretical Background

The solution algorithm for the bioheat equation (Equation (1.1)) is derived from the Green's function solution to the partial differential equation. The steady-state Green's function for Equation (1.1) is computed from a continuous point source of heat at $\vec{r} = \vec{r}_p$ satisfying, [56]:

$$\nabla^2 u - \lambda^2 u = 0 \tag{3.1}$$

where u is the Green's function which is used to construct the full solution with the associated initial and boundary conditions. For example, in a region with applied heating, zero initial temperature, and boundaries at specified temperatures, $T_B(s)$, the solution for the temperature field is:

$$T(\vec{r}) = \int_V \frac{Q(\vec{r}_p)}{k_m} u(\vec{r}, \vec{r}_p)\, dV - \int_S T_B(s)\, \vec{n} \cdot \nabla u\, ds \tag{3.2}$$

where V and S are the tissue volume and surface over which the integral is carried out and $\vec{n}$ is the unit normal vector from the boundary surface. This general solution decouples the initial problem into different components, each representing separately the individual effects of the power deposition (first term on the right side of Equation (3.2)) and the boundary conditions (second term on the right side of Equation (3.2)). In the context of interactive hyperthermia therapy planning, only those components of the temperature field which are affected by a change in the treatment plan need be recalculated. This offers a potential increase in speed, and also allows the separate effect of various changes to be individually examined.

This approach has further advantages, which are better illustrated by considering the Green's function for an infinite non-perfused domain:

$$u_{np}(|\vec{r} - \vec{r}_p|) = \frac{1}{4\pi|\vec{r} - \vec{r}_p|} \tag{3.3}$$

in contrast to the Green's function in an infinite domain *with* perfusion:

$$u(|\vec{r} - \vec{r}_p|) = \frac{e^{-\lambda|\vec{r} - \vec{r}_p|}}{4\pi|\vec{r} - \vec{r}_p|} \tag{3.4}$$

In comparing Equations (3.3) and (3.4), note that perfusion has the effect of damping the influence of thermal perturbations with an exponential weight factor. The magnitude of the

Table 3.1: Typical perfusion lengths for various tissues.

Tissue	Perfusion [ml/min-100 g]	L_p [cm]
muscle	5	1.2
tumor	45	0.40
liver	100	0.27

exponential factor is governed by a length scale, called the perfusion length (L_p), which is inversely proportional to perfusion.

$$L_p = \sqrt{\frac{k_m}{\omega \rho_b c_b}} = \frac{1}{\lambda} \tag{3.5}$$

Table 3.1 shows some representative perfusion lengths for typical values of perfusion with k_m = 0.5 W/m-°C, c_b=4.2 J/g-°C, and ρ_b = 1.0 g/cm^3.

With consideration of the thermal damping, the integration volume can be broken up into two separate components: 1) the volume, V_{int}, which incorporates the thermally significant sources and 2) the volume, $V - V_{int}$, which includes all the other sources.

$$T(\vec{r}) = \int_{V-V_{int}} \frac{Q(\vec{r}_p)}{k_m} u(\vec{r}, \vec{r}_p)\, dV_p + \int_{V_{int}} \frac{Q(\vec{r}_p)}{k_m} u(\vec{r}, \vec{r}_p)\, dV_p \tag{3.6}$$

$$V_{int} = \frac{4}{3} \pi (N_p L_p)^3$$

$$V_{int} < V$$

where the volume V_{int} is necessarily smaller than volume V and N_p is an arbitrary constant. These two terms in Equation (3.6) are treated separately according to the desired speed-accuracy trade-off. The volume integral over V_{int}, which contains the thermally significant sources, is performed with greater accuracy than the volume integral over $(V - V_{int})$ which contains the less influential sources. This approach can potentially realize a great savings in computational effort as the volume V_{int} is reduced (smaller N_p).

The BEM achieves significant efficiency at several levels of the computation. First, savings in effort is realized as the volume of integration for each point is reduced. Second,

changes in the heating field can be further decoupled into those which produce local changes in temperature and those which are sufficiently far from the point of interest such that their contribution to local temperature need not be considered. Third, tissue volumes which include regions of non-uniform thermal properties, specifically perfusion, can be considered within the context of this model. Although each specific Green's function strictly applies to the entire volume, in practice the damping effect of perfusion allows each Green's function to be an approximate, local solution to the bioheat equation, exerting influence on the tissue temperature only in the immediate vicinity of the point source.

3.2 Algorithm Formulation

The method is formulated to solve steady-state 3-D tissue heat transfer problems on an irregular geometry with variable internal heat generation, piece-wise homogeneous thermal properties and perfusion and non-homogeneous boundary conditions. The Green's function solution of Equation (1.1) forms the heart of the solution method and thus the algorithm requires the appropriate Green's function for each of the heat transfer situations encountered within the context of tissue thermal modeling.

The formulation of the necessary Green's functions is greatly simplified by the limited spatial influence of thermal disturbances. The main simplification afforded by the thermal damping permits the Green's functions associated with the irregular geometry, to be approximated with Green's functions of regular geometry. For instance, an arbitrarily shaped boundary is modeled as being in the limit either locally planar or locally spherical. Further, the approximate Green's functions need not consider all the thermal effects in the domain. Only those effects in the thermally significant volume, V_{int}, need to be considered.

The algorithm formulation proceeds from the volume integral of Equation (3.6) by re-writing the expression as a finite sum of local volume integrals.

$$T(\vec{r}) = \int_{V-V_{int}} \frac{Q(\vec{r}_p)}{k_m} u(\vec{r},\vec{r}_p) dV_p + \sum_{j=1}^{N} \int_{V_j} \frac{Q(\vec{r}_p)}{k_m} u(\vec{r},\vec{r}_p)\, dV_p = \Theta_0 + \sum_{j=1}^{N} \Theta_j \quad (3.7)$$

where the point source position, $\vec{r}_p$, is in the volume over which the integral is performed

and:

$$V_{int} = P_f \sum_{j=1}^{N} V_j \tag{3.8}$$

where P_f is the "packing factor". For completely efficient and continuous packing of the integration volumes, P_f is equal to 1.

The algorithm achieves further computational efficiency by analytically integrating the expression in Equation (3.7) to give an approximate closed form result, Θ_j, for the local integration volumes, V_j. The particular Θ_j's, however, depend on the actual thermal situation influencing the source at $\vec{r}_p$. It can be imagined that Θ_j is the temperature increment resulting from a source of finite dimension, located at $\vec{r}_p$ and whose source volume is V_j. For clarity, the temperature increment Θ_j, is called the *Basis Element.*

3.2.1 Finite Spherical Sources

For mathematical and computational simplicity, the local volume integral, V_j, is taken over a sphere centered at the point $\vec{r}_p$ and forms a spherical source. The sources are close-hexagonally packed in the heated volume and weighted according to the magnitude of the tissue internal heat generation at $\vec{r}_p$. Figure 3-1 shows schematically how a general heating function is approximated as a set of finite spherical sources.

Figure 3-2 shows the temperature construction from the sum of the contributions of the sources in the near-field (the volume V_{int}) to the temperature at the point marked "X". The sources in the far-field, outside the volume V_{int} but inside the heated volume V, are lumped together to form a single "macroscopic" Basis Element (Θ_o).

The sources are densely packed into the heated tissue volume, as represented by Figure 3-1, to approximate the total power deposition. Each source gives rise to a Basis Element and the temperature at a given point in the tissue is constructed from the sum of the contributions of each source to the temperature at that point:

$$T(\vec{r}) = \sum_{j=1}^{N} \Theta_j(|\vec{r}_j - \vec{r}|) \tag{3.9}$$

where N is the number of sources; $\vec{r}$ is the position vector of the point at which temperature is computed; and $\vec{r}_j$ is the position vector of the source j. A distinct advantage of Equation

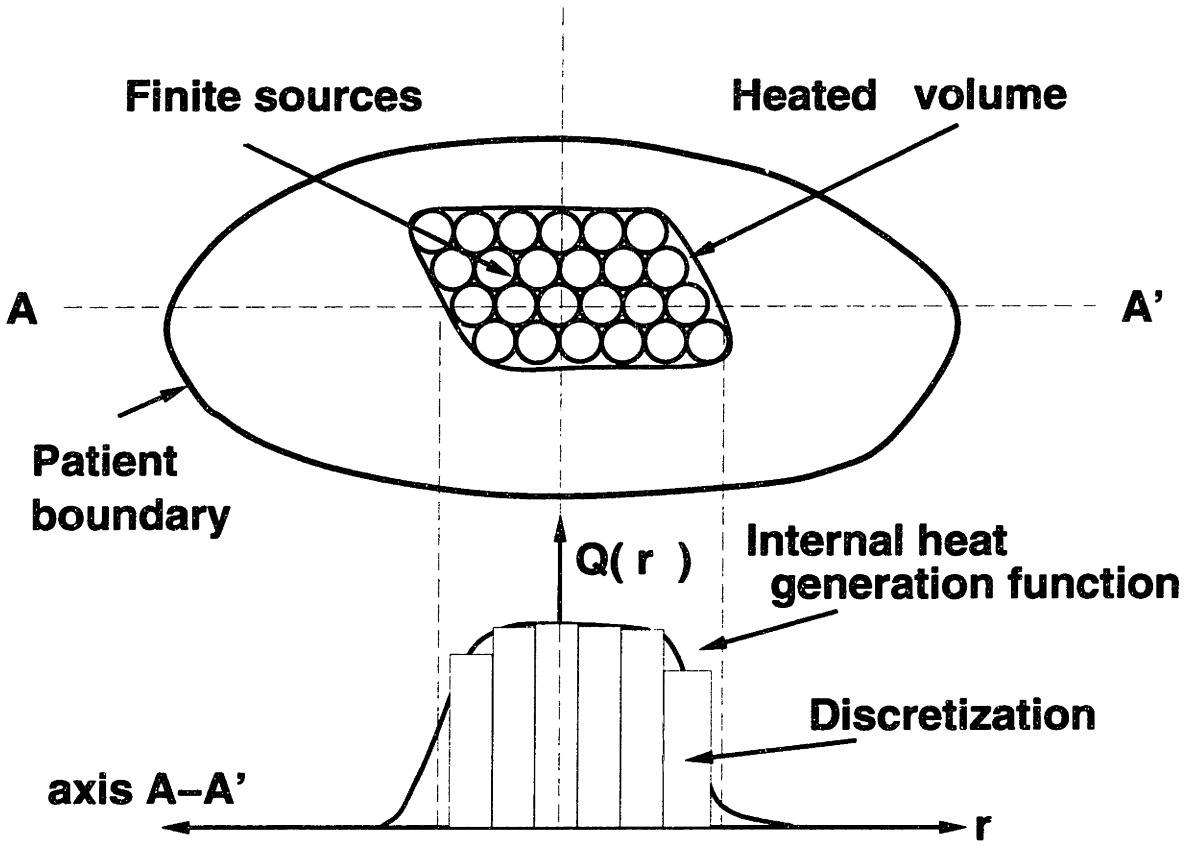

Figure 3-1: Finite spherical and uniform sources representing the heated volume.

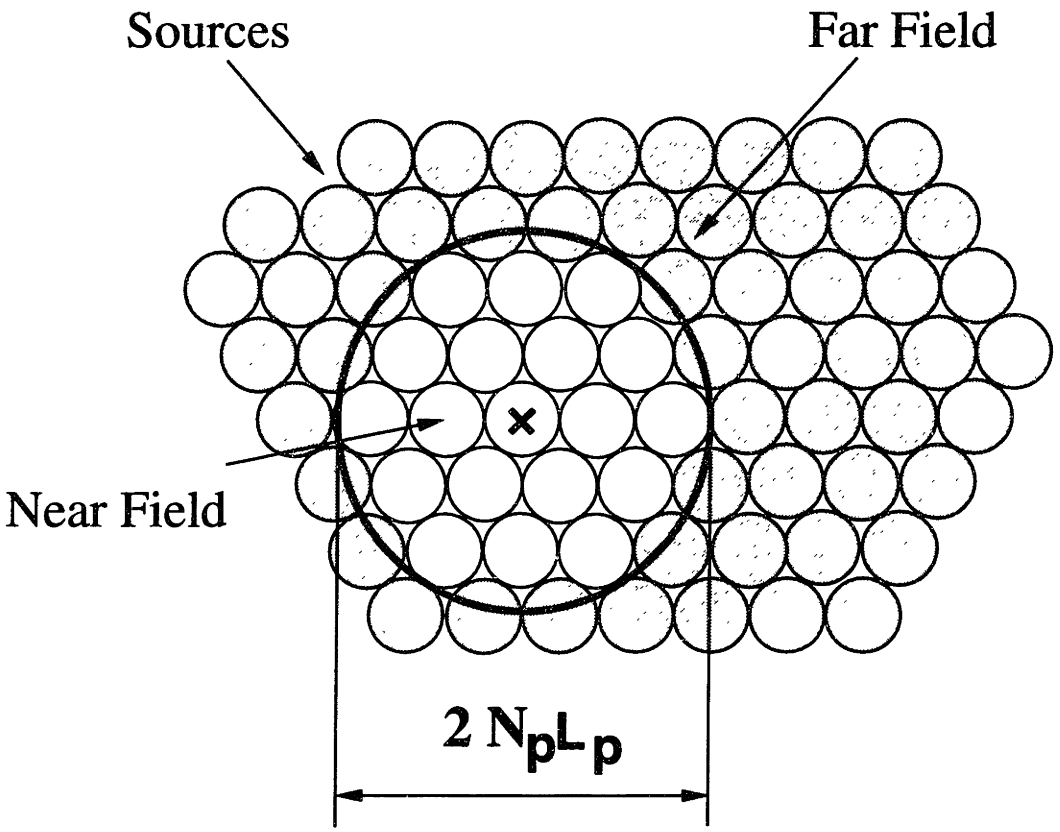

$$L_p = \sqrt{\frac{k_m}{\omega \rho_b c_b}}$$

Figure 3-2: The construction of temperature from the near-field sources.

(3.9) is that the BEM is consistent with physical intuition. Thus, insight into the tissue heat transfer can easily be employed within the context of the solution algorithm to simplify and speed the temperature calculations. The temperature contribution from sources at a distance of more than several perfusion lengths can neglected. This simplification allows Equation (3.9) to be modified by summing the Basis Elements over a sub-volume which is smaller than the heated volume. The temperature at a point is then:

$$\begin{aligned} T(\vec{r}) &= \sum_{j=1}^{M} \Theta_j(|\vec{r}_j - \vec{r}|) \\ M &\sim L_p^3 \\ M &< N \end{aligned} \tag{3.10}$$

where M is the number of sources over which the sum is made and is necessarily smaller than N. The sources at each $\vec{r}_j$ position are contained within a tissue sub-volume around the position $\vec{r}$ whose characteristic dimension is of the order L_p.

In the following subsections, the derivations of the Basis Elements (Θ_j's) are presented for the thermal situations explicitly considered. For these derivations, some dimensionless variables are defined:

$$\theta_j = \frac{\Theta_j\, k_m}{Q_j\, a^2} \qquad R = \frac{R'}{a} \qquad R_+ = \frac{R'_+}{a} \qquad Pe = \frac{\omega\, \rho_b\, c_b\, a^2}{k_m} \tag{3.11}$$

where θ_j is the dimensionless temperature increment (Basis Element), k_m is the conductivity, a is the Basis Element radius, Q_j is the magnitude of the source, R' is the source local radial coordinate, R is the dimensionless radial coordinate, and Pe is a dimensionless parameter which characterizes the ratio of energy convected by blood flow to the energy conducted through the tissue. Figure 3-3 shows a schematic diagram of the process by which the Basis Elements are derived. A source function is selected and the Basis Element is solved from the source in the domain of the thermal situation being considered.

Individual Basis Elements are derived for a number of heat transfer conditions encountered in hyperthermic temperature field calculations. These Basis Elements apply to a domain point near a planar or spherical boundary of the first, second or third kind, and near a planar or spherical boundary separating subdomains of different thermal properties and

perfusion. The following subsections detail the derivation of these Basis Elements and the relevant assumptions made in their formulation.

3.2.2 Free Space Basis Elements

The free space Basis Element is used in situations where the spherical source is thermally distant from any thermal disturbance, thus the tissue domain can be approximated as spatially infinite with uniform thermal properties and perfusion. Three free space Basis Elements are derived, each with different internal heat generation distributions: uniform, exponential and Gaussian.

Uniform Basis Element

This Basis Element function is computed from the solution of the bioheat Equation (1.1) for a sphere with uniform internal heat generation located in an infinite tissue volume with uniform perfusion. The governing equation is:

$$\frac{1}{r}\frac{d^2(r\theta_j)}{dr^2} - Pe\,\theta_j = -q_o \tag{3.12}$$

$$q_o = 1 \quad r \leq 1 \tag{3.13}$$

$$q_o = 0 \quad r > 1 \tag{3.14}$$

where θ_j is the Basis Element j which results from the source j. Equation (3.12) is solved with:

$$\theta_j = \frac{1}{Pe}\left[1 - e^{-\sqrt{Pe}}\frac{\sinh(\sqrt{Pe}\,r)}{r} - \frac{e^{-\sqrt{Pe}}}{\sqrt{Pe}}\frac{\sinh(\sqrt{Pe}\,r)}{r}\right] \quad 0 < r \leq 1 \tag{3.15}$$

$$\theta_j = \frac{e^{-\sqrt{Pe}\,r}}{r}\left[\cosh(\sqrt{Pe}) - \frac{\sinh(\sqrt{Pe})}{\sqrt{Pe}}\right]\frac{1}{Pe} \qquad 1 < r \tag{3.16}$$

Note that Equation (3.16) consists of the point source solution multiplied by a weight factor. This characteristic is used later to aid in the derivation of approximate solutions for uniform sources from the point source solution.

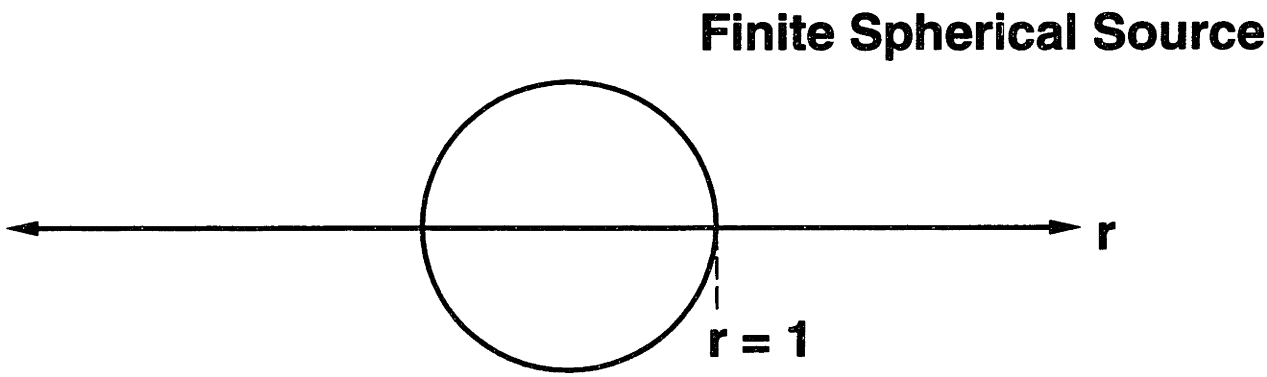

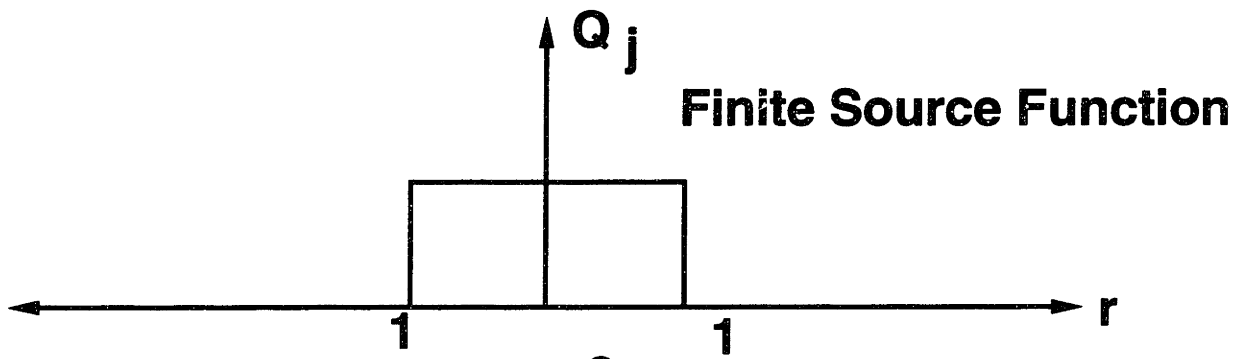

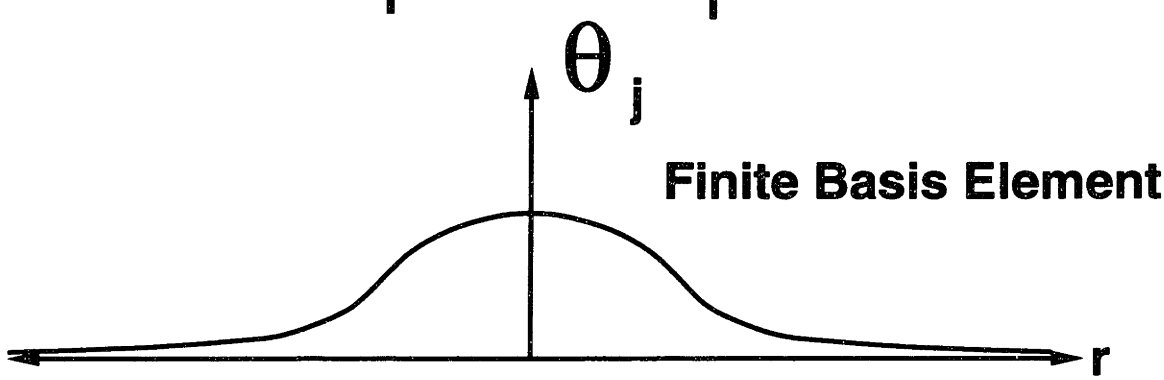

$$\frac{1}{r}\frac{d^2}{dr^2}(r\theta_j) - \lambda^2\theta_j = -q_j \qquad r < 1$$

$$\frac{1}{r}\frac{d^2}{dr^2}(r\theta_j) - \lambda^2\theta_j = 0 \qquad r > 1$$

Figure 3-3: Finite Basis Element for a uniform source function.

Exponential Basis Element

The exponential Basis Element function is computed from the solution of the Equation (1.1) for an exponentially heated volume in a free (infinite) tissue volume:

$$\frac{d^2\theta_j}{dr^2} + \frac{2}{r}\frac{d\theta_j}{dr} - Pe\,\theta_j = -e^{-r} \tag{3.17}$$

To solve Equation (3.17), a substitution is made:

$$\frac{d^2(r\theta_j)}{dr^2} - Pe\,(r\theta_j) = -re^{-r} \tag{3.18}$$

The general solution to the differential equation is:

$$r\theta_j = C_1 e^{-\sqrt{Pe}r} + C_2 e^{\sqrt{Pe}r} - \frac{re^{-r}}{1-Pe} - \frac{2e^{-r}}{(1-Pe)^2} \tag{3.19}$$

The boundary conditions stipulate that (1) the temperature tends towards zero as r tends toward infinity and (2) the temperature is finite at $r = 0$. Condition (1) requires C_2 to be zero and C_1 is solved from condition (1). The Basis Element function is thus:

$$\theta_j = \frac{2}{r(1-Pe)^2}\left[e^{-\sqrt{Pe}r} - e^{-r}\right] - \frac{e^{-r}}{1-Pe} \tag{3.20}$$

Gaussian Basis Element

The Gaussian Basis Element function is computed from the solution of the Equation (1.1) for a Gaussian heated tissue volume in free (infinite) space

$$\frac{d^2\theta_j}{dr^2} + \frac{2}{r}\frac{d\theta_j}{dr} - Pe\,\theta_j = -e^{-r^2} \tag{3.21}$$

To solve the previous equation, a substitution is made:

$$u = r\theta_j \tag{3.22}$$

$$\frac{d^2u}{dr^2} - Pe\,u = -re^{-r^2} \tag{3.23}$$

Equation (3.23) can be solved by means of a Fourier sine integral transform. The transform is defined as follows:

$$v(\beta) = \int_0^\infty \sqrt{\frac{2}{\pi}}\sin(\beta r)u(r)dr \tag{3.24}$$

And the inversion formula is:

$$u(r) = \int_0^\infty \sqrt{\frac{2}{\pi}} \sin(\beta r) v(\beta) d\beta \tag{3.25}$$

The term-by-term application of the integral transform turns equation 3.23 into an algebraic equation [57].

$$-\beta^2 v - Pe\, v = -\frac{\sqrt{2}\beta}{4} e^{\frac{-\beta^2}{4}} \tag{3.26}$$

The transform variable is then algebraically solved:

$$v(\beta) = \frac{\sqrt{2}\,\beta}{4(Pe + \beta^2)} e^{\frac{-\beta^2}{4}} \tag{3.27}$$

The transform inversion formula from [57] is applied and θ_j is solved.

$$\theta_j = \frac{1}{4r} e^{Pe/4} \left[e^{-\sqrt{Pe}\,r} erfc(\frac{1}{2}\sqrt{Pe} - r) - e^{\sqrt{Pe}\,r} erfc(\frac{1}{2}\sqrt{Pe} + r) \right] \tag{3.28}$$

The top panel in Figure 3-4 shows the internal heat generation distribution through the source and the bottom panel shows the resulting Basis Element.

3.2.3 Boundary Conditions

In order to consider the effect of boundary conditions on the domain temperature, special boundary Basis Elements are derived. The procedure for deriving these Basis Elements is different from the free space Basis Elements. In that case, the free space Basis Elements were solved directly from the differential equation which describes the temperature resulting from one of the finite source functions. In this case, the Basis Elements are found by a convolution volume integral of the particular Green's function over the finite source distribution.

Non-homogeneous boundary conditions are satisfied as the superposition of the temperature resulting from the homogeneous and the non-homogeneous component. Figure 3-5 shows a schematic diagram of this superposition. The bioheat transfer equation in the domain Ω with a boundary condition imposed on the surface S is split up into its homogeneous and non-homogeneous boundary components:

$$T = T_h + T_{nh} \tag{3.29}$$

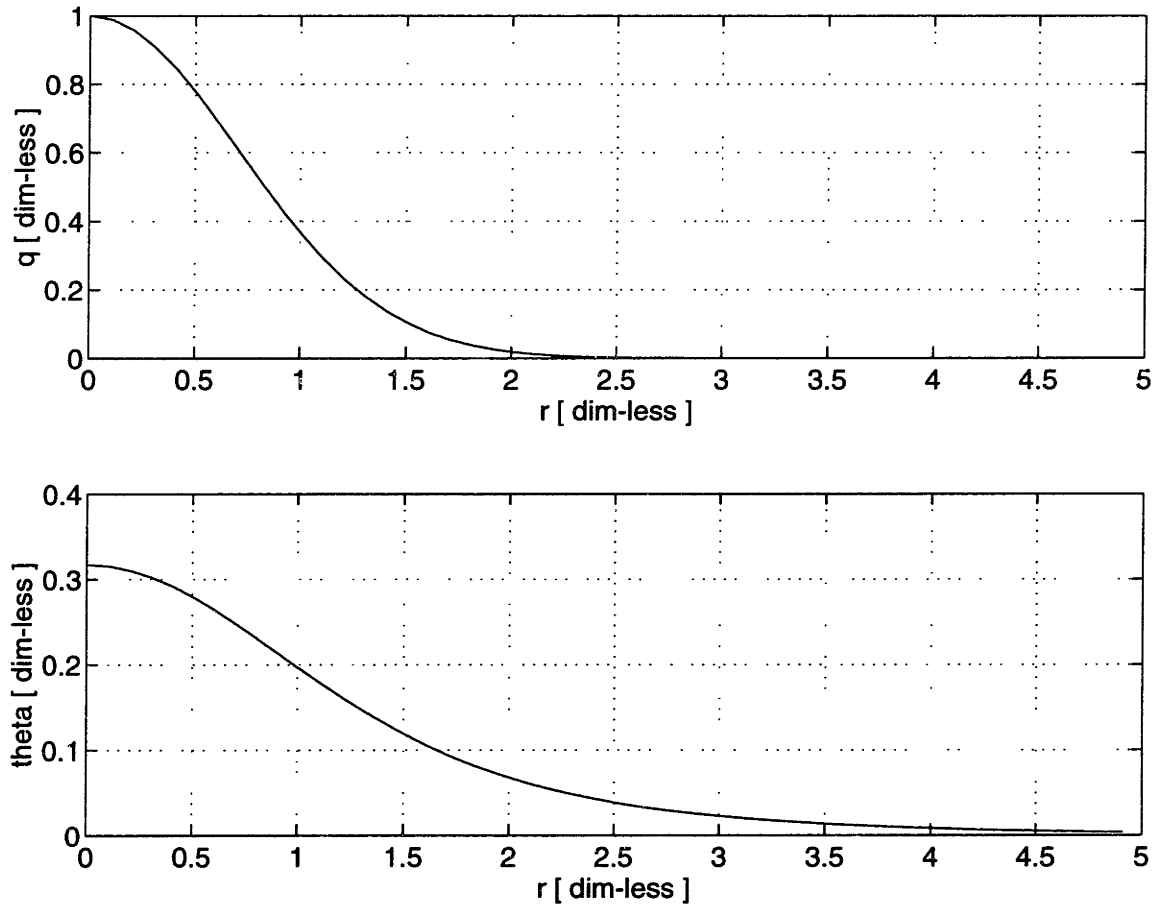

Figure 3-4: The internal heat generation distribution through the source is shown in the top panel and the bottom panel shows the resulting Basis Element with Pe = 0.5.

$$\Omega \; : \quad k_m \nabla^2 T_h \; - \; \omega \, \rho_b \, c_b \, T_h \; = \; -Q(\vec{r}) \tag{3.30}$$

$$S \; : \quad k_m \frac{\partial T_h}{\partial \vec{n}} \; + h \, T_h \; = \; 0 \tag{3.31}$$

$$\Omega \; : \quad k_m \nabla^2 T_{nh} \; - \; \omega \, \rho_b \, c_b \, T_{nh} \; = \; 0 \tag{3.32}$$

$$S \; : \quad k_m \frac{\partial T_{nh}}{\partial \vec{n}} \; + \; h \, T_{nh} \; = \; f \tag{3.33}$$

where T_h and T_{nh} are respectively the homogeneous and non-homogeneous temperature components, h is the heat transfer coefficient and f is the boundary condition function.

Due to the effect of thermal damping by perfusion, the boundaries can be approximated as either piece-wise planar or spherical surfaces. The solution for the homogeneous component of the temperature (T_h) is provided by the superposition of boundary Basis Elements which maintain the homogeneous condition. These Basis Elements are derived from a Green's function influenced by a planar or spherical boundary with uniform homogeneous boundary conditions. It is assumed that these Green's functions take the form of the free space Green's function, w, (Equation (3.4)) plus a matching function, v, which insures that the boundary condition is satisfied.

$$\Omega : \; u(\vec{r}, \vec{r}_p) \; = \; w(\vec{r}, \vec{r}_p) \; + \; v(\vec{r}, \vec{r}_p) \tag{3.34}$$

The form of the particular matching function, v, depends on the type of boundary condition and the boundary geometry. The matching functions for boundary conditions of the first, second and third kind applied on planar and spherical boundaries are formulated in the following subsections.

The homogeneous boundary Basis Elements are determined from the convolution integral of the Green's function, u, over the finite source distribution function, q, (uniform, exponential, or Gaussian).

$$\Theta_j(\vec{r}) \; = \; \int_{V_s} \frac{q(\vec{r}_p)}{k_m} u(\vec{r}, \vec{r}_p) dV \tag{3.35}$$

where V_s is the volume of the finite source. Thus far in the method formulation, the boundary Basis Elements have been derived only for the uniform source distribution function.

Nonhomogeneous Boundary Conditions

$$k \frac{\partial T}{\partial n} + hT = f$$

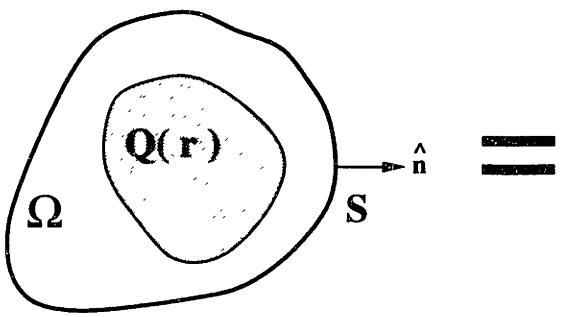

=

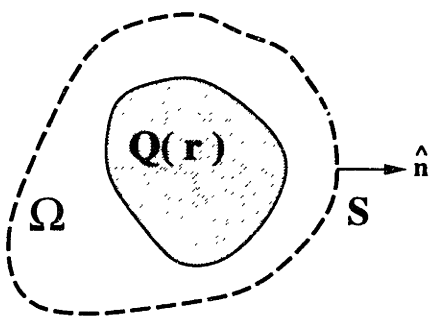

+

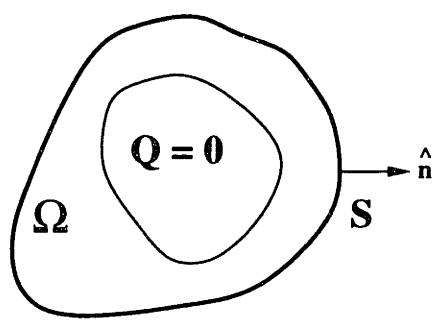

$$k \frac{\partial T_h}{\partial n} + hT_h = 0$$

$$k \frac{\partial T_{nh}}{\partial n} + hT_{nh} = f$$

$$\mathbf{T = T_h + T_{nh}}$$

Figure 3-5: Superposition of homogeneous and non-homogeneous boundary conditions.

Planar Surface Boundary Conditions

The Green's function for homogeneous boundary condition applied on a planar surface is computed by transforming the coordinates of the free space Green's function and matching function to a polar system where the point source is at $r' = 0$, $y = -y_p$ and the boundary is at $y = 0$. The Green's function with, v, the matching function in open form is as follows:

$$u = \frac{e^{-\lambda\sqrt{r'^2+(y+y_p)^2}}}{4\pi\sqrt{r'^2+(y+y_p)^2}} + \frac{1}{4\pi}\int_0^\infty A\, e^{-\nu|y-y_p|}\,\frac{J_o(\eta r')}{\nu}\,\eta\, d\eta \tag{3.36}$$

$$\nu = \sqrt{\eta^2 + \lambda^2} \tag{3.37}$$

$$r' = \sqrt{x^2 + z^2} \tag{3.38}$$

where $J_o(z)$ is the zeroth order Bessel function of the first kind. The Fourier-Bessel coefficient, A, is found depending on the type of boundary condition.

For the zero temperature condition on the planar boundary of a semi-infinite body, A is found to be equal to -1, [58], and the complete Green's function is:

$$u = \frac{e^{-\lambda R'}}{4\pi R'} - \frac{e^{-\lambda R'_+}}{4\pi R'_+} \tag{3.39}$$

$$R'^2 = x^2 + (y + y_p)^2 + z^2 \tag{3.40}$$

$$R'^2_+ = x^2 + (y - y_p)^2 + z^2 = r'^2 + (y - y_p)^2 \tag{3.41}$$

where x, y, and z are defined in Figure 3-6. It is evident that this Green's function is the combination of a source and a mirror sink positioned outside the domain. The Green's function u is then used in the volume integral of Equation (3.35) to compute the Basis Element for this type of boundary condition. Since this integral has already been computed for the free space uniform Basis Element, the result for the boundary Basis Element can be immediately written.

$$\theta_j = \frac{1}{Pe}\left[\cosh(\sqrt{Pe}) - \frac{\sinh(\sqrt{Pe})}{\sqrt{Pe}}\right]\left[\frac{e^{-\sqrt{Pe}\,R}}{R} - \frac{e^{-\sqrt{Pe}\,R_+}}{R_+}\right] \tag{3.42}$$

This method is also used to find the Green's functions for the other boundary conditions applied on the plane. For the zero heat flux condition on the planar boundary, A is found to be equal to -1 and the complete Green's function is:

$$u = \frac{e^{-\lambda R'}}{4\pi R'} + \frac{e^{-\lambda R'_+}}{4\pi R'_+} \tag{3.43}$$

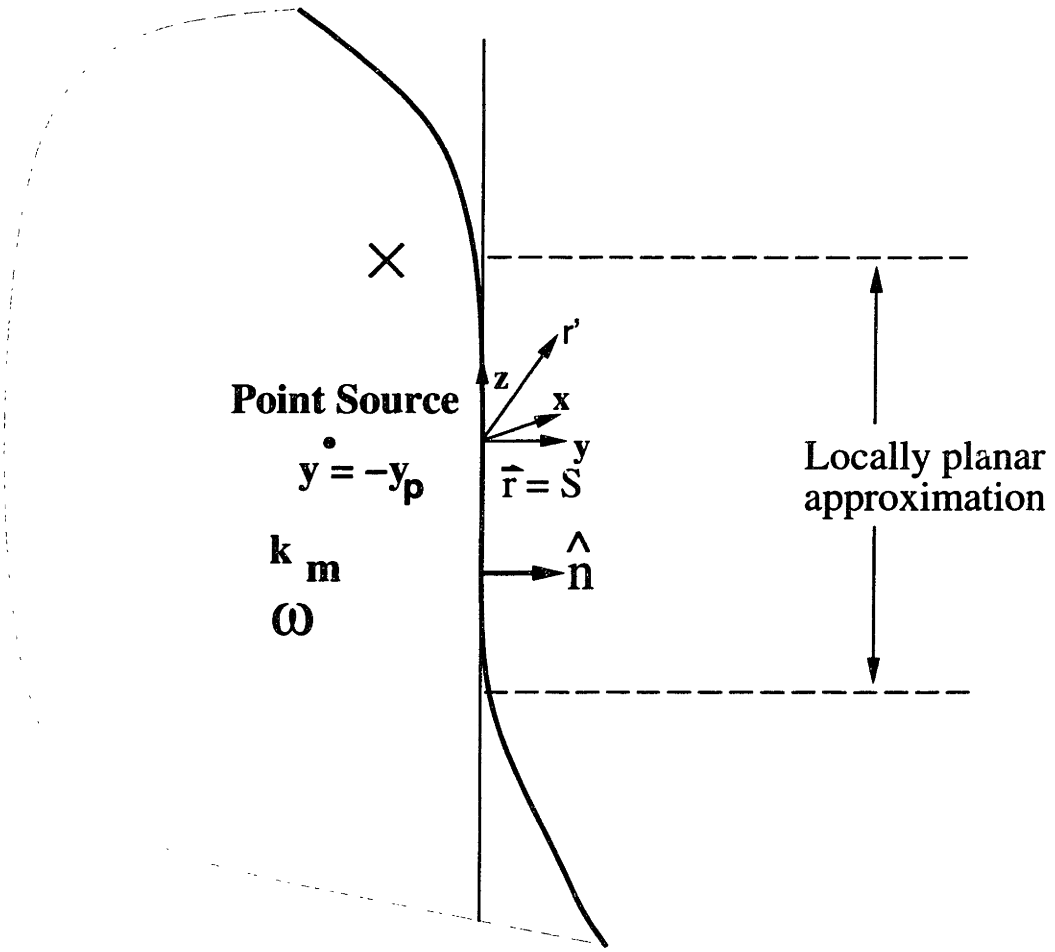

Figure 3-6: Schematic diagram of a planar boundary Basis Element for external boundaries.

The volume integral of Equation (3.35) for the uniform Basis Element of the boundary condition of the second kind is:

$$\theta_j = \frac{1}{Pe}\left[\cosh(\sqrt{Pe}) - \frac{\sinh(\sqrt{Pe})}{\sqrt{Pe}}\right]\left[\frac{e^{-\sqrt{Pe}R}}{R} + \frac{e^{-\sqrt{Pe}R_+}}{R_+}\right] \tag{3.44}$$

In the case of a boundary condition of the third kind (convection), the coefficient A is:

$$A = \frac{1 + \frac{Bi}{\eta}}{Bi + \eta} \tag{3.45}$$

$$Bi = \frac{h\,a}{k_m} \tag{3.46}$$

For this boundary condition, a closed form of the integral in Equation (3.36) has not been found. Thus, the Green's function is approximated with a free space Green's function plus

a function which matches the boundary condition. The approximation is as follows.

$$u \approx \frac{e^{-\lambda R'}}{4\pi R'} + \frac{e^{-\lambda R'_+}}{4\pi R'_+}\left[\frac{\frac{a y_p}{r'}(\lambda + \frac{1}{r'}) - Bi}{\frac{a y_p}{r'}(\lambda + \frac{1}{r'}) + Bi}\right] \tag{3.47}$$

The exact closed form convolution integral of this Green's function over the uniform source has not been found, but has been approximated using the results for the other boundary Basis Elements.

$$\theta_j \approx \frac{1}{Pe}\left[\cosh(\sqrt{Pe}) - \frac{\sinh(\sqrt{Pe})}{\sqrt{Pe}}\right]\left\{\frac{e^{-\sqrt{Pe}R}}{R} + \frac{e^{-\sqrt{Pe}R_+}}{R_+}\left[\frac{\frac{y_p}{r'}(\sqrt{Pe} + \frac{a}{r'}) - Bi}{\frac{y_p}{r'}(\sqrt{Pe} + \frac{a}{r'}) + Bi}\right]\right\} \tag{3.48}$$

The temperature component from the non-homogeneous boundary condition is computed from the 1-D approximation for an infinite planar boundary:

$$\Omega \; : \quad k_m \frac{d^2 T_{nh}}{d y^2} - \omega \rho_b c_b T_{nh} = 0 \tag{3.49}$$

$$S(y=0) \; : \quad k_m \frac{dT_{nh}}{d\vec{n}} + h T_{nh} = f \tag{3.50}$$

where y is the spatial coordinate and the boundary is at $y = 0$. For a boundary condition of the first kind, the dimensionless temperature component is:

$$\theta_{nh} = \frac{T_{nh}}{T_B} = e^{\lambda y} \tag{3.51}$$

where the boundary is fixed at temperature T_B. For a boundary condition of the second kind, the dimensionless temperature component is:

$$\theta_{nh} = \frac{T_{nh} k_m}{qL} = \frac{e^{\lambda y}}{\lambda L} \tag{3.52}$$

where q is the heat flux and L is an arbitrary length scale. For the boundary condition of the third kind, the the dimensionless temperature component is:

$$\theta_{nh} = \frac{T_{nh}}{T_f} = \frac{Bi\, e^{\lambda y}}{Bi + \lambda L} \tag{3.53}$$

$$Bi = \frac{h L}{k_m} \tag{3.54}$$

where T_f is the fluid temperature, Bi is the Biot number and h is the heat transfer coefficient.

Spherical Surface Boundary Conditions

As mentioned above, irregularly curved external boundaries are approximated as being locally spherical. Such an approximation requires the formulation of the Green's function for a spherical tissue domain with a boundary condition applied at the surface. Figure 3-7 shows a schematic diagram of the domain geometry with the point source. From Carslaw and Jaeger, 1959, (page 381) [59] the free space Green's function and the "matching" function are:

$$u = \frac{e^{-\lambda R'}}{4\pi R'} - \frac{1}{4\pi\sqrt{r' r_p}} \sum_{n=0}^{\infty} A_n P_n(\mu) I_{n+\frac{1}{2}}(\lambda r') \tag{3.55}$$

$$\mu = \cos(\phi) \tag{3.56}$$

$$R'^2 = r'^2 + r_p^2 - 2 r' r_p \cos(\phi) \tag{3.57}$$

where $I_{n+\frac{1}{2}}(z)$ is the modified Bessel function of the first kind, and $P_n(\mu)$ is the Legendre polynomial of the first kind. The coefficients A_n are determined from the particular boundary condition. For instance, in the case of zero temperature rise on the sphere surface, the Green's function is:

$$u = \frac{e^{-\lambda R'}}{4\pi R'} - \frac{1}{4\pi\sqrt{r' r_p}} \sum_{n=0}^{\infty} (2n+1) P_n(\mu) K_{n+\frac{1}{2}}(\lambda R_c) I_{n+\frac{1}{2}}(\lambda r') \frac{I_{n+\frac{1}{2}}(\lambda r_p)}{I_{n+\frac{1}{2}}(\lambda R_c)} \tag{3.58}$$

where R_c is the radius of curvature for the surface and $K_{n+\frac{1}{2}}(z)$ is the modified Bessel function of the second kind.

In order to obtain an efficient Basis Element, it is desirable to simplify the infinite series into a closed form expression. Since an exact closed form is unrealizable, approximations must be made to recast the solution. The approach taken is to eliminate two of the modified Bessel functions of the first kind by expanding them into an infinite series representation, [60], and combining terms.

$$\sqrt{\frac{\pi}{2 z_1}} I_{n+\frac{1}{2}}(z_1) = \frac{z_1^n}{1 \cdot 3 \cdot 5 \ldots (2n+1)} [1 + f(z_1, n)] \tag{3.59}$$

$$\sqrt{\frac{\pi z_3}{2 z_1 z_2}} \frac{I_{n+\frac{1}{2}}(z_1) I_{n+\frac{1}{2}}(z_2)}{I_{n+\frac{1}{2}}(z_3)} = \left(\frac{z_1 z_2}{z_3}\right)^n \frac{1}{1 \cdot 3 \cdot 5 \ldots (2n+1)} \frac{[1 + f(z_1, n)][1 + f(z_2, n)]}{[1 + f(z_3, n)]} \tag{3.60}$$

$$\frac{I_{n+\frac{1}{2}}(z_1)\, I_{n+\frac{1}{2}}(z_2)}{I_{n+\frac{1}{2}}(z_3)} \approx I_{n+\frac{1}{2}}(\frac{z_1\, z_2}{z_3}) \tag{3.61}$$

This approximation is sufficiently valid in several cases: (1) z_1 or z_2 is a small number; (2) z_3 is close to z_1; or (3) z_3 is close to z_2. The approximation is then combined with the identity, [58]:

$$\frac{e^{-\lambda R'}}{R'} = \sum_{n=0}^{\infty}(2n+1)P_n(\mu)\, K_{n+\frac{1}{2}}(\lambda r')\, I_{n+\frac{1}{2}}(\lambda r_p) \tag{3.62}$$

where $r' > r_p$, otherwise r' and r_p are interchanged. Thus, the approximate Green's function is:

$$u \approx \frac{e^{-\lambda R'}}{4\pi R'} - \frac{e^{-\lambda R'_+}}{4\pi R'_+} \tag{3.63}$$

$$R'^2_+ = R_c^2 + (\frac{r' r_p}{R_c})^2 - 2 r' r_p \cos(\phi) \tag{3.64}$$

where the spherical coordinates r', r_p and ϕ are defined in Figure 3-7.

The complete Basis Element for spherical external boundaries is determined from the integral of the Green's function in Equation (3.35) over the uniform source distribution. The results from the free space and planar boundary Basis Elements can be borrowed to give this approximate integral.

$$\theta_j \approx \frac{1}{Pe}\left[\cosh(\sqrt{Pe}) - \frac{\sinh(\sqrt{Pe})}{\sqrt{Pe}}\right]\left[\frac{e^{-\sqrt{Pe}\,R}}{R} - \frac{e^{-\sqrt{Pe}\,R_+}}{R_+}\right] \tag{3.65}$$

$$R_+^2 = \frac{R_c^2}{a^2} + (\frac{r' r_p}{a\, R_c})^2 - \frac{2 r' r_p}{a^2}\cos(\phi) \tag{3.66}$$

Figure 3-8 shows a comparison between the Basis Element near a spherical boundary held at zero temperature rise (Equation (3.65) plotted as symbols) and the exact solution for the same problem (the numerical volume integral performed over Equation (3.55) plotted as the solid line). The finite source has a radius of 1 and is centered at $r = 0$. The external spherical boundary is located at $r = 1.5$ and has a radius of curvature of 6. The Péclèt number in the domain is 1. For these test parameters, the error is less than 2 percent and the agreement is excellent over the entire range of physiological values of perfusion.

The Green's functions for a spherical tissue volume with a homogeneous boundary condition of the second kind differs from equation (3.55) by only a sign change.

$$u = \frac{e^{-\lambda R'}}{4\pi R'} + \frac{1}{4\pi\sqrt{r' r_p}}\sum_{n=0}^{\infty}(2n+1)\, P_n(\mu)\, K_{n+\frac{1}{2}}(\lambda r_p) I_{n+\frac{1}{2}}(\lambda R_c)\frac{K_{n+\frac{1}{2}}(\lambda r')}{K_{n+\frac{1}{2}}(\lambda R_c)} \tag{3.67}$$

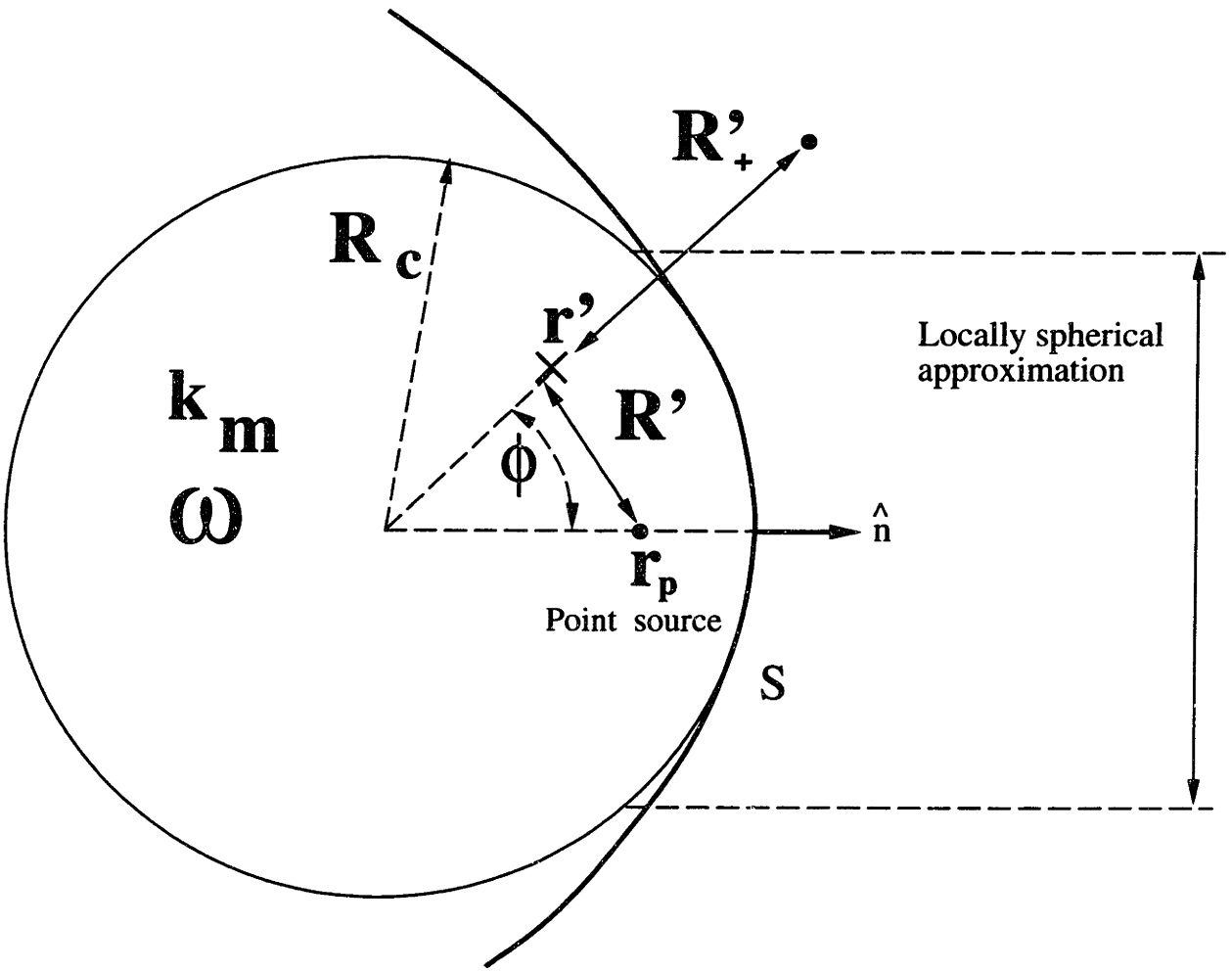

Figure 3-7: Schematic diagram of a spherical boundary Basis Element for external boundaries.

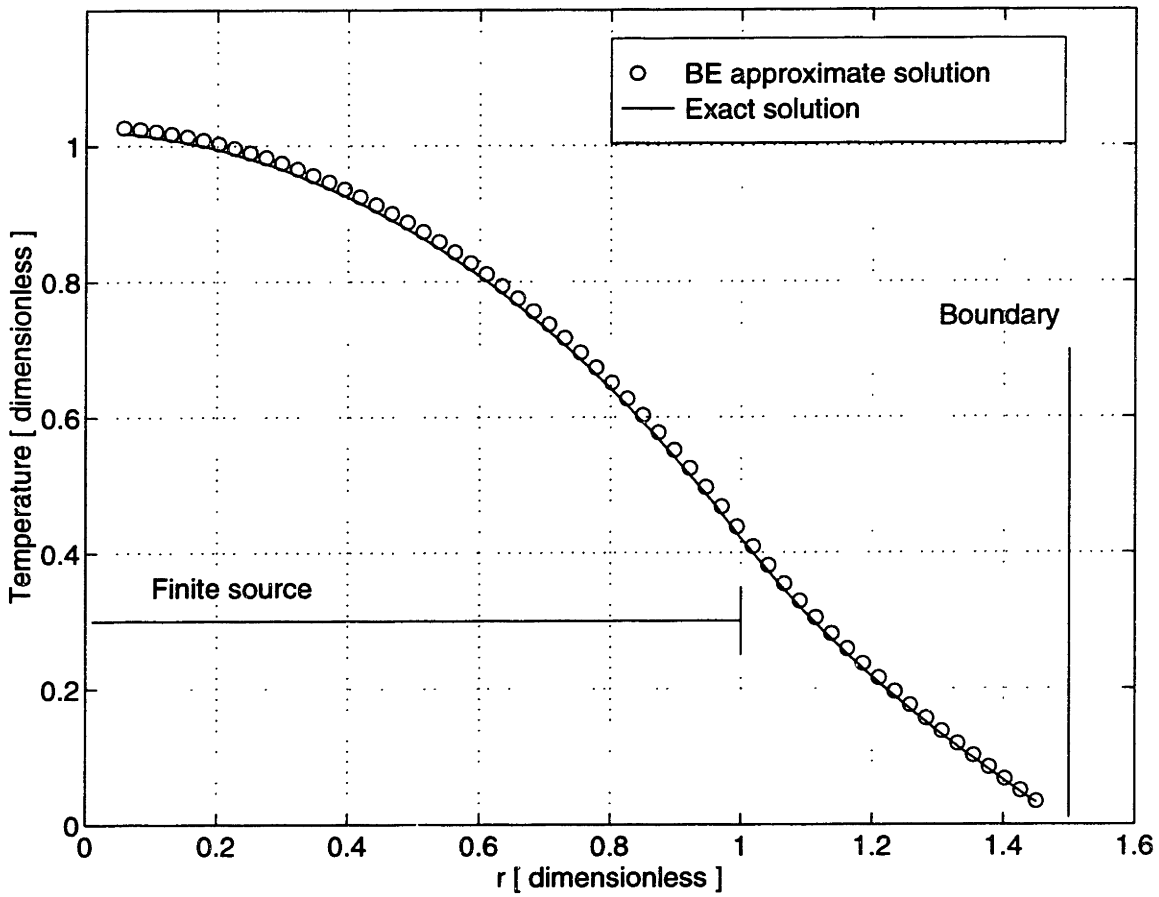

Figure 3-8: Comparison between the exact and approximate solutions for a uniform source near a spherical boundary of the first kind.

By following the same methodology as used above, the closed form Basis Element for a homogeneous boundary of the second kind is found to be:

$$\theta_j \approx \frac{1}{Pe}[\cosh(\sqrt{Pe}) - \frac{\sinh(\sqrt{Pe})}{\sqrt{Pe}}][\frac{e^{-\sqrt{Pe}R}}{R} + \frac{e^{-\sqrt{Pe}R_+}}{R_+}] \tag{3.68}$$

The non-homogeneous temperature component for a spherical boundary is computed from:

$$\Omega \; : \quad k_m \frac{d^2 T_{nh}}{d r'^2} + \frac{2}{r'} k_m \frac{d T_{nh}}{d r'} - \omega \rho_b c_b T_{nh} = 0 \tag{3.69}$$

$$S(r = R_c) \; : \quad k_m \frac{dT_{nh}}{d\vec{n}} + h T_{nh} = f \tag{3.70}$$

where r' is the radial coordinate and R_c is the sphere radius. The solution for the non-homogeneous boundary condition of the first kind is:

$$\theta_{nh} = \frac{T_{nh}}{T_B} = \frac{\sinh(\sqrt{Pe}\, r)}{r \sinh(\sqrt{Pe})} \tag{3.71}$$

where R_c forms the length scale for Pe and r. The non-homogeneous second kind solution is:

$$\theta_{nh} = \frac{T_{nh}\, k_m}{q\, R_c} = \frac{\sinh(\sqrt{Pe}\, r)}{r \sqrt{Pe} \cosh(\sqrt{Pe})} \tag{3.72}$$

And the non-homogeneous third kind solution is:

$$\theta_{nh} = \frac{T_{nh}}{T_f} = \frac{\sinh(\sqrt{Pe}\, r)}{r} \frac{Bi}{Bi \sinh(\sqrt{Pe}) + \sinh(\sqrt{Pe}) - \sqrt{Pe}\cosh(\sqrt{Pe})} \tag{3.73}$$

$$Bi = \frac{h R_c}{k_m} \tag{3.74}$$

3.2.4 Variable Thermal Properties and Perfusion

The Basis Element methodology models thermal properties and perfusion as varying spatially in a piece-wise homogeneous fashion. The tissue domain is divided into subdomains, each with different properties and perfusion. Figure 3-9 diagrams this model of spatially varying perfusion. Regions in a subdomain thermally distant from the internal boundaries are denoted as the continuous zones. The continuous zones lie several perfusion lengths from any thermal perturbation, thus the free space Basis Element, Equations (3.15) and

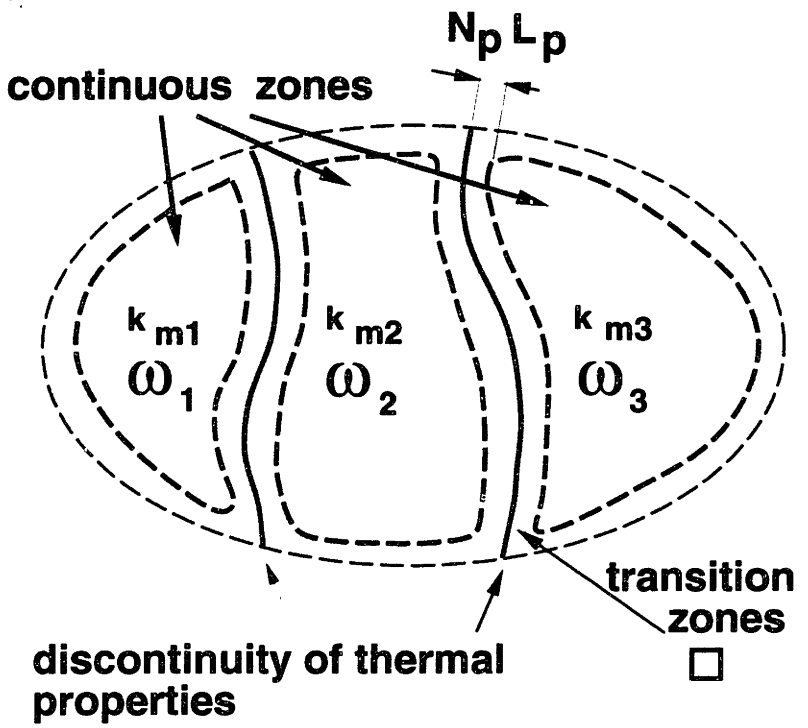

Figure 3-9: Model for varying thermal properties and perfusion.

(3.16), is a valid approximation for the superposition of temperature in these zones. The transition zones mark the areas where the contributions from more than one subdomain must be considered. The solution for temperature in the transition zones near an arbitrarily shaped internal surface is approximated as the superposition of Basis Elements influenced by piece-wise planar or spherical internal surfaces.

The formulation of Basis Elements for computing the temperature in the transition zones requires the derivation of the appropriate Green's functions. The effect of the thermal damping permits the entire domain to be locally approximated as consisting of no more than two adjacent subdomains with either a planar or spherical boundary separation. Thus, for instance, the Green's function in subdomain 1 of Figure 3-9 is derived to consider only the thermal effects of subdomains 1 and 2 and neglects the effect of subdomain 3.

For piece-wise properties and perfusion, the complete Green's function, u_1, in subdomain 1, is assumed to be the free space Green's function plus a matching function which insures continuity of heat flux and temperature across the subdomain separation. In the

case where the point source is in subdomain 1, the Green's function in subdomain 1 is:

$$\Omega_1 : \quad u_1(\vec{r}, \vec{r}_p) \;=\; w_1(\vec{r}, \vec{r}_p) \;+\; v_1(\vec{r}, \vec{r}_p) \tag{3.75}$$

where w_1 is the free space Green's function and v_1 is the "matching" function. In subdomain 2, the Green's function is:

$$\Omega_2 : \quad u_2(\vec{r}, \vec{r}_p) \;=\; B\, w_2(\vec{r}, \vec{r}_p) \tag{3.76}$$

where w_2 is the free space Green's function and B is a weight function that insures continuity of temperature and heat flux across the subdomain boundary. The complete Green's functions, in both domains, are solved using various techniques, depending of the internal boundary geometry. The formulation of these Green's functions is detailed in the following subsections.

The Basis Elements are determined from the convolution integral of the Green's function, u_1 and u_2, over the finite source distribution function, q, (uniform, exponential, or Gaussian).

$$\Theta_{j1}(\vec{r}) \;=\; \int_{V_s} \frac{q(\vec{r}_p)}{k_{m1}} u_1(\vec{r}, \vec{r}_p) dV \tag{3.77}$$

$$\Theta_{j2}(\vec{r}) \;=\; \int_{V_s} \frac{q(\vec{r}_p)}{k_{m2}} u_2(\vec{r}, \vec{r}_p) dV \tag{3.78}$$

where V_s is the volume of the finite source. Thus far in the method formulation, the Basis Elements have been derived only for the uniform source distribution function.

Planar Internal Boundary Basis Element

Figure 3-10 shows a schematic diagram for the formulation of the Green's function for an internal planar boundary which separates two semi-infinite subdomains of different thermal properties and perfusion. This Green's function has been solved by Carslaw and Jaeger, (page 375) 1959 [59]. In subdomain 1, the solution is a free space Green's function plus a free space sink and a matching function in integral form and in subdomain 2, the solution is integral form is:

$$u_1 \;=\; \frac{e^{-\lambda_1 R'}}{4\,\pi\, R'} \;-\; \frac{e^{-\lambda_1 R'_+}}{4\,\pi\, R'_+} \;+\; \frac{1}{2\pi} \int_0^\infty \frac{e^{-\eta_1 (y+y_p)}}{\eta_1 + \kappa\, \eta_2}\, \xi\, J_o(\xi\, r')\, d\xi \tag{3.79}$$

$$u_2 = \frac{1}{2\pi}\int_0^\infty \frac{\kappa\, e^{-\eta_2 y - \eta_1 y_p}}{\eta_1 + \kappa\,\eta_2}\,\xi\, J_o(\xi\, r')\, d\xi \tag{3.80}$$

$$\eta_1 = \sqrt{\xi^2 + \lambda_1^2} \qquad \eta_2 = \sqrt{\xi^2 + \lambda_2^2} \tag{3.81}$$

$$\lambda_1^2 = \frac{\omega_1 \rho_b\, c_b}{k_{m1}} \qquad \lambda_2^2 = \frac{\omega_2 \rho_b\, c_b}{k_{m2}} \tag{3.82}$$

$$\kappa = k_{m2} \,/\, k_{m1} \tag{3.83}$$

$$r' = \sqrt{x^2 + z^2} \tag{3.84}$$

In order to obtain an efficient Basis Element, it is desirable to simplify the open form Green's function into an approximate analytical expression. An approximate, closed form solution consists of the free space point source and a closed form matching function. It is further assumed that the matching function is a free space Green's functions times a weight function where the weight function is not a function of the source position. In each of the two subdomains, the weight functions are solved by maintaining continuity of temperature

$$u_1 = \kappa u_2 \qquad \text{at} \quad \text{y} = 0 \tag{3.85}$$

and heat flux across the internal boundary.

$$\frac{\partial u_1}{\partial y} = \frac{\partial u_2}{\partial y} \qquad \text{at} \quad \text{y} = 0 \tag{3.86}$$

The approximate solution for for Green's function in subdomain 1 is:

$$u_1 \approx \frac{e^{-\lambda_1 R'}}{4\,\pi\, R'} + \frac{e^{-\lambda_1 R'_+}}{4\,\pi\, R'_+}\left[\frac{\lambda_1\,\kappa\, r' + \kappa - \lambda_2\, r' - 1}{\lambda_1\,\kappa\, r' + \kappa + \lambda_2\, r' + 1}\right] \tag{3.87}$$

and subdomain 2 is:

$$u_2 \approx \frac{1}{4\,\pi}\,\frac{e^{-\lambda_2 R'}}{R'}\,\kappa\, e^{-r_b(\lambda_1 - \lambda_2)}\left[1 + \frac{\lambda_1\,\kappa\, r' + \kappa - \lambda_2\, r' - 1}{\lambda_1\,\kappa\, r' + \kappa + \lambda_2\, r' + 1}\right] \tag{3.88}$$

where:

$$R' = \sqrt{x^2 + (y + y_p)^2 + z^2} \tag{3.89}$$

$$R'_+ = \sqrt{x^2 + (y - y_p)^2 + z^2} \tag{3.90}$$

and the source is at ($x = 0$, $y = -y_p$, $z = 0$) and R'_+ is the distance of the observation point (x, y, z) from the weighted mirror source associated with the matching function at ($x = 0$, $y = y_p$, $z = 0$). The corresponding Basis Elements are thus:

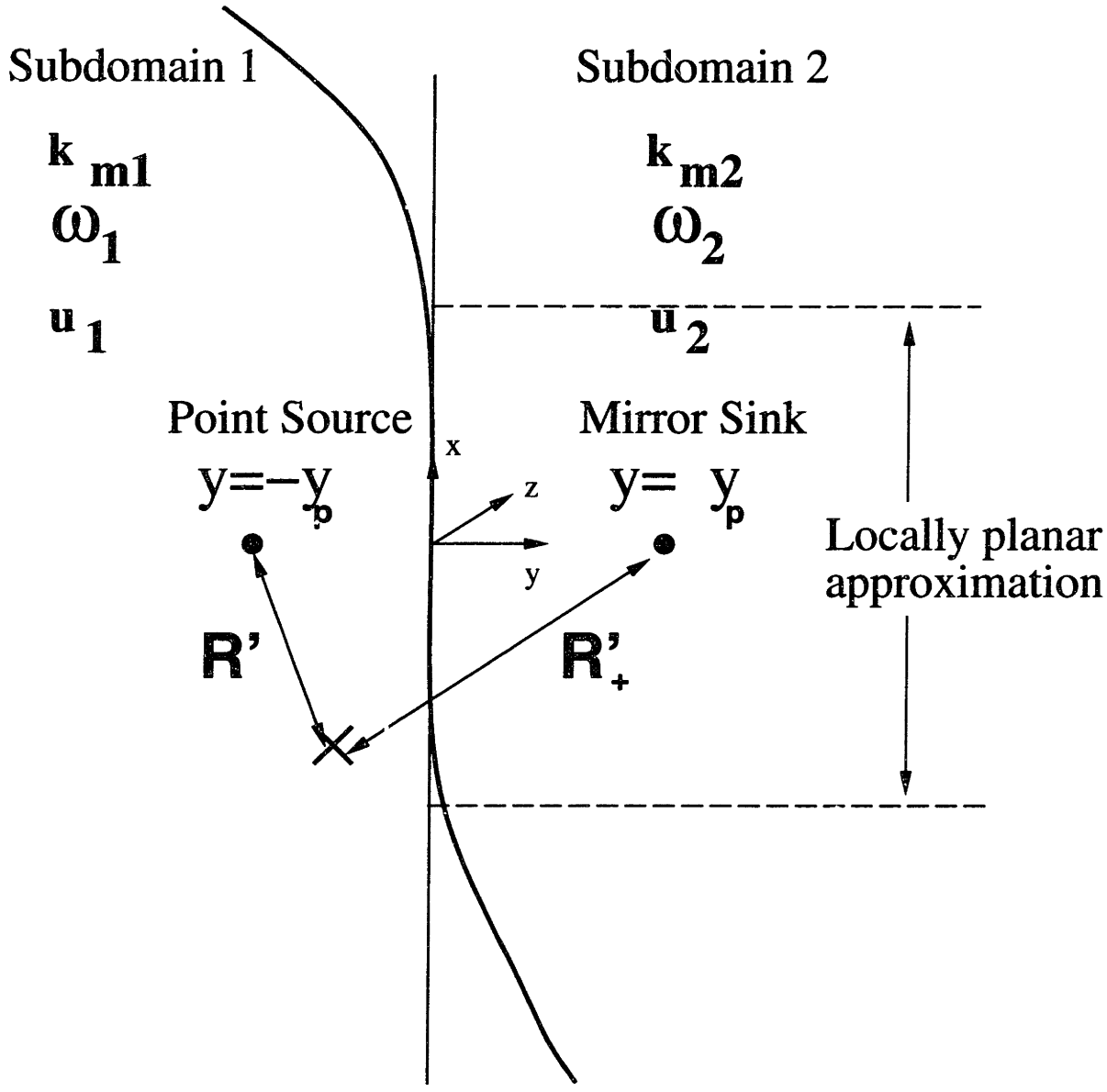

Figure 3.10: Schematic diagram of an internal planar boundary Basis Element.

$$\theta_{j1} \approx \frac{1}{Pe_1}\left[\cosh(\sqrt{Pe_1}) - \frac{\sinh(\sqrt{Pe_1})}{\sqrt{Pe_1}}\right] \times \tag{3.91}$$

$$\times \left\{\frac{e^{-\sqrt{Pe_1}R}}{4\pi R} + \frac{e^{-\sqrt{Pe_1}R_+}}{4\pi R_+}\left[\frac{\sqrt{Pe_1}\kappa r + \kappa - \sqrt{Pe_2}r - 1}{\sqrt{Pe_1}\kappa r + \kappa + \sqrt{Pe_2}r + 1}\right]\right\} \tag{3.92}$$

$$\theta_{j2} \approx \frac{1}{Pe_1}\left[\cosh(\sqrt{Pe_1}) - \frac{\sinh(\sqrt{Pe_1})}{\sqrt{Pe_1}}\right] \times \tag{3.93}$$

$$\times \frac{1}{4\pi}\frac{e^{-\sqrt{Pe_2}R}}{R}\kappa e^{-r(\sqrt{Pe_1}-\sqrt{Pe_2})}\left[1 + \frac{\sqrt{Pe_1}\kappa r + \kappa - \sqrt{Pe_2}r - 1}{\sqrt{Pe_1}\kappa r + \kappa + \sqrt{Pe_2}r + 1}\right] \tag{3.94}$$

Spherical Internal Boundary Basis Element

Figure 3-11 shows the schematic diagram for the formulation of the Green's function for an internal boundary which separates a finite spherical subdomain from an infinite subdomain of different thermal properties and perfusion. The finite tissue sphere has a perfusion of ω_1, a thermal conductivity of k_{m1}, a point source at $(r = r_p, \phi = 0)$ and is surrounded by infinite tissue volume with perfusion of ω_2 and and a thermal conductivity of k_{m2}. This Green's function has been solved by Carslaw and Jaeger, (page 381) 1959, [59], with, in subdomain 1, a free space point source plus a matching function in integral form and in subdomain 2, with an open form integral.

$$u_1 = \frac{e^{-\lambda_1 R'}}{4\pi R'} + \sum_{n=0}^{\infty} A_n P_n(\mu)\frac{I_{n+\frac{1}{2}}(\lambda_1 r')}{\sqrt{r'}} \tag{3.95}$$

$$u_2 = \frac{1}{4\pi}\sum_{n=0}^{\infty} B_n P_n(\mu)\frac{K_{n+\frac{1}{2}}(\lambda_2 r')}{\sqrt{r'}} \tag{3.96}$$

$$\mu = cos(\phi); \tag{3.97}$$

$$R'^2 = r'^2 + r_p^2 - 2r' r_p cos(\phi); \tag{3.98}$$

where A_n and B_n are series coefficients and $K_{n+\frac{1}{2}}(z)$ is the modified Bessel function of the second kind. The coefficients, A_n and B_n are determined from the continuity of temperature and heat flux condition at the internal boundary.

In order to obtain an efficient Basis Element, it is necessary to simplify the open forms into approximate analytical expressions. The primary difficulty in this task arises from

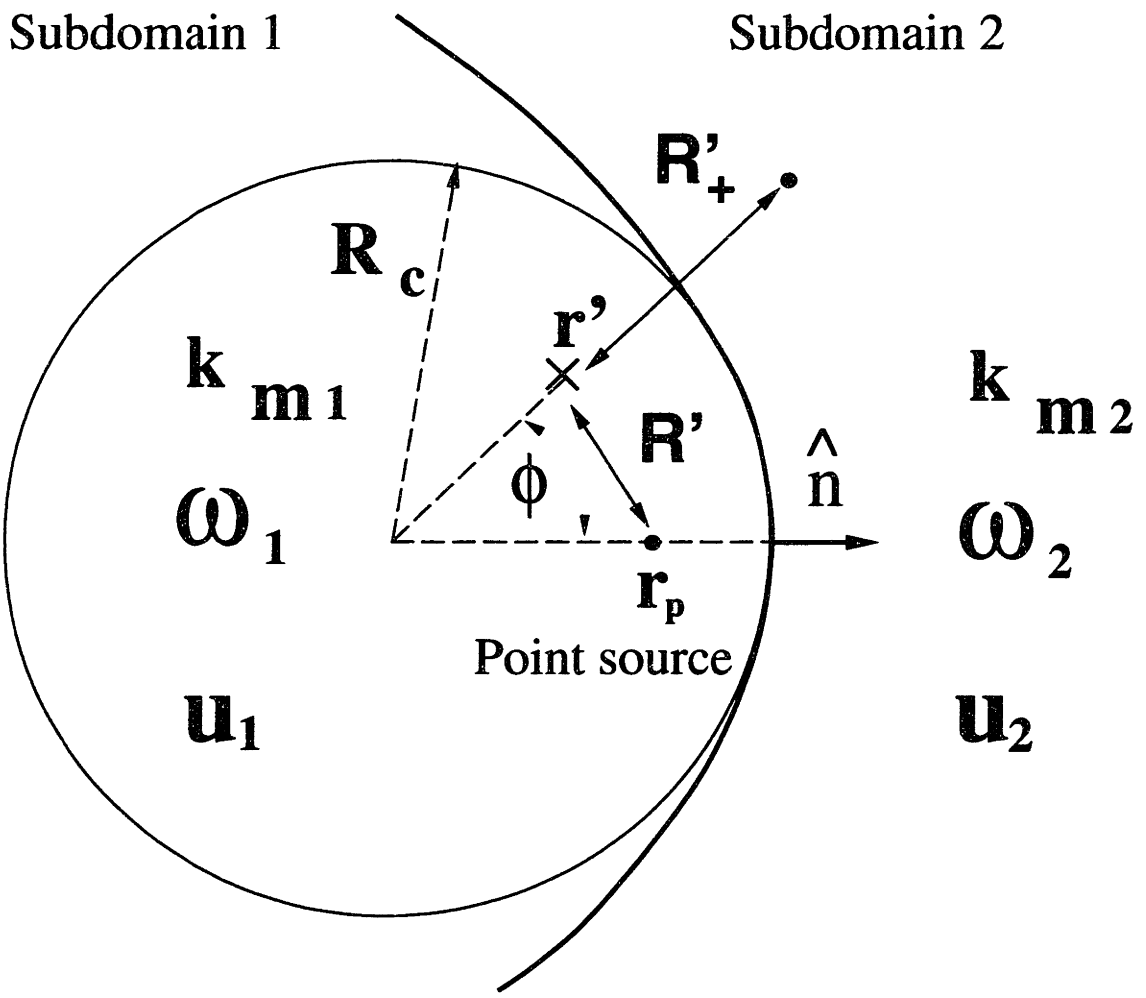

Figure 3-11: Schematic diagram of a spherical boundary Basis Element for an internal boundary.

satisfying the continuity of heat flux condition at the boundary. An approach uses the low order (n=0) derivative of the modified Bessel functions of the first and second kind.

$$\frac{I_\nu(z)}{\sqrt{z}} \approx \frac{e^z}{z\sqrt{2\pi}} \tag{3.99}$$

$$\frac{d}{dz}\left(\frac{I_\nu(z)}{\sqrt{z}}\right) \approx \frac{e^z}{z\sqrt{2\pi}}\left(1 - \frac{1}{z}\right) \approx \frac{I_\nu(z)}{\sqrt{z}}\left(1 - \frac{1}{z}\right) \tag{3.100}$$

$$\frac{K_\nu(z)}{\sqrt{z}} \approx \sqrt{\frac{\pi}{2}}\frac{e^{-z}}{z} \tag{3.101}$$

$$\frac{d}{dz}\left(\frac{K_\nu(z)}{\sqrt{z}}\right) \approx -\sqrt{\frac{\pi}{2}}\left(\frac{e^{-z}}{z} + \frac{e^{-z}}{z^2}\right) \approx \frac{K_\nu(z)}{\sqrt{z}}\left(1 + \frac{1}{z}\right) \tag{3.102}$$

Continuity of temperature across the boundary requires that:

$$u_1 = \kappa u_2 \qquad \text{at } r' = R_c \tag{3.103}$$

$$\frac{e^{-\lambda_1 R'_c}}{4\pi R'_c} + \sum_{n=0}^{\infty} A_n P_n(\mu)\frac{I_{n+\frac{1}{2}}(\lambda_1 R_c)}{\sqrt{R_c}} = \kappa\frac{1}{4\pi}\sum_{n=0}^{\infty} B_n P_n(\mu)\frac{K_{n+\frac{1}{2}}(\lambda_2 R_c)}{\sqrt{R_c}} \tag{3.104}$$

$$R'^2_c = R_c^2 + r_p^2 - 2R_c r_p cos(\phi); \tag{3.105}$$

and continuity of heat flux across the boundary requires:

$$\frac{\partial u_1}{\partial r'} = \frac{\partial u_2}{\partial r'} \qquad \text{at } r' = R_c \tag{3.106}$$

$$\frac{-1}{4\pi\sqrt{R_c}}\sum_{n=0}^{\infty}(2n+1)P_n(\mu)\frac{I_{n+\frac{1}{2}}(\lambda_1 R_c)}{\sqrt{R_c}}K_{n+\frac{1}{2}}(\lambda_1 R_c)\left(1 + \frac{1}{\lambda_1 R_c}\right) \tag{3.107}$$

$$+ \sum_{n=0}^{\infty} A_n P_n(\mu)\frac{I_{n+\frac{1}{2}}(\lambda_1 R_c)}{\sqrt{R_c}}\left(1 - \frac{1}{\lambda_1 R_c}\right) \tag{3.108}$$

$$\approx \sum_{n=0}^{\infty} B_n P_n(\mu)\frac{K_{n+\frac{1}{2}}(\lambda_2 R_c)}{\sqrt{R_c}}\left(1 + \frac{1}{\lambda_2 R_c}\right) \tag{3.109}$$

where R_c is the radius of curvature of the tissue sphere.

The coefficients A_n and B_n are solved using Equation (3.61) and the continuity conditions. The approximation of Equation(3.61) allows the solution of the Green's function to be put in closed form.

$$u_1 \approx \frac{e^{-\lambda_1 R'}}{4\pi R'} - \left[\frac{1 + \frac{1}{\lambda_1 R_c} - \frac{1}{\kappa} - \frac{1}{\kappa\lambda_2 R_c}}{1 + \frac{1}{\lambda_1 R_c} + \frac{1}{\kappa} + \frac{1}{\kappa\lambda_2 R_c}}\right]\frac{e^{-\lambda_1 R'_+}}{4\pi R'_+} \tag{3.110}$$

$$u_2 \approx \frac{e^{-\lambda_2 R'}}{4\pi R'} \left[1 - \frac{1 + \frac{1}{\lambda_1 R_c} - \frac{1}{\kappa} - \frac{1}{\kappa \lambda_2 R_c}}{1 + \frac{1}{\lambda_1 R_c} + \frac{1}{\kappa} + \frac{1}{\kappa \lambda_2 R_c}} \right] \frac{e^{(\lambda_1 - \lambda_2) R'_+}}{\kappa} \tag{3.111}$$

This approximate Green's function is used in the volume integral of Equations (3.77) and (3.78) to compute the Basis Element near internal spherical boundaries. In order to demonstrate that this is a valid approximation, the exact solution for a uniform spherical source near a spherical internal boundary is compared to the approximate formulation derived from Equations (3.110) and (3.111). Figure 3-12 shows the comparison where the finite source is centered at $r = 0$ and extends to $r = 1$. Inside the internal and spherical tissue subdomain, the Péclèt number is 1 and outside the spherical subdomain ($R_c = 1.5$), the Péclèt number is 2. The results show excellent agreement between the approximate and exact solutions (1 percent and less) over the entire range of perfusion values available in physiology.

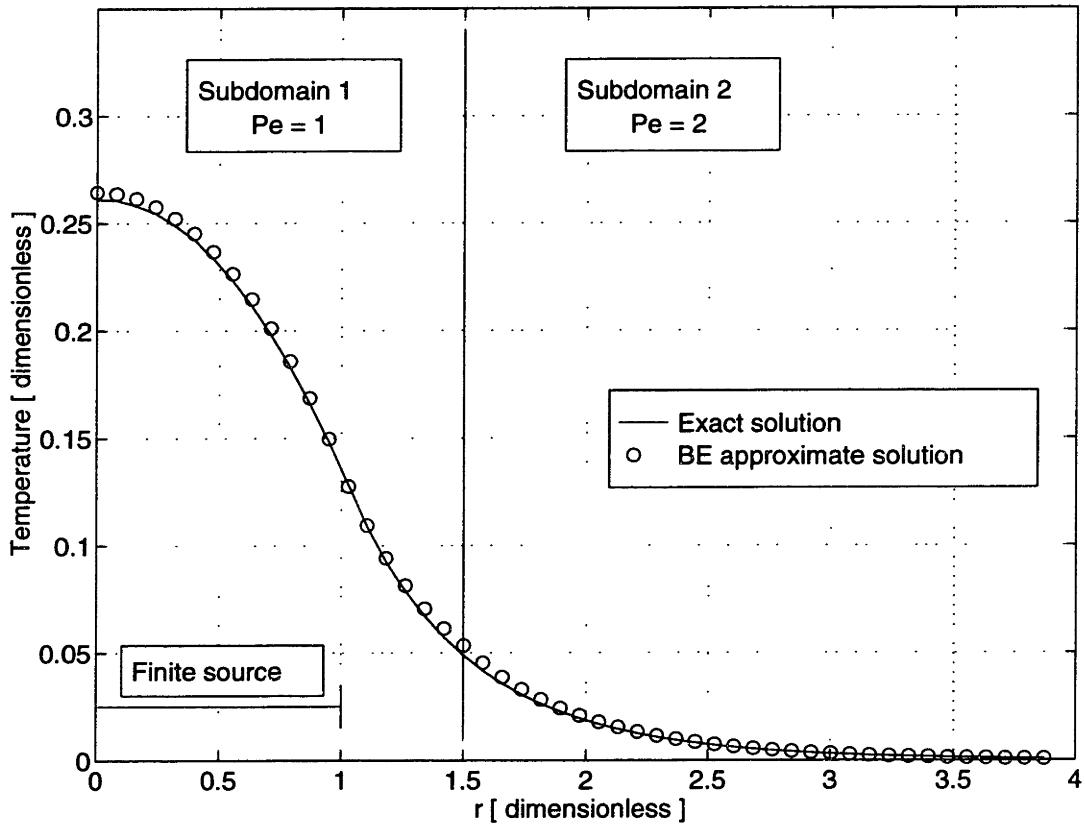

Figure 3-12: Comparison of exact and approximate solution for a uniform source near a spherical internal boundary between subdomains with differential thermal properties and perfusion.

Chapter 4

Implementation of the Basis Element Method

This chapter describes the implementation of the Basis Element algorithm specific to this thesis. The BEM is a generally applicable methodology for the solution of tissue heat transfer problems. However, the implementation on which many of the results in this thesis are based is by no means the only implementation possible. Much of the present algorithm has been designed based on what was perceived to be both computationally fast and easy to implement.

The algorithm takes as input a discrete representation of perfusion, thermal conductivity, internal heat generation and the coordinates of each domain node, and outputs the temperature at the nodes. Issues specific to the method implementation concern the discrete model representation of the continuous problem and the computer code incarnation of the method. These are discussed below, along with the integration of the method into the treatment visualization system.

4.1 Discrete Model Representation

4.1.1 Geometry

The model represents the tissue as a three-dimensional Cartesian mesh of non-uniformly spaced discrete domain nodes. It is at each domain node that thermal properties, perfusion and SAR are stored and the temperature is computed. Each of the three coordinate axes has a coordinate index (i for the X direction, j for the Y direction, and k for the Z direction). Thus the position of any domain node in the tissue field is given by the position vector:

$$\vec{r}_{i,j,k} = (X_{i,j,k}, Y_{i,j,k}, Z_{i,j,k}) \tag{4.1}$$

These points can be irregularly spaced with the restriction that:

$$X_{i+1,j,k} > X_{i,j,k} \tag{4.2}$$

$$Y_{i,j+1,k} > Y_{i,j,k} \tag{4.3}$$

$$Z_{i,j,k+1} > Z_{i,j,k} \tag{4.4}$$

where i ranges from 0 to N_x, j ranges from 0 to N_y, and k ranges from 0 to N_z. The number of domain nodes along a coordinate axis is typically between 20 and 60 depending on the problem being modeled.

Domain nodes which lie on an external boundary are distinguished by their coordinate index which is set to either 0, N_x, N_y, or N_z. Thus the boundaries, which are on the extremes of the tissue domain, are also on the extremes of the coordinate index. Figure 4-1 shows the configuration of the geometric representation. The domain nodes are the locations at which thermal properties, perfusion, and heat generation are discretized and temperature is computed.

4.1.2 Basis Element Packing

Figure 4-2 shows a diagram of the close-hexagonal packing of the Basis Elements to compute temperature. The configuration shows the relative position of the Basis Elements

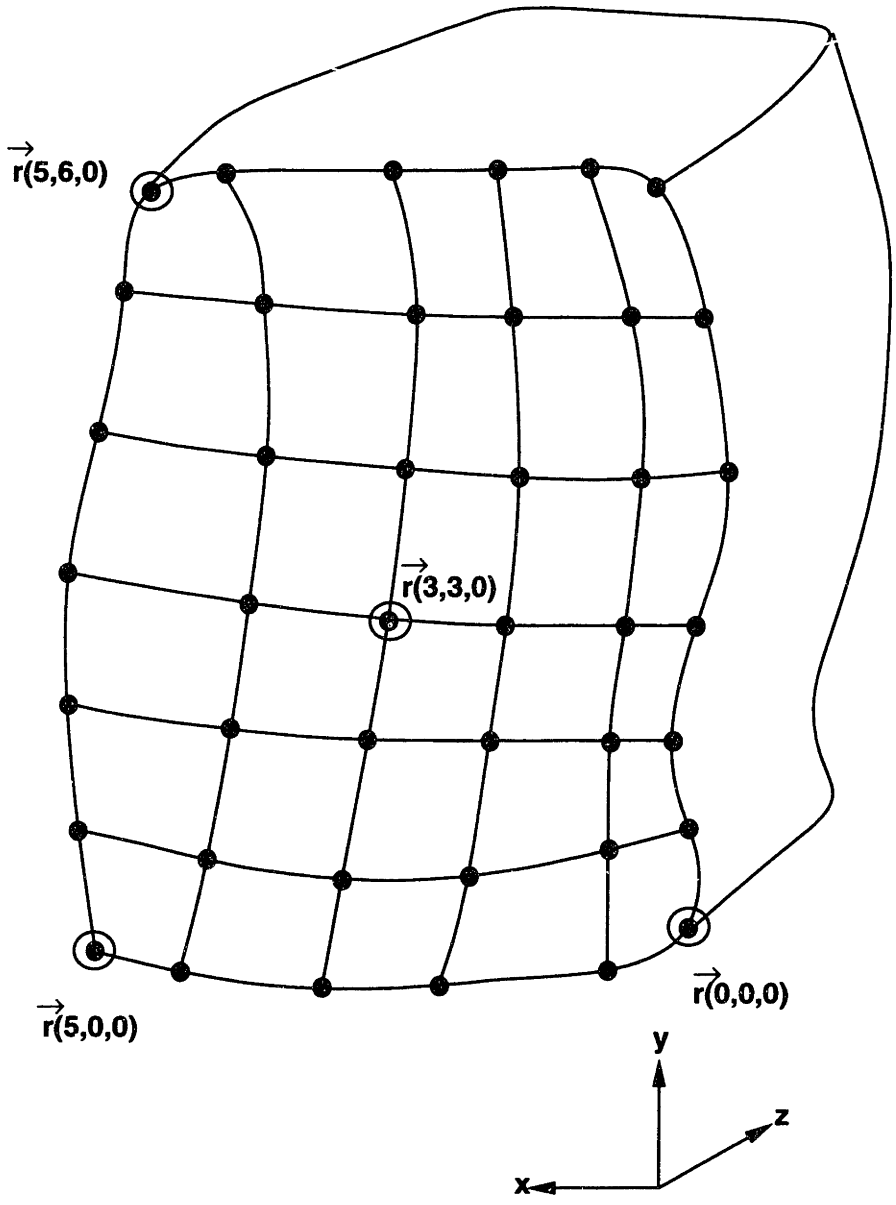

Figure 4-1: Schematic diagram of the representation of geometry.

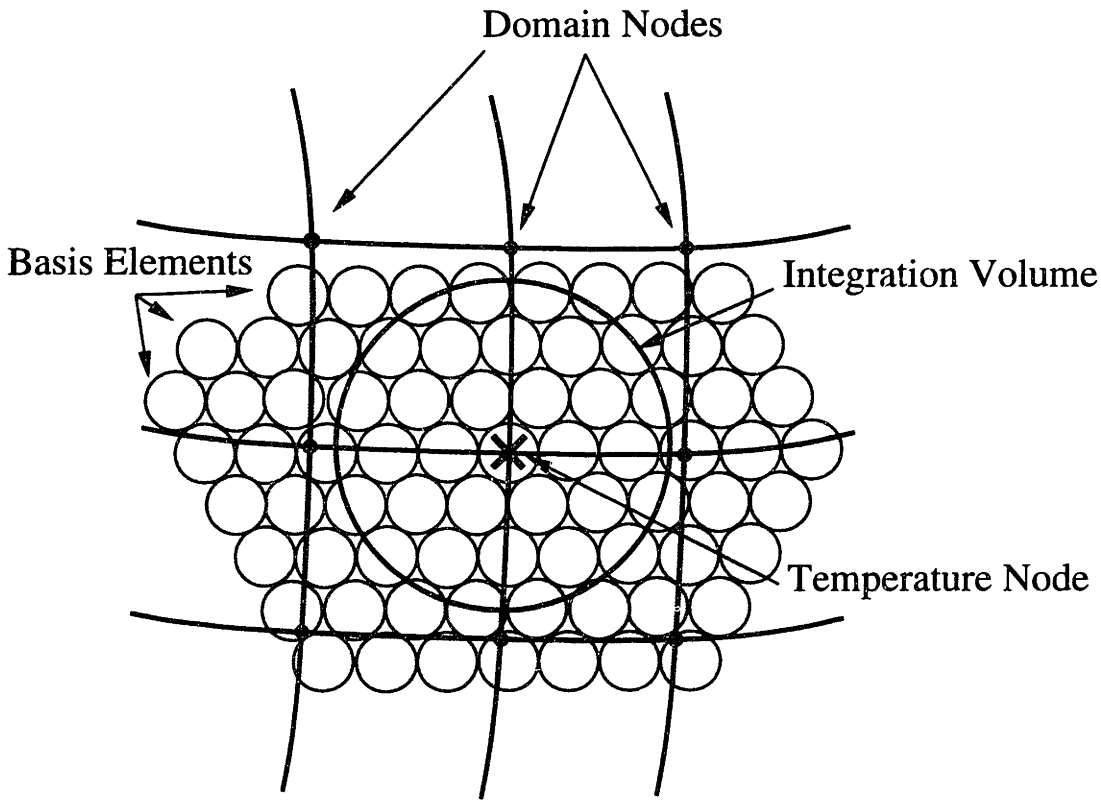

Figure 4-2: Close hexagonal packing of the Basis Elements in the domain.

and the domain nodes for the computation of temperature at the nodes. The centers of the unshaded Basis Elements are inside the volume of integration and thus their contribution to the temperature is summed, while the shaded Basis Elements are either ignored or lumped together to form a macroscopic Basis Element. The conglomeration of the packed Basis Elements, also called the lattice, is constructed for each node and aligned such that a Basis Element center exactly coincides with the temperature node position, as shown in Figure 4-2. All the other Basis Elements in the lattice, however, do not necessarily coincide with nodes and their position in the domain may vary somewhat arbitrarily.

Thermal properties, perfusion and internal heat generation must be determined for the Basis Elements at these locations in the domain. Internal heat generation for each Basis Element is computed by a trilinear interpolation using the ight nodes that surround the position of the Basis Element center. The value of internal heat generation for a uniform Basis Element is set equal to this interpolation value and the peak internal heat generation of exponential and Gaussian Basis Elements are set to this value. The close hexagonal

packing of the lattice implemented here is by no means the only possible method. Other as of yet unexplored packing schemes, vary the Basis Element source radius as a function of the distance from the temperature node.

4.1.3 Boundaries

The boundaries are surfaces which can be one of two types: 1) *internal boundaries* which divide the tissue into subdomains that have different thermal properties and/or perfusion; and 2) *external boundaries* which separate the tissue domain from the external environment and therefore necessitate special consideration as thermal boundary conditions.

The mesh generation routines evaluate each domain node and determine if a node is within N_p perfusion lengths of an internal or external boundary. If the node is found to be thermally influenced by a boundary, the index of the nearest node which is either on the boundary or just beyond the boundary (from the domain node) is stored. After this boundary information is gathered for each domain node thermally influenced by a boundary, the unit normal vectors, radius of curvature and the position of the boundary nodes are computed. This processing is done "up-front" before any temperature computation is started.

Figure 4-3 shows a schematic diagram of the normal vector computation using a very simple algorithm. The boundary node is shown in the center of the grid. The algorithm proceeds by locating all the surrounding nodes in the grid which lie on the boundary and computing the local position vectors relative to the center boundary node ($\vec{v}_i$). The normal vector, for the center boundary node, is equal to the average of the cross-products of successive vectors. This result is normalized to give the unit normal vector:

$$\hat{n} = \sum_{i=1}^{N} \vec{v}_i \times \vec{v}_{i+1} \frac{1}{\left| \sum_{i=1}^{N} \vec{v}_i \times \vec{v}_{i+1} \right|} \tag{4.5}$$

where N is the number of neighboring boundary nodes. This method for computing the normal vectors weighs more heavily the contributions from the larger triangles of Figure 4-3.

Once the unit normal vectors at all the boundary nodes are computed, the radius of curvature at each boundary node can be determined using the geometry shown in Figure 4-4. The algorithm first locates the surrounding boundary nodes and computes the local

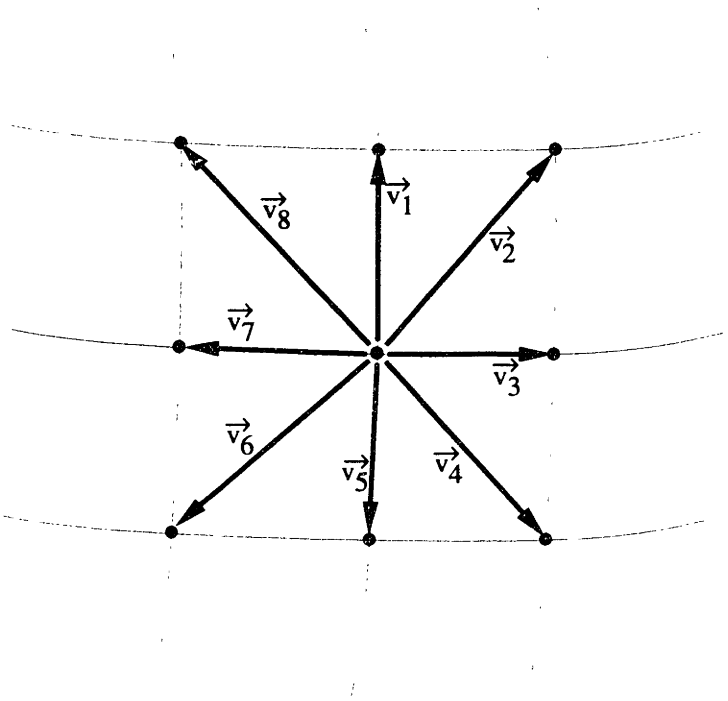

Figure 4-3: A schematic diagram of the algorithm for computing unit normal vectors at each boundary point.

position vectors ($\vec{v}_i$) relative to the center boundary point. The inverse cosine of the dot product of the unit normal vectors gives the angle for the arc. All the arcs surrounding a node are averaged and the complete expression for the radius of curvature associated with the node i is as follows:

$$R_i = \frac{1}{N} \sum_{i=1}^{N} \frac{| \vec{v}_i - \vec{v}_{i+1} |}{2\, sin[\, \frac{1}{2} cos^{-1}(\hat{n}_i \cdot \hat{n}_{i+1})\,]} \tag{4.6}$$

where N is the number of neighboring boundary nodes.

External Boundaries

External boundary surfaces are defined by the coordinates of the domain nodes which lie on these surfaces (i = 0, N_x; j = 0, N_y; k = 0, N_z). Each external boundary node is associated with a boundary area which is a continuous collection of boundary nodes having the same thermal boundary condition. Each boundary area is characterized by its thermal type: first, second or third kind; and the boundary parameters: boundary temperature, heat flux, heat

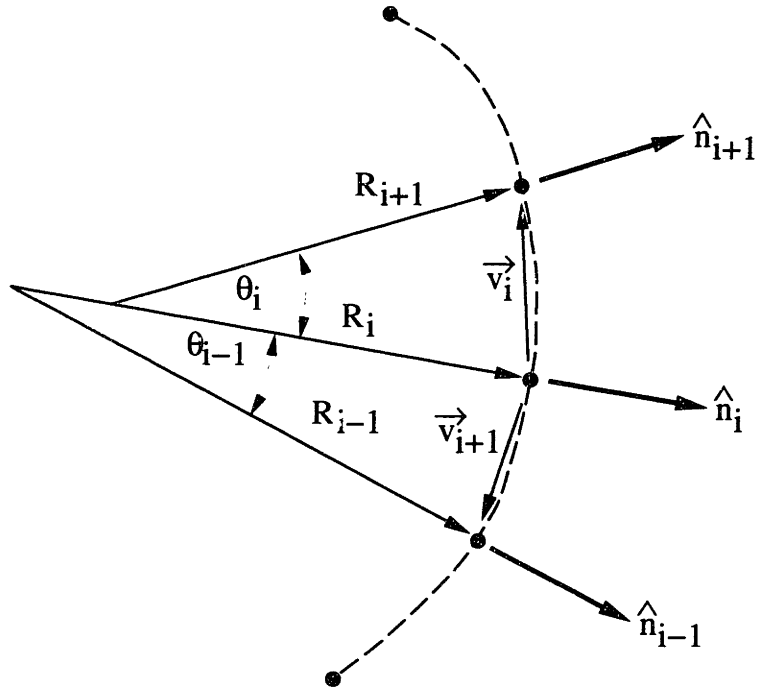

Figure 4-4: A schematic diagram of the algorithm for computing the radius of curvature at each boundary node.

transfer coefficient and convection fluid temperature.

Internal Boundaries

Internal boundaries differ from external boundaries in that domain nodes do not lie on the boundary surface. The Basis Element algorithm takes as input a 3-D matrix of perfusion and thermal properties. There is no further provision for the representation of the tissue internal boundaries. When the mesh generation routines determine the normal vectors for the internal surfaces, the approximate position of the internal boundaries are computed.

4.2 Code Architecture

The computer code implementation of the Basis Element algorithm is built on a modular design. Figure 4-5 shows a block diagram of the communication between the various routines of different levels. The heart of the algorithm, the Basis Element routines, forms

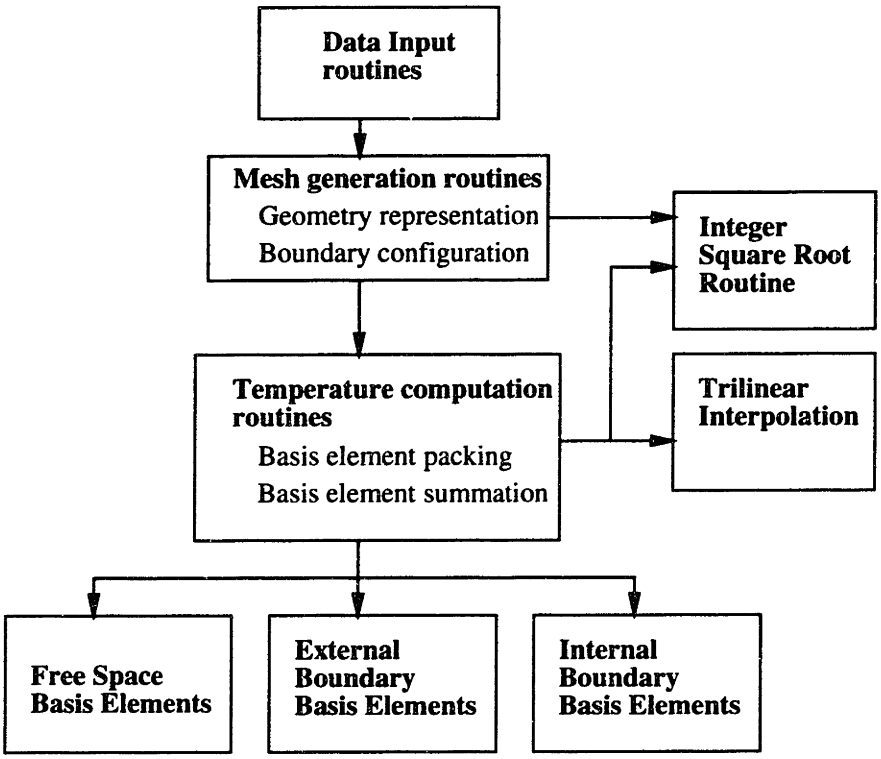

Figure 4-5: Block diagram of the Basis Element code implementation.

the lowest level of the diagram. They are called directly by the temperature calculation routines which mediate the Basis Element packing and the Basis Element summation. The trilinear interpolation and integer square root routines are called by the mid-level temperature calculation and mesh generation routines.

In the context of a hyperthermia planning system, the inputs are from the patient model and the perfusion-property database and the outputs are sent to the interactive visualization system. The actual mediation of the temperature calculations depends on the desired computation features: accuracy, CPU time, and spatial resolution. The complete interactive planning system will incorporate routines to automatically determine the algorithm parameters (Basis Element source size, integration volume, etc.) based on the computation features.

4.2.1 Code Implementation

The Basis Element code consists of a total of about 7000 lines of standard ANSI C. The routines are modular and self-contained in order to be linked to the treatment planning and visualization system. The modular approach allows the same code to form the temperature computation core which could potentially be accessed by several different input sources for planning, reconstruction and ultimately real-time on-line computation. Appendix C contains a line listing of the Basis Element *C* code routines.

The native ULTRIX Version 4.3 RISC C compiler was used to generate the machine code which produced all the results in this thesis. The source code was always compiled with full optimization (option -O3) and the resulting object code was stripped of debugging information.

4.2.2 Optimization

Optimization occurs throughout the BEM code and starts with an intelligent formulation of the heat transfer problem and includes the implementation of highly efficient routines. Higher level optimization in the code minimizes the total number of computations, for instance, by the use of dimensionless variables. The lower level optimization removes "bottle-necks" in the computation by techniques such as the use of fast integer computation.

Dimensionless Parameters

Two sets of dimensionless variables are used in the BEM - one that normalizes the variables at the global problem level and the other that normalizes the local variables for the individual Basis Elements. The global dimensionless variables include:

$$Q = \frac{q}{q_{max}} \tag{4.7}$$

where q is the dimensioned heat generation, q_{max} is the maximum dimensioned heat generation and Q is the dimensionless 3-D heat generation;

$$Pe = \frac{\omega \, \rho_b \, c_b \, L^2}{k_m} \tag{4.8}$$

where Pe is the 3-D Péclèt number matrix and L is an arbitrary length scale for the problem. The choice of the length scale should correspond to the size of the heated volume.

The Basis Element routines are all formulated to take dimensionless inputs: geometry, perfusion and thermal properties; and compute the dimensionless temperature. The Basis Element source radius forms the length scale for the local problem:

$$r = \frac{r'}{a} \tag{4.9}$$

where a is the source radius, r' is the dimensioned coordinate and r is the dimensionless variable. The local length scale necessitates that the global Péclèt number be converted to a local Péclèt number:

$$Pe_l = \frac{\omega \rho_b c_b a^2}{k_m} \tag{4.10}$$

The local dimensionless temperature output is:

$$\theta = \frac{T k_m}{q a^2} \tag{4.11}$$

where T is the dimensioned temperature.

Integer Coordinates

A typical patient model includes a tissue domain of dimension 30x30x30 cm. As discussed in Section 2.1, the patient model is derived from CT scans, whose spatial accuracy in the Z direction is no more than 3 mm. Therefore, it is unnecessary to represent the patient geometry with 32 bit floating point precision. An optimal discretization of the geometry need only have a spatial resolution less than 3 mm in the longitudinal direction of the patient. The 1 mm maximum spatial resolution allows the use of integers for the geometric representation, which requires less memory than floating point storage. Manipulation of the integer geometry takes advantage of fast integer computation thus requiring less CPU time than floating point geometry.

Square Root Algorithm

An analysis of the code execution time on a test problem revealed that about 80% of the CPU time was taken up by computing square roots when the native compiler square root

routine was used. Thus it was reasoned that the most savings of processor time is obtainable by optimizing the computation of square roots. By far, the major part of these calculations is performed on the domain geometry to compute the distance of a Basis Element from a domain node by taking the magnitude of the difference of the position vectors. Since integers are used to discretize the geometry, conversion of the square root calculations to an optimized integer based calculation was envisioned. Higginbotham, [61], developed an integer square root algorithm using only addition and subtraction. Barrera and Olsson, [62], developed a fast and accurate integer square root routine which uses only addition and bit shifts. This algorithm was implemented into the Basis Element code as a high level (C) language routine and it proved to be only marginally faster than the native, low level (assembly) language square root routine.

A square root algorithm based on a "look-up table" was then implemented and achieved significant savings in time. In such a scheme, the integer input to the routine is also the index of an array which stores all the floating point values of the square roots from zero to some maximum, MAX_SQUARE_ROOT. Above this value, the look-up table is bypassed and the native square root routine is used. The result was a factor of 5 in savings of the look-up table over the exclusive use of the native square root routine.

Chapter 5

Analytical and Numerical Validation

In this chapter, the Basis Element solution of the bioheat transfer equation is validated by direct comparison to problems with exact analytical solutions and to problems with approximate numerical solutions. The configuration of these problems models various anatomical situations found in hyperthermia practice. The exact analytic solutions, while not realistic clinically, provide a means to test mathematically the limits of the accuracy of the BEM in situations which mimic certain aspects of tissue heat transfer. The numerical solutions allow comparisons using more complex configurations such as varying thermal properties and perfusion, nonuniform power deposition, and irregular geometry. The numerical solutions are realized by a finite element code to which comparisons are made with regard to both accuracy and computational speed and effort.

5.1 Comparisons with Exact Analytical Problems

To demonstrate that the BEM is a valid solution of the bioheat transfer equation, this section presents comparisons between the BEM and exact solutions to problems with simple geometries. These problems, though too simple to actually be encountered in practice, contain different aspects of situations relevant to tissue thermal modeling. The results from the BEM are compared to exact analytical solutions of one dimensional problems. Except where otherwise noted, the Basis Element radius used in these simulations is 1.5 mm and the number of perfusion lengths (N_p) in the radius of integration is 9.

In these comparisons, the concept of *error* as a measure of the closeness between the BEM and the exact solution is not easily represented. Error could be defined as a percentage where the difference between the exact and the BEM temperature is normalized to a reference temperature. If a relative measure of error is desired, then the reference temperature is chosen to be the maximum or average temperature. For an absolute measure of error, the reference is the exact temperature.

The standard unit of error measurement which has been adopted for these comparisons is the *temperature difference* in °C between the exact and BEM solutions. In this way, the relative percent error is not misrepresented as being too low when normalized with a high reference temperature, nor is the absolute percent error misrepresented as being too high when normalized with a low reference temperature. Further, the concept of percent temperature error may have little meaning in hyperthermia practice where temperature differences less than 0.1 °C are insignificant. The standard application of temperature difference as a measure of error requires a common peak temperature for all the comparison problems. This has been insured by setting the peak temperature in all the test cases to 45 °C - the target temperature for local hyperthermia.

5.1.1 Infinite Domain with Uniform Properties

Uniform Internal Heat Generation

The first and simplest test case is an infinite tissue region with uniform internal heat generation and uniform perfusion. Figure 5-1 shows a schematic diagram of this test case. In such a case the thermal gradients are everywhere zero and the dimensionless temperature is:

$$\frac{T\,k_m}{Q_o\,L^2} = \theta = \frac{1}{Pe} = \frac{k_m}{\omega\,\rho\,c}\,\frac{1}{L^2} \tag{5.1}$$

where L is an arbitrary length scale and Pe is the Péclèt number. This test case is used to demonstrate the effect of the size of the integration volume on the solution accuracy. The top panel of Figure 5-2 shows a plot of the temperature error of the BEM as a function of N_p from Equation (3.6) - the number of perfusion lengths in the radius of the volume of integration. The perfusion everywhere is 20 ml/min-100g and the internal heat generation

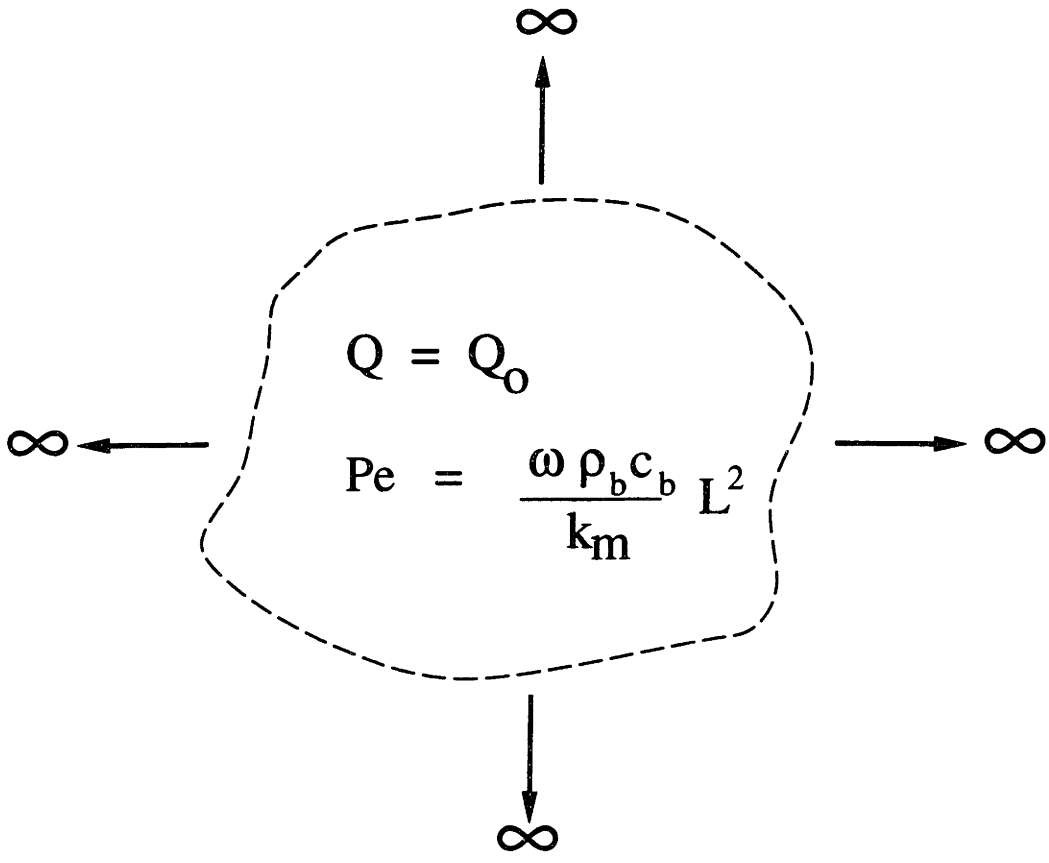

Figure 5-1: Schematic diagram of the infinite tissue region with uniform internal heat generation, uniform perfusion and uniform thermal properties.

is 0.1132 W/cm^3. As expected, this error decreases as the size of the integration volume increases. The bottom panel shows the exponential increase in the number of Basis Elements with an increase in N_p.

Discontinuous Internal Heat Generation

The second test case consists of an infinite tissue region with uniform thermal properties (k_m=0.5 W/m-°C), uniform perfusion (W=10 ml/min-100g) and discontinuous internal heat generation (Q = 0.05566 W/cm^3). Figure 5-3 shows a schematic diagram of the test case. An exact solution for the temperature is easily achievable by solving the two coupled 1-D, second order differential equations in each of the regions. The dimensionless temperature

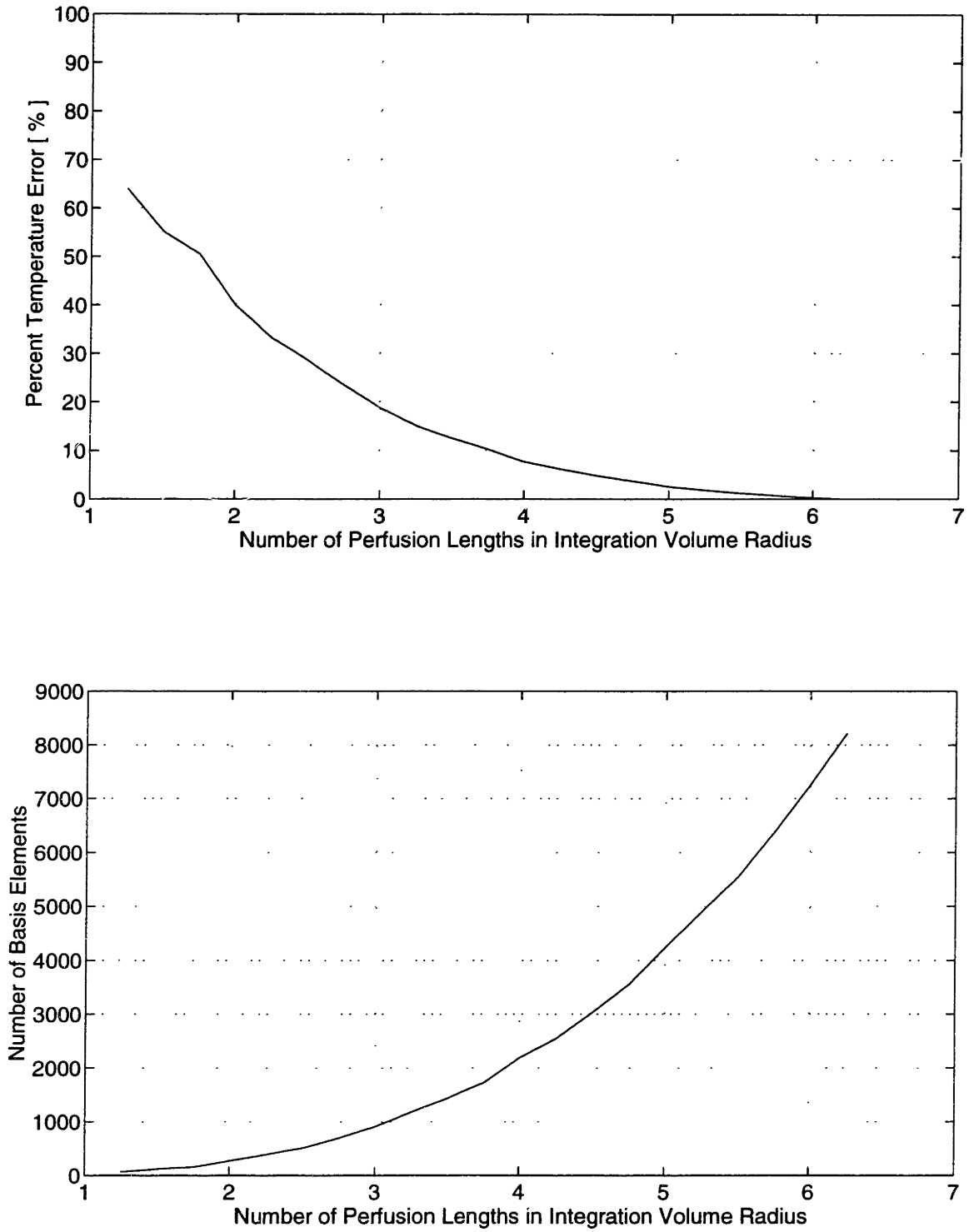

Figure 5-2: Percent temperature error as a function of the integration volume radius (top panel) and the number of Basis Elements as a functions of the integration volume radius (bottom panel).

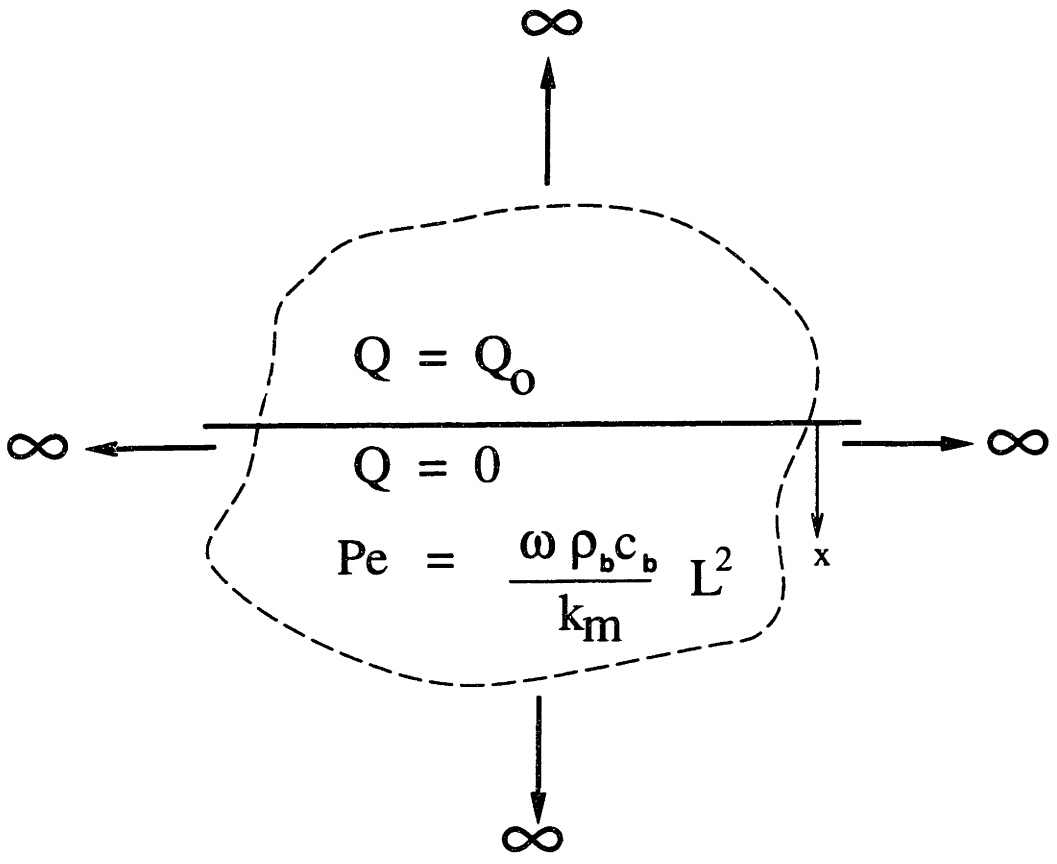

Figure 5-3: Schematic diagram of the infinite tissue region with discontinuous internal heat generation, uniform perfusion and uniform thermal properties.

in the heated region is:

$$\theta = \frac{1}{Pe}\left(1 + \frac{e^{-\sqrt{Pe}|x|}}{2}\right) \tag{5.2}$$

and in the unheated region, the temperature is:

$$\theta = \frac{e^{-\sqrt{Pe}x}}{2\,Pe} \tag{5.3}$$

where the division between the heated and unheated region is at x=0.

In the BEM algorithm, the infinite domain is modeled as a finite domain (a 300x300x300 mm cube) with $N_p = 9$. The top panel of Figure 5-4 shows the temperature profile from the heated region into the unheated region with exact solution (solid line) and the BEM solution (symbols) with Basis Elements of uniform size. In the lower panel, the solid line shows the temperature difference between the exact solution and uniform size Basis Elements with a

maximum error of 0.27 °C. This level of error is due to the Basis Elements with a radius of 1.5 mm being unable to well represent the heating discontinuity. The dashed line shows the difference between the exact solution and the BEM solution where the temperature on the heating boundary was solved with Basis Elements of radius 0.375 mm and Basis Elements with a 1.5 mm radius were used to compute temperature everywhere else. In this case, the smaller Basis Elements are used to compute temperature at the discontinuity to give the higher accuracy.

5.1.2 Infinite Domain with Differential Properties

Planar Tissue Boundary

The planar tissue boundary test case consists of an infinite tissue domain with uniform internal heat generation. The tissue domain is divided by a planar boundary into two subdomains: one subdomain with perfusion of ω_1 and thermal conductivity of k_{m1} and the other with perfusion of ω_2 and thermal conductivity of κ_{m2}. Figure 5-5 shows a schematic diagram of the test case. The exact solution for the temperature in subdomain 1 is:

$$\theta_1 = \frac{1}{Pe_1} - \frac{\sqrt{Pe_2}}{\sqrt{Pe_1}} \frac{\frac{\kappa}{Pe_1} - \frac{1}{Pe_2}}{1 + \kappa \frac{\sqrt{Pe_2}}{\sqrt{Pe_1}}} e^{\sqrt{Pe_1}x} \tag{5.4}$$

and the temperature in subdomain 2 is:

$$\theta_2 = \frac{1}{Pe_2} - \frac{\frac{\kappa}{Pe_1} - \frac{1}{Pe_2}}{1 + \kappa \frac{\sqrt{Pe_2}}{\sqrt{Pe_1}}} e^{-\sqrt{Pe_2}x} \tag{5.5}$$

where $\kappa = k_{m2}/k_{m1}$ and subdomain 1 is located at $x < 0$ and subdomain 2 is located at $x > 0$.

The top panel in Figure 5-6 shows a plot of the temperature across the interface. For the case where $W_1 = 10$ ml/min-100g and $W_2 = 15$ ml/min-100g, the solid line is the exact, analytical solution, while the circular symbols represent the temperature computed by the BEM. For $W_1 = 10$ ml/min-100g and $W_2 = 35$ ml/min-100g, the dashed line is the exact, analytical solution and the asterisk symbols represent the BEM solution. In both cases the uniform internal heat generation is 0.055666 W/cm^3. The bottom panel of Figure 5-6 is the error in °C between the exact solutions and the BEM solutions. Here the solid

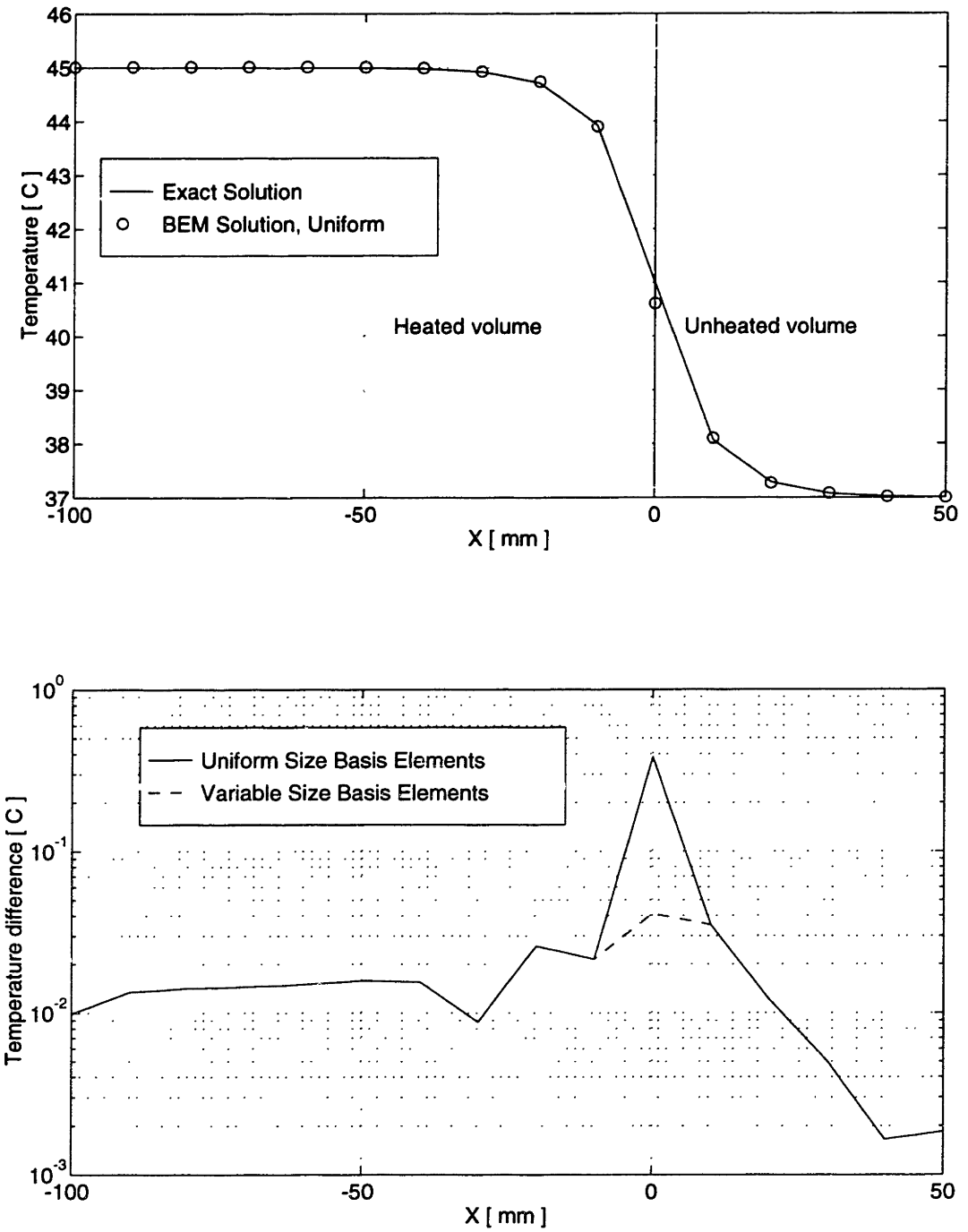

Figure 5-4: Temperature profile for discontinuous internal heat generation (top panel) and temperature difference for the exact solution minus the BEM solution.

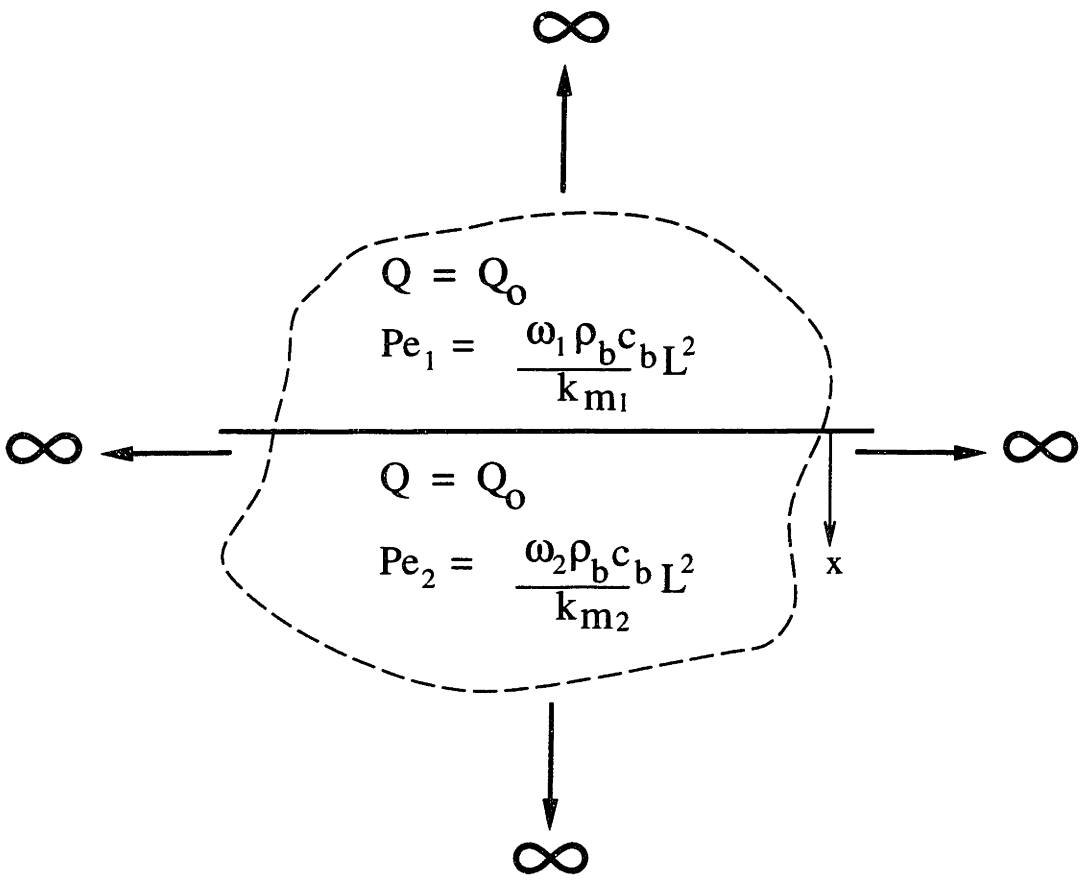

Figure 5-5: Schematic diagram of the infinite tissue region with uniform internal heat generation and a plane separating the subdomains of differential perfusion and differential thermal properties.

line is the difference for $W_2 = 15$ ml/min-100g and the dashed line is the difference for $W_2 = 35$ ml/min-100g.

The test case shows that the error is a maximum in the region nearest to the internal boundary. This is consistent with the approximate treatment of the Basis Elements for planar internal boundaries developed in Section 3.2.4. Further, the magnitude of the error is not a strong function of the increased perfusion (dashed line in the bottom panel). In both the high and low perfusion cases, several perfusion lengths distant from the boundary, the error drops to the levels as seen in Figure 5-2 above for the case of uniform perfusion and uniform heating.

A variation on the planar tissue boundary test case includes the same problem as above, except the thermal conductivity in subdomain 1 is 0.5 W/m-^{o}C while the conductivity in subdomain 2 is 0.25 W/m-^{o}C. The top panel in Figure 5-7 shows a plot of the temperature across the interface. For the case where $W_1 = 10$ ml/min-100g and $W_2 = 15$ ml/min-100g, the solid line is the exact, analytical solution, while the circular symbols represent the temperature computed by the BEM. For $W_1 = 10$ ml/min-100g and $W_2 = 35$ ml/min-100g, the dashed line is the exact, analytical solution and the asterisk symbols represent the BEM solution. In both cases the uniform internal heat generation is 0.055666 W/cm^3. The bottom panel of Figure 5-7 is the error in ^{o}C between the exact solutions and the BEM solutions. Here the solid line is the difference for $W_2 = 15$ ml/min-100g and the dashed line is the difference for $W_2 = 35$ ml/min-100g. In this case the error is higher due to the larger perfusion difference between the subdomains.

Spherical Tissue Boundary

The spherical tissue boundary test case concerns a spherical tissue subdomain with perfusion of ω_1 and thermal conductivity of k_{m1}, surrounded by an infinite tissue domain with perfusion of ω_2 and thermal conductivity of k_{m2} with uniform internal heat generation over the entire tissue domain. Figure 5-8 shows a schematic diagram of this test case.

The exact solution for the temperature inside the sphere is:

$$\theta_1 = \frac{1}{Pe_1} + \frac{\frac{1}{Pe_2} - \frac{\kappa}{Pe_1}}{\kappa \sinh(\sqrt{Pe_1}) + \frac{\sqrt{Pe_1}\cosh(\sqrt{Pe_1}) - \sinh(\sqrt{Pe_1})}{\sqrt{Pe_2}+1}} \frac{\sinh(\sqrt{Pe_1}\, r)}{r} \qquad (5.6)$$

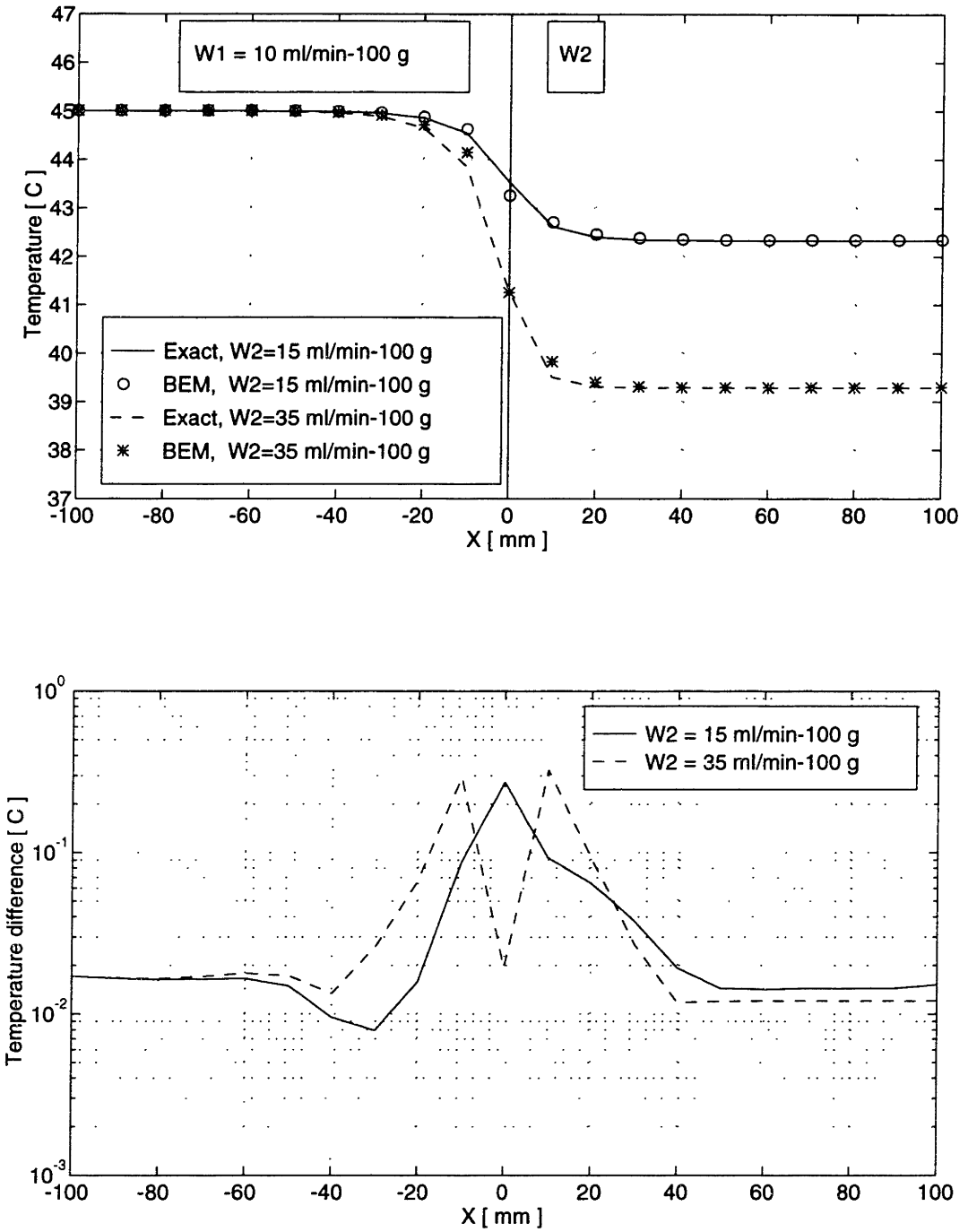

Figure 5-6: Temperature profile through a perfusion tissue boundary with uniform internal heat generation (top panel) and temperature difference for the exact solution minus the BEM solution.

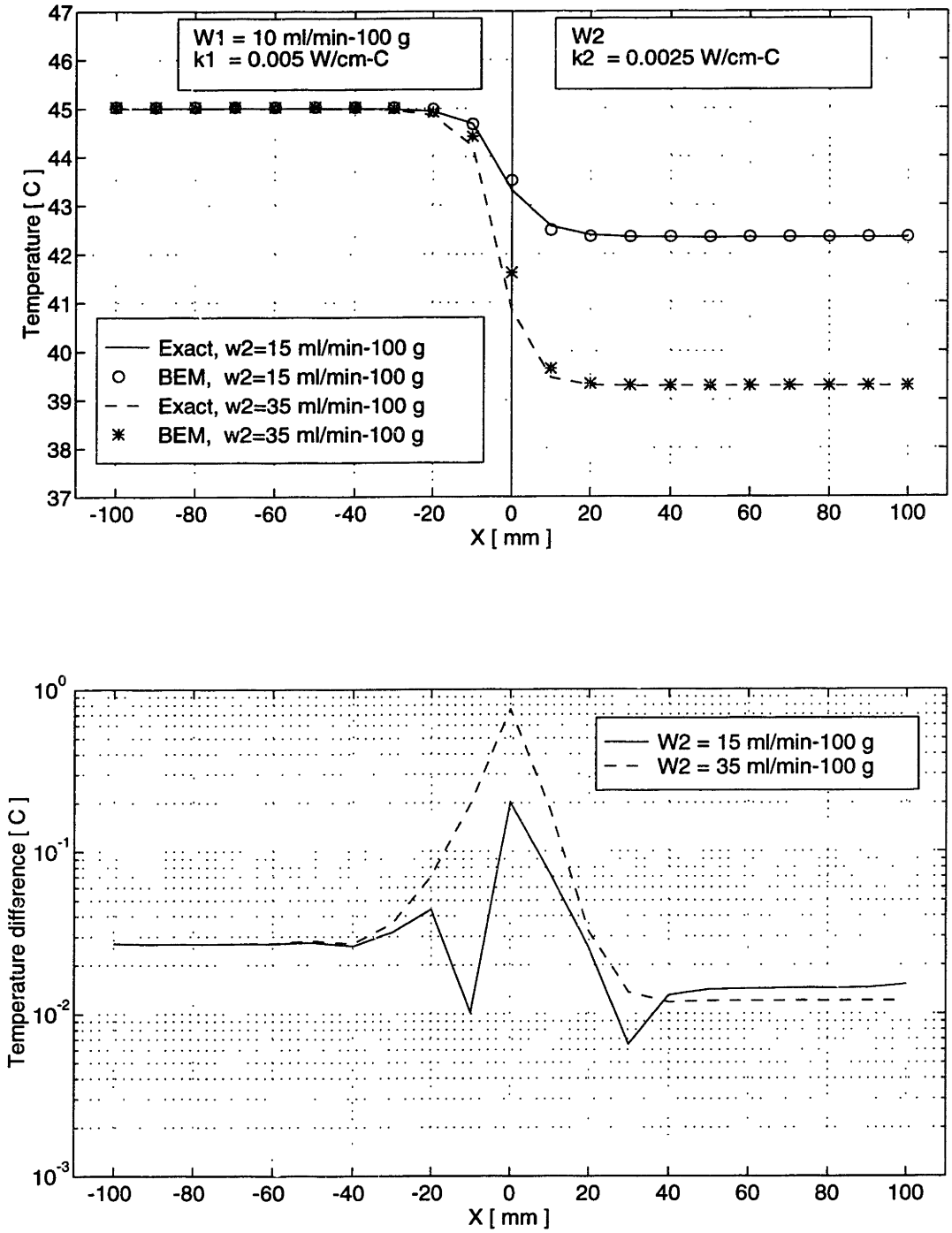

Figure 5-7: Temperature profile through a perfusion and conductivity tissue boundary with uniform internal heat generation (top panel) and temperature difference for the exact solution minus the BEM solution.

and outside the sphere, the temperature is:

$$\theta_2 = \frac{1}{Pe_2} - \frac{e^{-\sqrt{Pe_2}(r-1)}}{r} \frac{\frac{\kappa}{Pe_1}}{\kappa \sinh(\sqrt{Pe_1}) + \frac{\sqrt{Pe_1}\cosh(\sqrt{Pe_1}) - \sinh(\sqrt{Pe_1})}{\sqrt{Pe_2}+1}} \tag{5.7}$$

$$\times \frac{\sqrt{Pe_1}\cosh(\sqrt{Pe_1}) - \sinh(\sqrt{Pe_1})}{\sqrt{Pe_2}+1} \tag{5.8}$$

where the sphere center is $r = 0$ and the sphere surface is at $r = 1$.

In this comparison, the perfusion in the tissue sphere, W_1, is equal to 10 ml/min-100g and the thermal conductivity throughout the entire tissue volume is 0.5 W/m-°C. The top panel in Figure 5-9 shows the temperature through the spherical subdomain. The solid line represents the exact solution and the circular symbols mark the BEM solution for the case where the surrounding perfusion, W_2, is equal to 15 ml/min-100g. The dotted line is the exact solution and the asterisk is the BEM solution for W_2 equal to 35 ml/min-100g. In both cases the uniform internal heat generation is 0.055666 W/cm^3. The bottom panel of Figure 5-9 shows the error in terms of the difference in temperature between the exact and BEM solutions. As expected, the error is largest near the boundaries and is a minimum where the thermal gradient is small.

Figure 5-10 shows a comparison of the exact and BEM solutions for the same problem as in Figure 5-9, but, the thermal conductivity outside the sphere (subdomain 2) is 0.25 W/m-°C. The top panel in Figure 5-10 shows the temperature through the spherical subdomain. The solid line is the exact solution and the circular symbols is the BEM solution for the case where the surrounding perfusion, W_2, is equal to 15 ml/min-100g. The dotted line is the exact and the asterisk is the BEM solution for W_2 equal to 35 ml/min-100g. The bottom panel of Figure 5-10 shows the error in terms of the temperature difference between the exact and BEM solutions. In this case, the variation in error has the same shape as in Figure 5-9, but the magnitude is larger.

5.1.3 Semi-Infinite Domain with Planar Boundary Conditions

In this subsection, a series of test cases are defined which have uniform internal heat generation, uniform perfusion, uniform thermal properties and a semi-infinite geometry bounded, at $X = 0$, by a planar surface at which a boundary condition of the first, second,

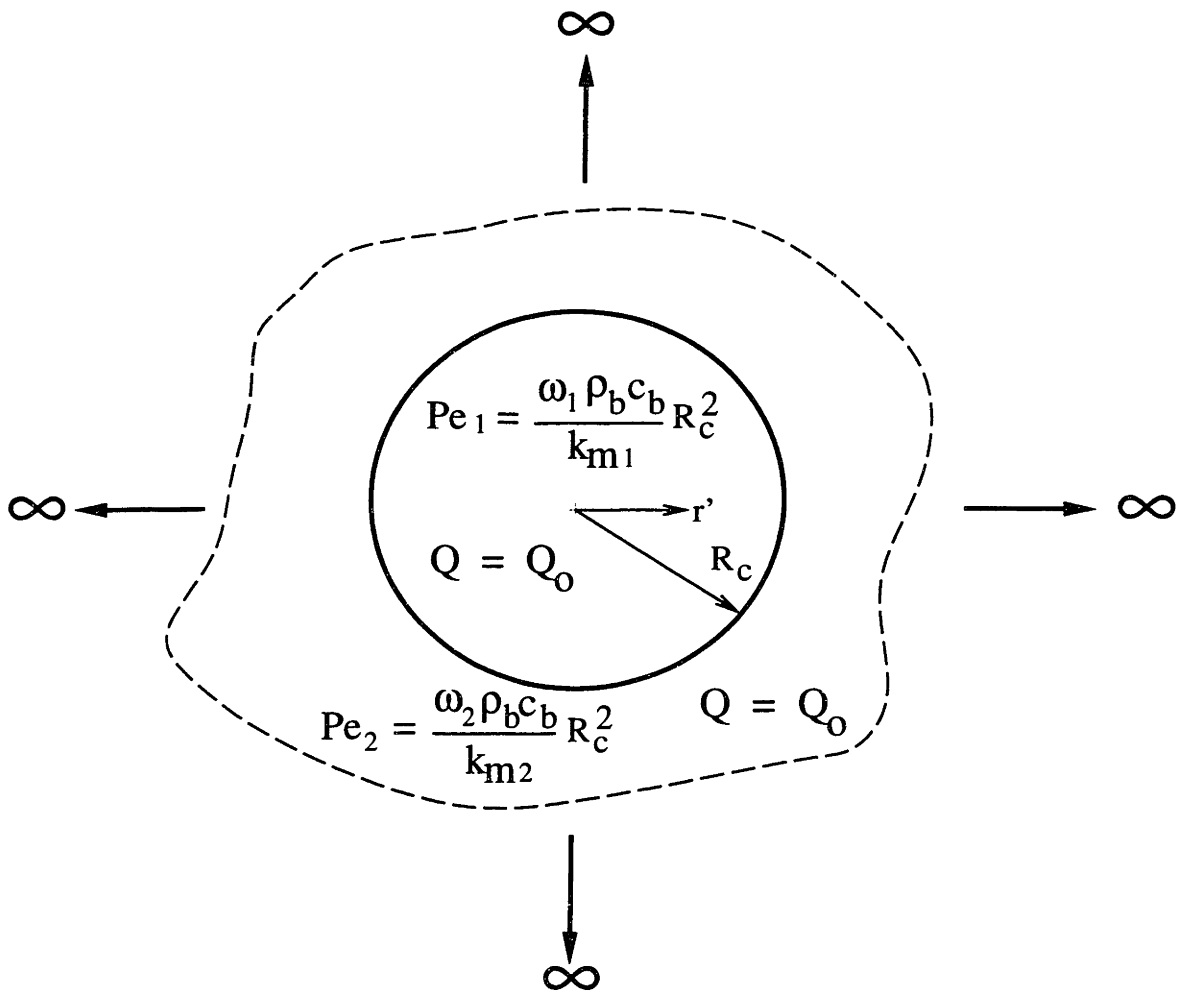

Figure 5-8: Schematic diagram of the infinite tissue region with uniform internal heat generation and a spherical tissue subvolume dividing separating the subdomains with differential perfusion and differential thermal properties.

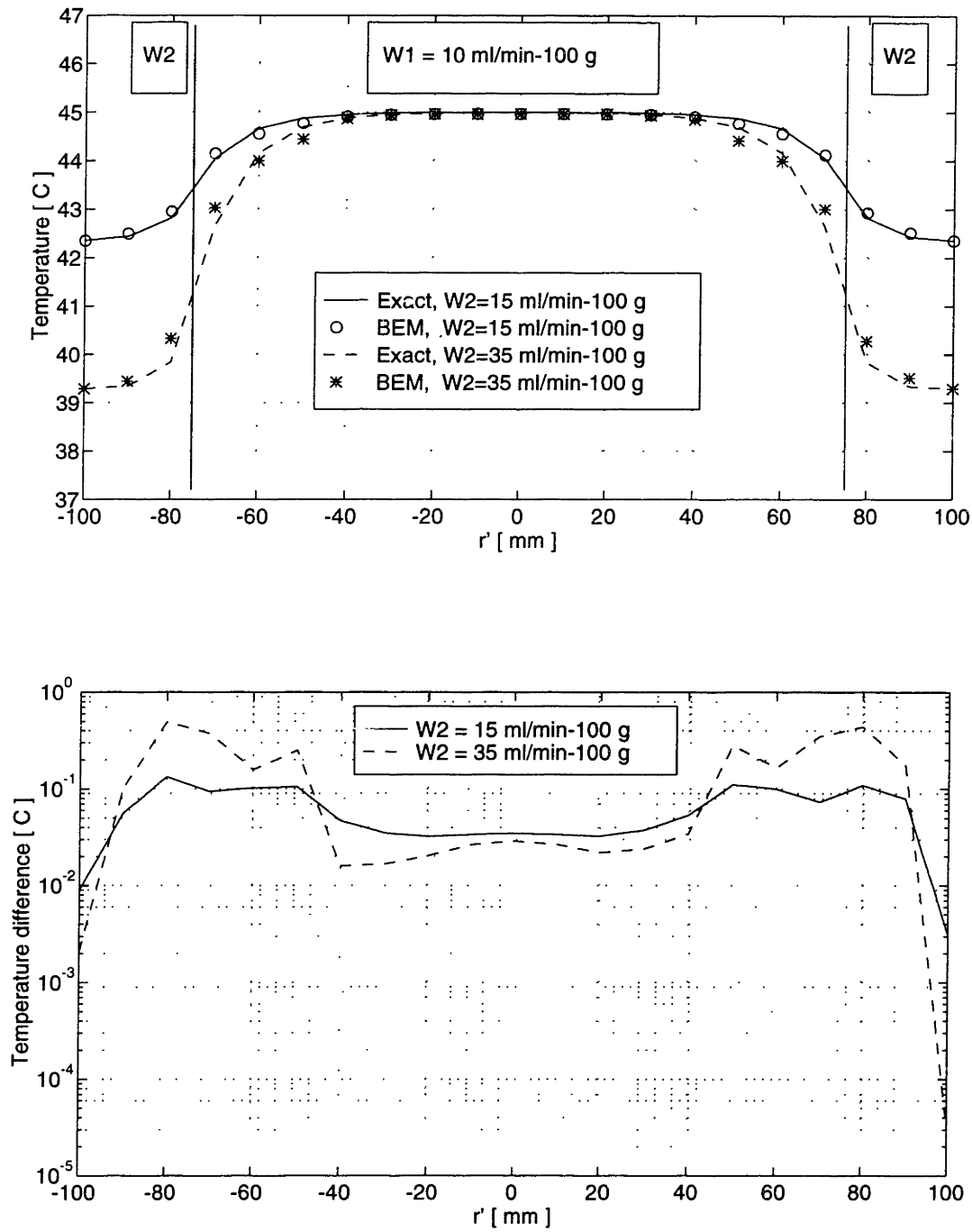

Figure 5-9: Temperature profile through the spherical tissue subdomain with uniform internal heat generation (top panel) and the temperature difference for the exact minus the BEM solution.

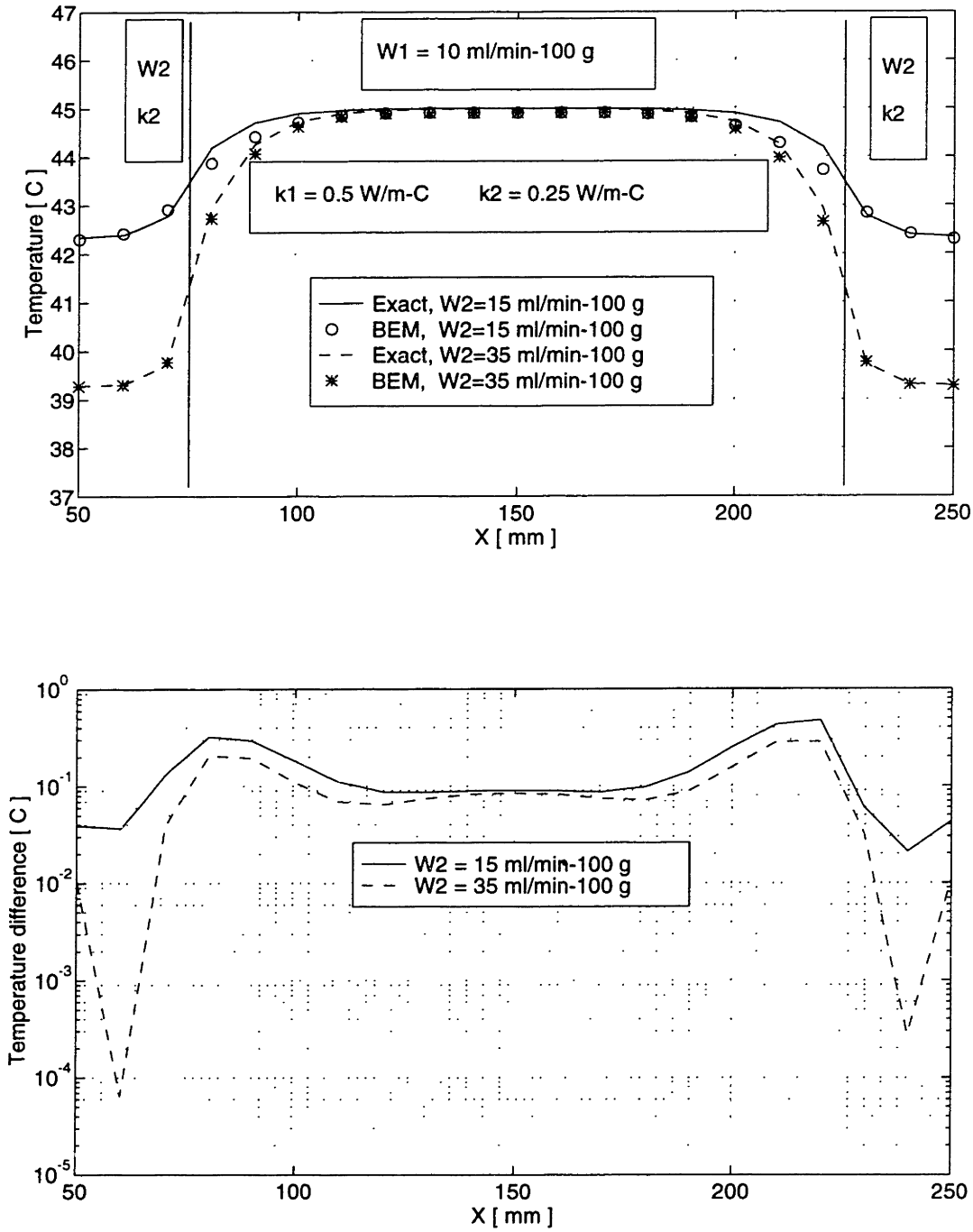

Figure 5-10: Temperature profile through the spherical tissue subdomain with uniform internal heat generation (top panel) and the temperature difference for the exact minus the BEM solution.

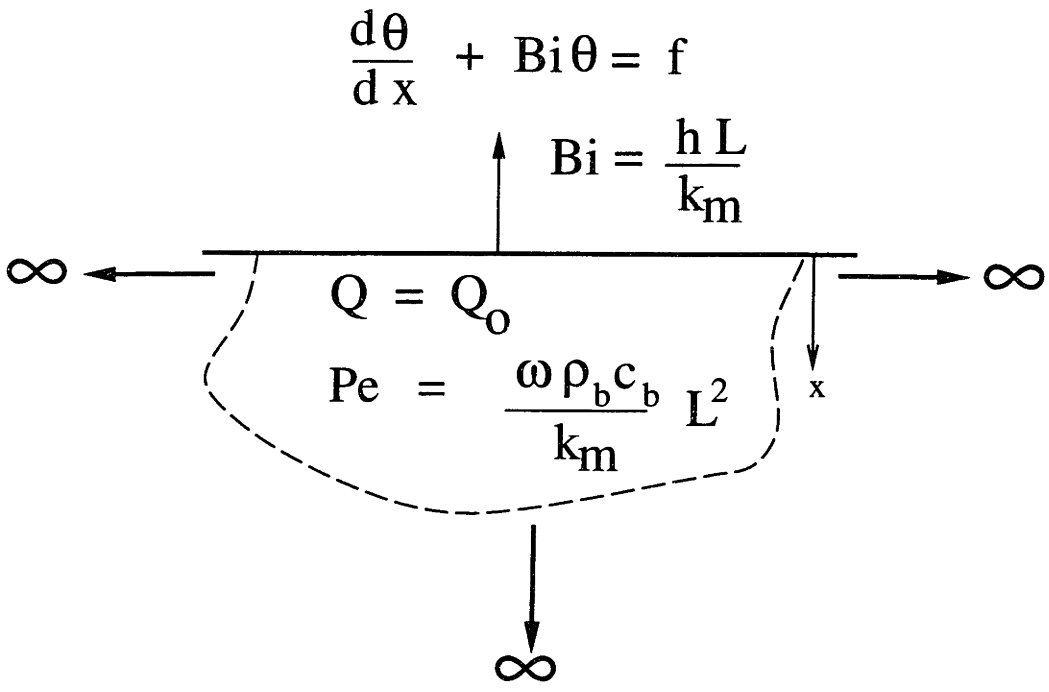

Figure 5-11: Schematic diagram of the semi-infinite tissue region with uniform internal heat generation, perfusion and properties with a boundary condition at the planar surface.

or third kind is applied. Figure 5-11 shows a schematic diagram of this class of test cases, with a general boundary condition at the surface. The exact solutions for the temperature rise in these simple cases are easily available by the analytic solution of the 1-D differential equation. The results from the BEM are compared with the exact solution to determine the BEM's ability to solve for the temperature at or near planar external boundaries.

First Kind

The semi-infinite domain is bounded by a plane at which a boundary condition of the first kind is applied (constant surface temperature). With the boundary at $x = 0$, the exact temperature is:

$$\theta = \frac{1}{Pe} - (\frac{1}{Pe} - \theta_b)\, e^{-\sqrt{Pe}x} \tag{5.9}$$

$$\theta_b = \frac{T_b\, k_m}{Q\, L^2} \tag{5.10}$$

where θ_b is the dimensionless boundary temperature.

The top panel of Figure 5-12 shows the temperature profile from the surface, held at zero temperature rise, into the semi-infinite body for uniform internal heat generation (Q = 0.05566 W/cm^3), uniform perfusion (W = 10 ml/min-100g) and uniform thermal conductivity (k_m=0.5 W/m-^{o}C). The solid line is the exact solution and the symbols represent the BEM solution. The bottom panel of Figure 5-12 shows the temperature difference between the exact and BEM solutions. The error is small and is of the same order as the minimum error in Figure 5-2.

Figure 5-13 shows the results for the same problem as in Figure 5-12, except the surface boundary condition is non-homogeneous and held at 25 °C. The top panel is the temperature profile from the surface into the semi-infinite body where the solid line is the exact solution and the symbols are the BEM solution. The bottom panel shows the error in terms of the temperature difference between the exact and BEM solutions.

Second Kind

For a boundary condition of the second kind, the exact solution for temperature is:

$$\theta = \frac{1}{Pe} - \frac{\Gamma}{\sqrt{Pe}}\, e^{-\sqrt{Pe}\,x} \tag{5.11}$$

$$\Gamma = \frac{q}{Q\, L} \tag{5.12}$$

where q is the dimensioned and Γ is the dimensionless boundary heat flux, both defined as positive flow out of the tissue domain.

The top panel in Figure 5-14 shows the temperature profile from the planar surface of a semi-infinite body with uniform internal heat generation (Q = 0.05566 W/cm^3), uniform perfusion (W = 10 ml/min-100g) and uniform thermal conductivity (k_m=0.5 W/m-^{o}C) with a boundary condition of the second kind (constant heat flux, $q = 0$) at the surface. The solid line is the exact solution and the symbols represent the BEM solution. The bottom panel of Figure 5-14 shows the temperature difference between the exact and the BEM solution.

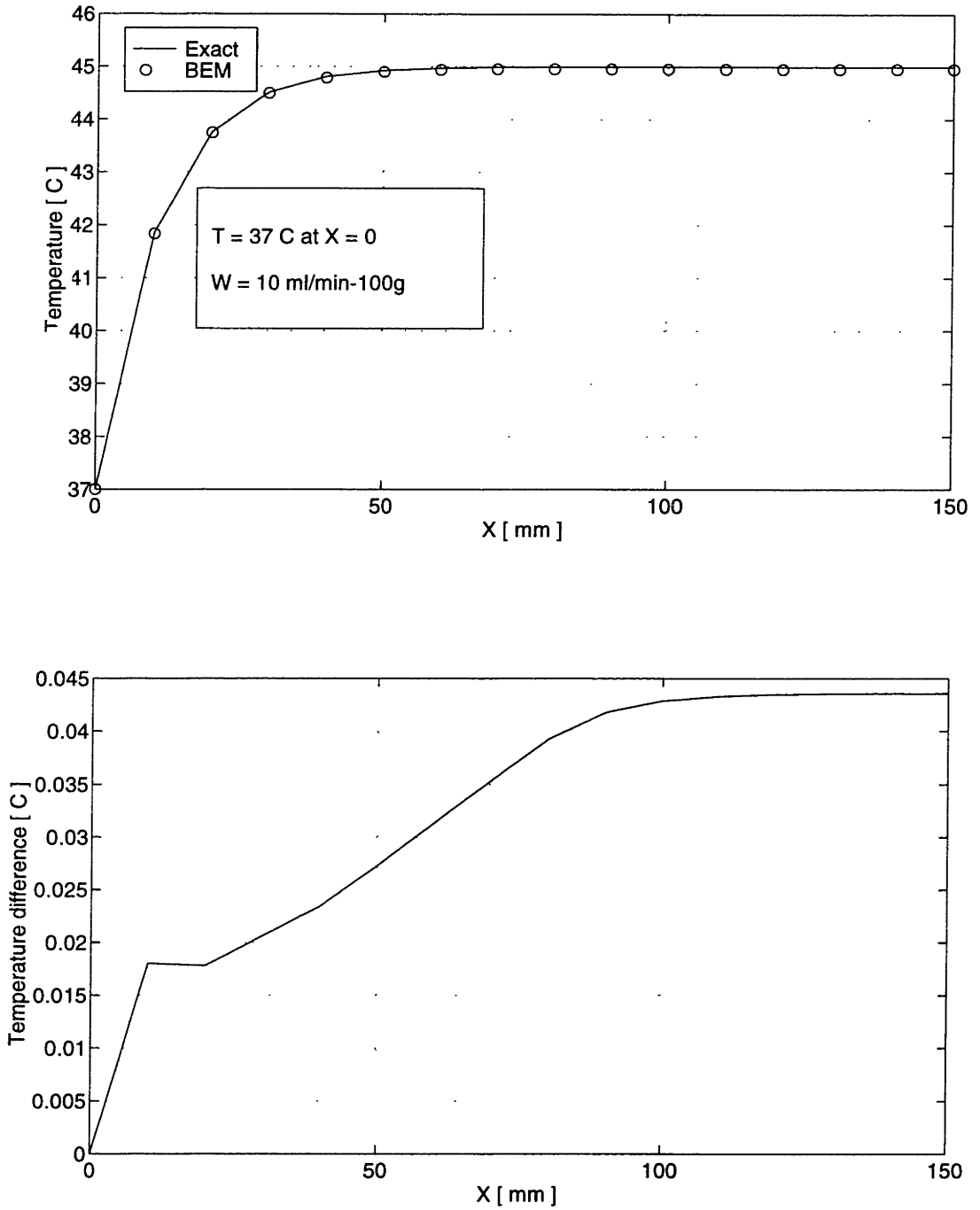

Figure 5-12: Temperature profile from the surface of the semi-infinite body with uniform internal heat generation, uniform perfusion and a homogeneous boundary condition of the first kind (top panel). The bottom panel shows the temperature difference for the exact minus the BEM solution.

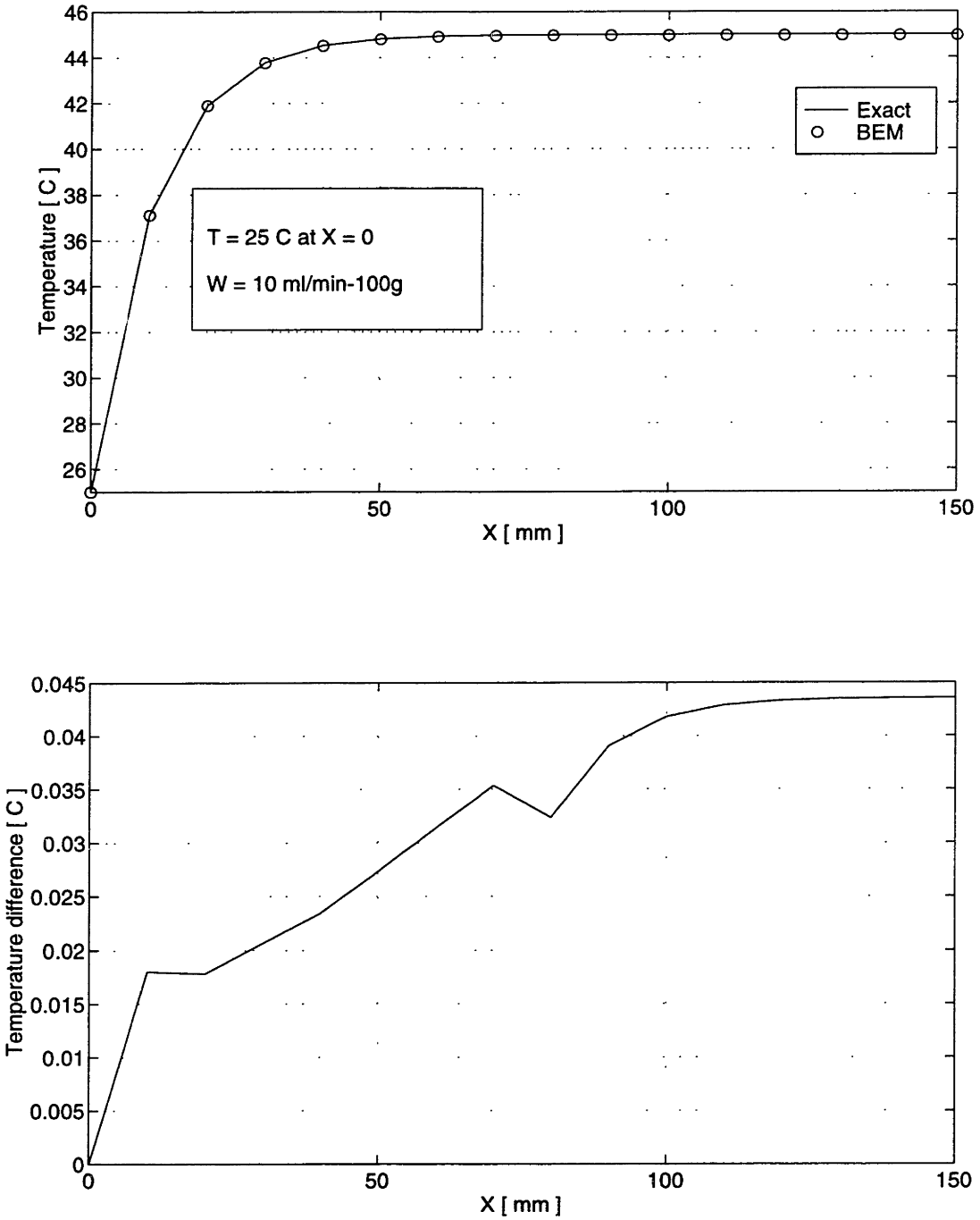

Figure 5-13: Temperature profile from the surface of the semi-infinite body with uniform internal heat generation, uniform perfusion and a non-homogeneous boundary condition of the first kind (top panel). The bottom panel shows the temperature difference for the exact minus the BEM solution.

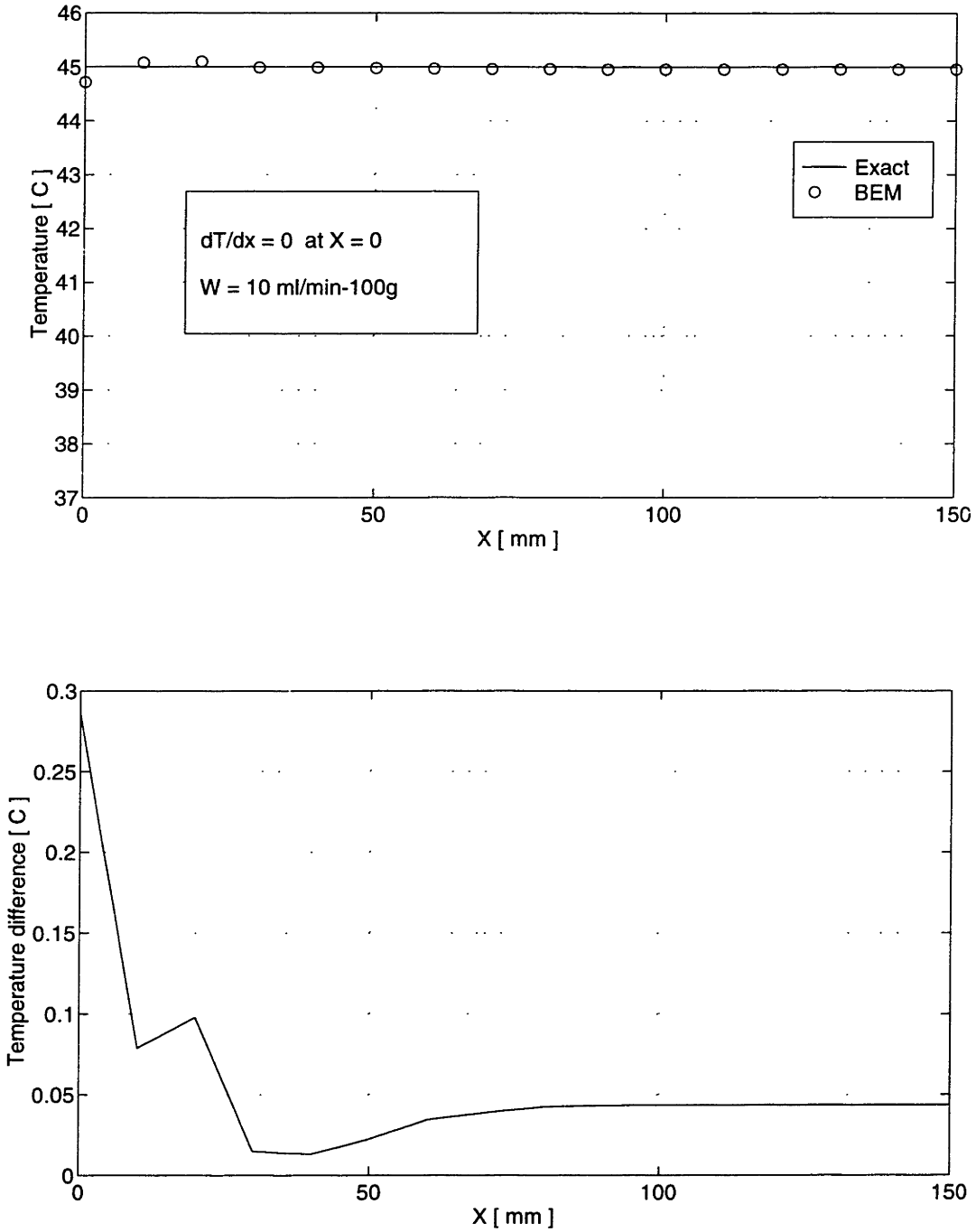

Figure 5-14: Temperature profile from the surface of the semi-infinite body with uniform internal heat generation, uniform perfusion and a homogeneous boundary condition of the second kind (top panel). The bottom panel shows the temperature difference for the exact minus the BEM solution.

Figure 5-15 shows the results for the same problem as in Figure 5-14, except the surface boundary condition is non-homogeneous and $q = 0.5$ W/cm^2. The top panel is the temperature profile from the surface into the semi-infinite body where the solid line is the exact solution and the symbols are the BEM solution. The bottom panel shows the error in terms of the temperature difference between the exact and BEM solutions.

Third Kind

For a boundary condition of the third kind applied to the boundary, the exact solution is:

$$\theta = \frac{1}{Pe} + \frac{Bi(\theta_f - \frac{1}{Pe})}{\sqrt{Pe} + Bi} e^{-\sqrt{Pe}\,x} \tag{5.13}$$

$$Bi = \frac{h\,L}{k_m} \tag{5.14}$$

$$\theta_f = \frac{T_f\,k_m}{Q\,L^2} \tag{5.15}$$

where Bi is the Biot number, h is the heat transfer coefficient, T_f and θ_f are the dimensioned and the dimensionless fluid temperature respectively.

The top panel in Figure 5-16 shows the temperature profile from the planar surface of a semi-infinite body with uniform internal heat generation (Q = 0.05566 W/cm^3), uniform perfusion (W = 10 ml/min-100g) and uniform thermal conductivity (k_m=0.5 W/m-^{o}C) with a boundary condition of the third kind (heat transfer coefficient, $h = 0.01$ W/cm^2-^{o}C and T$_f$ = 25 ^{o}C) at the surface. The solid line is the exact solution and the symbols represent the BEM solution. The bottom panel of Figure 5-16 shows the temperature difference between the exact and the BEM solution.

Figure 5-17 shows the results for the same problem as in Figure 5-16, except that here, the surface boundary condition is non-homogeneous with the external fluid temperature, T_f, equal to 25 ^{o}C. The top panel is the temperature profile from the surface into the semi-infinite body where the solid line is the exact solution and the symbols are the BEM solution. The bottom panel shows the error in terms of the temperature difference between the exact and BEM solutions.

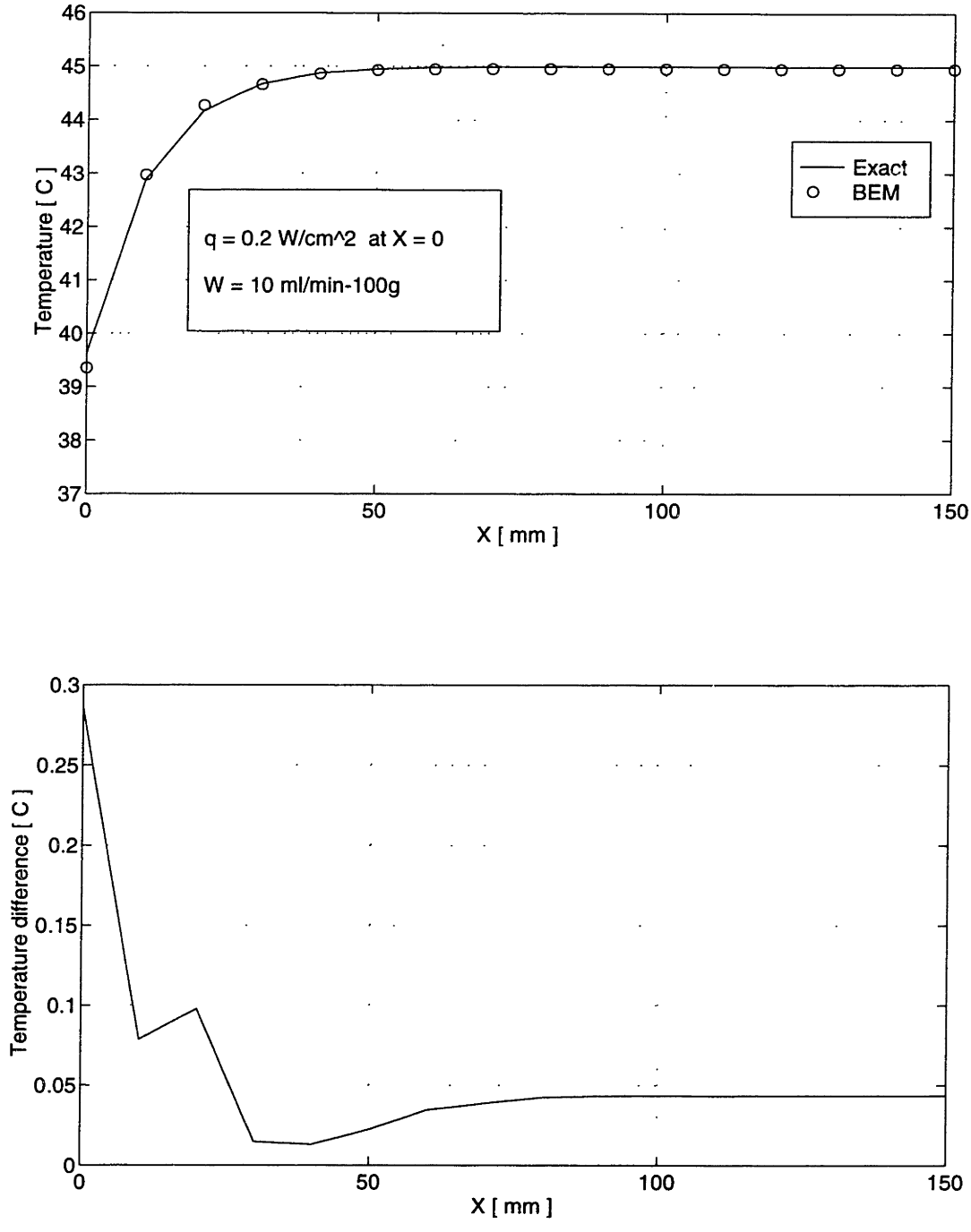

Figure 5-15: Temperature profile from the surface of the semi-infinite body with uniform internal heat generation, uniform perfusion and a non-homogeneous boundary condition of the second kind (top panel). The bottom panel shows the temperature difference for the exact minus the BEM solution.

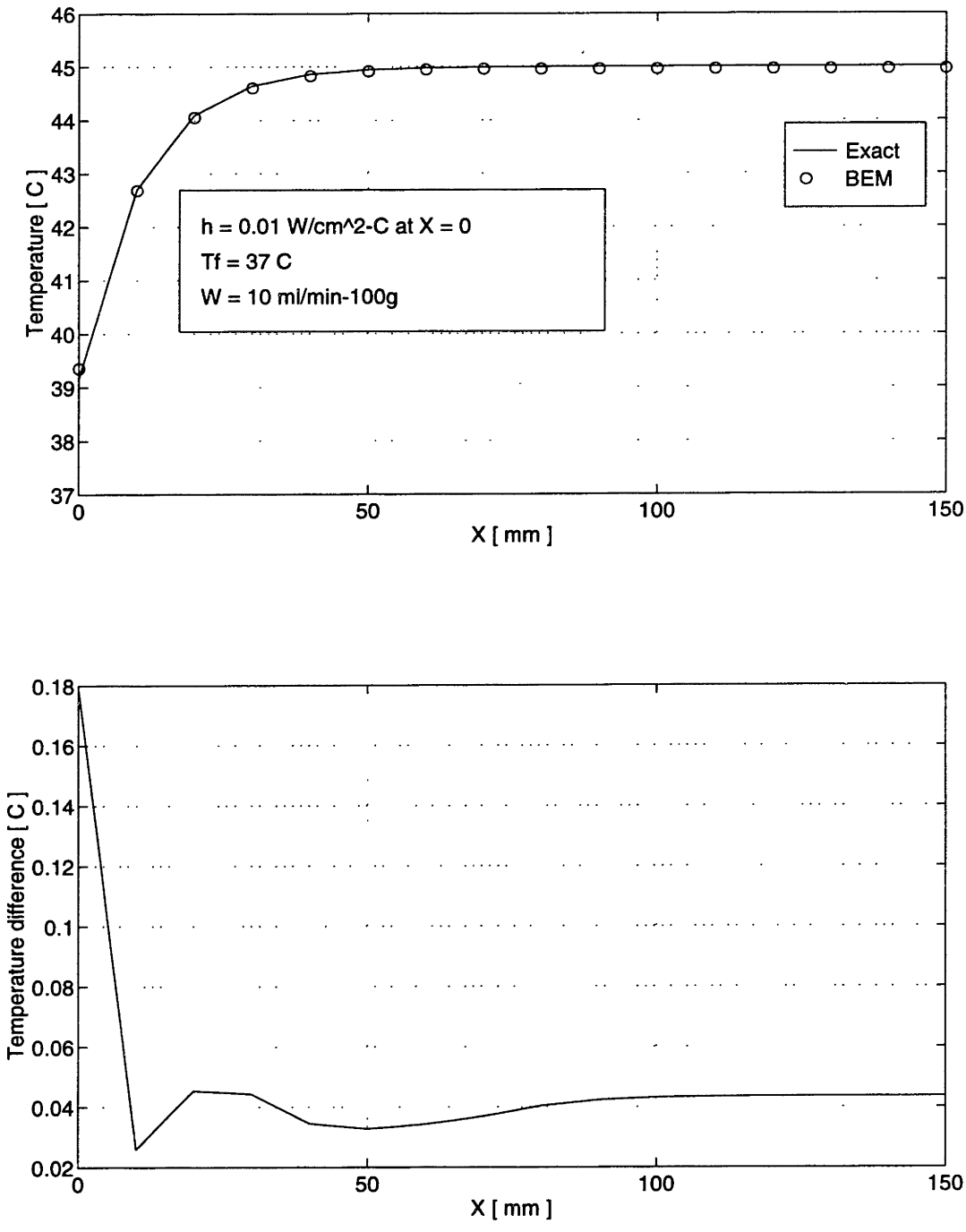

Figure 5-16: Temperature profile from the surface of the semi-infinite body with uniform internal heat generation, uniform perfusion and a homogeneous boundary condition of the third kind (top panel). The bottom panel shows the temperature difference for the exact minus the BEM solution.

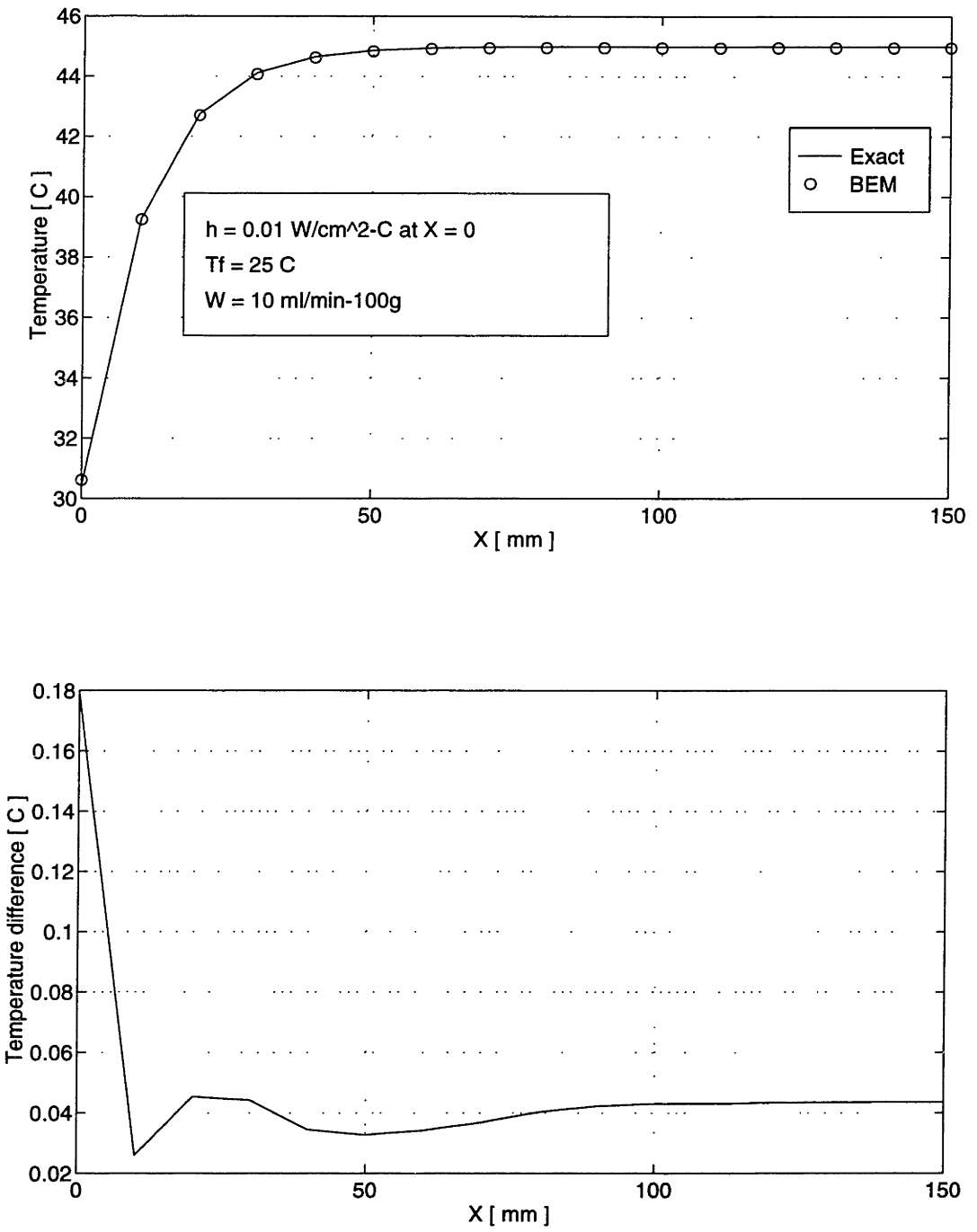

Figure 5-17: Temperature profile from the surface of the semi-infinite body with uniform internal heat generation, uniform perfusion and a non-homogeneous boundary condition of the third kind (top panel). The bottom panel shows the temperature difference for the exact minus the BEM solution.

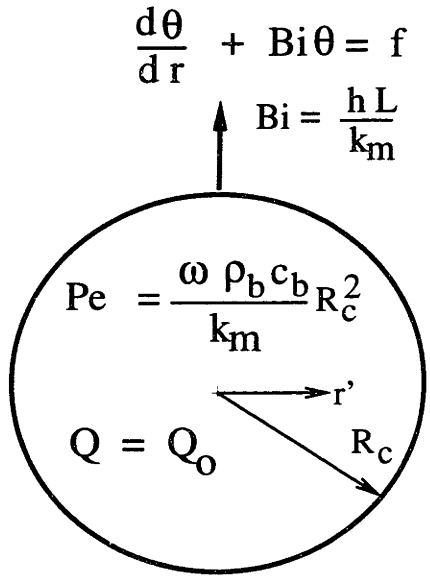

Figure 5-18: Schematic diagram of the finite tissue region with uniform internal heat generation, perfusion and properties with a boundary condition applied at the spherical surface.

5.1.4 Finite Spherical Domain Boundary Conditions

In this subsection, a series of test cases is defined which have uniform internal heat generation, uniform perfusion, and uniform thermal properties in a finite and spherical tissue volume at which a boundary condition of the first, second, or third kind is applied. Figure 5-18 shows a schematic diagram of this class of test cases, with a general boundary condition applied at the surface. The exact solutions for the temperature rise in these simple cases are easily available by the analytic solution of the 1-D differential equation in spherical coordinates. The results obtained from the BEM are compared with the exact solution to determine the BEM's ability to solve for the temperature at or near spherical shaped external boundaries.

First Kind

In this test case, the finite tissue sphere has a boundary condition of the first kind applied to the surface (zero surface temperature rise). The exact solution for the temperature is:

$$\theta = \frac{1}{Pe} - (\frac{1}{Pe} - \theta_b)\frac{\sinh(\sqrt{Pe}\, r)}{\sinh(\sqrt{Pe})\, r} \tag{5.16}$$

where the center of the sphere is at $r = 0$ and the boundary is at $r = 1$. In this solution, the length scale which forms the dimensionless variables is the tissue sphere radius, R_c.

The top panel of Figure 5-19 shows the temperature profile from the sphere center to the surface which is held at zero temperature rise. The domain has uniform internal heat generation (Q = 0.05566 W/cm^3), uniform perfusion (W = 10 ml/min-100g) and uniform thermal conductivity (k_m=0.5 W/m-^{o}C). The solid line is the exact solution and the symbols represent the BEM solution. The bottom panel of Figure 5-19 shows the temperature difference between the exact and BEM solutions.

A test case similar to the previous case is where the finite tissue sphere has a non-homogeneous boundary condition of the first kind (non-zero surface temperature rise). The top panel of Figure 5-20 shows the temperature profile from the sphere center to the surface which is held at a constant temperature rise. The domain has uniform internal heat generation (Q = 0.05566 W/cm^3), uniform perfusion (W = 10 ml/min-100g) and uniform thermal conductivity (k_m=0.5 W/m-^{o}C). The solid line is the exact solution and the symbols represent the BEM solution. The bottom panel of Figure 5-19 shows the temperature difference between the exact and BEM solutions.

Second Kind

In this case, the finite tissue sphere has a homogeneous boundary condition of the second kind applied to the surface (constant heat flux). The exact solution for temperature in this case is:

$$\theta = \frac{1}{Pe} - \frac{\Gamma \sinh(\sqrt{Pe}\, r)}{\sqrt{Pe}\cosh(\sqrt{Pe})r} \tag{5.17}$$

$$\Gamma = \frac{q}{Q_o R_c} \tag{5.18}$$

where Γ is the dimensionless heat flux, defined as positive out of the tissue sphere.

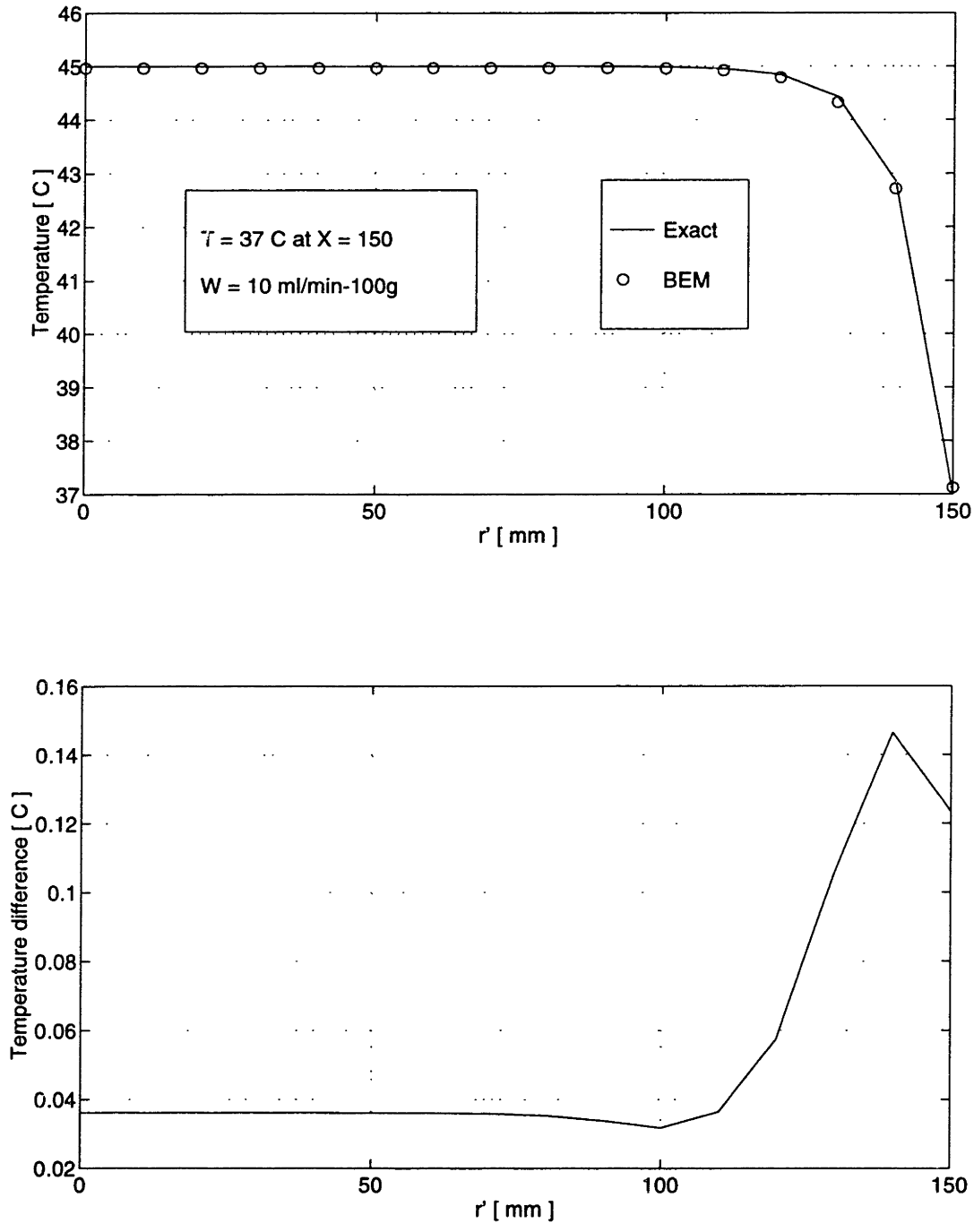

Figure 5-19: Temperature profile from the center of a finite, spherical tissue volume with uniform internal heat generation, uniform perfusion and a homogeneous boundary condition of the first kind (top panel). The bottom panel shows the temperature difference for the exact minus the BEM solution.

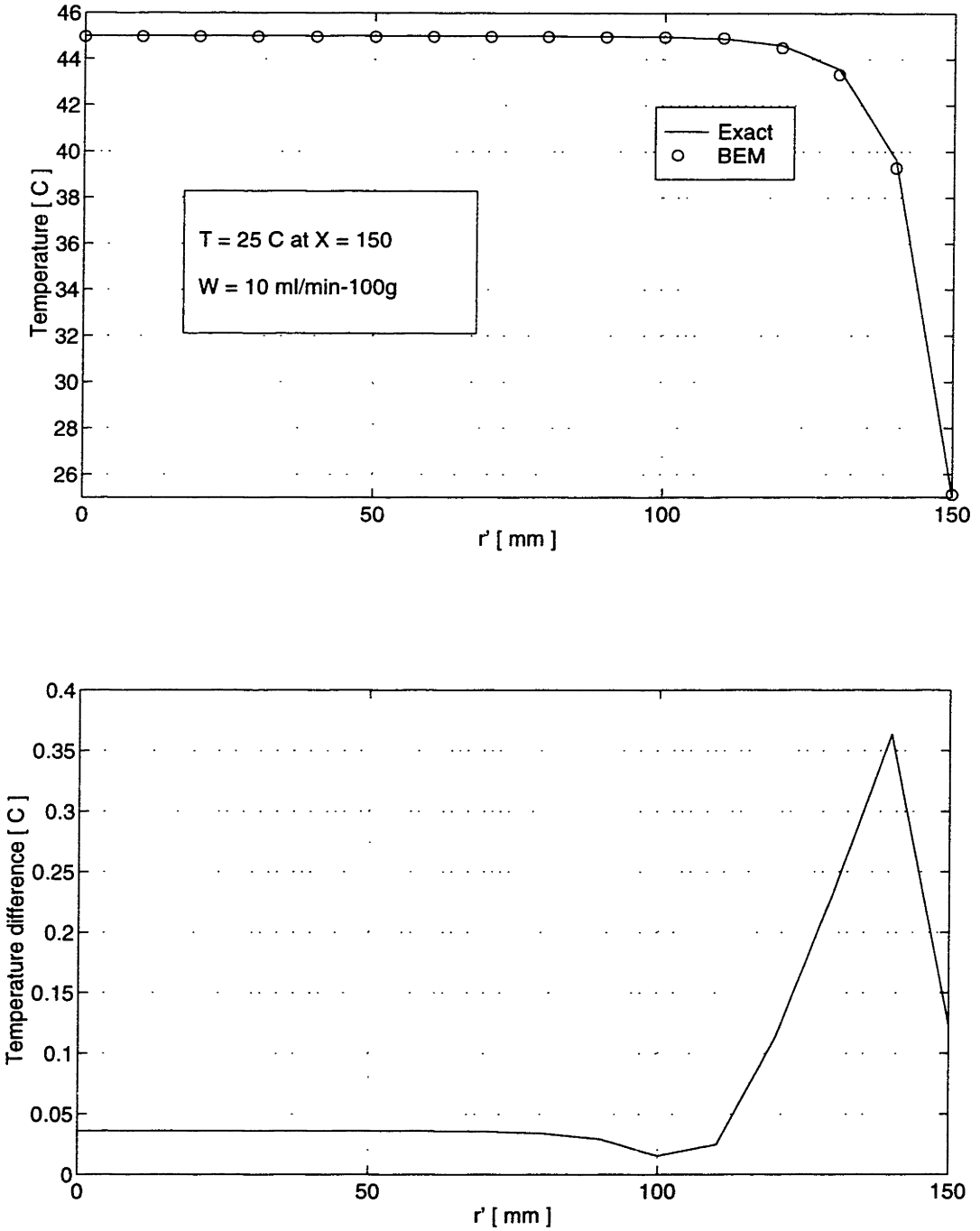

Figure 5-20: Temperature profile from the center of a finite, spherical tissue volume with uniform internal heat generation, uniform perfusion and a non-homogeneous boundary condition of the first kind (top panel). The bottom panel shows the temperature difference for the exact minus the BEM solution.

The top panel of Figure 5-21 shows the temperature profile from the sphere center to the surface. The domain has uniform internal heat generation (Q = 0.05566 W/cm^3), uniform perfusion (W = 10 ml/min-100g) and uniform thermal conductivity (k_m = 0.5 W/m-^{o}C). The solid line is the exact solution and the symbols represent the BEM solution. The bottom panel of Figure 5-21 shows the temperature difference between the exact and BEM solutions. As expected, the temperature profile is uniform.

Similar to the previous case is where the finite tissue sphere has a non-homogeneous boundary condition of the second kind (non-zero heat flux). The top panel of Figure 5-22 shows the temperature profile from the sphere center to the surface. The domain has uniform internal heat generation (Q = 0.05566 W/cm^3), uniform perfusion (W = 10 ml/min-100g) and uniform thermal conductivity (k_m=0.5 W/m-^{o}C). The solid line is the exact solution and the symbols represent the BEM solution. The bottom panel of Figure 5-22 shows the temperature difference between the exact and BEM solutions.

Third Kind

In this case, the finite tissue sphere is convectively cooled at the surface. The exact solution for temperature is:

$$\theta = \frac{1}{Pe} - \frac{Bi(\frac{1}{Pe} - \theta_f)}{\sqrt{Pe}\cosh(\sqrt{Pe}) + Bi\sinh(\sqrt{Pe})}\frac{\sinh(\sqrt{Pe}\,r)}{r} \qquad (5.19)$$

where Bi is the Biot number and θ_f is the dimensionless cooling fluid temperature.

The top panel in Figure 5-23 shows the temperature profile from the center of the sphere with uniform internal heat generation (Q = 0.05566 W/cm^3), uniform perfusion (W = 10 ml/min-100g) and uniform thermal conductivity (k_m=0.5 W/m-^{o}C) with a homogeneous boundary condition of the third kind (heat transfer coefficient, h = 0.01 W/cm^2-^{o}C) at the surface. The solid line is the exact solution and the symbols represent the BEM solution. The bottom panel of Figure 5-23 shows the temperature difference between the exact and the BEM solution.

Figure 5-24 shows the results for the same problem as in Figure 5-23, except that here, the surface boundary condition is non-homogeneous with the external fluid temperature, T_f, equal to 25 ^{o}C. The top panel is the temperature profile from the center of the sphere to

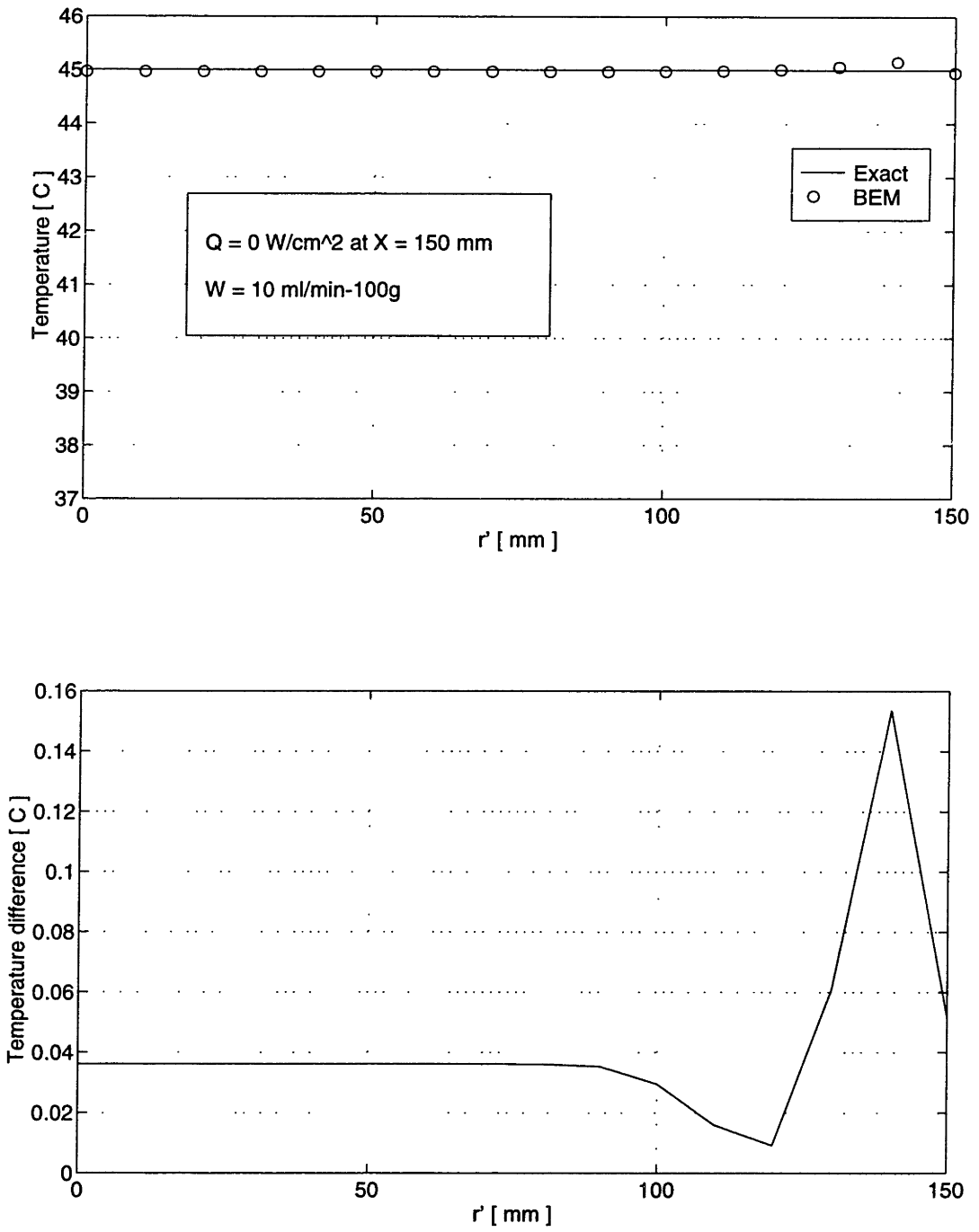

Figure 5-21: Temperature profile from the center of a finite, spherical tissue volume with uniform internal heat generation, uniform perfusion and a homogeneous boundary condition of the second kind (top panel). The bottom panel shows the temperature difference for the exact minus the BEM solution.

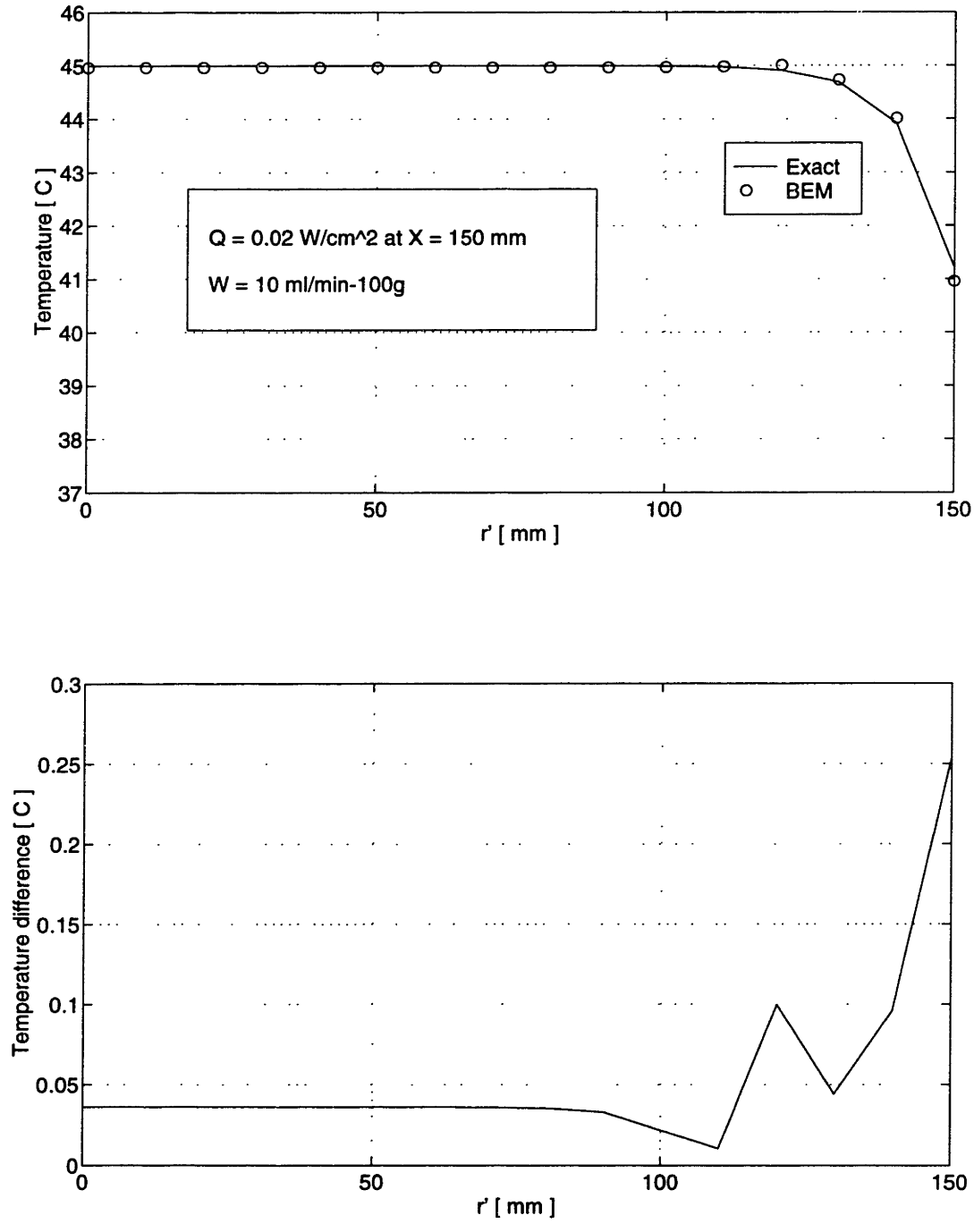

Figure 5-22: Temperature profile from the center of a finite, spherical tissue volume with uniform internal heat generation, uniform perfusion and a non-homogeneous boundary condition of the second kind (top panel). The bottom panel shows the temperature difference for the exact minus the BEM solution.

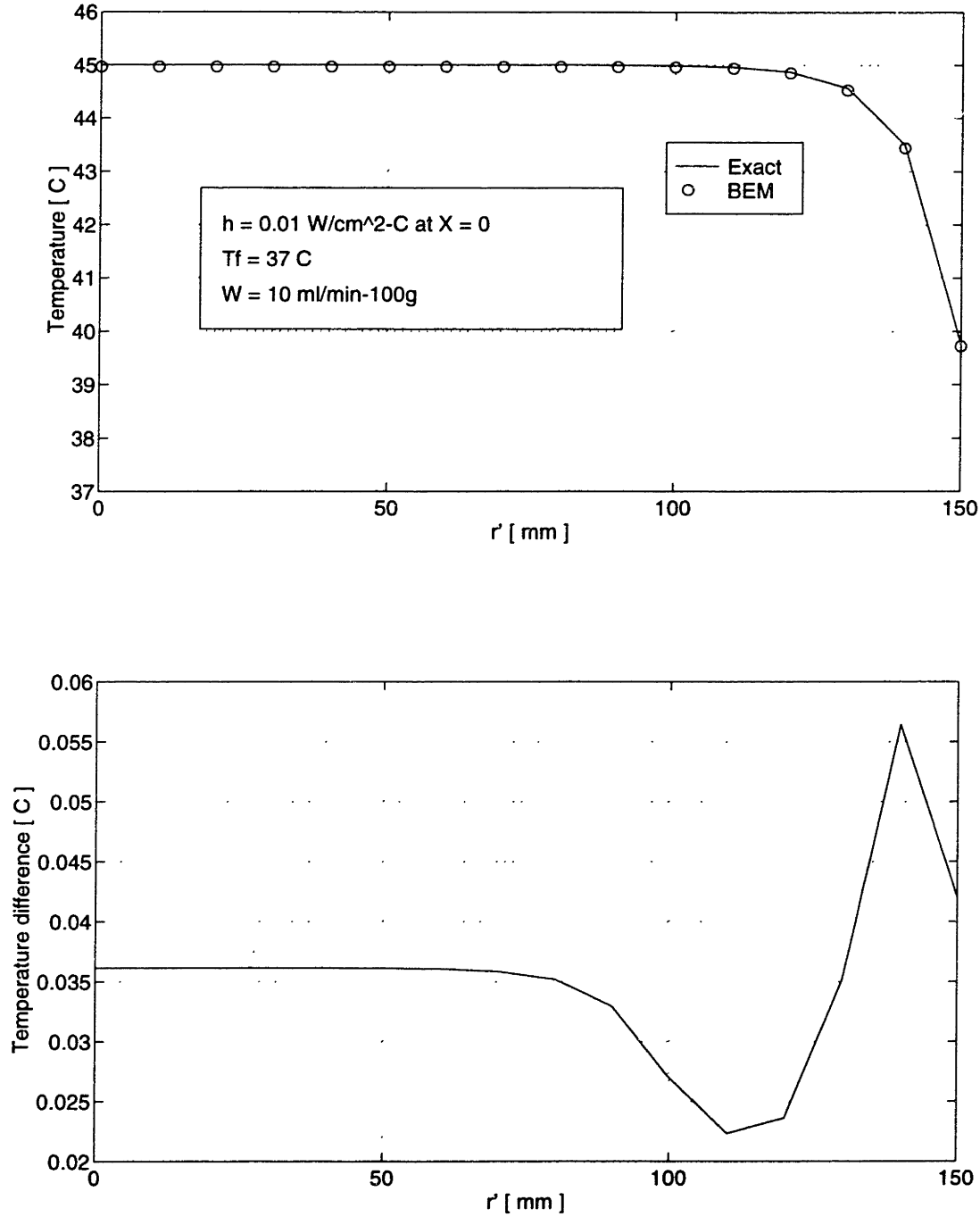

Figure 5-23: Temperature profile from the center to the surface of the sphere with uniform internal heat generation, uniform perfusion and a homogeneous boundary condition of the third kind (top panel). The bottom panel shows the temperature difference for the exact minus the BEM solution.

the surface where the solid line is the exact solution and the symbols are the BEM solution. The bottom panel shows the error in terms of the temperature difference between the exact and BEM solutions.

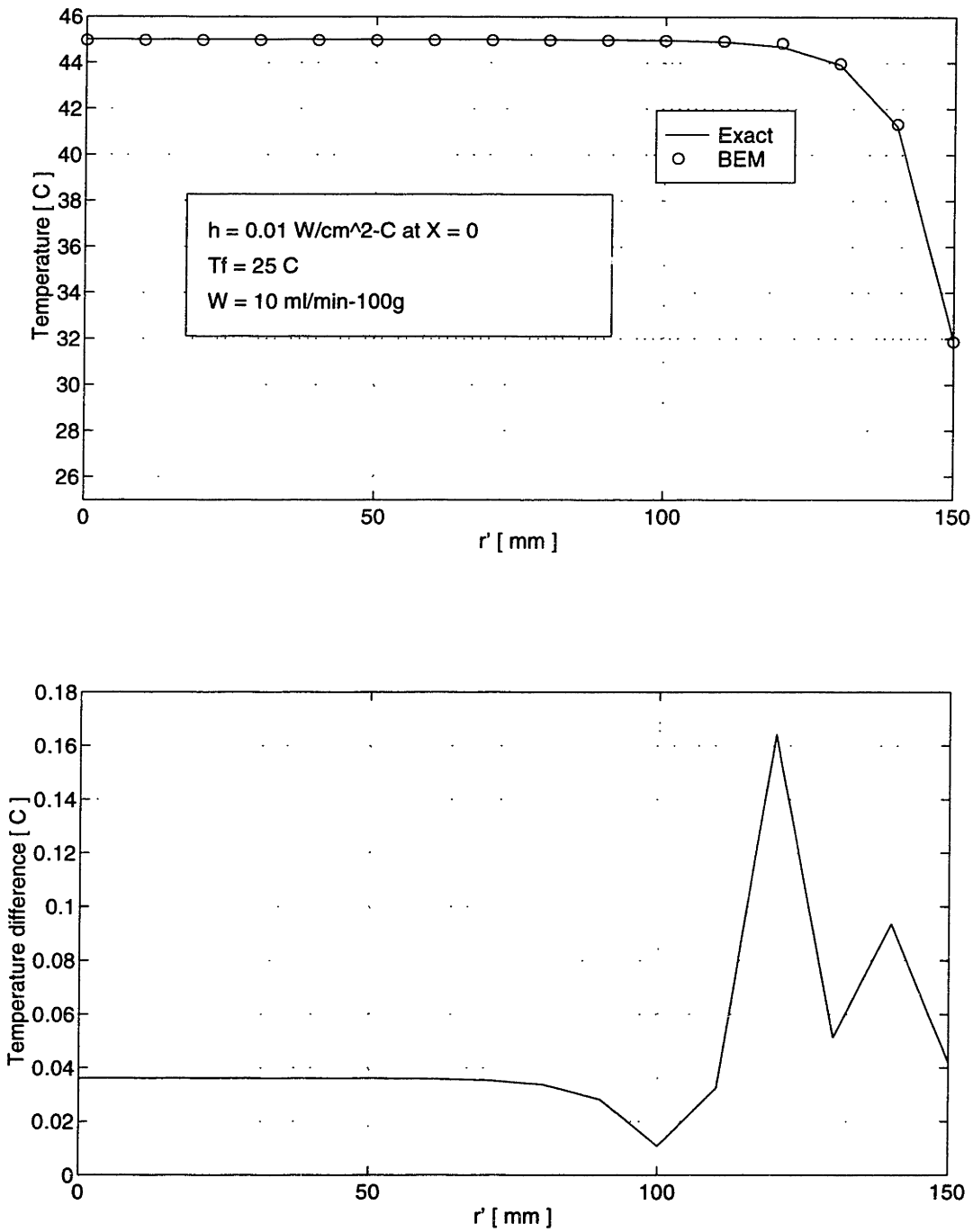

Figure 5-24: Temperature profile from the center to the surface of the sphere with uniform internal heat generation, uniform perfusion and a non-homogeneous boundary condition of the third kind (top panel). The bottom panel shows the temperature difference for the exact minus the BEM solution.

5.2 Comparisons with Finite Element Solutions

The previous comparisons of the BEM with analytical solutions to the bioheat transfer equation demonstrate the validity of the BEM and the level of accuracy obtainable for certain conditions found in hyperthermia heat transfer. A more rigorous test of the method requires problems that more closely match the clinical situation in which the geometry is derived from patient anatomy. In such cases of irregular geometry and variable perfusion, an independent reference solution whose accuracy is far greater than that of the BEM, must be used. Such an independent numerical solution is provided by the finite element method (FEM), the results of which are compared to the BEM for the case with irregular geometry and differential perfusion.

5.2.1 Description of the Finite Element Method

The FEM is an extension of the Rayleigh-Ritz and Galerkin techniques to solve partial differential equations where the continuous domain is discretized into elements and placed into a variational form. Piece-wise continuous polynomials are used as trial functions over each element, and the approximate solution consists of a sum of weighted trial functions. The Rayleigh-Ritz technique solves for the weights by minimizing the potential "energy" contained in the linear combination of the trial functions. The more general Galerkin technique solves for the weights using the weak form. The discrete set of equations is assembled into a matrix, called the stiffness matrix, and direct elimination is used to solve for the weights [63].

The power of the finite element method lies in its general applicability to solve many different types of differential equations (parabolic, hyperbolic, elliptical, etc.) on an arbitrary three-dimensional geometry. The degree of accuracy possible is very high (a fraction of a percent temperature error), however vast computational resources are necessary to achieve this accuracy. For example, Gaussian elimination is generally used for the matrix inversion, requiring on the order of N^3 operations, where N is the number of nodes or degrees of freedom, [64]. In any case, the entire field must be solved for at once. In addition, the method depends on an adequate transformation of the continuous problem

to a discrete representation. Improper discretization (mesh generation) leads to inaccurate results and solution divergence. Often, finite element meshes need to be solved multiple times to demonstrate convergence.

For comparisons with the BEM, the FEM, as implemented in the NEKTON software package, is used, [65]. Strictly speaking, NEKTON uses the spectral element method which employs a variational form with high order (Legendre) polynomials as the trial functions, [66]. The system "stiffness" matrix is solved by an iterative scheme.

5.2.2 Accuracy of the Finite Element Comparison

In order to determine the accuracy of NEKTON in solving problems with differential perfusion, a comparison is made with the test case presented in Section 5.1.2 which consists of a tissue sphere with perfusion of W_1 in an infinite domain with perfusion of W_2. For comparison, the NEKTON mesh consists of 204 elements and each element has 125 nodes for a total of 25,500 nodes. Fifth order polynomials were used for the trial functions across each element. The BEM used finite sources with a radius of 1.5 mm and an integration volume with a radius of 7 perfusion lengths (L_p's). A dedicated *Digital* DECstation 5000/133 running the ULTRIX 4.3 operating system was the platform used in both the NEKTON computation and BEM. Figures 5-25 and 5-26 contain the results of Figure 5-9, but plotted here in contrast to the NEKTON solution of the same problem. The top panels of the Figures 5-25 and 5-26 show the temperature profiles across the spherical tissue volume for the BEM, NEKTON and the exact solutions, while the bottom panels show the error for NEKTON and the BEM. In these two cases, the results indicate that NEKTON is about an order of magnitude more accurate than the BEM. Thus NEKTON provides sufficient accuracy to serve as a standard against which the BEM can be judged.

The previously described problem can be used to investigate the trade-off between computational speed and solution accuracy for the BEM and the speed relative to NEKTON. For the BEM, finite source size and integration volume size are independent parameters that determine the degree of solution accuracy (and thus computational time). In this comparison, the BEM was required to compute temperature at as many nodes as NEKTON (29,791). Figure 5-27 shows the results when these parameters are varied together to

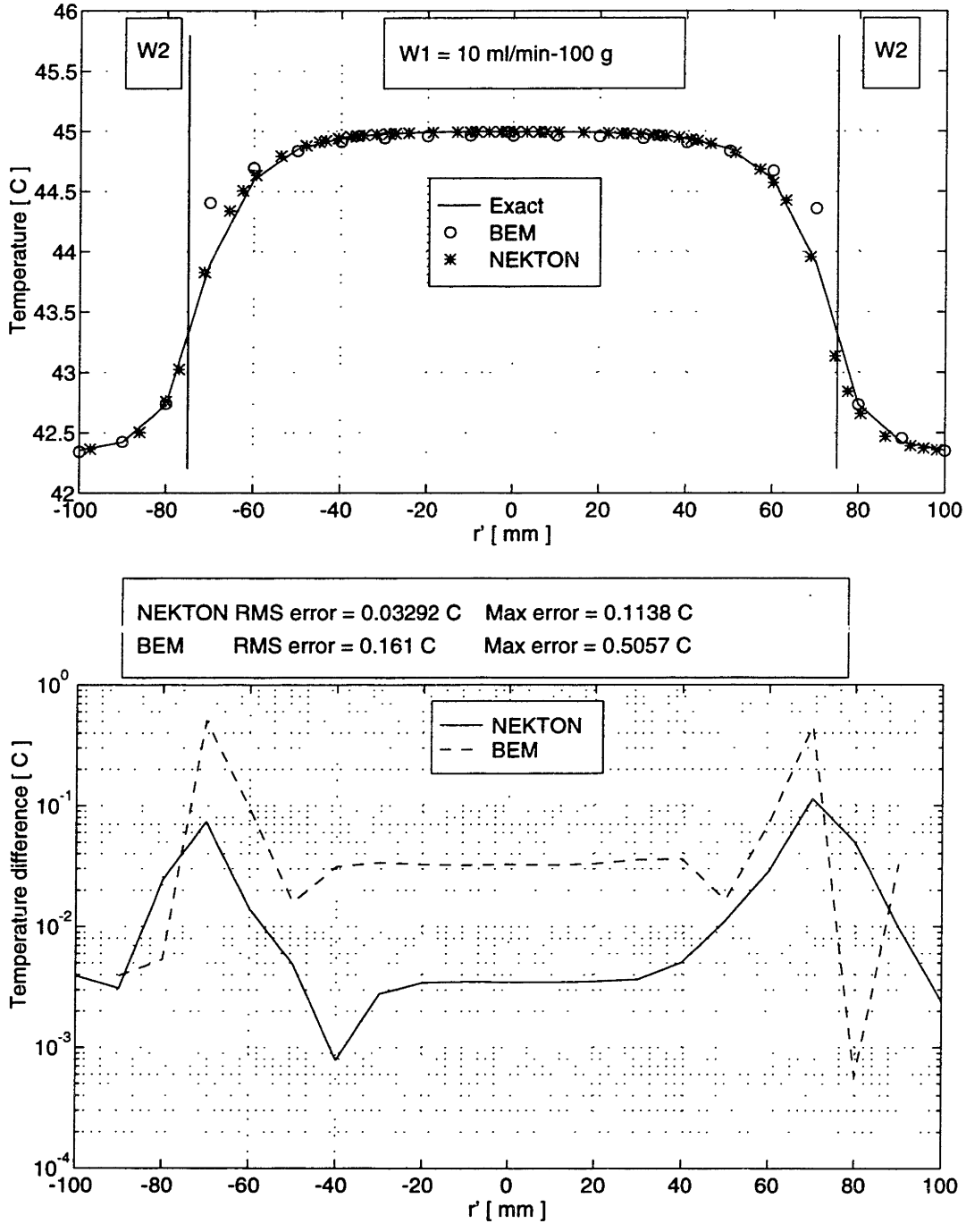

Figure 5-25: Temperature profile through the spherical tissue subdomain with uniform internal heat generation, uniform thermal properties and $W_1 = 10$ and $W_2 = 15$ ml/min-100g (top panel) as computed by NEKTON, the BEM and the exact solution. The bottom panel is the error, in terms of a temperature difference for NEKTON and the BEM.

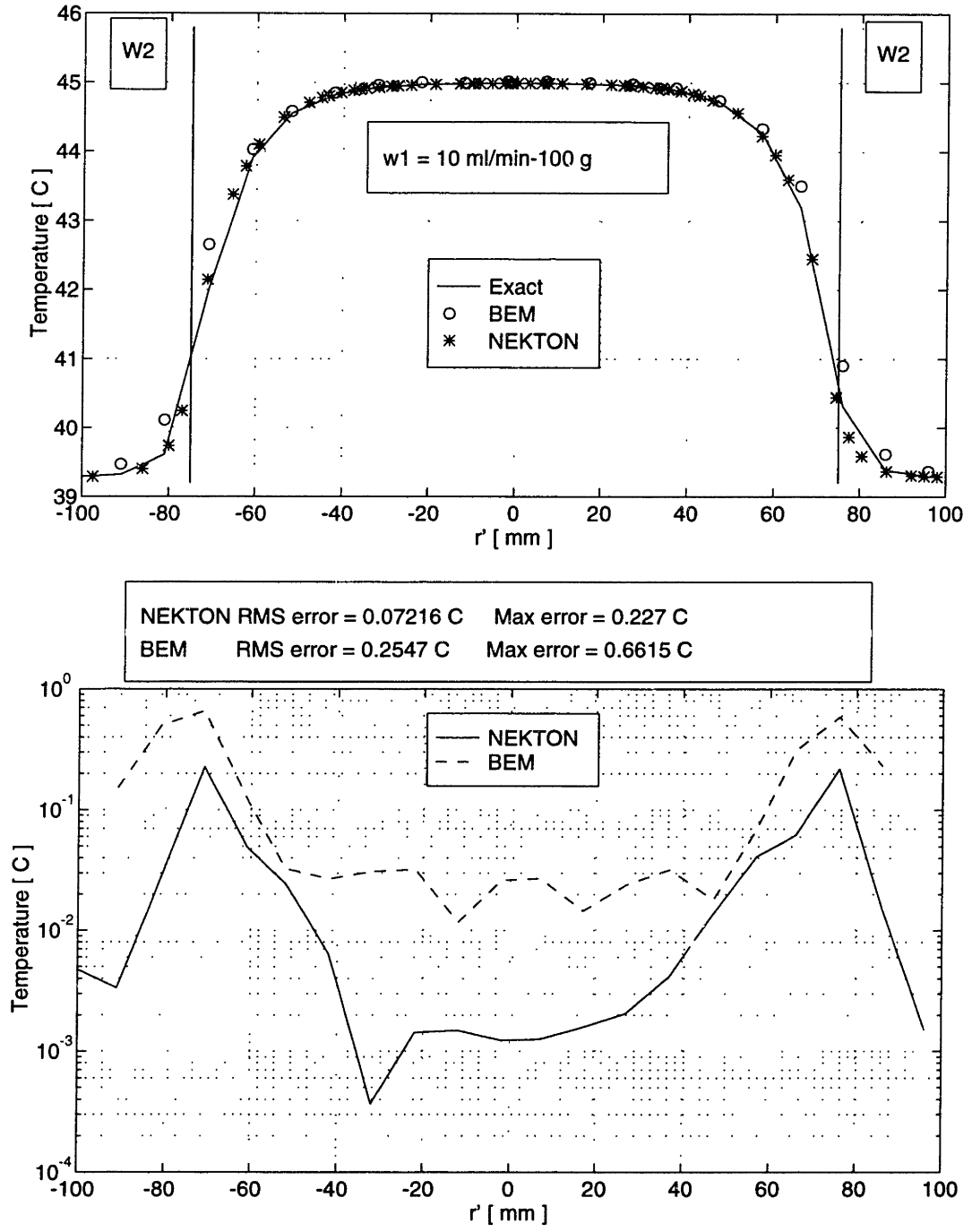

Figure 5-26: Temperature profile through the spherical tissue subdomain with uniform internal heat generation, uniform thermal properties and W_1= 10 and W_2 = 35 ml/min-100g (top panel) as computed by NEKTON, the BEM and the exact solution. The bottom panel is the error, in terms of a temperature difference for NEKTON and the BEM.

solve the same problem in Figure 5-26. The figure shows the RMS temperature error as a function of computational time for NEKTON and the BEM with various settings of the computational parameters. Each curve of connected symbols represents the temperature error of the BEM with constant size Basis Elements and N_p varied from 2 to 8. Error in the BEM comes from two primary components: 1) the limited size of the integration volume which causes a small under-estimation of temperature and 2) the finite size of the Basis Elements which causes a small over-estimation of temperature. For small N_p, the error from the limited integration volume is dominant and at higher N_p the error from the Basis Element size is dominant. Figure 5-27 clearly shows these two components of error and note that the minima of each curve corresponds to where the errors cancel each other out. The asterisk symbols are for three different NEKTON solutions which use third, fifth and seventh order polynomials as the trial functions with the higher order polynomials requiring more computation time.

Given the two governing parameters which control the BEM - the Element size and the integration volume - the BEM has more degrees of freedom in selecting an operating point for the desired speed-accuracy trade-off. The temperature field computation for interactive treatment planning needs to take place in less than 5 minutes. Figure 5-27 shows that for a desired speed of 5 minutes, the RMS error is about 0.3 °C for a Basis Element size of 3 mm. If higher accuracy is required, the BEM is capable of providing accuracy as high as NEKTON, but with longer computation time.

5.2.3 Irregularly Shaped Tissue Subdomain

The irregularly shaped tissue subdomain is representative of the geometry found in anatomical structures. It is used in this section to create a test problem for comparison between NEKTON and the BEM. A three-dimensional cardioid-ellipsoidal shape, shown in Figure 5-28 is used to parameterize the irregularly shaped tissue region. The geometry is mathematically described, yet can possess irregular features, [67]. In this example, the subvolume is used to model a tumor which has perfusion different from the surrounding tissue.

In the first test, the model "kidney" structure is located in an infinite tissue volume with uniform internal heat generation (Q = 0.05566 W/cm^3) and uniform thermal conductivity

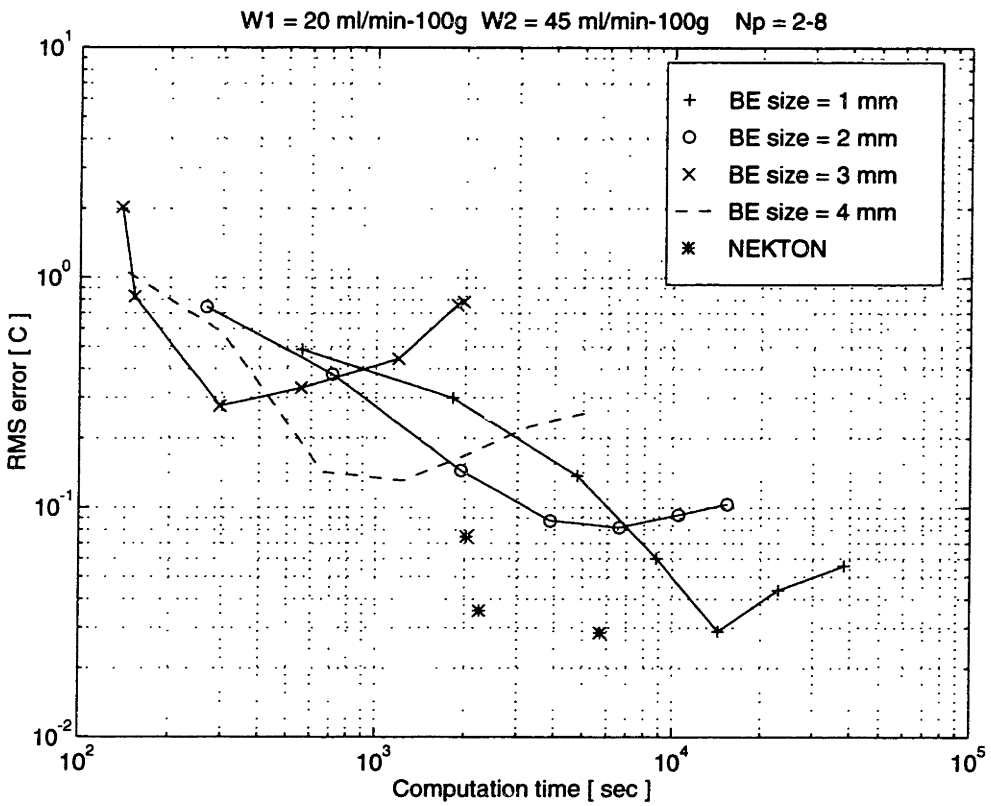

Figure 5-27: RMS temperature error for the BEM and NEKTON as a function of time.

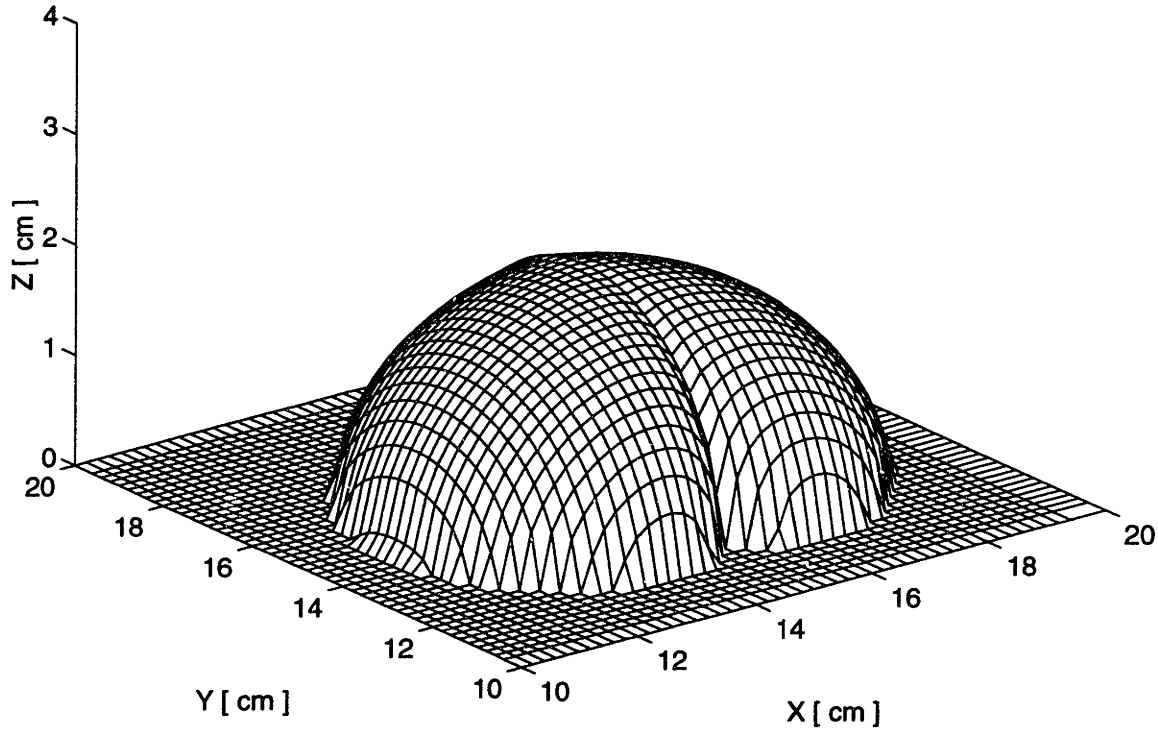

Figure 5-28: Cardioid-ellipse sub-volume used for the evaluation of the BEM.

(k_m = 0.5 W/m-°C). Perfusion inside the structure is 10 ml/min-100g, and outside, in the surrounding tissue, is 15 ml/min-100g. The NEKTON and BEM computation parameters are the same as those used in Section 5.2.2. Figure 5-29 shows the temperature profile through the central axis of the structure (Y = 14 cm and Z = 0 cm) as computed by NEKTON (the solid line) and the BEM (the symbols). The RMS temperature difference along this line is 0.18 °C and the maximum error is 0.33 °C. The second test using the kidney structure is the same as the first test above, except that the tissue outside of the structure has a perfusion of 35 ml/min-100g. Figure 5-30 shows the temperature through the central axis of the structure as computed by NEKTON (the solid line) and the BEM (the symbols). The RMS temperature difference along this line is 0.23 °C and the maximum error is 0.60 °C. Note that in both cases, the error is a maximum at the internal boundary and increases with the increase in the perfusion difference.

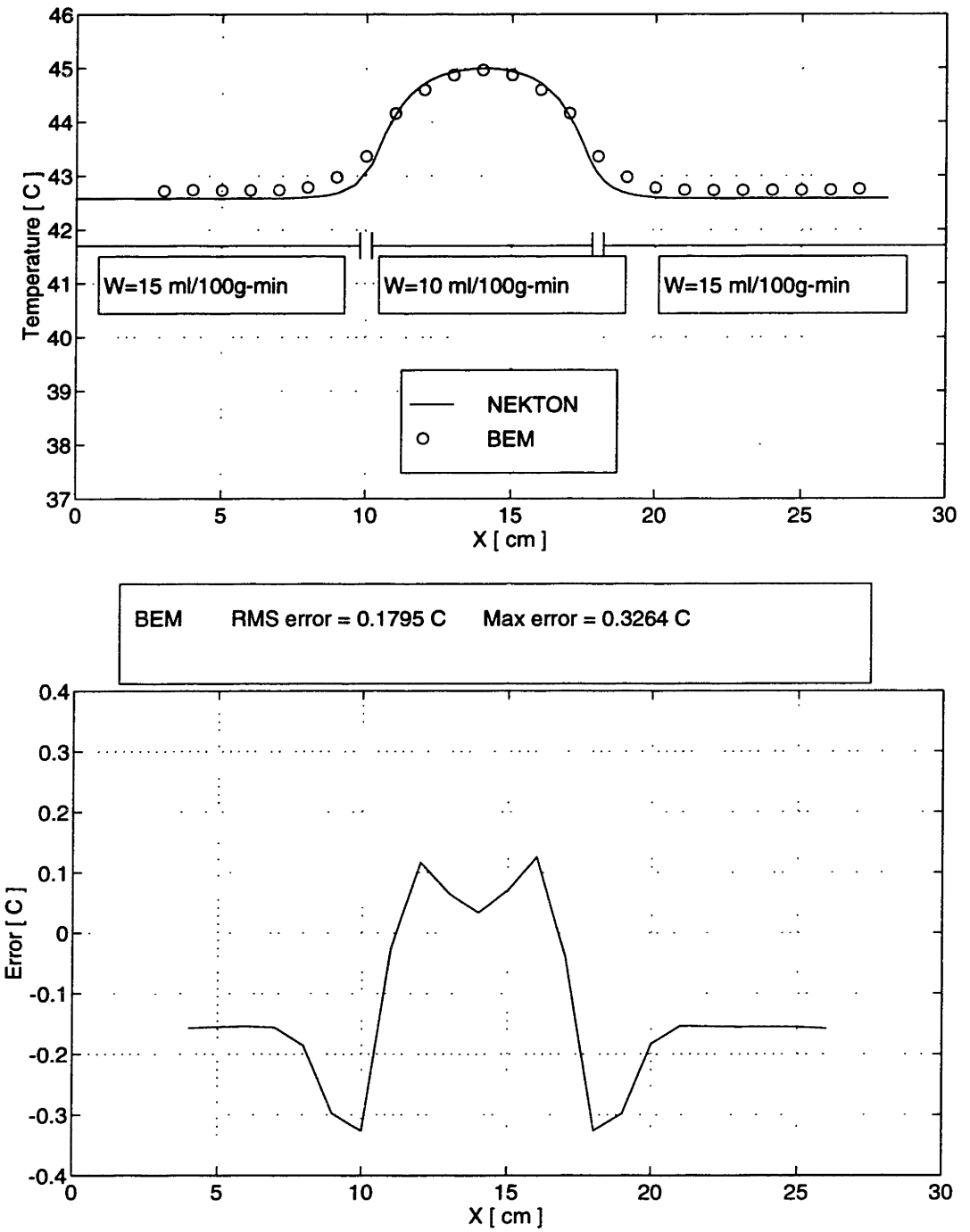

Figure 5-29: Temperature profile through the center of the structure (top panel) as computed by the BEM and NEKTON. The bottom panel shows the temperature difference between the two methods.

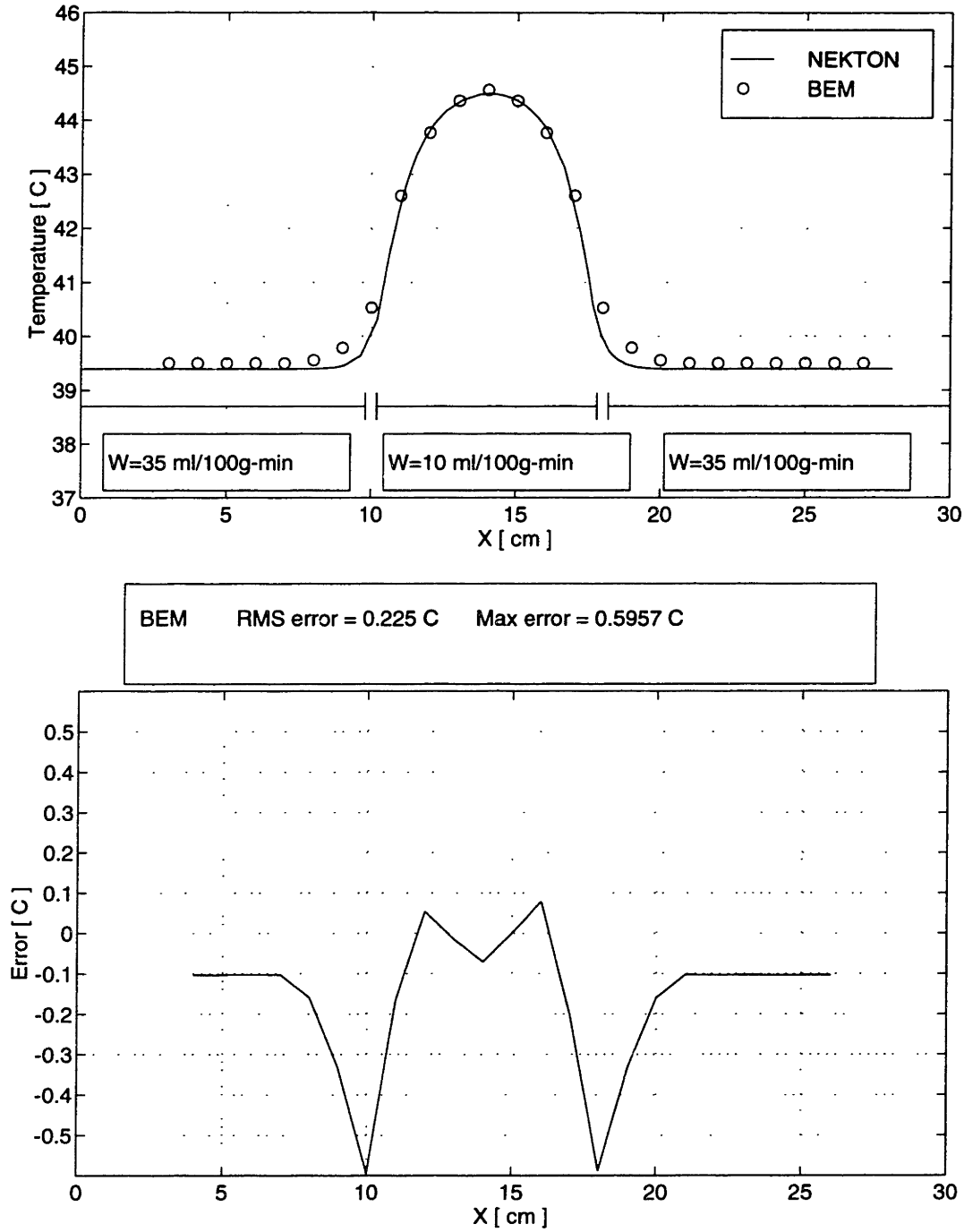

Figure 5-30: Temperature profile through the center of the kidney structure (top panel) as computed by the BEM and NEKTON. The bottom panel shows the temperature difference between the two methods.

5.3 Validation Discussion

In this section, the results of the analytical and numerical validation are discussed in terms of the accuracy of the BEM solutions. For the most part, the BEM errors are the sum of a combination of errors from the solution methodology and the algorithm implementation.

5.3.1 Methodological Errors

Methodological errors are those which result from the underlying formulation of the BEM. These errors arise from such conditions as the limited volume of integration, the size of the Basis Elements, the packing of the Basis Elements and the internal and external boundary Basis Element formulations.

Volume of Integration

The use of the limited volume of integration, as discussed in Section 3.1, neglects sources that are thermally distant from the domain node at which the temperature is being computed. "Thermally distant" is defined as being more than N_p perfusion lengths away, where N_p is an arbitrary constant whose increase in magnitude is proportional to an increase in solution accuracy.

For nominal values of N_p (3-8), the limited volume of integration is the source of the most significant errors and causes the BEM to necessarily under-estimate the temperature. This stands to reason because neglecting the distant sources, introduces less energy into the tissue. It is possible, at least in a theoretical sense, to compute this resulting temperature error. Consider an infinite tissue domain with uniform thermal properties, perfusion and internal heat generation that is everywhere uniform except in a spherical volume which surrounds the domain node. This spherical volume has a radius equal to $N_p L_p$ and an internal heat generation equal to zero. The deficit of power deposition models the finite sources which have already been considered by the BEM in the computation for temperature. A simple 1-D analytical solution for temperature at the center of the sphere (the domain

node) gives the following result for the dimensionless temperature error:

$$\epsilon_{NL} = \frac{e^{-\sqrt{Pe_{NL}}}}{Pe_{NL}}(\sqrt{Pe_{NL}} + 1) \tag{5.20}$$

$$Pe_{NL} = \frac{\omega \rho_b c_b}{k_m} N_p^2 L_p^2 \tag{5.21}$$

$$Pe_{NL} = N_p^2 \tag{5.22}$$

It is possible to recalculate the results of Figure 5-2 and compare with the theoretical error as computed by Equation (5.20). Figure 5-31 shows semi-log plot of the theoretical error (symbols) with the actual BEM error (solid line). The plot shows distinctly two regions for the actual BEM error. The region less than 5 perfusion lengths is predicted well by Equation (5.20), and the error is attributed primarily to the limited volume of integration which under estimates the temperature. The error in the region greater than 8 perfusion lengths is due to the combination of the other error sources, some of which are discussed below. These errors cause temperature to be slightly over-estimated and thus between 5 and 7 perfusion lengths the two types of error cancel each other out and create the "null" at about N_p=6.25. The position and the existence of the null depends on the problem geometry, the power deposition and the perfusion.

Basis Element Size

The theoretical foundation of the BEM, as discussed in Section 3.1, lies in the Green's function solution to the bioheat transfer equation. In this formulation, internal heat generation is transformed into the volume integration of weighted point sources over the heated volume. The BEM, however, approximately represents the internal heat generation with the summation of weighted finite sources in the heated volume. Mathematically, as the size of the finite sources becomes smaller, the exact point source transformation is approached and the solution for temperature becomes more exact.

This is illustrated by revisiting the example problem of Section 5.1.1, which has uniform thermal properties, uniform perfusion and uniform internal heat generation. Figure 5-32 shows a plot of percent temperature error as a function of Basis Element size where the integration volume radius is equal to 10 perfusion lengths. The dashed line shows

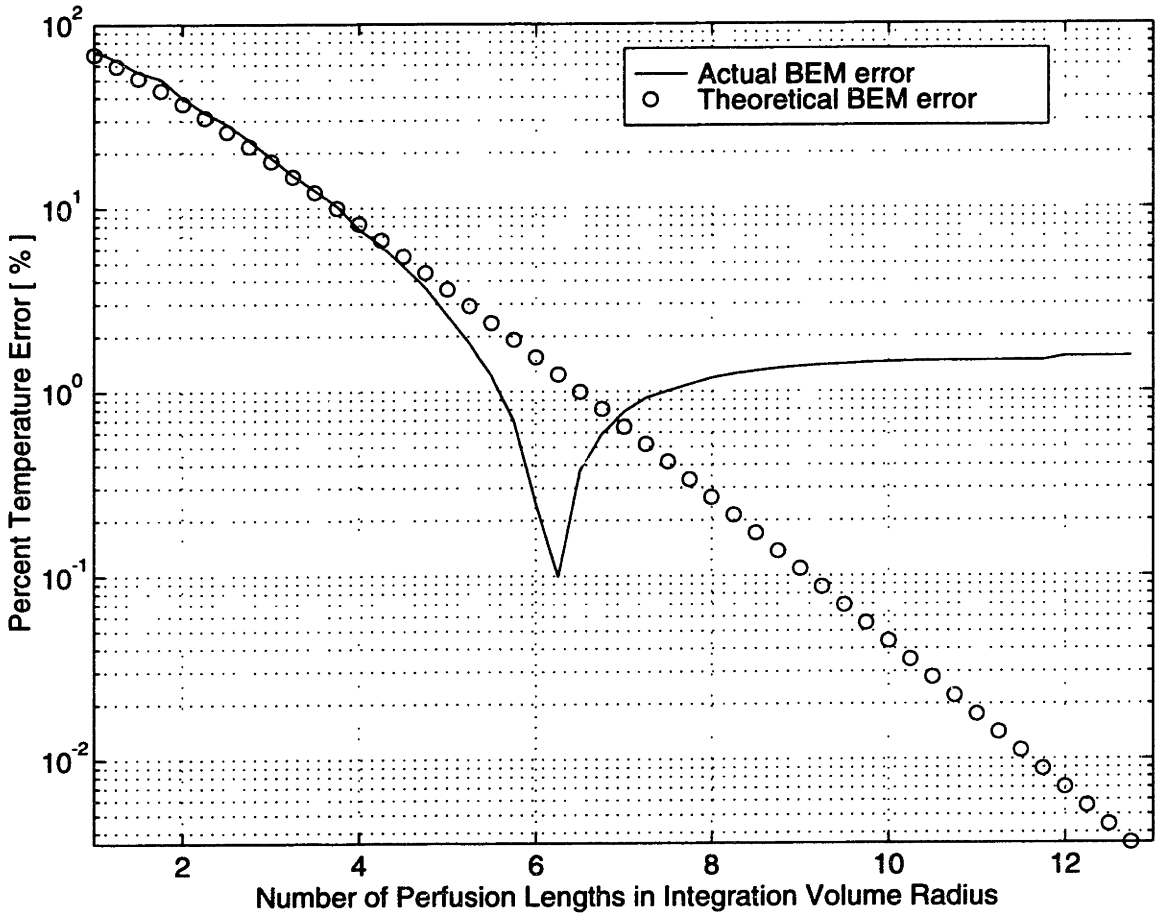

Figure 5-31: Percent temperature error as a function of the integration volume.

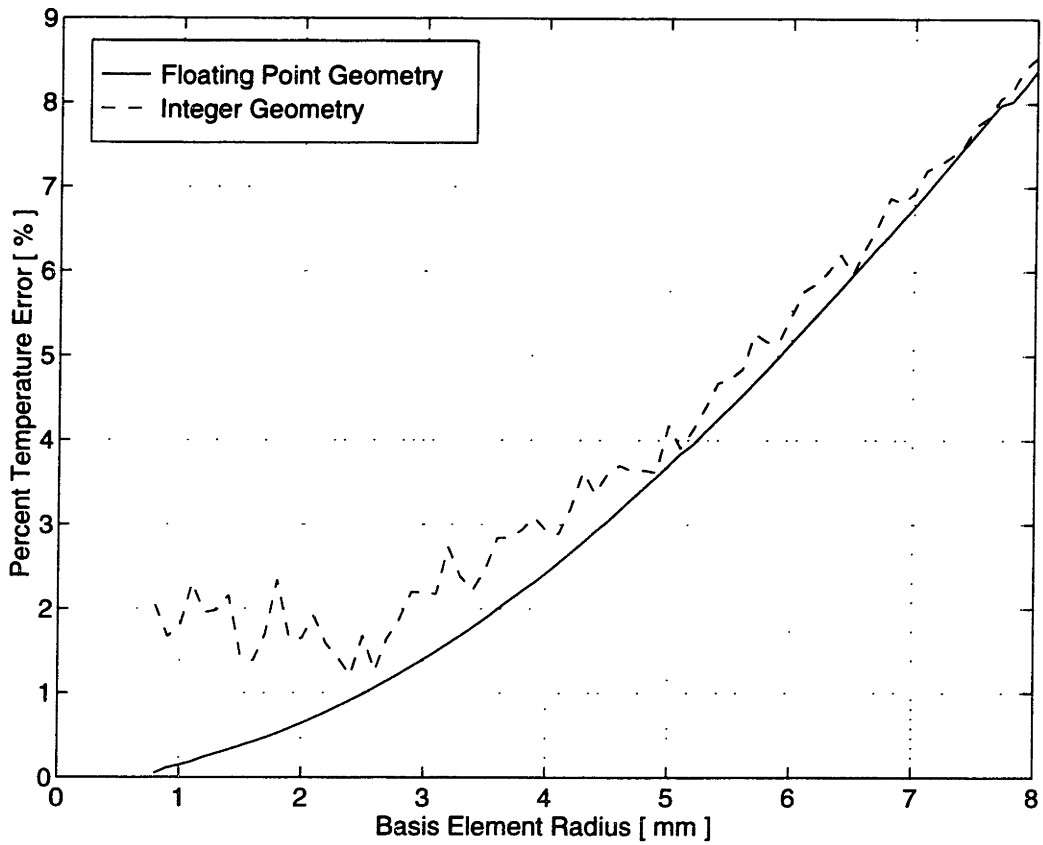

Figure 5-32: Percent temperature error as a function the Basis Element radius for floating point geometric computation (solid line) and integer geometric computation (broken line).

the temperature error using the standard integer geometric computation of the BEM implementation. The solid line shows the temperature error using floating point geometric computation. Note that as the Basis Elements become smaller, the error for both cases decreases. However, the error for the integer case reaches a minimum at about 2 percent, while the floating point case continues to decrease. This difference in error is due to the fact that the spatial resolution of the integer computation is 1 mm. At larger Basis Element radii, this resolution is insignificant and at smaller radii, the uncertainty in the Basis Element position causes this error.

Basis Element Packing

The current implementation of the BEM uses close-hexagonal packing of finite sources to represent the heated volume. This packing scheme, as well as others, introduces small

errors into the solution by the misrepresentation of the local internal heat distribution. The packing forms void space between neighboring sources in which there is no internal heat generation. Globally, energy conservation is satisfied by scaling up the power deposition to compensate for the power that is not deposited in the void-space. Locally, this causes spatial variations in the internal heat generation with a periodicity of the Basis Element diameter and causes errors in the temperature computation.

This effect can be illustrated using, again, the test case of Section 5.1.1. Figure 5-33 shows a plot of percent temperature error as a function of distance through the tissue domain, normalized for the Basis Element radius. The abscissa in Figure 5-33 cuts through the center of two adjacent Basis Elements at 0 and 2. The periodic variation of temperature error is quite apparent in this figure and as expected, the temperature is over-estimated at the Basis Element centers. In normal operation of the BEM and in the validation studies carried out in Sections 5.1 and 5.2, the Basis Element lattice is always shifted such that the center of a Basis Element coincides with the domain node. This is to insure consistency in the BEM results, however, it is not a limitation or constraint of the method or implementation.

Internal Boundary Basis Element Errors

Errors arising from the internal boundary Basis Elements are caused by a combination of the closed form approximation made to the exact, open form solutions for the Basis Elements, and the approximation of the internal boundaries as being locally planar or locally spherical.

For locally planar boundaries, the Basis Element formulation, which uses the method of images, matches the temperature and heat flux at the boundary, but approximately solves the bioheat transfer equation. In the limit however, as perfusion tends to zero, the exact solution is approached. Therefore, it is expected that lower perfusion decreases the errors associated with these Basis Elements. This is somewhat demonstrated in Figure 5-6, where the error is greater in the case of perfusion equal to 35 ml/min-100g (0.32 °C) than in the case of perfusion equal to 15 ml/min-100g (0.27 °C).

For locally spherical boundaries, the Basis Element formulation also maintains the continuity of temperature and heat flux across the internal boundary and approximately solves the bioheat transfer equation. As with the planar boundaries, the error associated

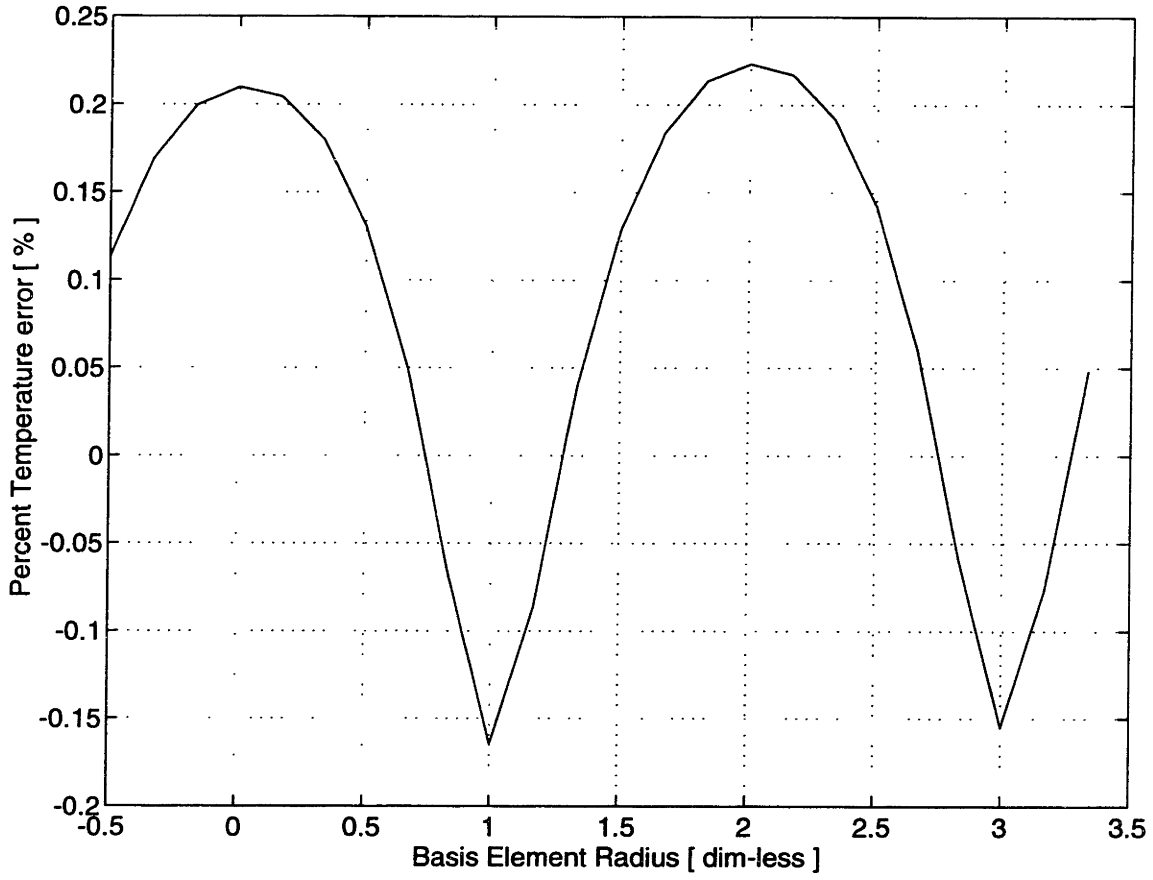

Figure 5-33: Percent temperature error as a function of distance through the center of two adjacent Basis Elements.

with the spherical boundary Basis Elements decreases with decreasing perfusion. Figure 5-9 shows the error in the case of perfusion equal to 15 ml/min-100g is 0.13 °C and in the case of perfusion equal to 35 ml/min-100g is 0.49 °C. From the exact and NEKTON comparisons, the effect of approximating internal boundaries as locally spherical is not completely clear. In the NEKTON-BEM comparison with the kidney structure problem, the boundary is ellipsoidal. Figure 5-29 shows the maximum temperature difference to be 0.32 °C, higher than the error of 0.13 °C in the exact comparison in Figure 5-9. This increase in error for the NEKTON-BEM comparison over the BEM-exact comparison is due to a combination of the error in non-spherical boundary of the kidney structure and the error in the discrete representation of the geometry. The error due to the discrete geometry is discussed further below.

External Boundary Basis Element Errors

Errors in the external boundary Basis Elements are also caused by approximations in the Basis Element derivation and the approximation of the external boundaries as being locally planar or locally spherical. Planar boundary Basis Elements are derived using the method of images. For homogeneous boundary conditions of the first and second kind, these Basis Elements are exact. The errors associated with these boundary conditions, shown in Figures 5-12 and 5-14, are due to the inefficient packing of Basis Elements close to the boundary. The Basis Elements for the boundary condition of the third kind are approximate, however, and the error is about the same order as that of the boundary condition of the second kind. Thus errors here are taken to be due also to the inefficient Basis Element packing near an external boundary. Spherical boundary Basis Elements are composed of approximate solutions and exhibit errors for the spherical test cases no larger than their planar counterparts.

5.3.2 Implementation Errors

Implementation errors arise through the current algorithm which is used to generate the results presented here, and are not fundamental to the method. Such errors are worth exploration and discussion in order to further understand the accuracy limits of the BEM.

These errors stem mainly from the discrete representation of geometry and the integer computation.

Discrete Representation of the Geometry

The BEM takes as input 3-D matrices of power deposition, perfusion, thermal conductivity, and the position vectors of each domain node. Since this is the complete problem definition for what concerns the BEM, there is an inherent error associated with transforming a continuous problem to discrete space. Though it was shown in Chapter 3 that the error in the BEM is decoupled from the domain mesh resolution, the mesh must contain at least enough nodes to adequately characterize the continuous problem. This is particularly important for the representation of the power deposition. For instance, to compute the power deposition at points in the domain, but in between nodes, a trilinear interpolation scheme is used. However, if the gradient of the power deposition function is large, as occurs in the discontinuous power deposition example of Figure 5-4, the trilinear interpolation is not able to accurately reconstruct the original function. This result can be improved by either using a higher order interpolation scheme, such a third order spline, or by increasing the number of domain nodes.

The internal and external boundary Basis Elements rely on the discrete geometry as inputs to compute the position of the boundary, the radius of curvature and normal vectors. The computation of these boundary parameters from the discrete geometry is discussed in Chapter 4. The comparisons presented above with exact solutions have only used the exact boundary parameters as computed directly from the continuous geometry. To demonstrate the error introduced with the computation of these parameters from the discrete geometry, the example of Figure 5-9 is revisited. The top panel of Figure 5-34 shows a plot of the temperature profile through the spherical tissue subdomain with uniform internal heat generation and differential properties (10 ml/min-100g inside the sphere and 15 ml/min-100g outside the sphere). The solid line is the exact solution and the circular symbols are the BEM solution computed from the exact boundary parameters - these results are taken directly from Figure 5-9 and reproduced here. The asterisks are the BEM solution, but with the boundary parameters computed from the discrete geometry. The bottom panel shows

the temperature difference between the exact solution and each of the two BEM solutions. Note that the error from the discrete geometry case is higher near the boundary and it varies more erratically than the continuous case. It is expected that as the number of domain nodes increases, the discrete geometry error would approach the error in the continuous geometry case. In general 50 percent of the error in this case is due to the discrete geometry. This error could also be decreased by the use of a more accurate algorithm for the computation of the boundary radius of curvature, the position vectors and the normal vectors.

Integer Computation

The effect of integer computation can readily be seen with the results of Figure 5-32. The heart of the integer computation is the use of a "look-up table" for the square roots when computing the distance between a Basis Element and a domain node. This table has a spatial resolution of 1 mm, thus the closer the Basis Element is to the node, the less accurate its distance is computed, and the less accurate the temperature computation is. According to Figure 5-32, this effect is significant only for Basis Elements with a radius of 4 mm or less.

5.3.3 Speed-Accuracy Comparison

The speed-accuracy comparison between NEKTON and the BEM in Figure 5-27 shows that the BEM is best suited for very fast solutions with moderate accuracy. It is clear that when high accuracy is desired (on the order of 0.05 °C), NEKTON is the better choice for achieving the solution. For what concerns hyperthermia treatment planning and evaluation, the solution should be complete in no more than 5 minutes total time. Thus, the results suggest that the error in the BEM, for the given time constraint, is about 0.3 °C. It will be seen in Chapter 6 whether the speed-accuracy differences between NEKTON and the BEM are significant in actual clinical use.

In the comparison, the BEM computed the temperature at as many domain nodes as NEKTON. In contrast to the finite difference and finite element techniques, the accuracy of the BEM does not depend on the number of domain nodes. Thus in practice, the BEM need

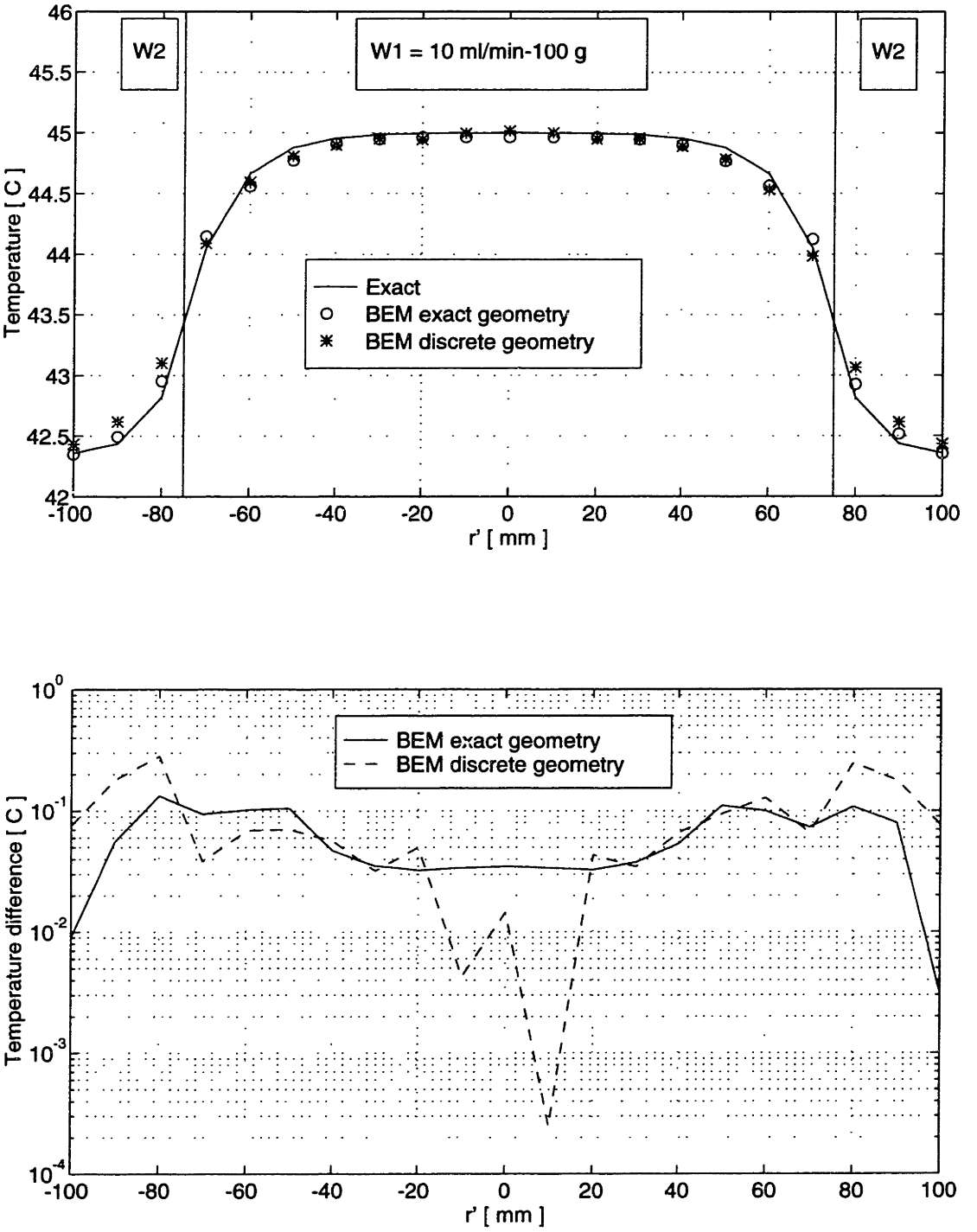

Figure 5-34: Temperature profile through the spherical tissue subdomain with uniform internal heat generation and differential properties (top panel) and the temperature difference for BEM solution with exact boundary parameters (solid line) and boundary parameters computed from the discrete geometry (dashed line).

not have to compute the temperature everywhere in the domain. This feature of the solution methodology, which has not been exploited here, allows for the further optimization of the algorithm at the level of the system interface. These features of the BEM should allow for the development of "push-bottom" thermal modeling technology which can be installed in the clinic for routine treatment planning and evaluation.

Chapter 6

Experimental Validation of the Basis Element Method

In order to determine the validity and the potential usefulness of the BEM in a clinical setting, experimental comparisons to actual hyperthermia sessions are carried out. In these experiments, large animals and human subjects are given hyperthermia while SAR, temperature and, when possible, perfusion are measured at discrete locations in and around the target tissue volume. SAR and perfusion measurements are used as inputs to the BEM, which computes, as output, the steady-state temperature field. This computed temperature field is then compared to the discrete temperature measurements.

6.1 Clinical Hyperthermia Technology

The experimental validation relies on the available clinical technology to provide the power delivery system and the measurement of the algorithm inputs (SAR, perfusion and geometry) and the measurement of temperature. The following four subsections detail the equipment used in the animal and human experimental studies.

6.1.1 FSUM Heating Applicator

The FSUM (Focused Segmented Ultrasound Machine, Labthermics Technologies, Inc., Champaign, IL) applicator consists of 56 individual square, planar ultrasound transducers mounted on a hemispherical shell with a 24 cm radius of curvature. A clear, flexible plastic membrane is stretched across the applicator aperture (30 cm diameter) to maintain the housing full of degassed water and to couple the transducers to the patient skin. Figure 6-4 is a schematic diagram of the applicator in the large animal experiment. The water-filled housing is cooled with water circulated through coils to maintain the transducer and skin surface at a set temperature. Each of the transducers operates at 1 MHz and is individually controllable from 0 to 40 W with an average efficiency of about 70% to give a maximum transducer output power of 28 W. The ultrasound field from each transducer overlaps to form a focal region about 15 cm from the aperture surface. In order to distribute the power more judiciously throughout the treatment volume, the hemispherical shell is capable of a circular, precessional motion with a frequency of 0.3 to 1 Hz.

6.1.2 Dense Thermometry

Dense thermometry measurements are provided by multiple temperature sensor probes using the Temperature Profilometer (Thermal Technologies, Inc., Cambridge, MA). Each probe has 14 thermistors spaced 1 cm apart on an 16-17 gauge needle for the animal experiments and spaced 0.5 cm apart on a 18-19 gauge needle for the human subjects. The thermistor arrays are calibrated in a special stirred water bath against a Hewlett-Packard 280A quartz thermometer (resolution < 0.00010 °C, absolute accuracy 0.040 °C). For each individual thermistor, calibration constants are determined according to the Steinhart-Hart relation [68]. These sensor and needle carriers have been shown to exhibit less than 0.1 °C temperature artifact in the FSUM ultrasound field. The temperature probes are driven by specially designed excitation circuitry and the data are acquired through a National Instruments Data Acquisition board model ATMIO16X inserted in an IBM PC compatible computer with an 80486 processor.

6.1.3 Specific Absorption Rate Measurement

The specific absorption rate (SAR) can be determined at each of the temperature profilometer sensors. The SAR gives the amount of internal heat generation in the tissue due to the conversion of the ultrasound energy to heat energy.

SAR is determined from the derivative of temperature as a function of time at the instant of power-off. From the temperature profilometer data, it is possible to approximate the SAR at each temperature sensor. Consider the bioheat transfer equation at time t_1, which is in steady-state:

$$0 = \nabla^2 T(t = t_1) - \lambda^2 T(t = t_1) + \frac{Q}{k_m} \tag{6.1}$$

After power-off at time t_2, the equation becomes:

$$\frac{1}{\alpha}\frac{\partial T}{\partial t} = \nabla^2 T(t = t_2) - \lambda^2 T(t = t_2) \tag{6.2}$$

If t_1 and t_2 are close in time, then $T(t = t_1) \approx T(t = t_2)$ and $\nabla^2 T(t = t_1) \approx \nabla^2 T(t = t_2)$. Therefore Equations (6.1) and (6.2) can be subtracted to yield:

$$\rho_t c_t \frac{\partial T}{\partial t} = Q \tag{6.3}$$

where ρ_t is the tissue density (1.0 g/cm^3), c_t is the tissue specific heat (4.2 J/g-°C), and Q is the internal heat generation (SAR).

The quantity $\partial T/\partial t$ is approximated at t_2 by fitting a line to a data window which begins at time t_2 and extends to some time t_3. The time t_3 must be appropriately chosen to gather enough data for a statistically sound line fit, yet the window must be short enough in time to allow the slope to accurately approximate the first derivative at time t_2.

Figure 6-1 is a schematic diagram of the temperature from a temperature sensor in a time window containing a power-off event. In order to determine the SAR, first the temperature artifact is identified. The artifact is a result of the absorption of ultrasound energy directly by the sensors and the needle carrier. Since the thermal time constant of the sensors and the needle (about 1 second) is much smaller than the tissue thermal time constant, the artifact diminishes in the first few seconds. The partial derivative of temperature as a function of time is determined by performing a line fit to the 7 seconds of data after the artifact

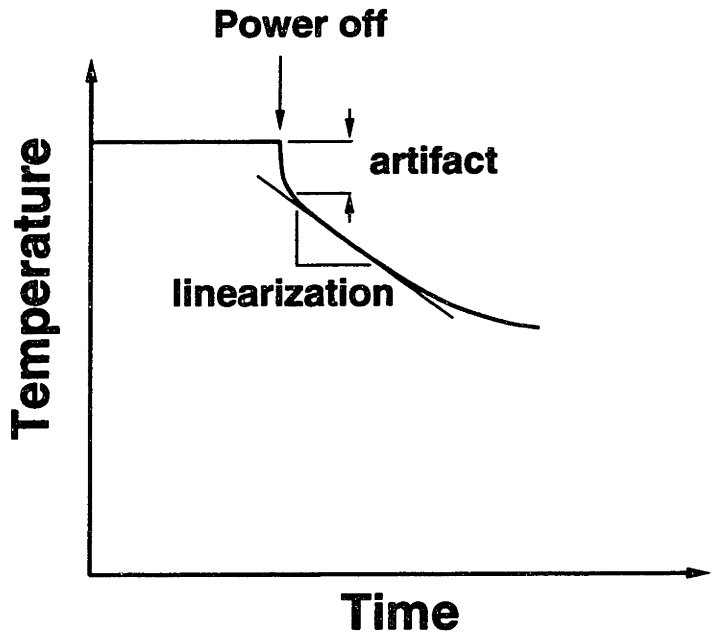

Figure 6-1: Schematic diagram of temperature versus time for a sensor during a power-off event.

has diminished. The entire procedure of finding the artifact and performing the line fit is performed semi-automatically using a custom made software package.

From the previous analysis, the SAR at each sensor location is obtained. For the BEM, however, SAR at each point in the tissue is required. Thus the sparse and discrete SAR data must be used to determine a best estimate of the SAR in the regions of tissue where there are no temperature sensors. This estimate is accomplished with the use of a Laplacian "Smoothing" algorithm [69]. The Smoothing algorithm takes as input the sensor coordinates in 3-D space and the field values at those locations, and gives as output estimated field values for a 3-D field about the sensor points. The algorithm starts by defining a regularly spaced field grid in a rectangular box around the sensor locations. The field values of grid points closest to a sensor are fixed at that sensor's field value. The other grid values are adjusted to minimize the sum of the squares of the second derivatives at the grid points. Figure 6-2 shows the reconstructed and normalized SAR field in a plane passing through the applicator center and into the tissue at $Y = 0$ cm where the applicator-skin contact is at $Z = 0$ cm. The SAR distribution correlates qualitatively with characteristics

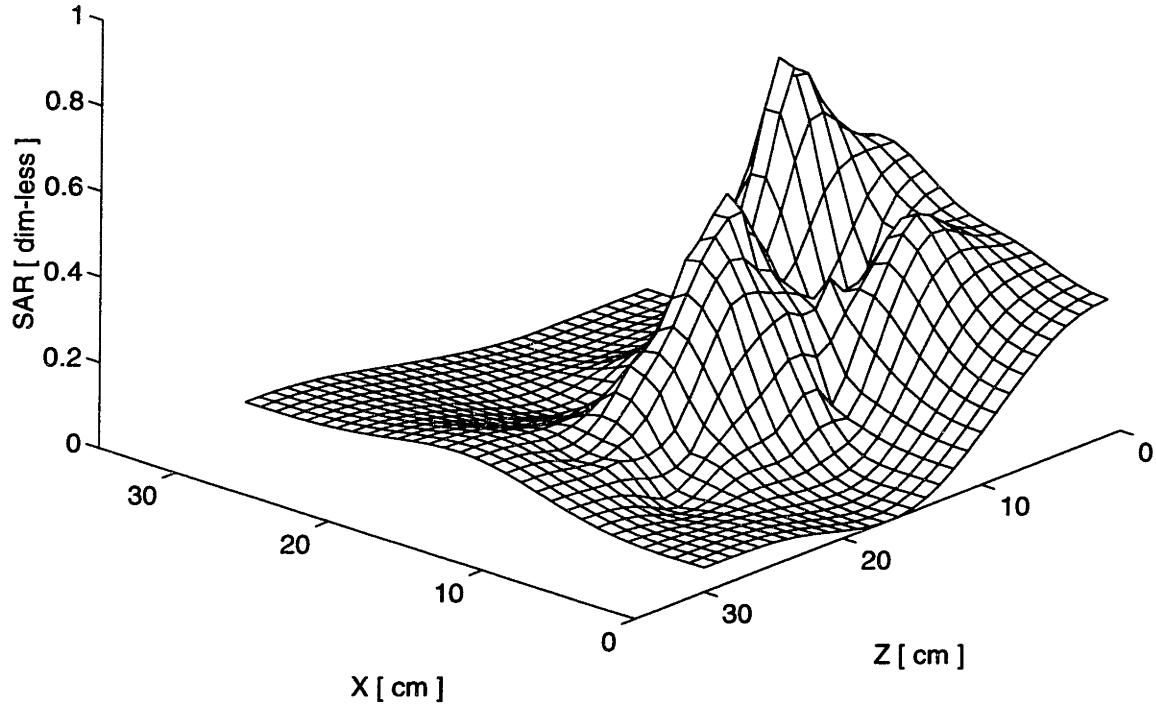

Figure 6-2: A plane of the smoothed SAR from the pig experiment.

of a weakly focused applicator with a second power deposition peak at about $Z = 15$ cm.

6.1.4 Blood Perfusion Measurements

Blood perfusion is measured with the Thermal Diffusion Probe (TDP) (Thermal Technologies, Inc., Cambridge, MA). The TDP probe uses the thermal dilution technique [46], which employs a self-heated thermistor to step the thermistor temperature to a prescribed level using a closed-loop feedback circuit. The power dissipated in the thermistor as a function of time, the temperature step and the calibration constants are used to determine the tissue thermal properties and perfusion. The perfusion values are extracted from the raw data using the *CRUN* data analysis software (Thermal Technologies, Inc., Cambridge MA).

The discrete measurements of blood perfusion with the TDP sensors are used to estimate the perfusion throughout the 3-D tissue space for input into the BEM algorithm. Figure

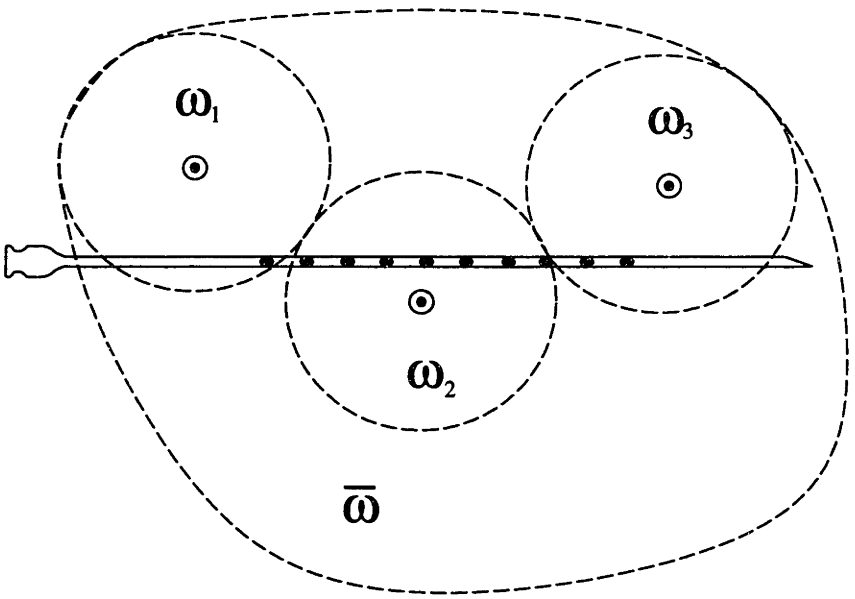

$$\bar{\omega} = \frac{1}{N} \sum_{i=1}^{N} \omega_i$$

Figure 6-3: Diagram of the method to determine the perfusion in 3-D space from the discrete point measurements.

6-3 is a schematic diagram of this estimation. In a spherical tissue region within a given radius of a perfusion sensor, the perfusion at each nodal point is assumed to be equal to the measurement value. However for the nodal points which are not near a perfusion sensor, the perfusion value is assumed to be equal to the average over all perfusion sensors.

6.2 Large Animal Experiment

The purpose of the large animal experiment is to test the ability of the BEM to predict and reconstruct the hyperthermic temperature in a simulated treatment of biological tissue. In these experiments, the target tissue volume is densely instrumented with multisensor temperature profilometer probes and multiple perfusion sensors. This high density of temperature, SAR and perfusion information obtained is necessary to validate the ability of the BEM to predict temperature from the SAR and perfusion inputs. Between September 1991 and December 1993, four porcine experiments were performed in collaboration with the Dana-Farber Cancer Institute. The results from one such experiment are detailed here. In general, experimental procedure involves the heating of a porcine thigh with an ultrasound hyperthermia applicator, measuring temperature and SAR with dense thermometry and measuring perfusion with multiple thermal diffusion probes.

Figure 6-4 is a schematic diagram of the FSUM docked on the experimental pig. During this steady-state heating experiment, 29 of the 56 transducers are excited according to the shaded pattern in the top right corner of Figure 6-4. Each transducer is powered to 33% of its maximum output. The applicator is coupled to the pig rump with diagnostic ultrasound gel and there is no precessional motion of the transducer shell.

Ten of the probes are inserted into the rump, pointing towards the head of the pig. These 10 probes are aligned in the tissue as two parallel planes of 6 and 4 probes using a specially made lucite template, as shown in Figure 6-4. Four probes are inserted perpendicular to these 10 probes. The remaining probe is inserted at an angle of about 45° between the set of 10 probes and the set of 4 probes.

The sensor locations are determined by a radiographic technique. A radio-opaque ring is placed on the rump surface under the center of the FSUM applicator and radio-opaque brachytherapy dummies are placed on the skin surface. Two orthogonal X-ray films are exposed, one with the X-ray source above the pig in the position of the applicator and the film placed under the pig, and the other with the X-ray source pointing towards the pig underside with the film placed in contact with the back of the pig. Computer digitization of the sensors on the X-rays films is then used to determine the three dimensional location

of each sensor in a coordinate system with the center of the ring as the origin.

The flexible TDP catheters are introduced at various depths into the tissue via 16 gauge stainless steel angio-catheters. Six of the 12 are aligned in the heated volume of the tissue through the use of the temperature probe template. The other six probes are inserted without the use of the template in the unheated tissue. Three dimensional and quantitative localization of the sensors is achieved by a combination of inspection of the X-ray films and knowledge of the sensors depth into the tissue from the skin surface.

Perfusion measurements are made prior to the applicator power-on, during thermal steady-state of the hyperthermia session, and several minutes after cool-down when the power-off thermal steady-state is reached.

6.2.1 Experimental Procedure

A summary of the experimental procedure is as follows:

1. Anesthetize the pig with a combination of Telezol and Xylazine. Maintain the pig anesthetized with periodic injections of 100 mg of Telezol throughout the experiment (total duration of 7 hours).

2. Place pig on the treatment table, lying on its left side with the radiographic cassette holder in place. Fix the hind legs in position with rope and a Styrofoam spacer.

3. Clean and shave the right flank.

4. Locate the central part of the right rump by palpation, keeping the femur out of the target volume.

5. Place the lucite probe template firmly against the pig rump and clamp the template to the radiographic cassette holder.

6. Insert 6 of the perfusion probes through the template into the target volume at depths of 4, 7, 10, 13, 16 and 18 cm from the contact point of the applicator and the skin surface.

7. Insert the other 6 perfusion probes outside the heated field at various depths without the aid of the probe template.

8. Insert 10 temperature profilometer probes, using the template, into the target volume.

9. Insert 4 profilometer probes with a ventral entrance point, perpendicular to the previously inserted probes.

10. Insert 1 profilometer probe with a ventral entrance point, at a 45^{o} angle to the template probes, at a depth of 20 cm from the applicator contact point.

11. Mark the skin surface, at the center of the applicator contact point, with longitudinal and transverse lines and a 30 cm radius circle about the center.

12. Place the radio-opaque ring about the center of the contact point and place radio-opaque brachytherapy dummies on the skin surface.

13. To locate the probes, expose 2 X-rays - one from the top of the treatment volume from the vantage point of the applicator and the other from the side of the treatment volume.

14. Apply diagnostic ultrasound gel to the flank surface.

15. Couple the applicator to the horizontal pig surface, centered in the 30 cm circle.

16. Administer sufficient anesthesia to maintain the pig motionless for about 45 minutes (the time to reach thermal steady-state).

17. Take perfusion data from all perfusion sensors.

18. Start recording temperature as a function of time at each sensor in the temperature profilometer probes.

19. Power-on 29 transducers according to the pattern contained in Figure 6-4 to 33 % of full power until thermal steady-state is reached (4300 seconds later).

20. While the applicator power it still on and when thermal steady-state is reached, attempt to make perfusion measurements.

21. Turn transducer power-off.

22. After cool down period (13 minutes) collect perfusion data.

6.2.2 Data Analysis

Perfusion, as input to the BEM, was taken from the data runs which occurred after cool down. Table 6.1 contains the perfusion values used and the locations of the sensors in the tissue. The coordinate system is as shown in Figure 6-4 with the Y axis pointing towards to the pig's head. As with SAR, the perfusion data are measured at discrete and sparse locations in the tissue, yet the BEM requires as input perfusion everywhere in the 3-D tissue field. The BEM allows for perfusion to vary as a function of space, however it is assumed that perfusion variation is piecewise homogeneous. In other words, the BEM considers the tissue as being made up of different regions, each region having its own uniform perfusion and thermal property values. Using the grid generated for the SAR field, the BEM preprocessor assigns each grid point the perfusion value of the perfusion sensor that is closest in space. However, if there are no perfusion sensors within 40 mm of a given grid point, the perfusion value for that point is assumed to be equal to the base-line perfusion (24.25 ml/min-100g). The base-line perfusion is computed by taking the average of all the perfusion measurements.

The steady-state temperature data taken with the Profilometer probe are compared with the output of the BEM algorithm. Since the BEM gives the temperature rise in the tissue above the base-line temperature, it is necessary to extract the temperature rise information from the raw temperature data. The base-line temperature at each sensor is determined from a 100 point average of the data prior to FSUM power-on and the steady-state temperature is determined from the 100 point average of the data previous to power-off. Temperature rise is then given by subtracting the base-line temperature from the steady-state temperature. Temperature artifacts arising from the ultrasound power have been found to be minimal (less than 0.1 ^{o}C) and thus are neglected. Of the 210 temperature sensors on the 15 profilometer probes, only 101 sensors could be localized using the orthogonal X-rays projections for comparison with the BEM.

Table 6.1: Perfusion values for heating run 5 in pig 3

Probe	Perfusion [ml/min-100 g]	X [mm]	Y [mm]	Z [mm]
scwd04	22	24	20	40
scwx09	28	27	31	70
btc136	22	35	31	100
btc130	19	26	26	130
btc134	37	32	43	160
btc135	13	20	43	180
btc147	3	0	36	115
btc146	34	1	28	140
btc126	40	-5	-43	40
btc143	34	-40	45	100
scwx02	17	-40	45	160
scwx04	22	60	-44	180

6.2.3 Comparison of BEM with Experimental Data

The BEM computation was performed on a mesh with 28 x 31 x 30 domain nodes spaced 1 cm apart. The BE size was set at 1 mm and N_p was set at 6. The external boundaries were approximated with insulating boundaries, however due to the thermal damping of perfusion, this consideration was not important.

The average RMS error between the BEM and the data over all 101 sensors is 0.7 °C. Figure 6-5 summarizes the results of the temperature field calculation. The horizontal axis is the difference in °C between measured and computed temperatures at each sensor location and the vertical axis is the percent sensors with errors greater than this value. Note that the BEM computes the temperature to within 0.54 °C or less for 50% of the sensors and the error is less than 1 °C for 82% of the sensors. In order to provide a reference for the BEM computation, the pig experiment was also simulated using NEKTON with a mesh of 220 elements and 5^{th} order polynomials as the trial functions for a total of 27,500 nodes. The NEKTON simulation utilized the same inputs for perfusion, thermal properties, and SAR as the BEM simulation. In order to solve this problem on a *Digital* DECstation 5000/133 with 32 megabytes of RAM, the NEKTON simulation requires 16 minutes of CPU time, while the BEM requires 5 minutes of CPU time.

Figure 6-6 shows the measured temperatures plotted versus the temperatures calculated by NEKTON (top panel) and the BEM (bottom panel). In the case of NEKTON, the RMS error from the measured values is 0.67 °C and for the BEM, the RMS error is 0.70 °C which are nearly identical results. Since both methods are capable of temperature calculations with an error less than 0.1 °C, most of the RMS error is due to the experimental uncertainty. This uncertainty, discussed in more detail below, is primarily due to error in the inputs to the calculations: sensor position and the perfusion and SAR in tissue volumes distant from the sensor locations.

Plots for all Temperature Profilometer probes are not given here, however some representative probes are shown. Figure 6-7 shows the measured and computed temperatures for Probe S-1. From the third panel, it is evident that the tissue around this probe has a perfusion sensor nearby, thus contributing to the low RMS error (0.78 °C). Figure 6-8 shows the measured and computed temperatures for Probe C-1. There is only one perfusion sensor

near this probe and the RMS error is 1.2 °C. Figure 6-9 shows the measured and computed temperatures for Probe C-2 which has one perfusion sensor nearby and an RMS error is 0.61 °C.

As shown in Section 5.2, the BEM is capable of achieving a temperature accuracy of less than 0.1 °C when the model inputs: thermal properties, perfusion, SAR, and the tissue geometry; are exactly known. Thus most of the error in the experimental comparison is due to errors in the model inputs and not due to the BEM solution nor the measured temperature values. A major source of error is the uncertainty in the SAR measurement. In general, parameters, such as SAR, which are determined from the derivative of a measured quantity, temperature, always suffer from increased noise over a directly measured quantity. The thermistors and the needle carriers, depending on their size, directly absorb ultrasound energy thus causing a temperature measurement artifact. For the sake of temperature measurement, this artifact is small (on the order of 0.1 °C). However at power-off, when the SAR is determined, the artifact transient couples into the temperature-time linearization for SAR. Even if SAR could be exactly determined at the sensor locations, it is still completely undetermined at the points in the tissue where there are no sensors. An attempt has been made to address this shortcoming by the use of the Laplacian Smoother, however the Smoother lacks a theoretical justification for its use with ultrasound fields and the errors associated with the Smoother remain to be investigated. An improvement on the Smoother would fit the SAR data to a functional form derived from a solution to the Raleigh diffraction integral.

Another major source of error is the uncertainty in the tissue perfusion. The measurements have a high accuracy (5 ml/min-100g) and resolution (0.2 ml/min-100g), however perfusion appears to vary continuously in time and in space. The human measurements reported in Section 2.2.1 and in the literature, (Bowman *et al*), [47], [70]), demonstrate that perfusion will vary up to about 30% due to patient position, administered drugs, and hyperthermia. In this animal experiment, it was not possible to measure perfusion during hyperthermia, thus the values are taken from the series of measurements 13 minutes after power-off. Thus, due to temporal changes in the flow state of the tissue, there is an unavoidable deviation between the measured tissue perfusion and the perfusion at the time of

steady-state temperature measurement. Further, perfusion was measured at discrete points in the tissue and among these, it was found to vary greatly as a function of space (mean flow rate equal to 24.24 ml/min-100g with a standard deviation of 10.8 ml/min-100g at 3 minutes after power-off). Uncertainty is introduced into the computation through estimating perfusion level in the tissue regions distant from sensor locations. A constitutive model for this estimation was described above, however, this lacks a complete justification that can be correlated with the tissue anatomy. An obvious improvement on the perfusion measurement would be to measure perfusion at each temperature sensor location to better correlate the spatial registration of temperature and perfusion.

Despite the many sources of uncertainty associated with the porcine experiment, the RMS temperature differences between the measured and the calculated values were remarkably low. As evidenced by the closeness in the temperature calculations given by both NEKTON and the BEM, the error is independent of the solution method used - provided the solution method is capable of solving the bioheat equation to about 0.25 °C. Errors not associated with the inputs to the model (geometry, SAR, perfusion and thermal properties) nor the transformation of the discrete measurement of inputs to continuous space, are most likely due to the limitations of the bioheat transfer equation in describing the tissue heat transfer.

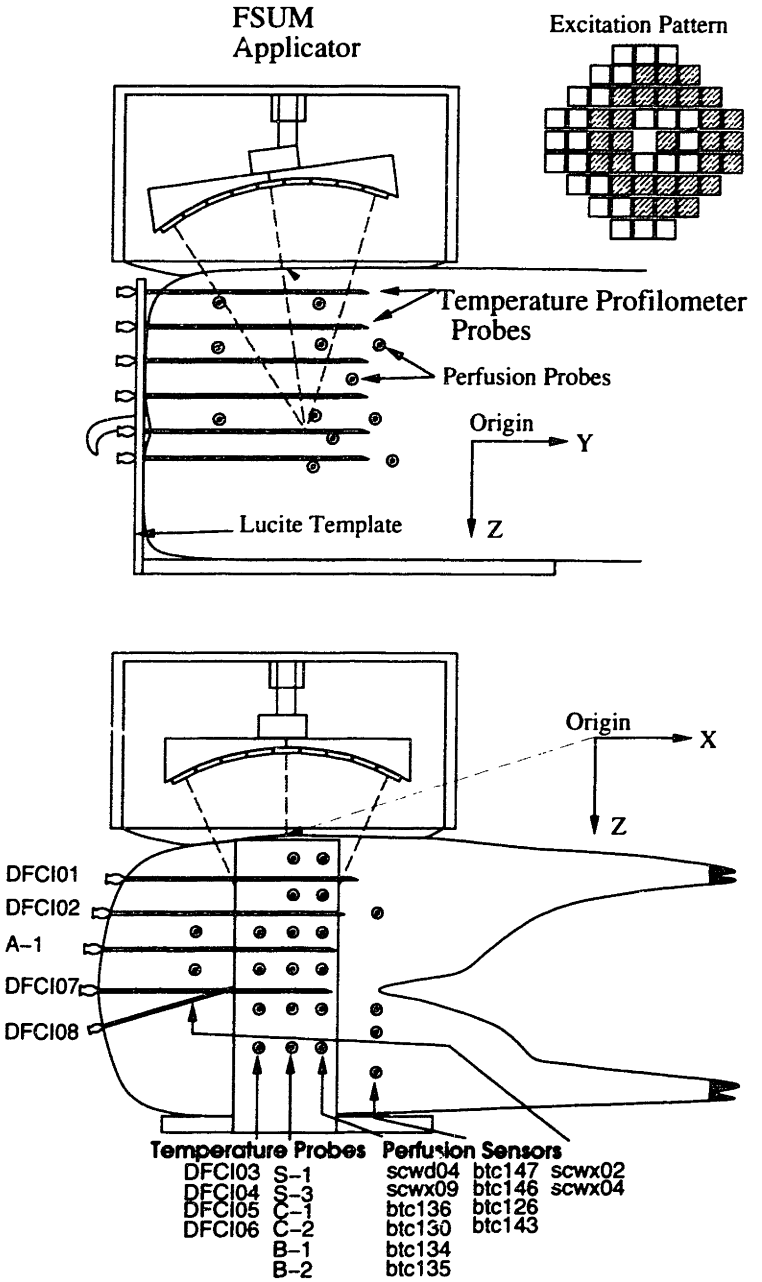

Figure 6-4: Schematic diagram of the experimental set-up with the FSUM docked on the pig. The top drawing is a side view of the pig and the bottom drawing is from the rear.

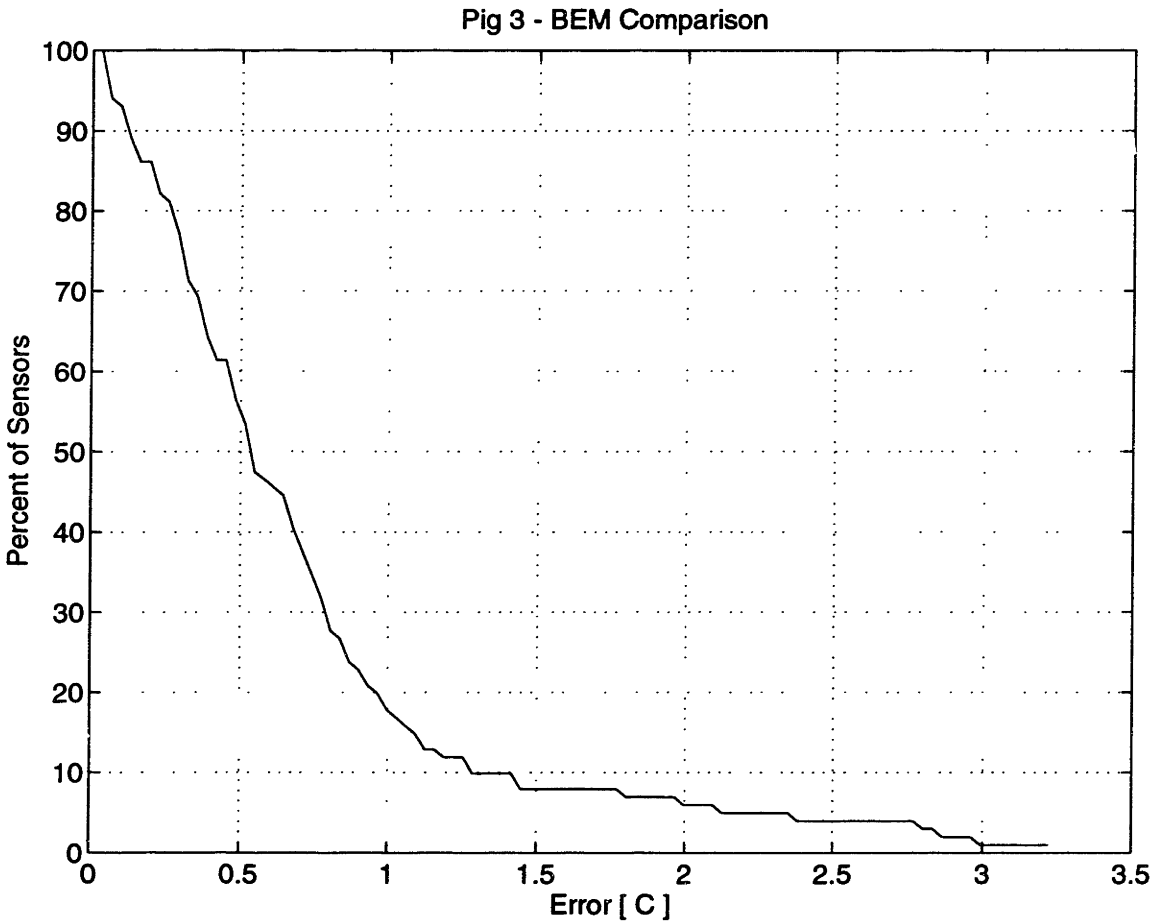

Figure 6-5: Performance of temperature calculation in the pig experiment as characterized by the percent of sensors with errors greater than a given value. The solid line is from the BEM and the dashed line is from the FEM.

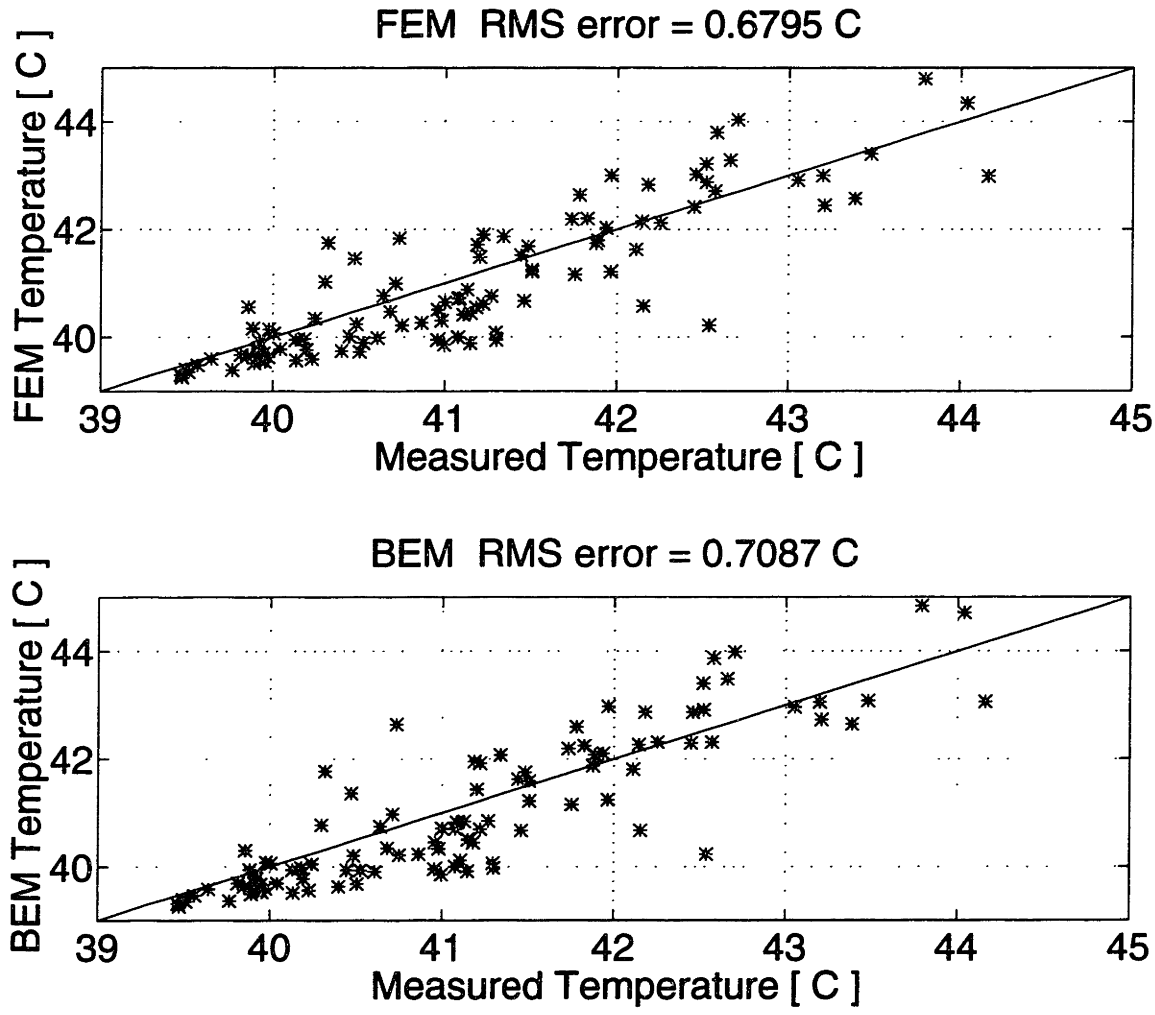

Figure 6-6: Calculated temperature versus measured temperature as computed by the finite element method (top panel) and the Basis Element Method.

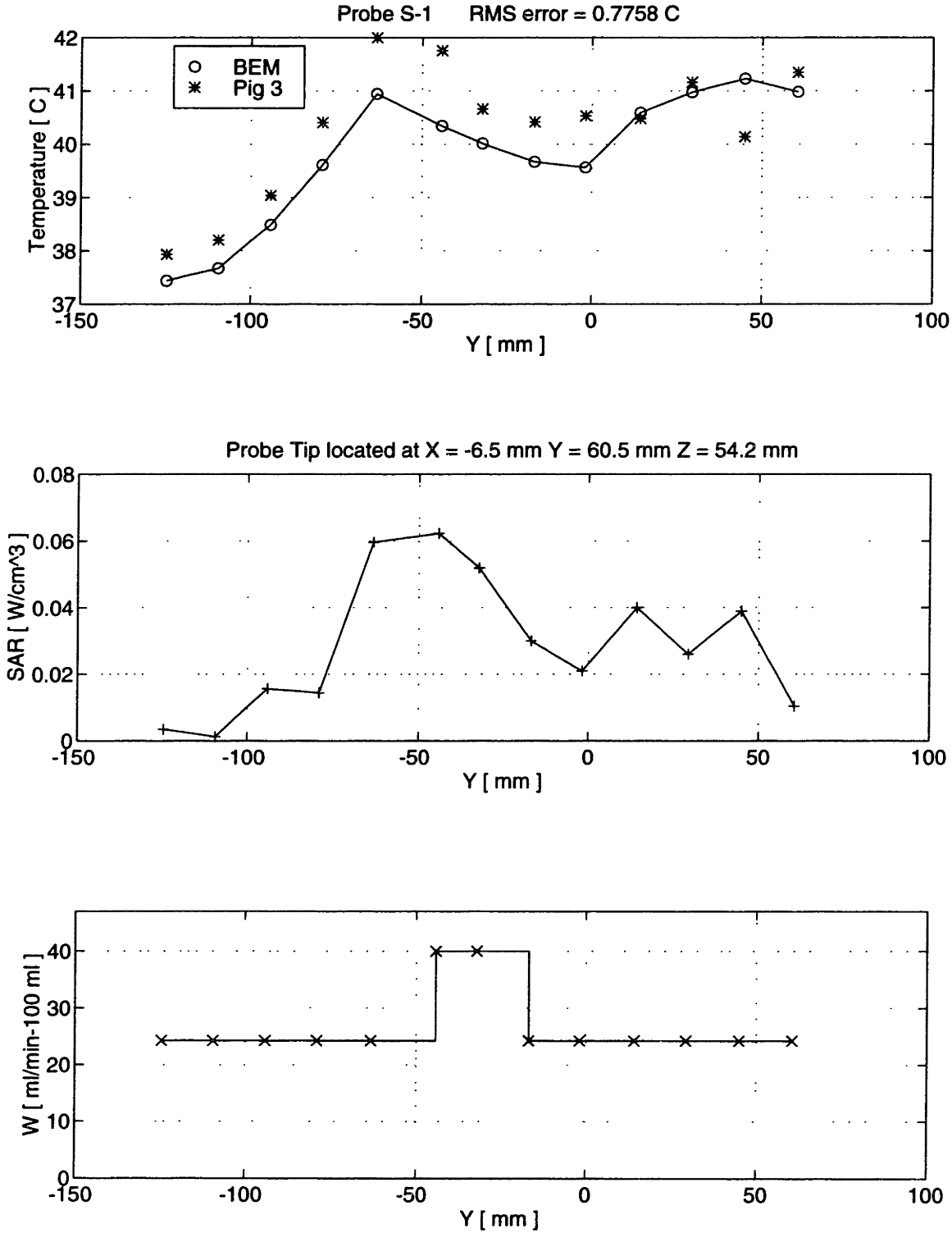

Figure 6-7: Measured and computed temperatures for Probe S-1.

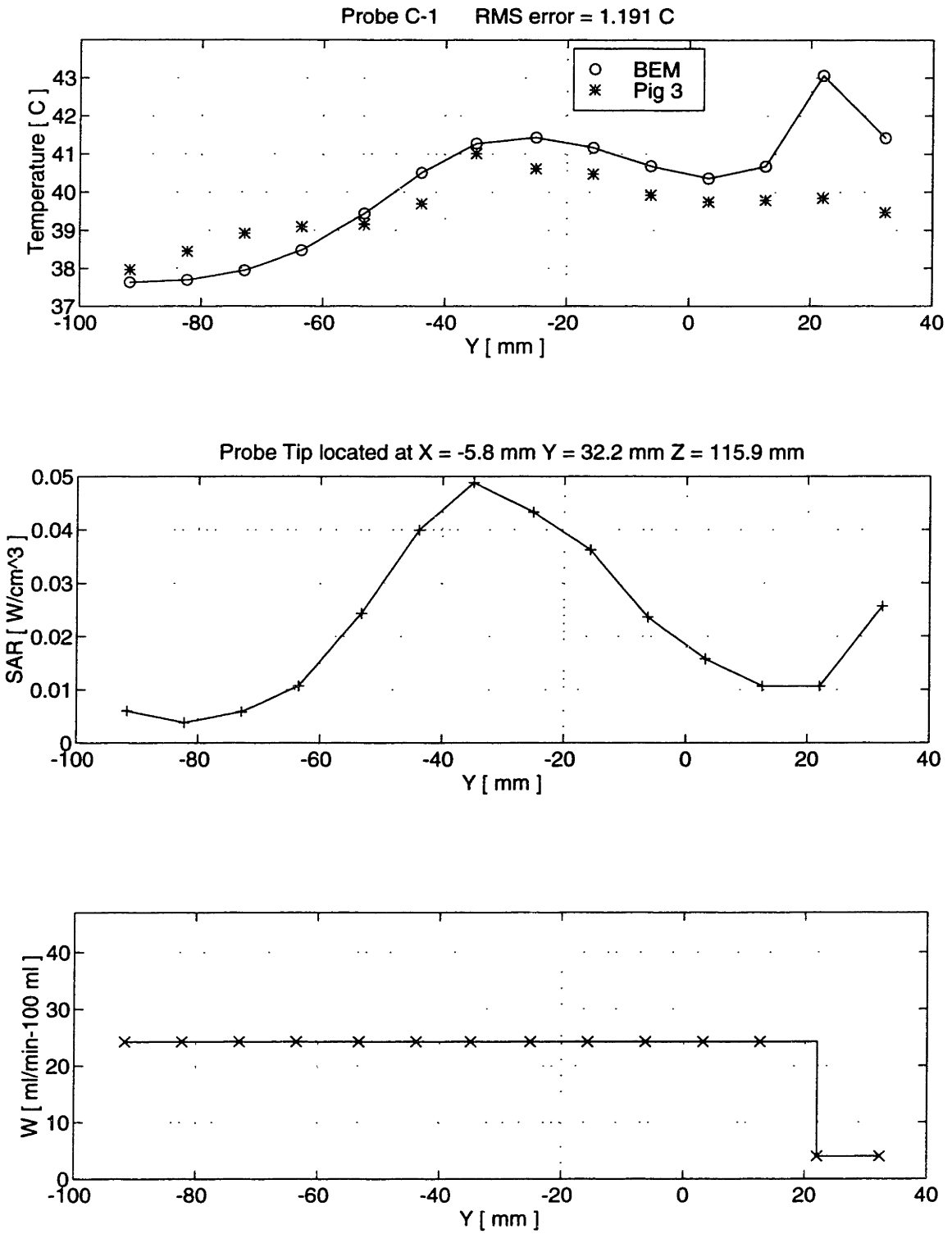

Figure 6-8: Measured and computed temperatures for Probe C-1.

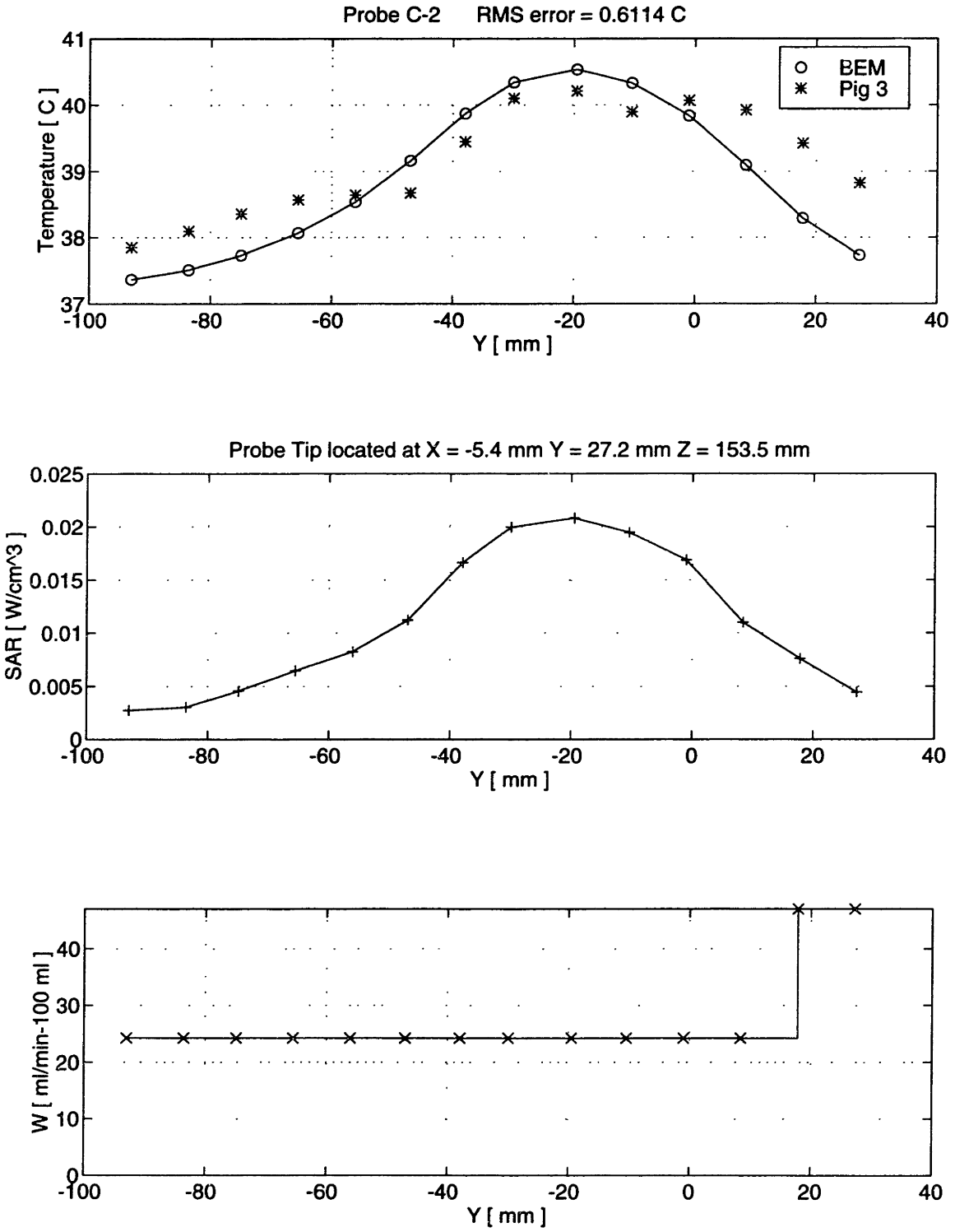

Figure 6-9: Measured and computed temperatures for Probe C-2.

6.3 Human Subjects Experiment

To demonstrate the usefulness of the BEM in the course of a routine clinical treatment, two patient post-treatment temperature reconstructions are undertaken. These studies were carried out in collaboration with the Dana-Farber Cancer Institute (DFCI), Boston, MA, where ultrasound hyperthermia therapy is being used in conjunction with radiation to treat large, deep-seated tumors. At the DFCI, the FSUM heating applicator is currently undergoing Phase I toxicity evaluation trials.

In this case, a human subject receives hyperthermia therapy administered using the FSUM applicator. The patients were instrumented with multiple temperature profilometer probes, each probe having 14 thermistor sensors and when possible TDP perfusion sensors were inserted into the tumor. From these sensors SAR, perfusion, and temperature are measured for input into and comparison with the BEM.

6.3.1 Experimental Protocol

Hyperthermia was administered with the FSUM applicator. The transducer excitation pattern and the power level was adjusted during the treatment in order to achieve a uniform temperature profile at the measured temperature points within the tumor. The applicator spherical shell was precessed with a frequency of 0.3 Hz and the applicator cooling fluid was set at 25 ^{o}C. The experimental patient treatment utilized the Temperature Profilometer system, described above in Section 6.1.2.

The protocol for the patient treatments is summarized below:

1. Insert Profilometer probes under ultrasound guidance.
2. Perform CT scans to verify probe locations.
3. Insert perfusion probes.
4. Start collecting perfusion data.
5. Position the FSUM applicator according to the treatment plan.
6. Record temperature every second at all temperature sensors.

7. Turn FSUM ultrasound power-on.

8. Heat for 60 minutes.

9. Adjust the power deposition pattern to achieve a uniform therapeutic temperature in the tumor volume.

10. Power-off applicator.

11. Continue to record temperature data for 300 seconds.

12. Continue collecting perfusion data.

6.3.2 Patient 1

Patient 1 was a 51 year old male with a 10x10x12 cm squamous cell carcinoma in the left axilla. Prior to treatment, informed consent was obtained and a full set of CT scans were made. The CT scans were contoured for use in a computer-aided planning program (HYPER/Plan, [42]) to identify the treatment portal and the patient and applicator position. The patient received hyperthermia treatment with the FSUM three times in January to February 1994, along with radiation therapy.

Three Profilometer probes with 14 sensors each were inserted into the tumor, under ultrasound imaging guidance, according to RTOG guidelines, [71]. Two co-planar probes were inserted perpendicularly through the center of the tumor and the third was inserted at the base of the tumor. The patient was CT-scanned to verify the probe locations.

Data Analysis

SAR in the patient treatment is determined using the same method as in the pig experiment (see Section 6.1.3). The derivative of temperature in time is measured at the instant of power-off and Equation 6.3 is used to determine SAR at each sensor location. To infer the SAR at other locations in the tissue where there was no sensor, the Smoothing algorithm was employed.

During this treatment, it was decided not to insert invasive perfusion probes into the tumor due to concerns for patient safety and comfort. However to compute the temperature field, the BEM requires perfusion values at each point in the tissue field. In order to address this situation two methods of perfusion estimation were explored. The first method assumes that perfusion is uniform throughout the tissue and the level of perfusion is adjusted to minimize the root-mean-square (RMS) of the difference between the BEM and the measured values at the sensor locations. The second method attempts to determine the perfusion at sensors located in tissue regions where the thermal gradient is small. For small thermal gradients heat flow due to conduction is negligible, thus the Laplacian term ($\nabla^2 T$) is neglected. The steady bioheat transfer equation (Equation (1.1)) then becomes:

$$0 = -\omega c_b \rho_b T + Q \tag{6.4}$$

where c_b is the specific heat of blood (4.2 J/g-°C) and ρ_b is the density of blood (1.0 g/cm^3). Since the temperature rise and SAR are known at each sensor, the perfusion can be solved for explicitly. This method of perfusion inference was performed at sensor locations where the difference with its two neighbors was less than 0.9 °C (thus the gradient was less than 0.9 °C/cm). Note that if the maximum thermal gradient for perfusion measurement is included in the scaling Equation (6.4), a perfusion error can be solved for and shown to be about 7 ml/min-100g. Thus the perfusion error, by this estimate, is on the order of 30%. Table 6.2 contains the locations and values of the estimated perfusion.

The temperature is recorded every second at 42 discrete locations with 3 temperature Profilometer probes. Steady-state temperature is determined, at each sensor, from the average of the 100 seconds of data prior to power-off. The tissue temperature rise above the base-line is determined by subtracting the base-line sensor temperature from the steady-state sensor temperature. The base-line temperature is computed from the average of the 100 seconds of data prior to power-on. Temperature artifact due to the ultrasound deposition was found to be small (less than 0.1 °C) and was neglected. Tables 6.3, 6.4 and 6.5 contain the base-line, steady-state and temperature rise for each sensor.

Table 6.2: Inferred perfusion values from temperature probes.

Sensor	Perfusion [ml/min-100 g]	X [mm]	Y [mm]	Z [mm]
DFCI_P04-2	11.8	125	-75	10
DFCI_P04-10	21.5	83	73	26
DFCI_P13-5	8.3	112	-37	23
DFCI_P13-13	7.0	84	-82	21
DFCI_P09-5	16.5	102	-24	50
DFCI_P09-13	19.4	68	-72	40

Table 6.3: Temperatures recorded during patient treatment for probe DFCI_P04.

Sensor	Base-line [°C]	Steady-State[°C]	Increment [°C]
DFCI_P04-1	37.6312	38.93601	1.304807
DFCI_P04-2	37.63836	39.22339	1.585037
DFCI_P04-3	37.60949	39.48991	1.880419
DFCI_P04-4	37.61532	39.89722	2.281906
DFCI_P04-5	37.64717	40.3551	2.707929
DFCI_P04-6	37.61552	40.82327	3.207756
DFCI_P04-7	37.7554	41.16537	3.40997
DFCI_P04-8	37.5805	41.75444	4.173945
DFCI_P04-9	37.60126	42.42062	4.819361
DFCI_P04-10	37.58887	41.5278	3.938925
DFCI_P04-11	37.55059	41.70221	4.151616
DFCI_P04-12	37.57558	42.59109	5.015512
DFCI_P04-13	37.57348	43.19967	5.626188
DFCI_P04-14	37.58539	43.39803	5.81264

Table 6.4: Temperatures recorded during patient treatment for probe DFCI_P13.

Sensor	Base-line [°C]	Steady-State[°C]	Increment [°C]
DFCI_P13-1	37.65426	43.87922	6.224964
DFCI_P13-2	37.65453	45.28024	7.625711
DFCI_P13-3	37.66786	46.1173	8.449437
DFCI_P13-4	37.66051	47.18629	9.525787
DFCI_P13-5	37.63322	46.96028	9.327056
DFCI_P13-6	37.58332	46.46483	8.881512
DFCI_P13-7	37.5077	45.41637	7.908672
DFCI_P13-8	37.37691	43.33022	5.953317
DFCI_P13-9	37.14609	40.52355	3.377461
DFCI_P13-10	37.10239	39.60284	2.500445
DFCI_P13-11	37.12157	39.09601	1.974437
DFCI_P13-12	36.94535	38.67579	1.730435
DFCI_P13-13	36.16709	38.02395	1.856867
DFCI_P13-14	35.57381	37.4108	1.836983

Table 6.5: Temperatures recorded during patient treatment for probe DFCI_P09

Sensor	Base-line [°C]	Steady-State[°C]	Increment [°C]
DFCI_P09-1	37.62152	40.3325	2.710973
DFCI_P09-2	37.6571	41.31324	3.65614
DFCI_P09-3	37.65113	43.04965	5.398514
DFCI_P09-4	37.66404	47.05312	9.38908
DFCI_P09-5	37.65235	46.65448	9.002135
DFCI_P09-6	37.64388	46.25074	8.606866
DFCI_P09-7	37.64542	45.04024	7.394827
DFCI_P09-8	37.63344	43.30201	5.66857
DFCI_P09-9	37.5694	41.52421	3.954815
DFCI_P09-10	37.53903	40.78671	3.247682
DFCI_P09-11	37.50842	40.19489	2.686472
DFCI_P09-12	37.49715	39.89769	2.400537
DFCI_P09-13	37.41359	39.56451	2.150923
DFCI_P09-14	37.30498	39.20423	1.899248

Patient 1 Experimental Results and Discussion

The computational patient mesh was generated from 64 consecutive CT scans spaced 0.5 cm apart. A geometric model of the patient was created by HYPER/Plan and the mesh was automatically generated with nodes equally spaced at 1 cm for a total of 46 x 21 x 28 nodes. Figure 6-10 shows the CT derived patient model in the top panel and the bottom panel contains a slice of the computational mesh. The patient geometry as contained in the mesh is fed to the BEM algorithm for processing. The Basis Element size was set at 1 mm and N_p was set at 6. Figure 6-11 shows measured and computed temperature along each of the three probes where temperature was computed with the BEM. There is excellent qualitative agreement between measured and computed values. Over all the 42 sensors, the RMS temperature difference is 1.2 °C where the perfusion is according to Table 6.2. For comparison, the middle panel displays a temperature calculation where perfusion was assumed to be constant and uniform. The level of perfusion, in this case, was adjusted to minimize the RMS difference over all the sensors. Here, RMS error over probe DFCI_P13 is much greater (3.8 °C) and qualitatively the character the temperature field is clearly different.

Figures 6-12, 6-13, and 6-14 plot the temperature next to the measured SAR and the inferred perfusion. For probe DFCI_P09, the temperature field follows the trend of the SAR data due to the relatively uniform perfusion. With probe DFCI_P13, the temperature does not follow the SAR - which only slightly varies in space - but rather inversely correlates with the inferred perfusion which drops along the needle from X = 100 mm to 130 mm. Temperature data along probe DFCI_P04 show excellent agreement with the BEM and follows the decreasing SAR more closely than the decreasing perfusion.

Figure 6-15 summarizes the results of the temperature field calculation. The horizontal axis is the difference in °C between measured and computed temperatures at each sensor location and the vertical axis is the percent sensors with errors greater than this value. Note that the BEM computes the temperature to within 0.75 °C or less for 50% of the sensors and the error is less than 1 °C for 65% of the sensors. Figure 6-16 plots the computed temperature versus the measured temperature for all 40 sensors. The dashed line is the unity slope and the solid line, with a slope of 0.959, represents least-squares-residual fit to

the data with the y intercept constrained at zero temperature rise.

As mentioned above, the BEM is capable of computing the tissue temperature to within 0.1 °C when the inputs are exactly known. Here with the patient experiment, temperature errors are primarily due to uncertainty in SAR and perfusion. As with the animal experiment, SAR was measured at each of the temperature sensors and the Laplacian Smoother was used to estimate SAR values at all other points in the field. Thus the error in temperature due to SAR uncertainty is of the same order as in the pig experiment. A major source of error is introduced by the lack of direct perfusion measurements. This is a serious limitation in the analysis of the data. The use of the inferred values, which has some validity based in heat transfer scaling relations, suffers from many sources of uncertainty which are concerned with the temperature gradient at the inference sensors. While the thermal gradient is known along the probe and this can be used to estimate the perfusion inference error, less is known about the thermal gradient in the directions perpendicular to the probes. Ultimately, perfusion and temperature measurements collected from the sensors capable of measuring both parameters will eliminate the need for perfusion inference and will allow more accurate treatment reconstructions.

The temperature results from the BEM permit the calculation of volumetric based tumor dose statistics, as opposed to the currently used sensor based statistics. Figure 6-17 shows a histogram of the steady-state treatment temperature which plots the percent number of points in the tumor (y axis) which are above a given temperature (x axis). From the mesh of the patient model, there are 464 points in the tumor volume at which temperature is calculated and the associated histogram is the solid line. For comparison, the sensor based histogram is also plotted as the dashed line. It is interesting to note that two lines are remarkably similar indicating that the probes were well placed in the tumor to capture the temperature distribution with the discrete sensor measurements. Often in hyperthermia evaluation, the quality of a treatment is assessed by the temperature which 90% of the sensors are above. This metric is known as T_{90}. For the BEM, the T_{90} is computed as 39.3 °C for all the domain nodes in the tumor and for the sensors the T_{90} is equal to 38.9 °C. The maximum temperature computed by the BEM is 49.7 °C while the maximum measured temperature is 48.4 °C.

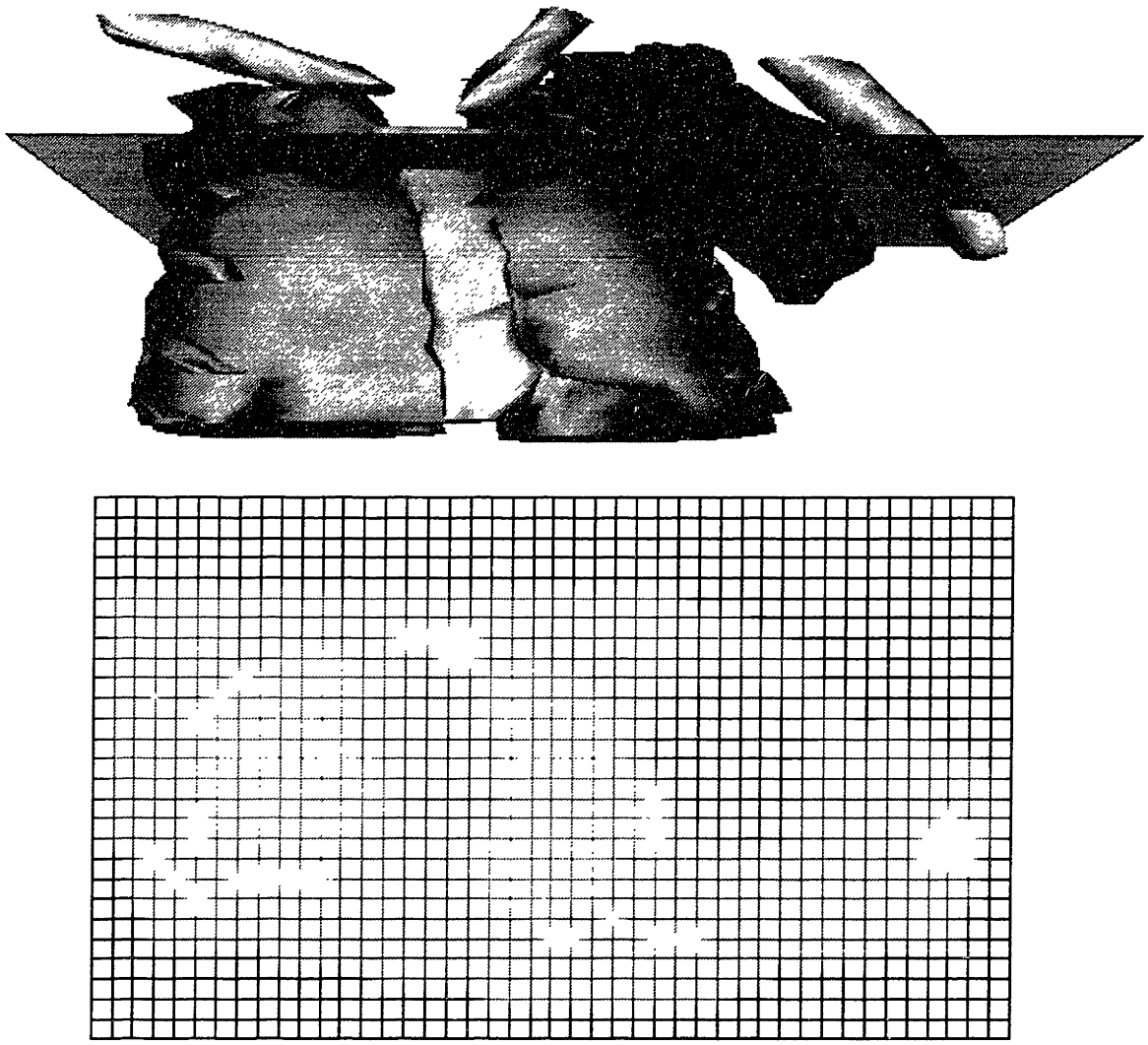

Figure 6-10: Computational grid (bottom) automatically generated from the CT derived patient model (top). The grid defines the problem geometry on which the BEM computes the temperature field. Picture courtesy of D.A. Sidney.

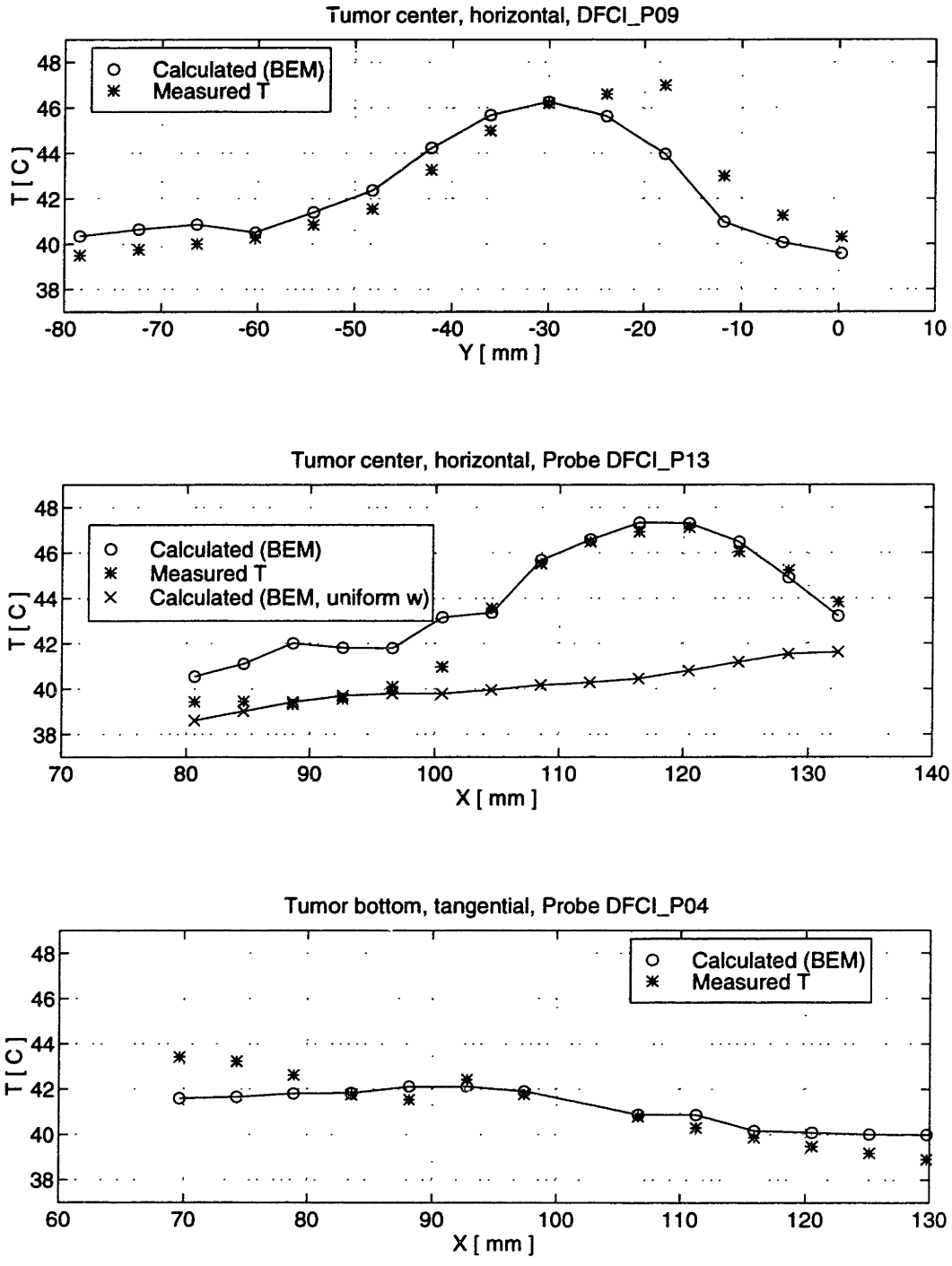

Figure 6-11: Temperature field calculation for the three temperature probes following clinical hyperthermia, using inferred perfusion values.

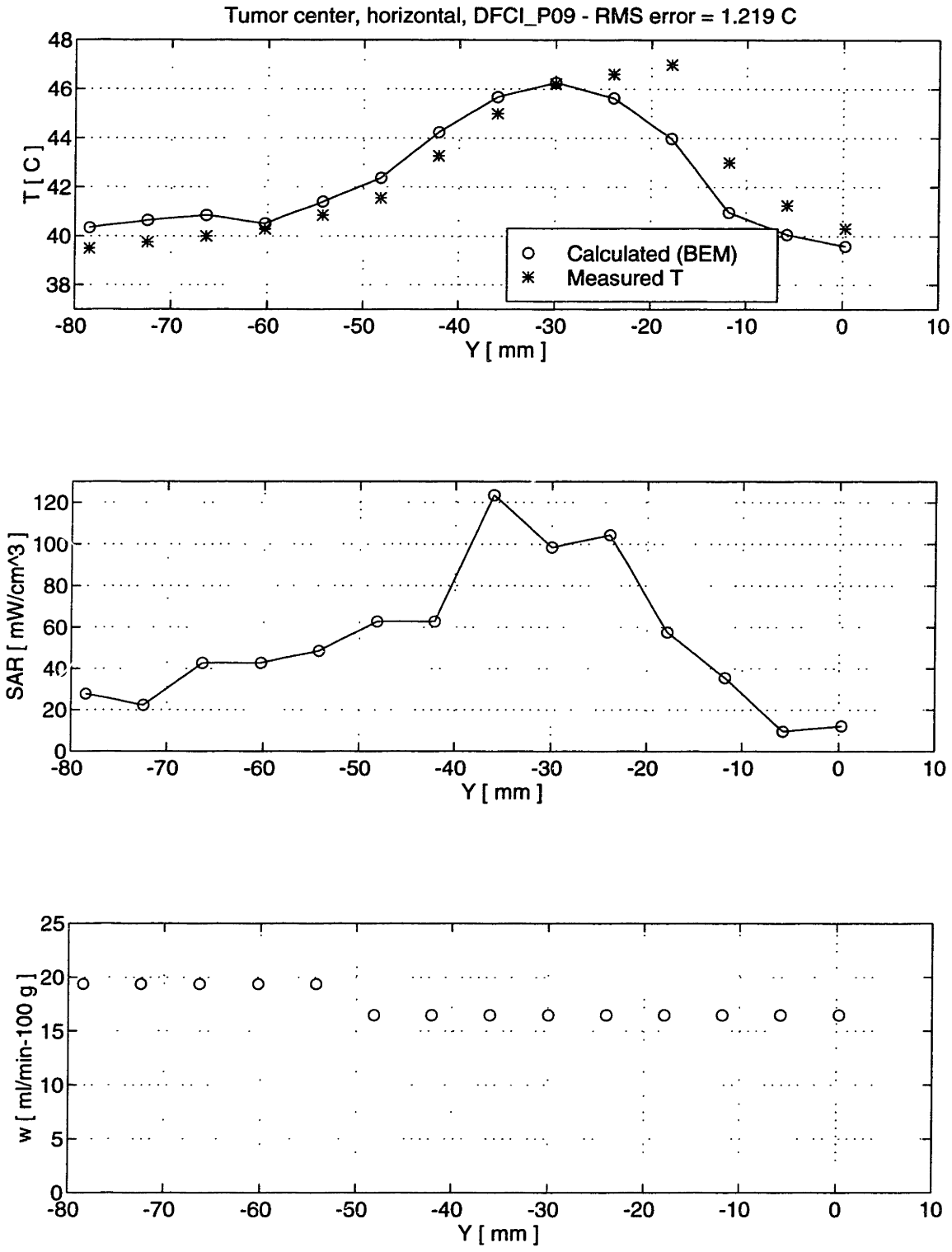

Figure 6-12: Temperature field calculation for probe DFCI_P09 with the measured SAR and the inferred perfusion.

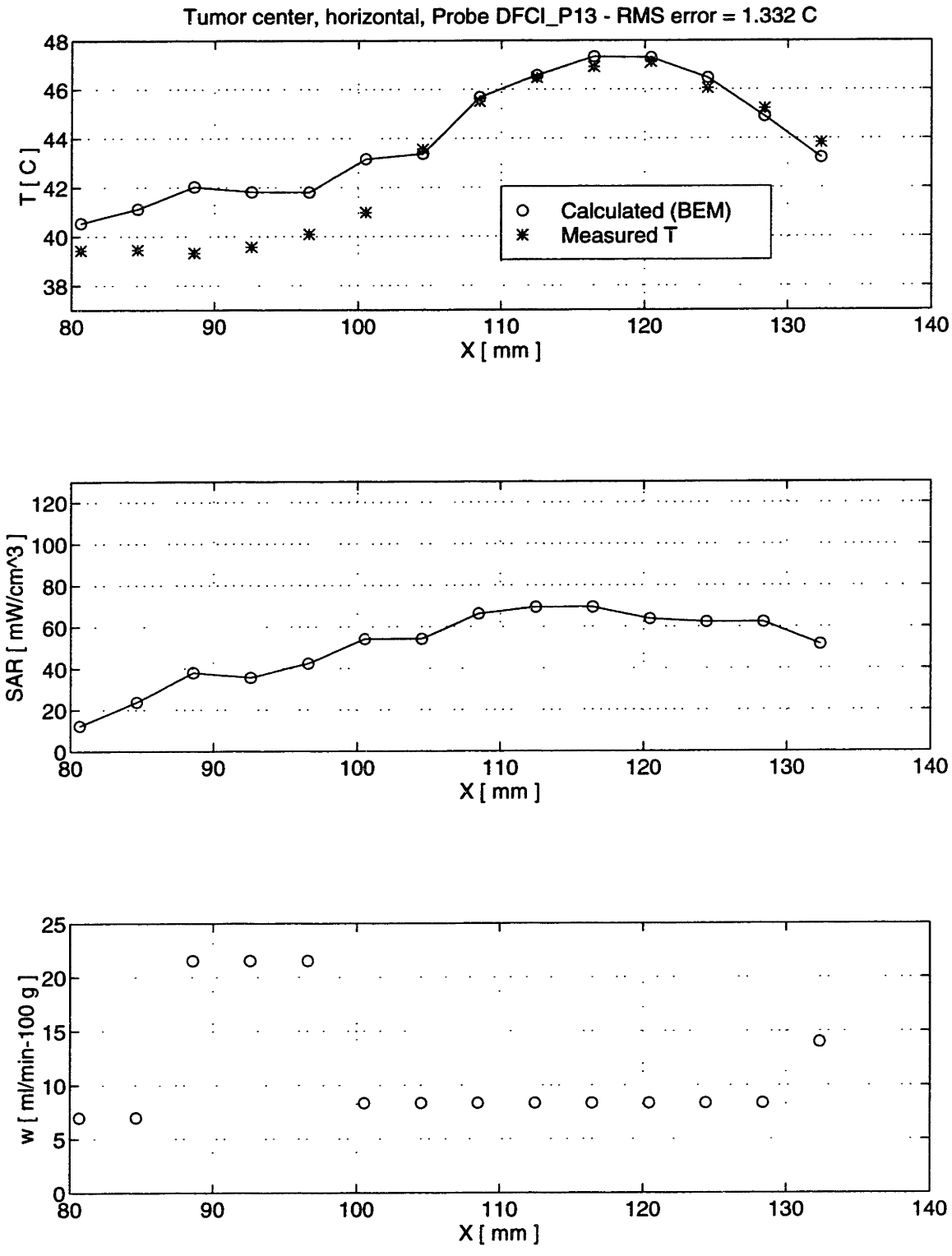

Figure 6-13: Temperature field calculation for probe DFCI_P13 with the measured SAR and the inferred perfusion.

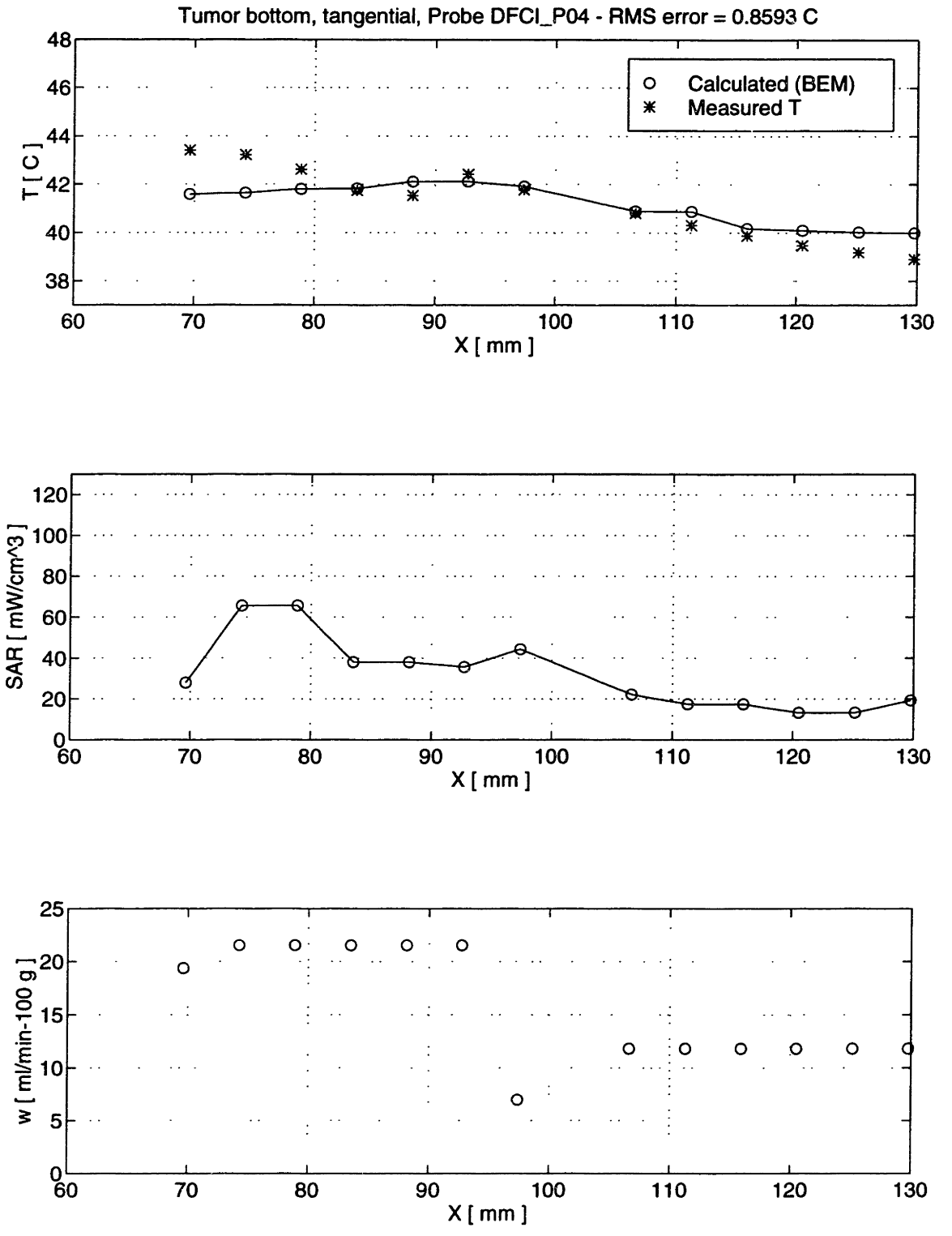

Figure 6-14: Temperature field calculation for probe DFCI_P04 with the measured SAR and the inferred perfusion.

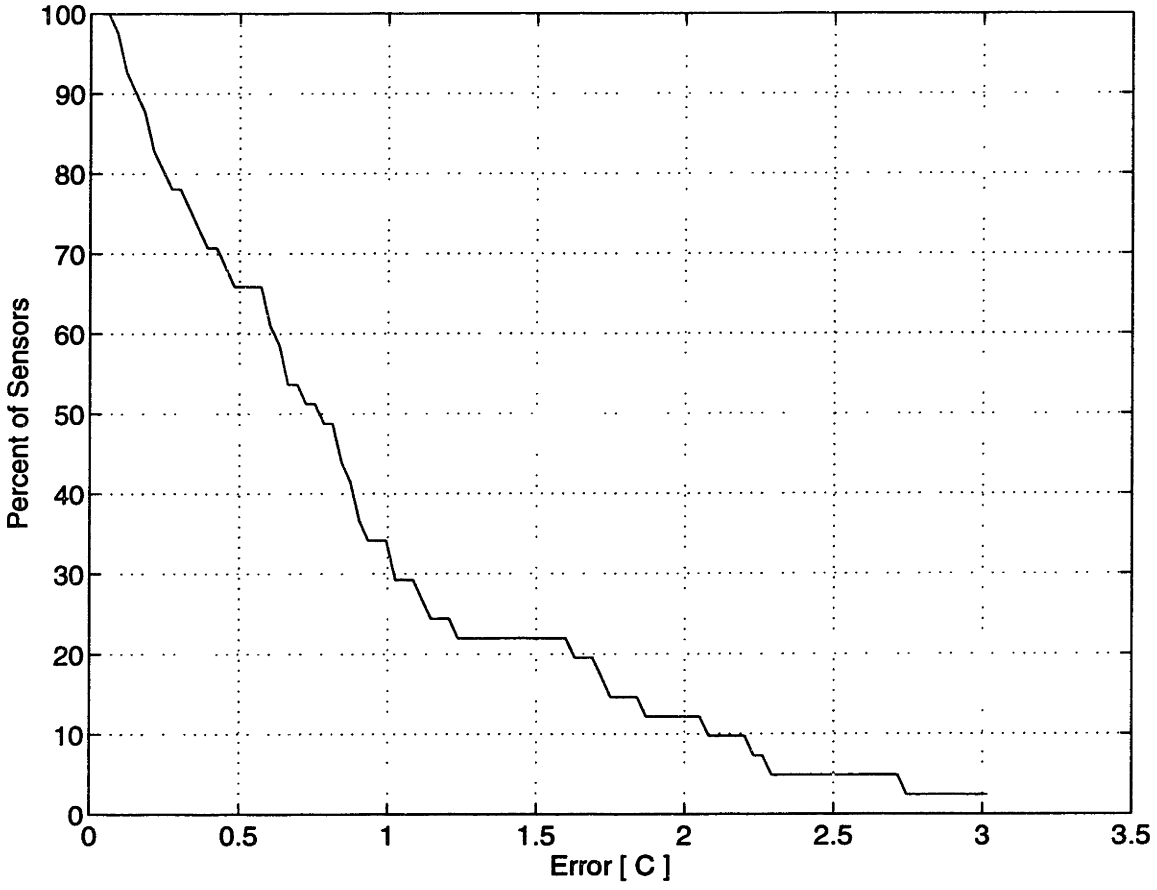

Figure 6-15: Percentage of sensors (y axis) with an error greater than a given value (x axis).

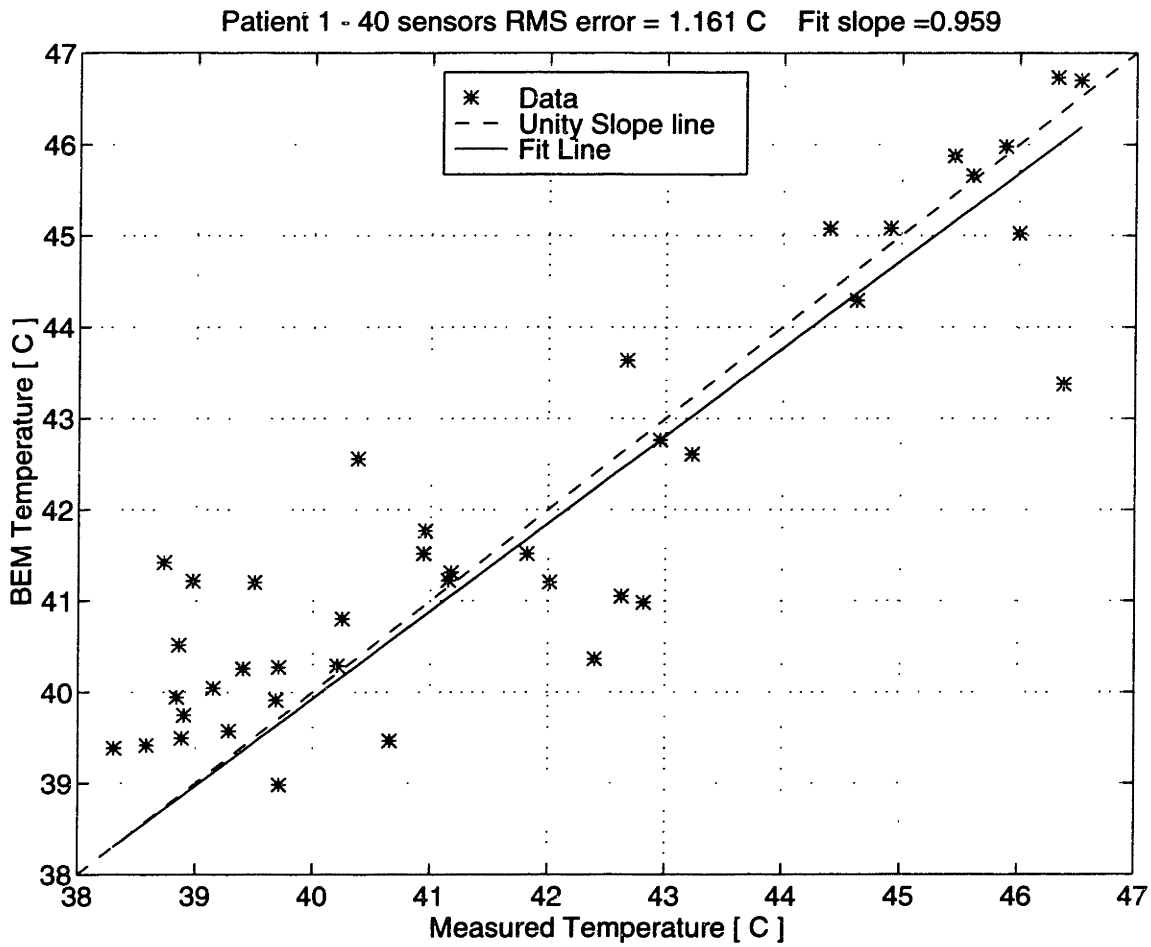

Figure 6-16: Temperature calculated with the BEM versus measured temperature in Patient 1. The dashed line is the unity slope line, while the solid line represents a least-squares-residual fit to the data with the *y* intercept constrained at zero temperature rise.

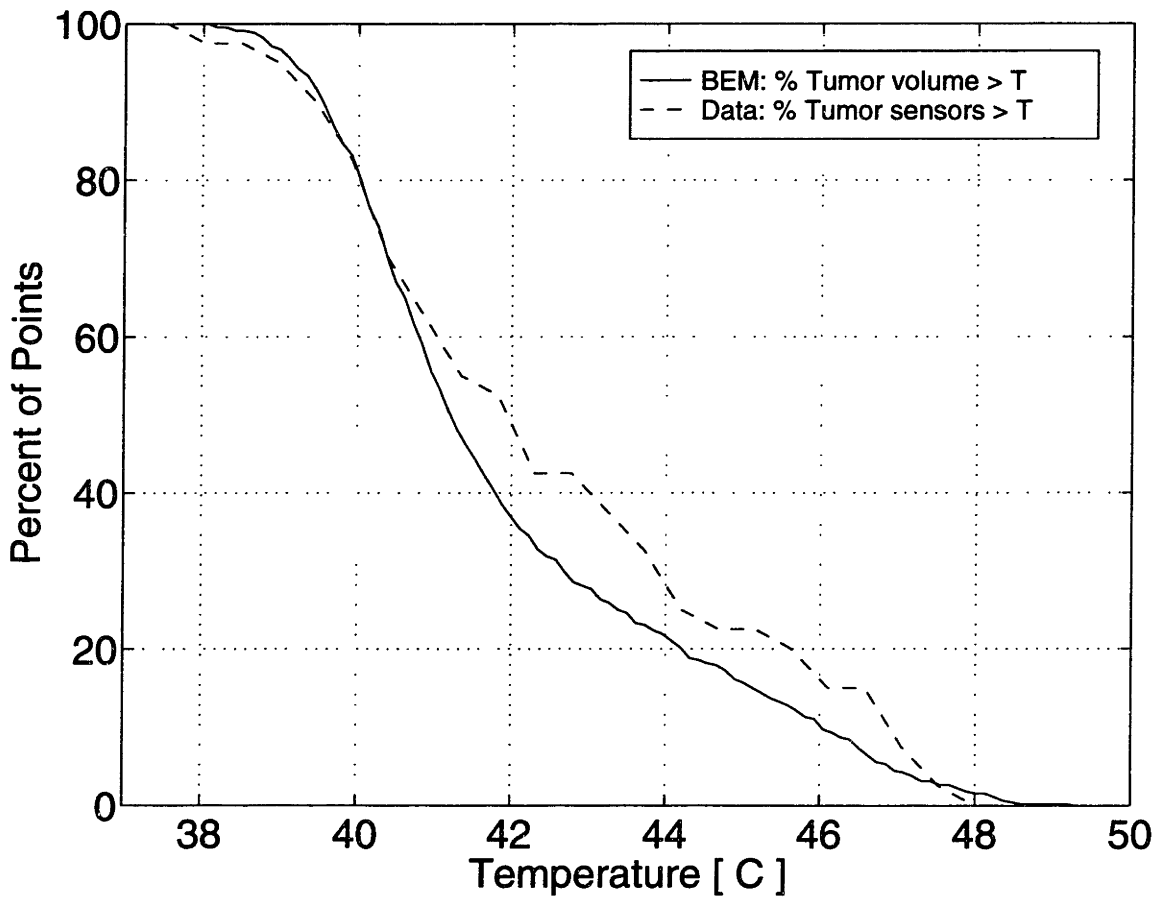

Figure 6-17: Patient 1 temperature histogram as computed by the BEM (solid line) and measured from the sensors (dashed line).

6.3.3 Patient 2

Patient 2 was a 42 old female with 10.2 x 7.0 x 12.2 cm recurrent breast cancer in the left axilla. Prior to treatment informed consent was obtained. A full set of CT scans were made and a surface patient model was created as was done with Patient 1. The patient received 5 hyperthermia treatments in January and February of 1995. The temperature reconstruction presented below is of the treatment on January 19, 1995.

In this treatment, five Profilometer probes with 14 sensors each were inserted into the tumor, under ultrasound imaging guidance. The probes were all inserted in the tumor pointing in the direction of the patient's head with the points converging at the opposite side of the tumor. The patient was CT-scanned to verify the probe locations.

Three flexible TDP catheters were introduced into the tumor via 16 gauge stainless steel angio-catheters. Three dimensional localization of the sensors was achieved by knowledge of the sensors depth into the tissue from the skin surface and of the catheter orientation. Perfusion was monitored before, after and, when possible, during treatment.

Data Analysis

As with Patient 1, SAR was measured at each temperature sensor at the instant of power-off and to infer the SAR at other locations in the tissue where there was no sensor, the Smoothing algorithm was employed.

Perfusion was determined from measurements made with 3 invasive sensors. Table 6.6 shows the perfusion values used in the temperature reconstruction which were taken from the average of the pre-treatment data sets. As with SAR, the perfusion data are measured at discrete and sparse locations in the tissue, yet the BEM requires as input perfusion everywhere in the 3-D tissue field. Using the computational mesh generated from the patient model, the BEM preprocessor assigns each grid point the perfusion value of the perfusion sensor that is closest in space. However, if there are no perfusion sensors within 30 mm of a given grid point, the perfusion value for that point is assumed to be equal to the base-line perfusion (89 ml/min-100g). The base-line perfusion is computed by taking the average of all the perfusion measurements.

Table 6.6: Measured perfusion values for Patient 2.

Sensor	Perfusion [ml/min-100 g]	X [mm]	Y [mm]	Z [mm]
BTC177	46.3	170.0	20.0	-25.0
BTC181	144.0	10.0	10.0	-15.0
BTC191	78.0	140.0	10.0	-20.0

The steady-state temperature at each of the 70 sensors is determined for Patient 2 in the same manner as Patient 1. For the sake of brevity the raw data, in this case, is omitted.

Patient 2 Experimental Results and Discussion

The BEM computational mesh was generated from 24 consecutive CT scans spaced 0.5 cm apart and contoured to form the surface representation of the anatomy. The surface representation was them used to create the volumetric representation of the tissue with nodes uniformly spaced on a 1 cm grid for a total of 46 x 13 x 26 nodes. Figure 6-18 shows the CT derived patient model (top panel) and the corresponding computational mesh that was automatically generated (bottom panel). This patient geometry, along with the perfusion and SAR measurements were fed to the BEM algorithm for processing. The Basis Element size was set at 1 mm and N_p was set at 6. Figures 6-19, 6-20, 6-21, 6-22, and 6-23 show the results of the temperature reconstruction along the probes Prof_006.050, Prof_014.050, Prof_009.075, Prof_003.050, and Prof_004.050 respectively. Each figure displays the computed temperatures plotted along side the measured values (top panels), the measured SAR along the probe (middle panels) and the perfusion values in the vicinity of the probe (bottom panels). The agreement between measured and computed values is good with an RMS temperature error of 0.96 °C over all 70 temperature sensors.

Figure 6-24 summarizes the results of the temperature field calculation. The horizontal axis is the difference in °C between measured and computed temperatures at each sensor location and the vertical axis is the percent sensors with errors greater than this value. Note that the BEM computes the temperature to within 0.7 °C or less for 50% of the sensors

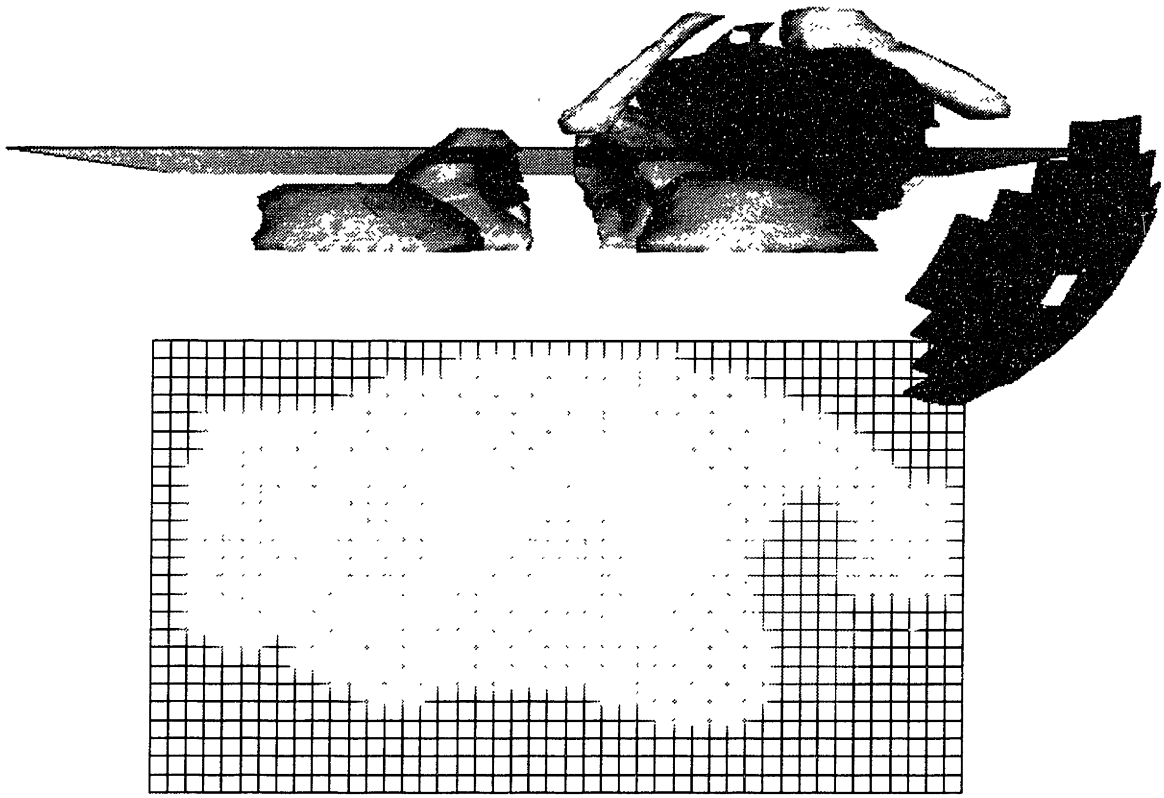

Figure 6-18: Computational grid (bottom) automatically generated from the CT derived patient model (top). The grid defines the problem geometry on which the BEM computes the temperature field. Picture courtesy of D.A. Sidney.

and the error is less than 1 °C for 65% of the sensors. Figure 6-25 plots the computed temperature versus the measured temperature for all 70 sensors. The dashed line is the unity slope and the solid line represents least-squares-residual fit to the data with the y intercept constrained at zero temperature rise.

As with the large animal experiment and the therapy reconstruction of Patient 1, the errors in the Patient 2 temperature reconstruction are primarily due to 1) uncertainty in the SAR and perfusion values at tissue locations distant from the sensors and 2) uncertainty in the sensor locations. In Patient 2, more sensors are available for the measurement of SAR and perfusion, and this is likely to contribute to the lower RMS error in Patient 2 (0.96 °C) than that found in Patient 1 (1.2 °C). Uncertainty in the Profilometer sensor locations can be decreased by increasing the number and density of the CT scans. While uncertainty in the perfusion sensor locations can be greatly decreased by inserting the TDP catheters before

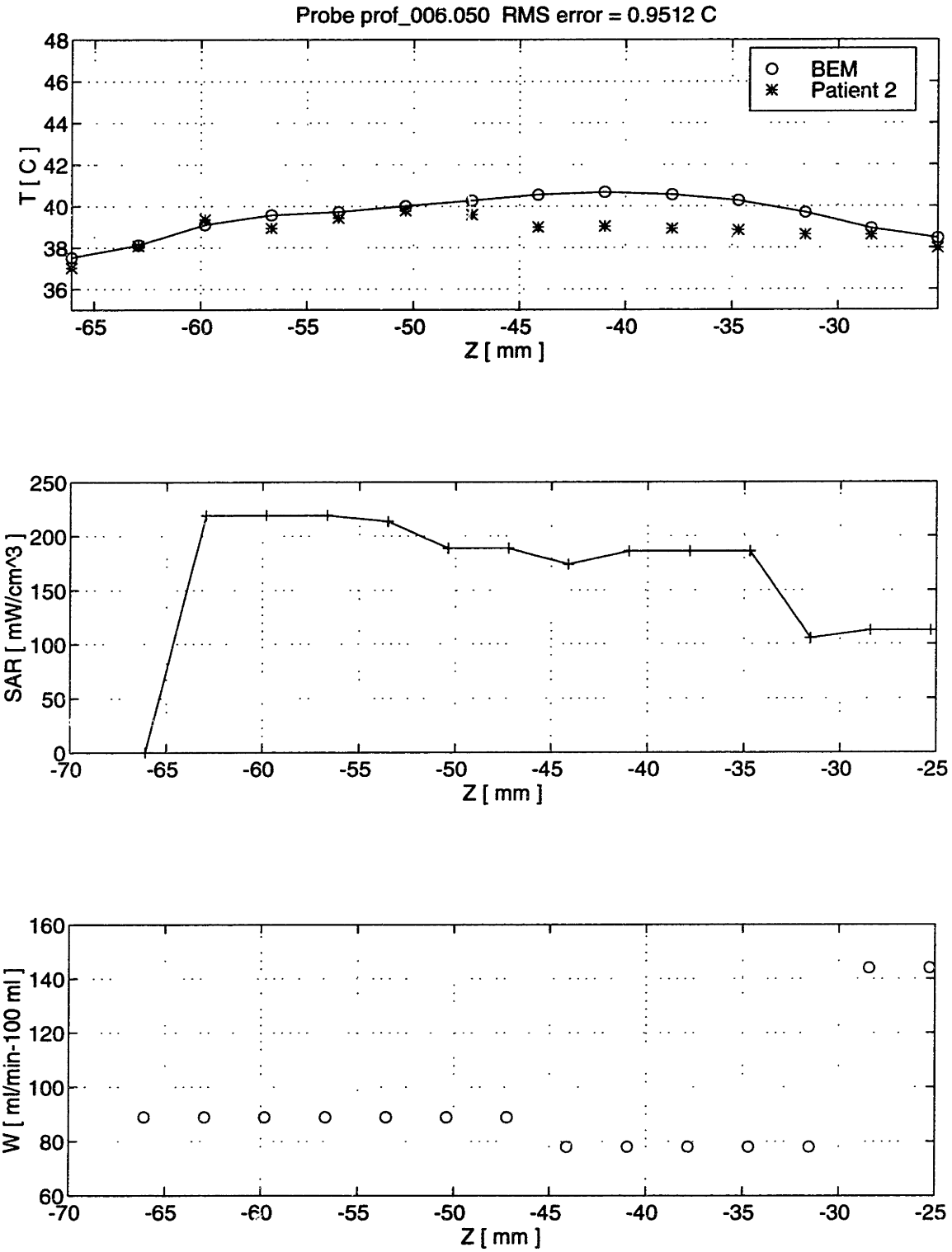

Figure 6-19: Temperature field calculation for probe Prof_006.050 with the measured SAR and perfusion.

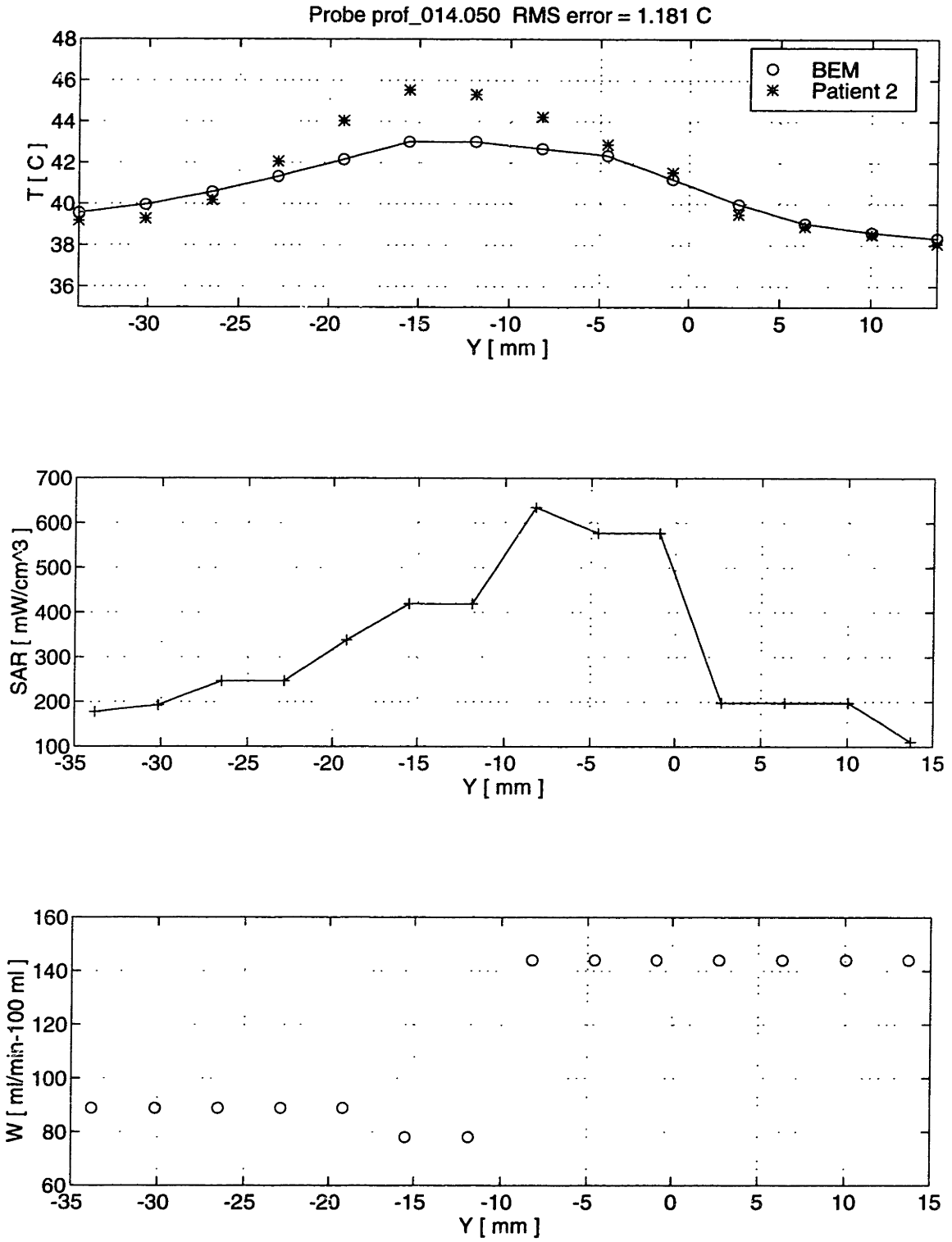

Figure 6-20: Temperature field calculation for probe Prof_014.050 with the measured SAR and perfusion.

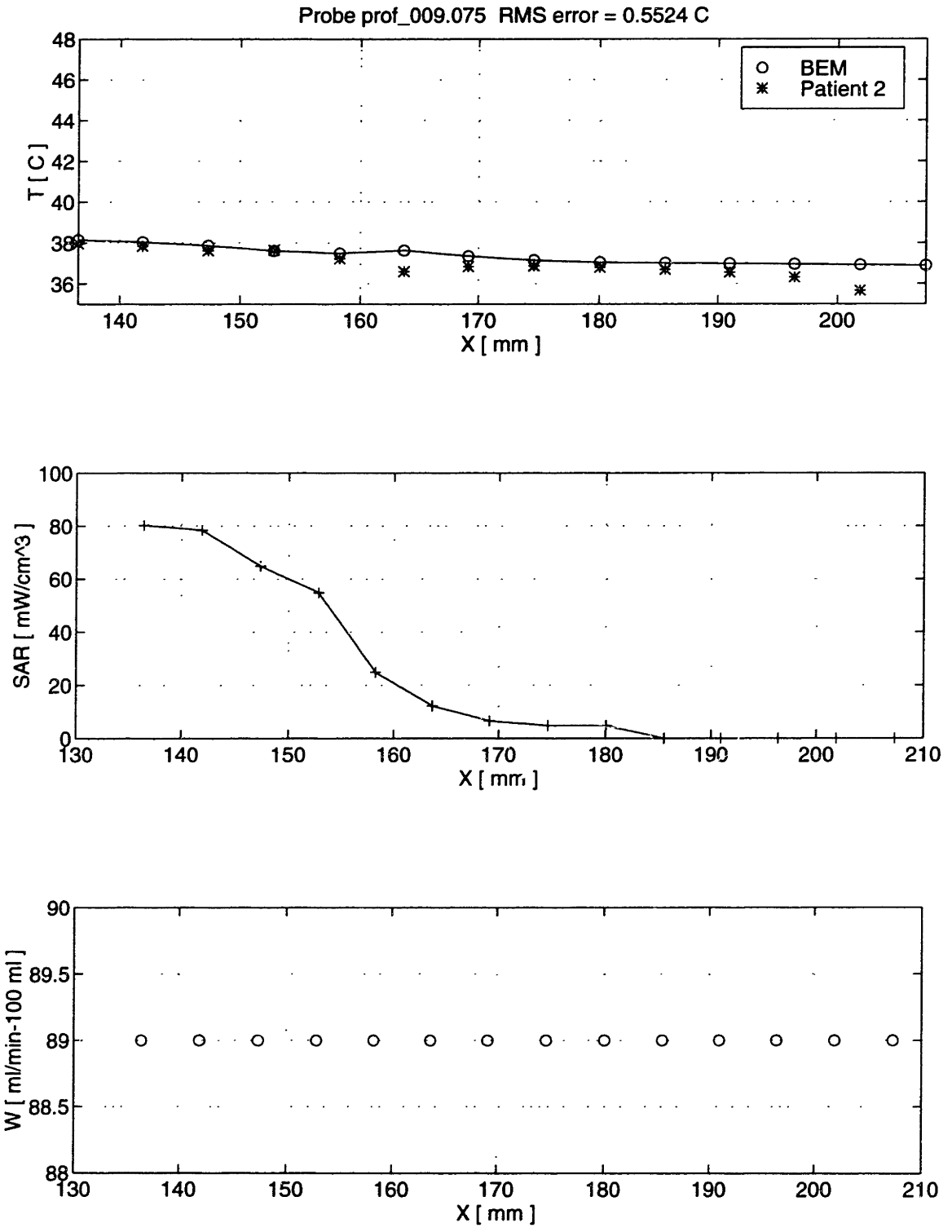

Figure 6-21: Temperature field calculation for probe Prof_009.075 with the measured SAR and perfusion.

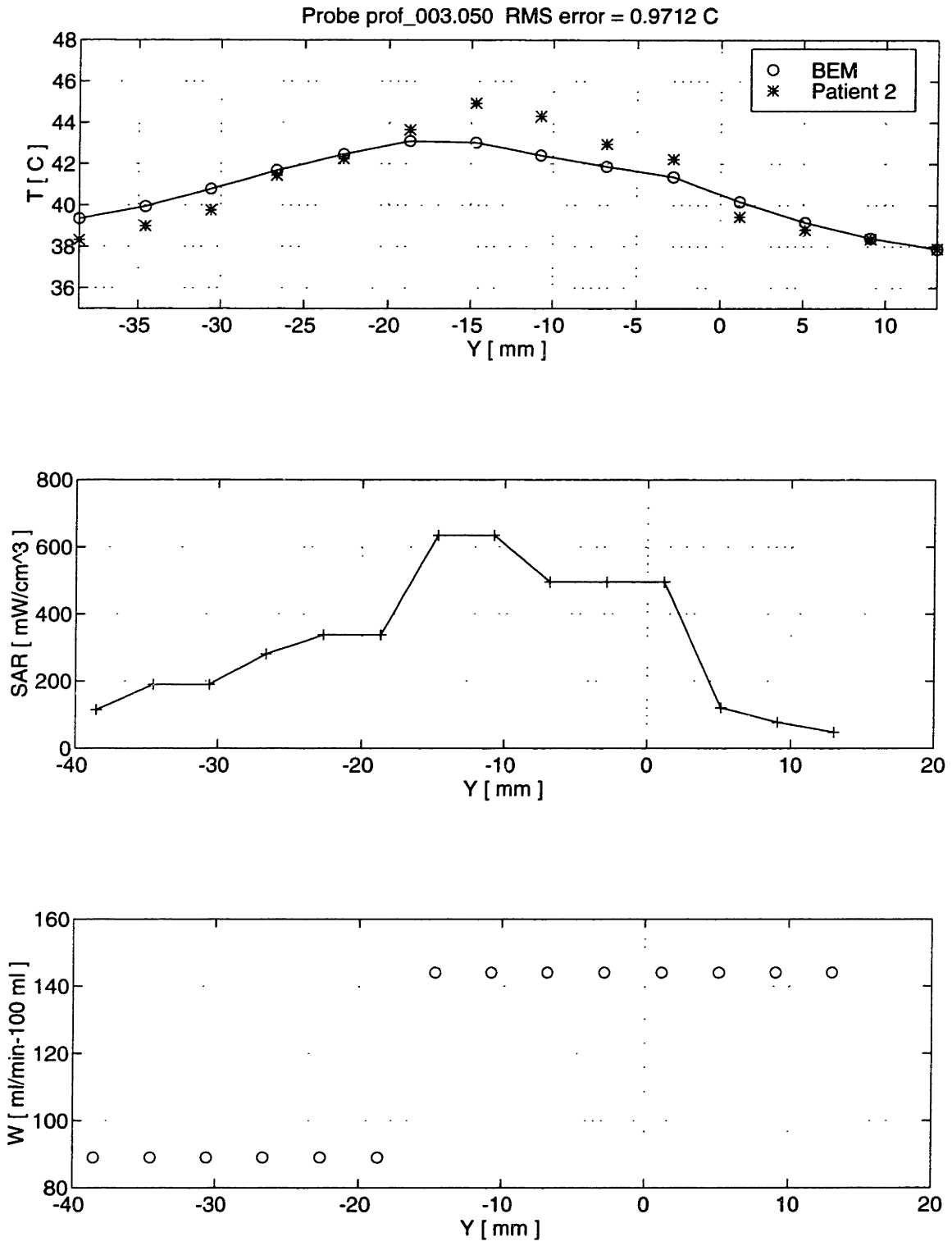

Figure 6-22: Temperature field calculation for probe Prof_003.050 with the measured SAR and perfusion.

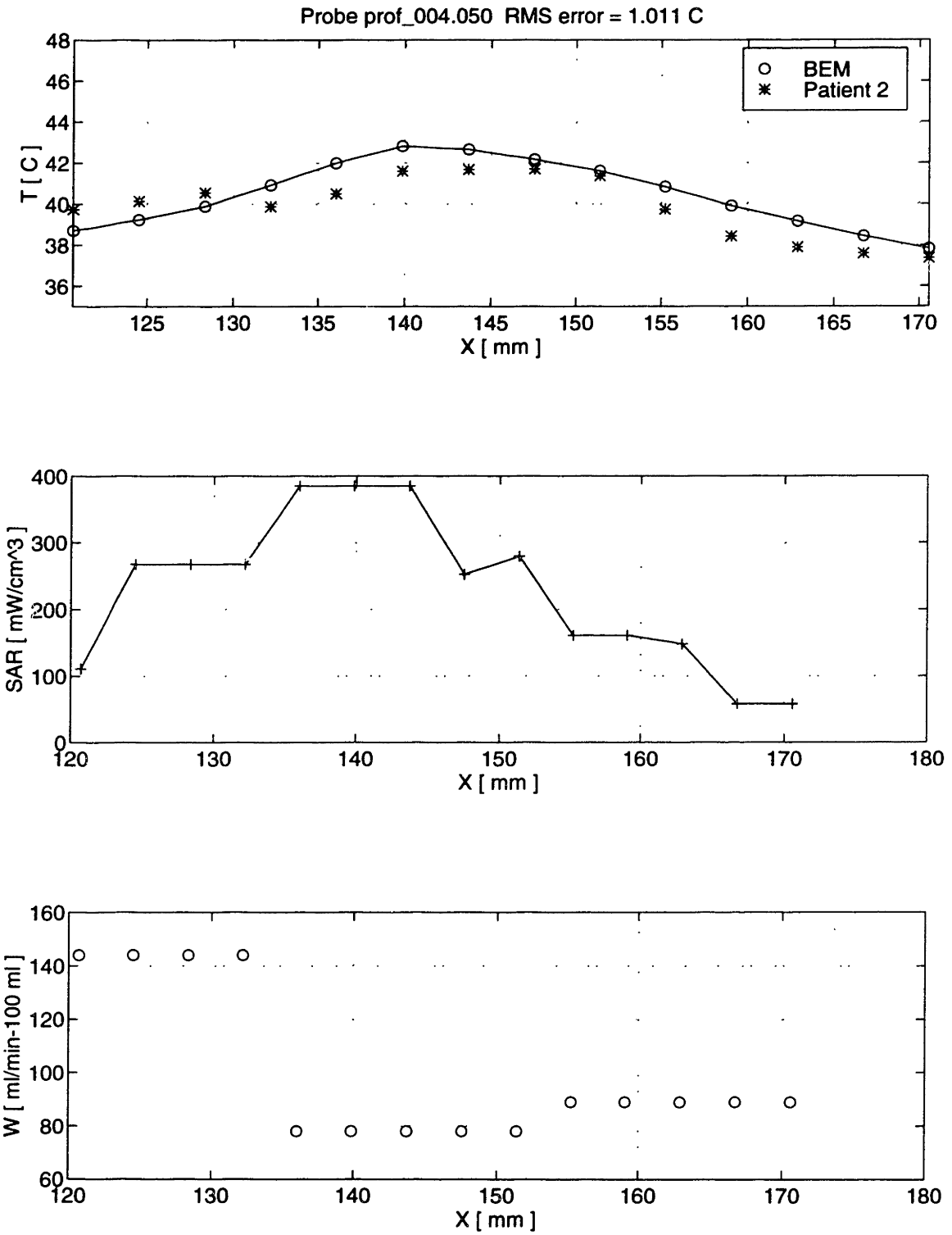

Figure 6-23: Temperature field calculation for probe Prof_004.050 with the measured SAR and perfusion.

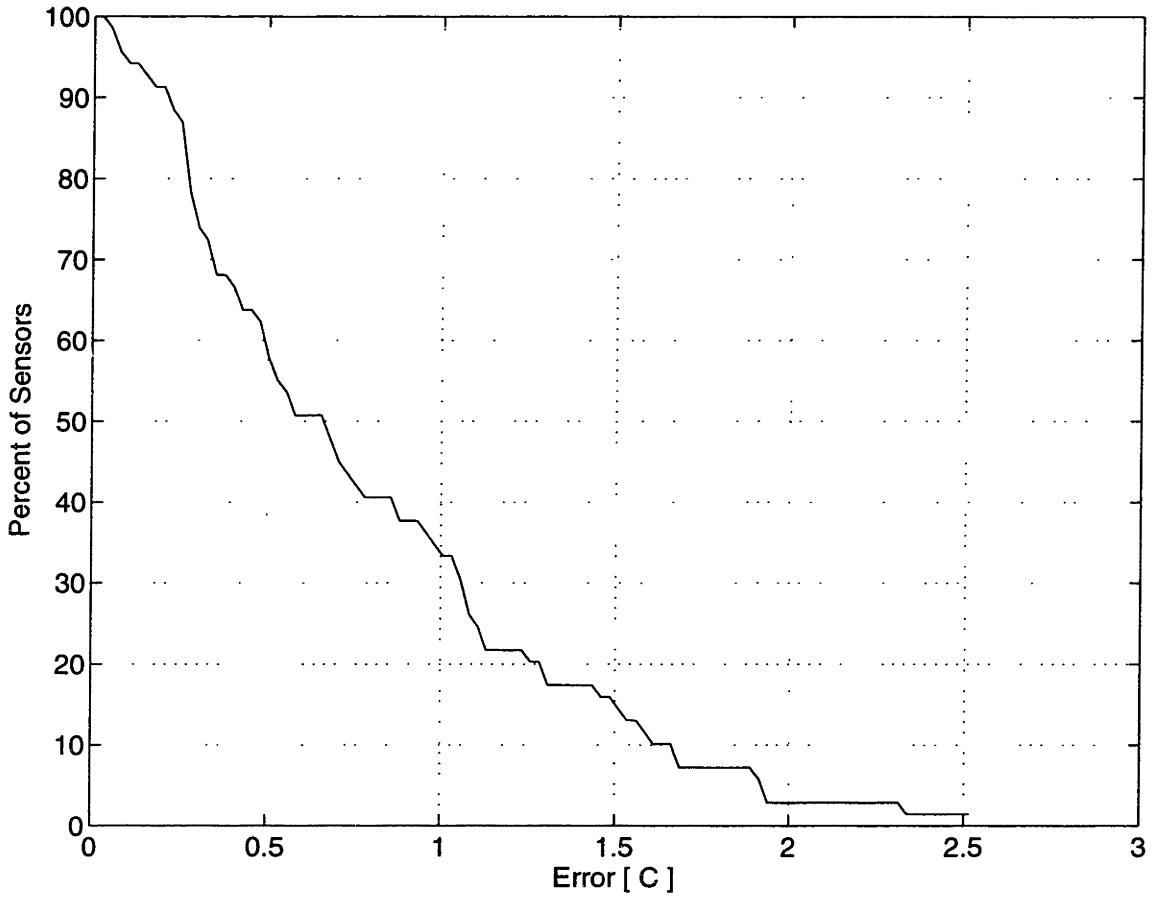

Figure 6-24: Percentage of sensors (y axis) with an error greater than a given value (x axis).

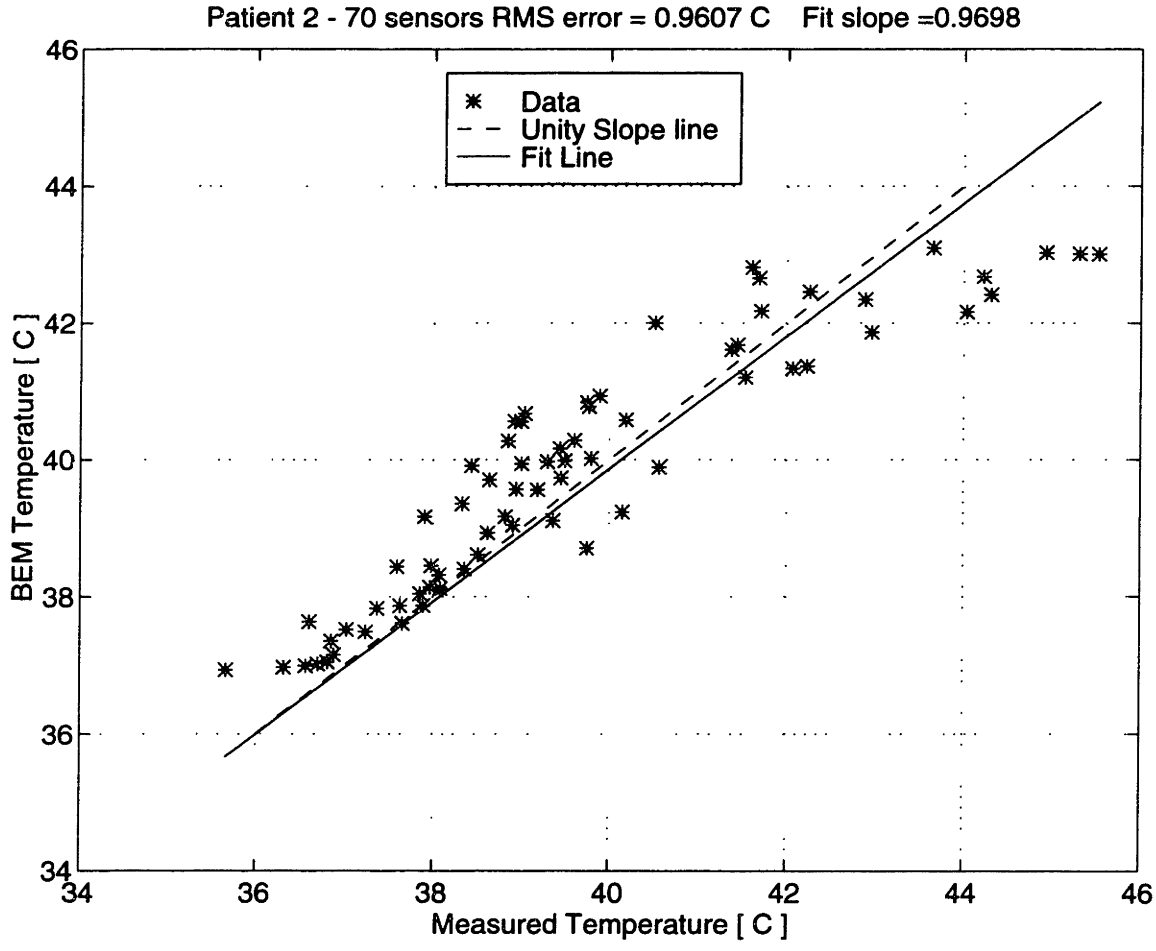

Figure 6-25: Temperature calculated with the BEM versus measured temperature in Patient 2. The dashed line is the unity slope line, while the solid line represents a least-squares-residual fit to the data with the *y* intercept constrained at zero temperature rise.

CT scans are taken.

The temperature reconstruction can be used to compare the sensor based tumor-temperature histogram with the volume based histogram. Figure 6-26 shows the steady-state histogram which plots the percent number of points in the tumor (y axis) which are above a given temperature (x axis). In the mesh generated from the patient model, there are 315 nodes in the tumor volume at which temperature is calculated. The solid line is the percentage of these nodes above the temperature on the x axis. The percentage of sensors above a given temperature is plotted as the dashed line. The Patient 2 histogram shows that according to the measurements, the patient received an apparently better treatment than that computed by the BEM. This may be due to the therapist preferentially treating the sensor sites rather than the entire tumor volume. As given by the sensors, T_{90} is 38.2 °C while the BEM computes T_{90} of 37.7 °C. An obvious benefit of the BEM is the ability to provide these treatment metrics in real-time during therapy in order to control the heat over the entire tumor volume, rather than just at the sensor locations.

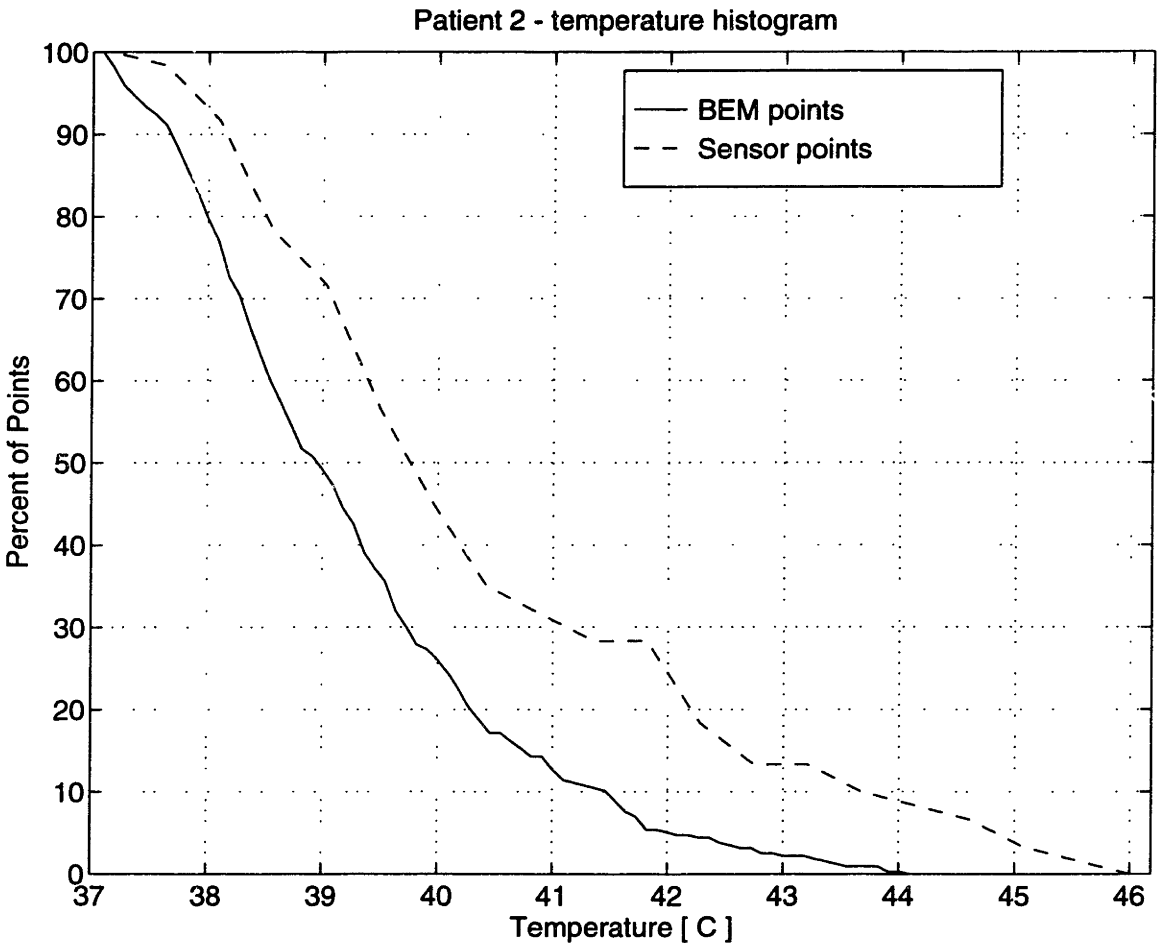

Figure 6-26: Patient 2 temperature histogram as computed by the BEM (solid line) and measured from the sensors (dashed line).

Chapter 7

Summary and Conclusion

This thesis describes a thermal model and solution algorithm for the fast, accurate and routine computation of the hyperthermia therapy induced tissue temperature distribution. Such a model is important to treatment planning and evaluation of the therapy to help maximize the thermal dose in the tumor volume and to minimize the temperature exposure of the normal tissue.

Chapter 1 starts with a brief description of hyperthermia therapy and describes how a clinically used thermal model will increase treatment efficacy. From practical considerations, the Pennes bioheat transfer equation is selected to form the theoretical basis of the thermal model. The chapter includes a comprehensive review of the current literature on thermal models for the analysis of hyperthermia therapy and the design criteria for a clinically useful thermal model is outlined.

Chapter 2 analyzes the patient specific treatment parameters which serve as inputs to the algorithm: patient anatomy, tissue thermal properties and perfusion, and power deposition. The patient model of the anatomy is derived from CT scans which are semi-automatically contoured, segmented and identified. Thermal properties and perfusion are either measured from the Thermal Diffusion Probe or recalled from a database. Power is deposited in the tissue using ultrasonic applicators. The Specific Absorption Rate (SAR) of the deposited power is either estimated from simple analytical models or measured during treatment.

Chapter 3 presents the model formulation. The theoretical background is derived from the Green's function solution to the bioheat equation where the volume integral is

divided into two subvolumes: 1) the sources thermally close to the domain point (where temperature is computed) and 2) the sources thermally distant from the domain point. The algorithm formulation further divides the thermally significant volume integral into the finite sum of subvolumes. Each subvolume forms a spherical source of finite dimension which is analytically solved - this is the Basis Element (BE). Boundary conditions and non-homogeneous thermal properties are considered by deriving the approximate Green's functions for these thermal situations.

Chapter 4 describes the implementation of the BEM algorithm. The algorithm represents the geometry of continuous problems in a discrete space. The power deposition is discretized as a lattice of weighted finite spherical sources, close-hexagonally packed together. The computer, *C* code is implemented in a modular and efficient manner and comprises over 7000 lines of code. Optimization is carried out by the use of dimensionless variables, integer geometry and a square root "look-up table".

Chapter 5 demonstrates the validity of the Basis Element Method (BEM) with comparisons to problems with exact analytical solutions and to approximate numerical solutions. The comparisons show that as the BE size is decreased and the integration volume is increased, the exact solutions are approached. The comparisons to numerical solutions use problems with irregular geometry and variable perfusion. They show that the BEM is capable of solving these problems with a root-mean-square difference of about 0.1°C. The speed of the method is shown to be about an order of magnitude faster than a finite element package for an error of 0.15 °C.

Chapter 6 contains the procedure and results for the experimental validation of the method in large animal (porcine) and human experiments. In the porcine model, a simulated hyperthermia treatment is administered, using ultrasound, to the rump which is densely instrumented with 101 temperature sensors and 12 perfusion sensors. SAR is measured at the temperature sensor locations and the SAR and perfusion are inputed into the BEM algorithm for temperature computation. The comparison of measured and computed temperature values shows a root-mean-square error of 0.7 °C over all the sensors and one half of the sensors have an error of less than 0.54 °C. The results from two human subjects experiments are given. In the first patient, hyperthermia is to a 10 x 10 x 12 cm tumor in

the left axilla. The tumor was instrumented with 3 probes, each containing 14 temperature sensors. Measured and computed steady-state temperature show an RMS error of 1.2 °C. In the second patient, hyperthermia was given to a 10.2 x 7.0 x 12.2 cm recurrent breast tumor in the left axilla. This tumor was instrumented with 5 probes, each with 14 temperature sensors. In addition 3 TDP perfusion probes were inserted into the tumor. Agreement between measured and computed temperatures show an RMS error of 0.97 °C. The use of the BEM algorithm in treatment reconstructions allows the computation of volumetric tumor dose statistics such as T_{90} which is the temperature at which 90% of the tumor volume is above.

Currently in hyperthermia therapy, parameters such as specific absorption rate (SAR), thermal properties and patient geometry are not generally known to an accuracy greater than 10 percent. Clearly, any model of the hyperthermic temperature field is bounded by such accuracy. Thus, the full potential of three dimensional finite element and finite difference methods for hyperthermia thermal modeling is not yet realizable for clinical hyperthermia practice, although use in a research setting is invaluable. The BEM provides a rational alternative. It is conceptually simple, computationally less intensive, and, most important, can be automatically tailored to provide a more accurate solution in specified regions of the tissue. These features make the basis element method practical for routine clinical thermal modeling of hyperthermia. Certainly, however, the results of more exact computational approaches, such as more sophisticated state and parameter estimation schemes, additions and enhancements to the bioheat equation, and treatment of specialized problems, will be used for model verification and improvement.

There are many possible improvements in the BEM formulation and the algorithm implementation which will increase the speed, accuracy and clinical applicability. For treatment evaluation, improvements in the algorithm speed will ultimately allow real-time thermal modeling to take place in the clinic, concurrent with the treatment. Real-time application will necessitate the formulation of the BEM for transient solution of the bioheat equation. In this case the functional form of the time dependence is included into the BEM, thus the solution does not depend on a Courant criteria (maximum time step size) for convergence. Significant increases in speed can be obtained through the optimal choice of

BE size. In the algorithm implemented in this thesis, the BE size was maintained constant for a given problem. It is possible to modulate the BE as a function of the distance from the domain node - making the BE's that are further from the domain node successively larger such that the smaller BE's have more thermal influence.

Once made sufficiently fast, the BEM could be applied to the solution of the inverse hyperthermia problem - where the therapist inputs the desired temperature field in the tissue and the BEM computes the transducer excitation pattern necessary to obtain it. Solution of the inverse problem generally requires the repeated solution of the forward problem until convergence is reached. The iteration takes place such that the following matrix is solved:

$$[T_{nx1}] = [BE_{nxm}][P_{mx1}] \tag{7.1}$$

where T_{nx1} are the desired temperatures at the nodes, n, P_m is the magnitude of the power emitted by each of the m elements, and BE_{nxm} is the feed-back matrix which is defined by the tissue model. Since the number of nodes, n, far exceeds the number of transducers, m, least squares can be used to solve this system of equations. The feed-back matrix, BE_{nxm} can be computed by the BEM. The BEM uses a limited volume of integration to compute the temperature, thus the feed-back matrix will be banded with a bandwidth that decreases with increasing perfusion. This gives the BEM a distinct advantage over other methods in the solution of the inverse problem.

The use of the Pennes bioheat transfer equation to describe tissue heat transfer in this thesis, does not account for the effect of large vessels. The BEM approach, however, could be modified and extended to treat these cases. In general, the BEM considers any such thermal perturbation - even those from large vessels - to be exponentially damped with a space constant inversely proportional to perfusion. Thus a vessel could be modeled as a sink in the tissue surrounded by a domain with Pennes-type heat transfer. The heat sinked by the vessel could be modeled with an approximate formulation of the coupled mass transfer and energy equations.

These improvements will increase the clinical applicability of the BEM and allow a "push button" interface between the thermal model and the clinician where results can be instantaneously displayed with the patient geometry. The routine use of thermal modeling

in the clinic will allow more accurate local thermal dose statistics based on the entire tumor volume instead of discrete temperature measurements. Ultimately, these statistics will help establish proper thermal dose - tumor response relations which will serve to guide treatment planning.

Appendix A

Derivation of Other Basis Element Functions

The Basis Element Method has been formulated in this thesis to solve steady-state heat transfer problems, however a transient formulation is possible. As a first step in developing this formulation, a free space transient Basis Element with exponential heating was derived and is given below.

A.1 Exponential, Transient Basis Element in an Infinite Medium

The transient Laplacian for an infinite and perfused media is:

$$-\frac{\partial\theta}{\partial\tau}+\frac{\partial^2\theta}{\partial r^2}+\frac{2}{r}\frac{\partial\theta}{\partial r}-Pe\,\theta=-e^{-r} \tag{A.1}$$

The solution method proceeds by taking the term-by-term Laplace transform of equation A.1. The Laplace transform is defined as follows.

$$\Theta(p)=\int_0^\infty \theta(t)\,e^{-pt}\,dt \tag{A.2}$$

And the inversion formula is:

$$\theta(t)=\int_0^\infty \Theta(p)\,e^{-pt}\,dp \tag{A.3}$$

The Laplace transform changes the partial differential equation into an ordinary differential equation with constant coefficients.

$$\frac{d^2\Theta}{dr^2} + \frac{2}{r}\frac{d\Theta}{dr} - (Pe + p)\Theta = \frac{-e^{-r}}{p} \tag{A.4}$$

$$\frac{d^2(r\Theta)}{dr^2} - (Pe + p)r\Theta = \frac{-re^{-r}}{p} \tag{A.5}$$

The general solution to equation A.5 is:

$$\Theta = C_1\frac{e^{-qr}}{r} - C_2\frac{e^{qr}}{r} - \frac{e^{-r}}{p(1-q^2)} - \frac{2e^{-r}}{pr(1-q^2)^2} \tag{A.6}$$

$$q = \sqrt{p + Pe} \tag{A.7}$$

The condition that temperature and thus the transformed temperature are bounded requires C_2 to be zero and sets the value of C_1. The transformed temperature is:

$$\Theta = C_1\frac{e^{-qr}}{r} + \frac{e^{-r}}{p(p + Pe - 1)} - \frac{2e^{-r}}{rp(s + Pe - 1)^2} \tag{A.8}$$

The method of partial fractions is then used to expand equation A.8 into a set of independent terms.

$$\Theta = C_1\frac{e^{-qr}}{r} + \frac{e^{-r}}{p(Pe - 1)} - \frac{e^{-r}}{(1 - Pe)(p + Pe - 1)} \tag{A.9}$$

$$- \frac{2e^{-r}}{r(1 - Pe)}\left[\frac{1}{p(1 - Pe)} - \frac{1}{(p + Pe - 1)(1 - Pe)} + \frac{1}{(p + Pe - 1)^2}\right]$$

At $r = 0$ the temperature must be finite, thus C_1 is found to be:

$$C_1 = \frac{2}{(1 - Pe)}\left[\frac{1}{p(1 - Pe)} - \frac{1}{(p + Pe - 1)(1 - Pe)} + \frac{1}{(p + Pe - 1)^2}\right] \tag{A.10}$$

and the complete transformed temperature is:

$$\Theta = \frac{e^{-r}}{(Pe - 1)}\left[\frac{1}{p} - \frac{1}{p + Pe - 1}\right] \tag{A.11}$$

$$+ \frac{2e^{-r}}{r(Pe - 1)}\left[\frac{1}{p(1 - Pe)} - \frac{1}{(p + Pe - 1)(1 - Pe)} + \frac{1}{(p + Pe - 1)^2}\right]$$

$$+ \frac{2e^{-qr}}{r(1 - Pe)}\left[\frac{1}{p(1 - Pe)} - \frac{1}{(p + Pe - 1)(1 - Pe)} + \frac{1}{(p + Pe - 1)^2}\right]$$

Applying the inversion formula from the tables of [72, 59] gives the temperature.

$$
\begin{aligned}
\theta \;=\; & \frac{e^{-r}}{Pe-1}\left[1-e^{-t(Pe-1)}\right] \qquad (A.12)\\
& + \frac{2e^{-r}}{r(Pe-1)}\left[\frac{1}{1-Pe}-\frac{e^{-t(Pe-1)}}{1-Pe}+te^{-t(Pe-1)}\right]\\
& + \frac{1}{r(1-Pe)^2}\left[e^{-\sqrt{Pe}r}\,erfc\left(\frac{r}{2\sqrt{t}}-\sqrt{Pe\,t}\right)+e^{\sqrt{Pe}r}\,erfc\left(\frac{r}{2\sqrt{t}}+\sqrt{Pe\,t}\right)\right]\\
& - \frac{e^{-t(Pe-1)}}{r(1-Pe)^2}\left[e^{-r}\,erfc\left(\frac{r}{2\sqrt{t}}-\sqrt{t}\right)+e^{r}\,erfc\left(\frac{r}{2\sqrt{t}}+\sqrt{t}\right)\right]\\
& + \frac{e^{-t(Pe-1)}}{r(1-Pe)}\left[(t-\tfrac{r}{2})e^{-r}\,erfc\left(\frac{r}{2\sqrt{t}}-\sqrt{t}\right)+(t+\tfrac{r}{2})e^{r}\,erfc\left(\frac{r}{2\sqrt{t}}+\sqrt{t}\right)\right]
\end{aligned}
$$

Appendix B

Thermally Significant Vessels

It is well known that larger vessels ($> 500\mu m$) passing through the hyperthermic tissue volume may not thermally equilibrate with the surrounding tissue, resulting inadequate heating of the tissue near these vessels. The BEM has been formulated using the Pennes bioheat transfer equation to describe the tissue heat and mass transport. A logical extension of the method would incorporate the effect of vessels on the thermal field where the vessels are modeled as an energy sink in the tissue field.

Consider the tissue near a vessel as consisting of 2 subdomains: one subdomain is the actual vessel whose position, size and fluid velocity is assumed to be known; and the other subdomain is the surrounding tissue whose transport is assumed to be described by the Pennes equation. Power deposition of hyperthermic energy is associated only with the Pennes tissue subdomain. The Basis Element for this thermal situation is derived from the point source for an infinite Pennes tissue subdomain, with a straight vessel of infinite length, passing through. The heat sinking effect of the vessel is mathematically described by the Green's function for the continuous line sink in a perfused domain. The Basis Element is assumed to be in the form of the sum of the vessel Green's function for the sink (at $r < a$, z) and the Pennes Green's function for the source (at r', z=0):

$$u = \frac{1}{4\pi k_m}\frac{e^{-\lambda R}}{R} + C_1 K_o(\lambda r) \tag{B.1}$$

$$R = \sqrt{(r - r')^2 + z^2} \tag{B.2}$$

where the coordinates are defined in Figure B-1. The weight function, C_1, is found such that

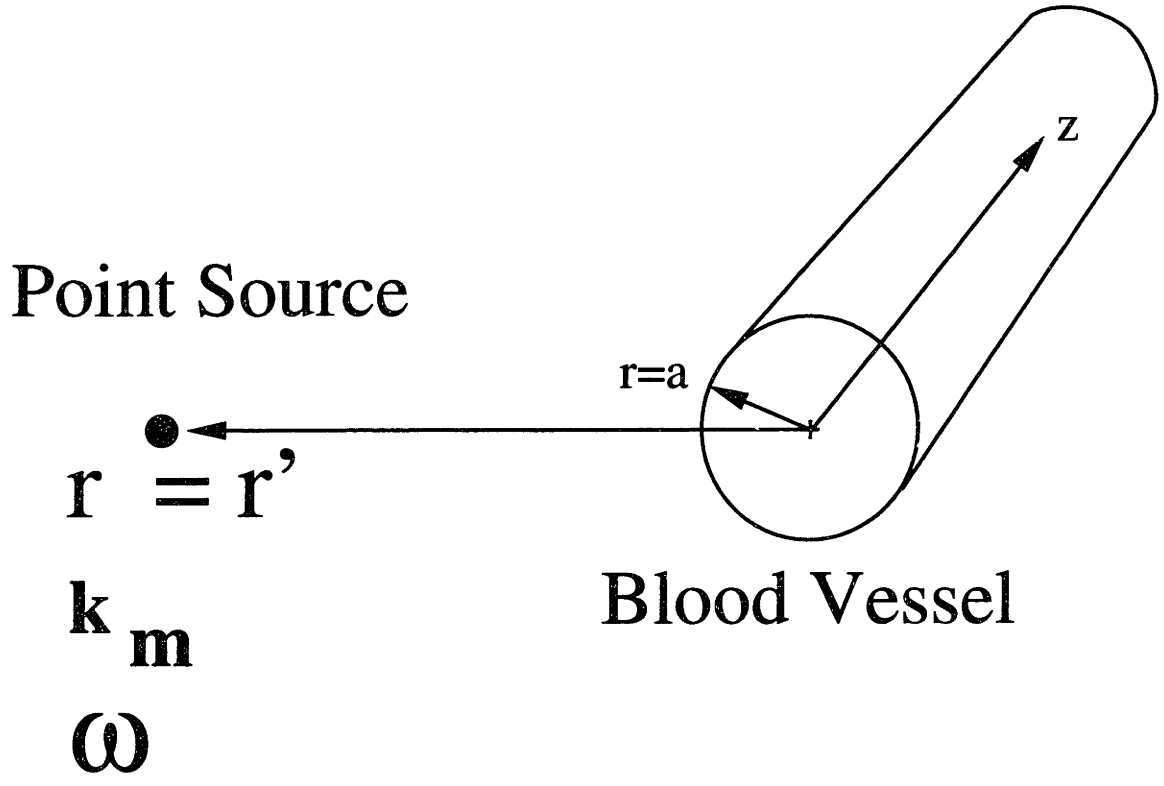

Figure B-1: Schematic diagram of the Basis Element for thermally significant vessels.

at the vessel wall ($r = a$) either the temperature or the heat flux is constant. For constant wall temperature, the approximate solution is:

$$u = \frac{1}{4\pi k_m}\frac{e^{-\lambda R}}{R} + \frac{1}{4\pi k_m}\frac{e^{-\lambda R_a}}{R_a}\frac{K_o(\lambda r)}{K_o(\lambda a)} \tag{B.3}$$

$$R_a = \sqrt{(a - r')^2 + z^2} \tag{B.4}$$

This vessel Basis Element has yet to be validated numerically with comparisons to finite element solutions and experimentally.

Appendix C

Basis Element Code

C.1 Basis Element Routines

```
/* (c) Copyright 1992-1995 by MIT All Rights Reserved */
#include <math.h>
#include <stdio.h>
/*
 FILE: hotstuff.mit.edu:/u1/users/gmartin/src/release/BEMelements.c
 AUTHOR: Gregory T. Martin
      Biomedical Engineering Center
           20A - 117
           MIT
           Cambridge, MA 02139 USA                                    10
           617-253-3605
           gmartin@hstbme.mit.edu
 DATE: April 1992
 DESCRIPTION:
   This file contains the routines which make up the "kernal" of the
   basis element method. There basis elements herein contained are
   for sources in an infinite medium (uniform, Gaussian, exponential),
   transient sources (exponential), boundary basis elements, and the
   macro basis elements for error correction.
                                                                      20
 REVISIONS:
 CONVENTIONS:
  -Variables that begin with capital letters are global, while variables
  that begin  with lower case letters are local.
*/
#include "BEMbem.h"
#include "BEMmain.h"
float *Sqrt;
float tinsphere(float Pe, float sqrtpe, float RStar);
float toutsphere(float Pe, float sqrtpe, float RStar);                30
float tsphere(float pe, float sqrtpe, float rstar);
float tshellss( float pe );
float tfirstkind(float pe, float r);
```

```
float tsecondkind( float pe, float r);
float tthirdkind(float pe, float bi, float r);
float tfirstkind_curve(float pe, float r);
float tsecondkind_curve( float pe, float r);
float tthirdkind_curve(float pe, float bi, float r);
float first_curve_sphere( float R,    float rpoint, float rsource,
                                  float theta, float pe,    float radcurve);
float second_curve_sphere( float R,    float rpoint, float rsource,
                                  float theta, float pe,    float radcurve);
float third_curve_sphere( float R,    float rpoint, float rsource,
                                  float theta, float pe,    float radcurve,
                                  float biot);
float approx_diff_curve_sphere( float R,    float rpoint, float rsource,
            float theta, float pe1, float pe2, float kappa, float radcurve);
double erfcc( double x );
float factor( int i );
float square( float x );
float min( float x, float y );
float max( float x, float y );
float sgn( float var );
void fswap(float *x, float *y);
float round( float x);
float BEMsqrt( Space x );
Space BEMsquare( Space x );
float (*BEMsqrtPtr) ( Space x );
int isclose( float x, float y, float e);
/* ************************************************************** */
#define PI M_PI
/* ************************************************************** */
float round( float x)
 float y;
#ifdef USE_FLOAT_GEOM
 return( x );
#else
 y = fabs( x );
 y *= 2.0;
 y = (int) (y + 1);
 y /= 2.0;
 y = (int) y;
 return( y*sgn( x ) );
#endif
}
/* ************************************************************** */
void fswap(float *x, float *y)
{
 float tmp;

 tmp = *x;
 *x = *y;
 *y = tmp;
 return;
}
/* ************************************************************** */
float tinsphere(float Pe, float sqrtpe, float RStar)
```

```
    /*
 This routine compute the non-dimensional temperature at a point RStar
 from the origin (RStar is in this heated sphere) in a sphere that has
 a uniform internal heat generation in it. Note that RStar is also
 non-dimensional and is r/a where a is the radius of the heated sphere
 and the length scale in Pe, the Peclet number is also a. Thus Pe is a
 local Peclet number.
    */
{
 register float arg1;

 arg1 = sqrtpe*RStar;
 if (RStar > ZERO_DISTANCE)
  return( (1.0-1.0/RStar*exp( -sqrtpe )*(1.0 + 1.0/sqrtpe)*sinh( arg1 ))/Pe );
 else
  return( (1.0 -      exp( -sqrtpe )*(1.0 + 1.0/sqrtpe)*sqrtpe)/Pe );
}
/* ********************************************************************** */
float toutsphere(float Pe, float sqrtpe, float RStar)
/*
This routine compute the non-dimensional temperature at a point RStar
from the origin (RStar is outside of this heated sphere) in a sphere
that has a uniform internal heat generation in it. Not that RStar is
also non-dimensional and is r/a where a is the radius of the heated
sphere and the length scale in Pe, the Peclet number is also a. Thus
 Pe is a local Peclet number.
*/
{
 register float arg2;

 arg2 = sqrtpe*RStar;
/* An equivalent expression is as follows. This expression should be
  computationally faster.    */
 return( exp( -arg2 )*0.5*
  (exp( sqrtpe )*(1.0 - 1.0 / sqrtpe) + exp(-sqrtpe)*(1.0 + 1.0 / sqrtpe) )
     /RStar/Pe );
}
/* ********************************************************************** */
float tsphere(float pe, float sqrtpe, float rstar)
/*
Here the non-dimensional temperature is computed for a uniformly heated
sphere in an infinitely, perfused medium.
*/
{
/*  return  x >= 0.0 ? ans : 2.0-ans; */
/*  return (rstar < 1.0) ? tinsphere(pe, rstar) : toutsphere(pe, rstar); */

 if ( rstar < 1.0 )
  return(  tinsphere(pe, sqrtpe, rstar) );
 else
  return( toutsphere(pe, sqrtpe, rstar) );
}
/* ********************************************************************** */
float tfirstkind(float pe, float r)
```

```
/*
 This routine computes the temperature contribution from a boundary node
 of the first kind. Note that pe and r are local and dimensionless. The
 length scale is arbitrary, but should be consistant.
 The routine returns dimensionless temperature;

        Theta = T/Tb
 where T is the dimensional temperature and Tb is the boundary temperature.
*/                                                                    150
{

 return( exp( -sqrt( pe ) * r ) );
}
/* ************************************************************************ */
float tsecondkind( float pe, float r)
/*
 This routine computes the temperature contribution from a boundary node
 of the second kind. Note that pe and r are local and dimensionless. The
 length scale is arbitrary, but should be consistant.                 160
 The routine returns dimensionless temperature;

            T Km
       Theta = -----
            q a

 where T is the temperature, Km is the thermal conductivity, a is
 the length scale and q is the boundary heat flux.
*/
                                                                      170
{
 float arg1;
 arg1 = sqrt( pe );

 return( exp( -arg1*r )/arg1 );
}
/* ************************************************************************ */
float tthirdkind(float pe, float bi, float r)
/*
 This routine computes the temperature contribution from a boundary node  180
 of the third kind. Note that pe, bi and r are local and dimensionless. The
 length scale is arbitrary, but should be consistant.
 The routine returns dimensionless temperature;

            T
       Theta = -----
            To

 where T is the temperture and To is the cooling fluid temperature.
 The Biot number is:                                                  190

            h a
       Bi = -----
            Km
```

```
  h is the heat transfer coefficient, Km is the thermal conductivity,
  and a is  the length scale.
*/
{
 return( exp( -sqrt( pe )*r ) / (1 + sqrt(pe)/bi) );                    200
}
/* ************************************************************************ */
/*
            STEADY CURVED BOUNDARY BASIS ELEMENTS (non-homogeneous)
Thes routine returns the dimensionless temperature rise for a
1-D conduction with perfusion and various boundary conditions.

   2
  d  (r' T)        w rho cb
  ----------   -   ---------- (r' T)  = 0                               210
    2
   dr'             km

Or in dimensionless form:

   2
  d  (r Theta)
  ---------   -   Pe  (r Theta) = 0
    2
   dr                                                                   220

/* ************************************************************************ */
float tfirstkind_curve(float pe, float r)
/*
 This routine computes the temperature contribution from a boundary node
 of the first kind. Note that pe and r are local and dimensionless. The
 length scale is arbitrary, but should be consistant.
 The routine returns dimensionless temperature;

        Theta = T/Tb                                                    230
 where T is the dimensional temperature and Tb is the boundary temperature.
*/
{
 float sqrtpe;

 sqrtpe = sqrt( pe );
 if (r > ZERO_DISTANCE)
  return( sinh( sqrtpe*r )/sinh(sqrtpe)/r );
 else
  return( sqrtpe/sinh(sqrtpe) );                                        240
}
/* ************************************************************************ */
float tsecondkind_curve( float pe, float r)
/*
 This routine computes the temperature contribution from a boundary node
 of the second kind. Note that pe and r are local and dimensionless. The
 length scale is arbitrary, but should be consistant.
 The routine returns dimensionless temperature;
```

```
                T Km                                                    250
        Theta = -----
                q a

  where T is the temperature, Km is the thermal conductivity, a is
  the length scale and q is the boundary heat flux.
*/
 float sqrtpe;

 sqrtpe = sqrt( pe );
 if (r > ZERO_DISTANCE)                                                 260
  return( sinh( sqrtpe*r )/r/(sqrtpe*cosh(sqrtpe) - sinh(sqrtpe)) );
 else
  return( sqrtpe/(sqrtpe*cosh(sqrtpe) - sinh(sqrtpe)) );
}
/* ********************************************************************** */
float tthirdkind_curve(float pe, float bi, float r)
/*
  This routine computes the temperature contribution from a boundary node
  of the third kind. Note that pe, bi and r are local and dimensionless. The
  length scale is arbitrary, but should be consistant.                  270
  The routine returns dimensionless temperature;

                T
        Theta = -----
                To

  where T is the temperture and To is the cooling fluid temperature.
  The Biot number is:

                h a                                                     280
         Bi =  -----
                Km

  h is the heat transfer coefficient, Km is the thermal conductivity,
  and a is  the length scale.
*/
{
 float sqrtpe;

 sqrtpe = sqrt( pe );                                                   290
 if (r > ZERO_DISTANCE)
 return( bi*sinh(sqrtpe*r)/r/(bi*sinh(sqrtpe)+sinh(sqrtpe)-sqrtpe*cosh(sqrtpe)));
 else
  return( bi*sqrtpe/(bi*sinh(sqrtpe)+sinh(sqrtpe)-sqrtpe*cosh(sqrtpe)));
}
/* ********************************************************** */
float factor( int i )
{
 if ( i == 0)
  {                                                                     300
   return( 1.0 );
  }
 else
```

```
    {
     return( i*factor( i - 1) );
    }
}
/* ********************************************************** */
float square( float x )
{
 return( x*x );
}
/* ********************************************************** */
SpaceAbs( Space x )
{
 return( abs( x ) );
}
/* ********************************************************** */
Space BEMsquare( Space x )
{
 return( x*x );
}
/* ********************************************************** */
float BEMsqrt1( Space x )
{
 return(  Sqrt[ (int) x ] );
}
/* ********************************************************** */
float BEMsqrt2( Space x )
{
 if(x < MAX_N_SQRT)
   {
    return( *(Sqrt + (int) x ) );
   }
 else
   {
    return( sqrt( (float) x ) );
   }
}
/* ********************************************************** */
float BEMsqrt3( Space x )
{
 return( (float) sqrt( (float)  x  ) );
}
/* ********************************************************** */
float BEMsqrt( Space x )
{
/*  return( (float) sqrt( (float)  x  ) );  */
 return(  (*BEMsqrtPtr) ( x ) );
/*
 if(x < MAX_N_SQRT)
   {
    return(  *(Sqrt + (int) x ) );
   }
 else
   {
    return( sqrt( (float) x ) );
```

```
    }
 */
}                                                                    360
/* ********************************************************** */
float min( float x, float y )
{
 if (x < y)
   {
    return( x );
   }
 else
   {
   return( y );                                                      370
 }
}
/* ********************************************************** */
float max( float x, float y )
{
 if (x > y)
   {
    return( x );
   }
 else                                                              380
   {
    return( y );
   }
}
/* ********************************************************** */
float sgn( float var )
{
 if (var == 0.0)
   {
    return( 0.0 );                                                390
   }
 else
   {
    return( fabs( var )/var );
   }
}
/* ********************************************************** */
int isclose( float x, float y, float e)
{
 e *= sgn( y );                                                    400
 if( ( x < y + e*y) && (x > y - e*y ))
   {
    return( 1 );
   }
 return( 0 );

}
/* ********************************************************** */
float first_curve_sphere( float R,    float rpoint, float rsource,
                          float theta, float pe,    float radcurve)  410
{
```

```
/*
 This routine computes the steady-state solution of temperature
 for a uniform source in a perfused medium with a curved external
 boundary whose temperature is held at zero. The solution is
 formulated in spherical coordinates.
*/
 int convex;
 float temp, r, rprime, C1, sqrtpe, Rprime, mu;
 sqrtpe = sqrt( pe );                                                    420
 mu = cos( theta );
 temp = 0.0;
/* Outside the curved struction the temperature is zero. */
 convex = 0;
 if (radcurve < 0.0)
  {
   convex = 1;
   radcurve = fabs( radcurve );
  }
 if (isclose(rpoint, radcurve, CLOSE)) return( temp );                   430
 if ( (!convex) && ((rsource > radcurve) || (rpoint > radcurve) ||
    (R > 2.0*radcurve) ))
  {
   return( (float) temp );
  }
 if (theta > TWO_PI) return( temp );
 rprime = rsource;
 r     = rpoint;
 Rprime = sqrt( radcurve*radcurve + r*r*rprime*rprime/radcurve/radcurve
                                  - 2.0*r*rprime*mu );                   440

 if (R > 1.0)
  {
   temp =  exp( -sqrtpe*Rprime )/Rprime;
   temp =  exp( -sqrtpe*R )/R - temp;
   temp *= (cosh( sqrtpe ) - sinh( sqrtpe ) / sqrtpe) / pe;
  }
 else
  {
   temp =  exp( -sqrtpe*Rprime )/Rprime;                                 450
   C1 = (1.0 - (cosh( sqrtpe )  - sinh( sqrtpe ) / sqrtpe)
          *(exp( -sqrtpe ) - temp ))/sinh( sqrtpe );
   if(R > ZERO_DISTANCE)
          {
           temp = 1.0/pe*(1.0 - C1*sinh( sqrtpe*R )/R);
          }
   else
          {
           temp = (1.0 - C1*sqrtpe)/pe;
          }                                                              460
  }
 if (temp < 0.0) temp = 0.0;
 return( temp );
}
/* ********************************************************** */
```

```
float second_curve_sphere( float R,    float rpoint, float rsource,
                           float theta, float pe,    float radcurve)
{
/*
 This routine computes the steady-state solution of temperature                    470
 for a uniform source in a perfused medium with a curved external
 boundary whose temperature is held at zero. The solution is
 formulated in spherical coordinates.
*/
 int convex;
 float temp, r, rprime, C1, sqrtpe, Rprime, mu;
 float D1;
 sqrtpe = sqrt( pe );
 mu = cos( theta );
 D1 = (cosh( sqrtpe ) - sinh( sqrtpe ) / sqrtpe) / pe;                             480
 temp = 0.0;
 if (theta > TWO_PI) return( temp );
 rprime = rsource;
 r      = rpoint;
 Rprime = sqrt( radcurve*radcurve + r*r*rprime*rprime/radcurve/radcurve
                                  - 2.0*r*rprime*mu );
 if (R > 1.0)
  {
   temp =  exp( -sqrtpe*Rprime )/Rprime;
   temp =  exp( -sqrtpe*R )/R + temp;                                              490
   temp *= D1;
  }
 else
  {
   temp =  exp( -sqrtpe*Rprime )/Rprime;
   C1 = (1.0 - D1 * pe * (exp( -sqrtpe ) - temp ))/sinh( sqrtpe );
   if(R > ZERO_DISTANCE)
         {
          temp = 1.0/pe*(1.0 - C1*sinh( sqrtpe*R )/R);
         }                                                                         500
   else
         {
          temp = (1.0 - C1*sqrtpe)/pe;
         }
  }
 if (temp < 0.0) temp = 0.0;
 return( temp );
}
/* ********************************************************** */
float third_curve_sphere( float R,    float rpoint, float rsource,                 510
                          float theta, float pe,    float radcurve,
                          float biot)
{
/*

 This routine computes the steady-state solution of temperature
 for a uniform source in a perfused medium with a curved external
 boundary whose temperature is held at zero. The solution is
 formulated in spherical coordinates.
```

```
 */                                                                    520
  int convex;
  float temp, r, rprime, C1, sqrtpe, Rprime, mu;
  float Rb, Rbprime, C2, D1;
  sqrtpe = sqrt( pe );
  mu = cos( theta );
  temp = 0.0;
  convex = 0;
  if (radcurve < 0.0)
   {
    convex = 1;                                                        530
    radcurve = fabs( radcurve );
   }
 /* if (isclose(rpoint, radcurve, CLOSE)) return( temp ); */
  if (theta > TWO_PI) return( temp );
  rprime = rsource;
  r    = rpoint;
  Rb =    sqrt(radcurve*radcurve + rprime*rprime - 2.0*radcurve*rprime*mu);
  if (Rb < 1.0) Rb = 1.0;
  C1 = (biot*Rb - (radcurve          - rprime*mu)*(sqrtpe + 1.0/Rb))/
     (biot*Rb - (rprime*rprime/radcurve - rprime*mu)*(sqrtpe + 1.0/Rb));  540
  D1 = (cosh( sqrtpe ) - sinh( sqrtpe ) / sqrtpe) / pe;
  Rprime = sqrt( radcurve*radcurve + r*r*rprime*rprime/radcurve/radcurve
                                   - 2.0*r*rprime*mu );

  if (Rprime < 1.0) Rprime = 1.0;
  if (R > 1.0)
   {
    temp =  C1*exp( -sqrtpe*Rprime )/Rprime;
    temp =  exp( -sqrtpe*R )/R - temp;
    temp *= D1;                                                        550
   }
  else
   {
    temp =  exp( -sqrtpe*Rprime )/Rprime;

    C2 = (1.0/pe - D1*(exp( -sqrtpe) - C1*temp))/sinh( sqrtpe );
 /*
    C1 = (1.0 - (cosh( sqrtpe ) - sinh( sqrtpe ) / sqrtpe)
          *(exp( -sqrtpe ) - temp ))/sinh( sqrtpe );
 */                                                                    560
    if(R > ZERO_DISTANCE)
          {
           temp = 1.0/pe - C2*sinh( sqrtpe*R )/R;
          }
    else
          {
           temp = 1.0/pe - C2*sqrtpe;
          }
   }
  if (temp < 0.0) temp = 0.0;                                          570
  return( temp );
}
/* ************************************************************ */
```

```
void init_sqrt( void )
{
/*
  This routine initializes the array for the integer computation
  (lookup) of square roots.
*/
 int i;                                                          580
 float x;
 if (Sqrt == NULL)
   Sqrt = (float *) malloc( (MAX_N_SQRT + 1) * sizeof( float ) );
 for (i = 0; i <= MAX_N_SQRT; i++)
   {
    Sqrt[ i ] = sqrt( (float) i );
   }


/* Here we optimize a bit the BEMsqrt routine. We must check       590
  the input to insure it is within the bounds of the array.
  However, this constant conditional checking costs about 20
  clock cycles. Here we do the checking up front and set a
  global point to either of 2 routines – one which will
  check and the other which will not.
*/
/*
 if (x < MAX_N_SQRT)
   {
    BEMsqrtPtr = BEMsqrt1;                                       600
   }
 else
   {
    BEMsqrtPtr = BEMsqrt2;
   }
*/

 if (Sqrt == NULL)
   {
    BEMsqrtPtr = BEMsqrt3;                                       610
   }
 else
   {
    BEMsqrtPtr = BEMsqrt2;
   }
#ifdef USE_FLOAT_GEOM
 BEMsqrtPtr = BEMsqrt3;
#endif
 return;
}                                                                620
/* ************************************************************ */
float approx_diff_curve_sphere( float R,    float rpoint, float rsource,
          float theta, float pe1, float pe2, float kappa, float radcurve)
/*
  This routine computes the basis element for a curved tissue boundary
  separating two tissue subdomains of different perfusion and thermal
  properties.
```

```
 */
 {
  float temp;                                                          630
  float r, rprime, mu, C1, C2;
  float sqrtpe1, sqrtpe2;
  float RadCurve;
  float Rprime,  Ra;
  float D1, D2;

  sqrtpe1 = sqrt( pe1 );
  sqrtpe2 = sqrt( pe2 );
 /*
  Rs = source radius                                                   640
  kappa = km2/km1

        w1 rho c
  Pe1 = ----------- Rs^2
         km1

        w2 rho c
  Pe2 = ----------- Rs^2
         km2

                                                                       650
         T1 km1
  Theta1 = --------
         Qo Rs^2

         T2 km2
  Theta2 = --------
         Qo Rs^2
 */
  temp = 0.0;
  mu = cos( theta );                                                   660
  D1 = (cosh( sqrtpe1 ) - sinh( sqrtpe1 ) / sqrtpe1) / pe1;
  D2 = (cosh( sqrtpe2 ) - sinh( sqrtpe2 ) / sqrtpe2) / pe2;
  RadCurve = fabs( radcurve );
  r = rpoint;
  rprime = rsource;
  Rprime = sqrt( radcurve*radcurve + r*r*rprime*rprime/radcurve/radcurve
                    - 2.0*r*rprime*mu );
  if (Rprime < 1.0) Rprime = 1.0;
  if ((rprime < RadCurve) && (rprime > RadCurve-1.0)) rprime = RadCurve - 1.0;
 /*                                                                    670


  If the source and the field point are both in subdomain 1.
  ----------------------------------------
 */
  if ((rpoint <= RadCurve) && (rsource <= RadCurve))
   {
    C1 = (1.0 + 1.0/sqrtpe1/radcurve - kappa - kappa/sqrtpe2/radcurve)/
       (1.0 + 1.0/sqrtpe1/radcurve + kappa + kappa/sqrtpe2/radcurve);
    if (R < 1.0)                                                       680
          {
```

```
            C2 = (1.0 - D1 * pe1 * (exp( -sqrtpe1 )+
                                    C1*exp( -sqrtpe1*Rprime ) / Rprime ) )
                / sinh( sqrtpe1 );
            if (R > ZERO_DISTANCE)
             {
              temp = (1.0 - C2*sinh( sqrtpe1*R )/R )/pe1;
             }
            else
             {                                                              690
              temp = (1.0 - C2*sqrtpe1)/pe1;
             }

          }
    else
          {
           temp = (    exp( -sqrtpe1*R    ) / R
                     - C1*exp( -sqrtpe1*Rprime ) / Rprime );
           temp *= D1;
          }                                                                 700
   }
/*
  Else If the source is in subdomain 1 and the field point is in subdomain 2.
  ---------------------------------------
*/
 else if ((rpoint > RadCurve) && (rsource < RadCurve))
  {
   C1 = (1.0 + 1.0/sqrtpe1/radcurve - kappa - kappa/sqrtpe2/radcurve)/
      (1.0 + 1.0/sqrtpe1/radcurve + kappa + kappa/sqrtpe2/radcurve);
   Ra  = sqrt( radcurve*radcurve + rprime*rprime - 2.0*rprime*radcurve*mu);  710
   C2 = exp(-Ra*(sqrtpe1 - sqrtpe2) )*(1.0 - C1);
   temp = D1 * C2 * exp( -sqrtpe2*R )/R*kappa;
  }
/*

  Else If the source and the field point are both in subdomain 2.
  ---------------------------------------
*/
 else if ((rpoint > RadCurve) && (rsource >= RadCurve))
  {                                                                         720
   kappa = 1.0/kappa;
   C1 = (1.0 + 1.0/sqrtpe2/radcurve - kappa - kappa/sqrtpe1/radcurve)/
      (1.0 + 1.0/sqrtpe2/radcurve + kappa + kappa/sqrtpe1/radcurve);
   if (R < 1.0)
         {
          C2 = (1.0 - D2 * pe2 * (exp( -sqrtpe2 )+
                                  C1*exp( -sqrtpe2*Rprime ) / Rprime ) )
              / sinh( sqrtpe2 );
          if (R > ZERO_DISTANCE)
           {                                                                730
            temp = (1.0 - C2*sinh( sqrtpe2*R )/R )/pe2;
           }
          else
           {
            temp = (1.0 - C2*sqrtpe2)/pe2;
```

```
            }
          }
    else
          {
           temp = (   exp( -sqrtpe2*R    ) / R                                    740
                                  - C1*exp( -sqrtpe2*Rprime ) / Rprime );
           temp *= D2;
          }
   }
/*
  Else If the field point is in subdomain 1 and the source is in subdomain 2.
  ---------------------------------------
*/
 else
  {                                                                               750
   kappa = 1.0/kappa;
   C1 = (1.0 + 1.0/sqrtpe2/radcurve - kappa - kappa/sqrtpe1/radcurve)/
      (1.0 + 1.0/sqrtpe2/radcurve + kappa + kappa/sqrtpe1/radcurve);
   Ra  = sqrt( radcurve*radcurve + rprime*rprime - 2.0*rprime*radcurve*mu);
   C2 =  exp(-Ra*(sqrtpe2 - sqrtpe1) )*(1.0 - C1);
   temp = D2 * C2 * exp( -sqrtpe1*R )/R*kappa;
  }
 return( temp );
}
/* ************************************************************** */                760
float tshellss( float pe )
{
 double tmp, sqrtpe;
 sqrtpe = sqrt( pe );
 tmp = (sqrtpe*cosh(sqrtpe) - sinh( sqrtpe ) )/(1.0 + sqrtpe);
 tmp = 1.0/(sinh( sqrtpe ) + tmp)/pe;
 tmp = tmp*sqrtpe;
 return( tmp );
}
```

Bibliography

[1] Proceedings of the 42^{nd} annual meeting of the radiation research society (RRS) and the 14^{th} annual meeting of the north american hyperthermia society (NAHS), April 1994.

[2] K.A. Leopold, M. Dewhirst, T. Samulski, J. Harrelson, J.A. Tucker, S.L. George, R.K. Dodge, W. Grant, S. Clegg, L.R. Prosnitz, and J.R. Oleson. Relationships among tumor temperature, treatment time, and histopathological outcome using preoperative hyperthermia with radiation in soft tissue sarcomas. *International Journal of Radiation Oncology, Biology and Physics*, 22:989–998, 1992.

[3] P.P. Lele. The MIT scanned, intensity modulated focused ultrasound (SIMFU) system. In *Hyperthermia Oncology*. 5th International Symposium on Hyperthermia Oncology, Kyoto, 1988.

[4] G. T. Martin, M. G. Haddad, E. G. Cravalho, and H. F. Bowman. Thermal model for the local microwave hyperthermia treatment for benign prostatic hyperplasia. *IEEE Transactions on Biomedical Engineering*, 39(8):836–844, August 1992.

[5] J.A. DeFord, C.F. Babbs, U.H. Patel, M.W. Bleyer, J.A. Marchosky, and C.J. Moran. Effective estimation and computer control of minimum tumour temperature during conductive interstitial hyperthermia. *International Journal of Hyperthermia*, 7(3):441–453, 1991.

[6] M.M. Chen and K.R. Holmes. Microvascular contributions in tissue heat transfer. *Ann. New York Acad. Sci.*, 335:137–151, 1980.

[7] L.M. Jiji, S. Weinbaum, and D.E. Lemons. Theory and experiment for the effect of vacular microstructure on surface tissue heat transfer. Part I: Anatomical foundation and model conceptualization. *ASME Journal of Biomechanical Engineering*, 106:321–330, 1984.

[8] L.M. Jiji, S. Weinbaum, and D.E. Lemons. Theory and experiment for the effect of vacular microstructure on surface tissue heat transfer. Part II: Model formulation and solution. *ASME Journal of Biomechanical Engineering*, 106:331–341, 1984.

[9] W.J. Song, S. Weinbaum, L.M. Jiji, and D. Lemons. A combined macro and microvascular model for whole limb heat trasnfer. *ASME Journal of Biomechanical Engineering*, 110:259, 1988.

[10] L.X. Xu, M.M. Chen, K.R. Holmes, and H. Arkin. The theoretical evaluation of the Pennes, the Chen-Holmes and the Wienbaum-Jiji bioheat transfer models in the pig renal cortex. In *Advances in Biological Heat and Mass Transfer*, volume BED-18, pages 15–21. ASME, 1991.

[11] H. H. Pennes. Analysis of tissue and arterial blood temperatures in the resting human forearm. *Journal of Applied Physiology*, 1(2):93–122, 1948.

[12] R.B. Roemer, E.G. Moros, and K. Hynynen. A comparison of bio-heat transfer and effective conductivity equation predictions to experimental hyperthermia data. In *Bioheat Transfer - Applications in Hyperthermia, Emerging Horizons in Instrumentation and Modeling*, volume BED-12, pages 11–15. ASME, 1989.

[13] J.C. Chato, J.J. Eckburg, and E. Hurlburt. Comparison of three bioheat transfer models using finite difference techniques. In *Bioheat Transfer - Applications in Hyperthermia, Emerging Horizons in Instrumentation and Modeling*, volume BED-12, pages 17–21. ASME, 1989.

[14] C.K. Charny, S. Weinbaum, and R.L. Levin. An evaluation of the Weinbaum-Jiji bioheat equation for normal and hyperthermic conditions. *ASME Journal of Biomechanical Engineering*, 112:81, 1990.

[15] H.Y. Abdelazim and M.A. Hashish. Model reduction approach to the hyperthermic analysis of cancerous tumors. In *Annual International Conference of the IEEE Engineering in Medicine and Biology Society*, pages 1302–1303. IEEE, 1987.

[16] F. Jafari and P.D. Higgins. Thermal modeling in cylindrical coordinates using effective conductivity. *IEEE Transactions on Ultrasonics, Ferroelectrics, and Frequency*, 36(2):191–196, 1989.

[17] L. Edelstein-Keshet, M.W. Dewhirst, and J.R. Oleson. Characterization of tumour temperature distribution in hyperthermia based on assumed mathematical forms. *International Journal of Hyperthemia*, 5(6):757–777, 1989.

[18] H.F. Bowman. Thermodynamics of tissue heating: Modeling and measurements for temperature distributions. In G.H. Nussbaum, editor, *Physical Aspects of Hyperthermia*, pages 511–548. American Institute of Physics, Boston, 1982.

[19] P.M. Van Den Berg, A.T. De Hoop, A. Segal, and N. Praagman. A computational model of the electromagnetic heating of biological tissue with application to hyperthermic cancer therapy. *IEEE Transactions on Biomedical Engineering*, BME-30(12):797–805, 1983.

[20] J.W. Strohbehn, K.D. Paulsen, and D.R. Lynch. Use of the finite element method in computerized thermal dosimetry. In J.W. Hand and J.R. James, editors, *Physical Techniques in Clinical Hyperthermia*, pages 383–451. Research Studies Press, Letchworth, England, 1986.

[21] R.J. Spiegel, M.B.E. Fatmi, and T.R. Ward. Computer model of animals for hyperthermia studies. In *IEEE Ninth Annual Conference of the Engineering in Medicine and Biology Society*, volume CH2513, pages 1300–1301, 1987.

[22] M. Panjehpour, J.B. Farison, A.J. Milligan, and P.S. Panjehpour. Interstitial hyperthermia temperature distribution prediction by FEM. In *Annual International Conference of the IEEE Engineering in Medicine and Biology Society*, volume 2, pages 869–871, 1988.

[23] C.K. Charny and R.L. Levin. Axial shifting with a MAPA: Thermal effects during hyperthermia. In *IEEE Engineering in Medicine and Biology Society 10th Annual International Conference*, pages 854–855, 1988.

[24] C.K. Charny and R.L. Levin. Three-dimensional finite element model of the lower leg heating during hyperthermia. In *26th National Heat Transfer Conference*, volume 85(269), pages 383–388. AIChE, 1989.

[25] W.L. Lin, R.B. Roemer, E.G. Moros, and K. Hynynen. Optimization of temperature distributions in scanned, focused ultrasound hyperthermia. *International Journal of Hyperthermia*, 8(1):61–78, 1992.

[26] E.G. Moros, A.W. Dutton, R.B. Roemer, M. Burton, and K. Hynynen. Experimental evaluation of two simple thermal models using hyperthermia in muscle *in vivo*. *International Journal of Hyperthermia*, 9(4):581–598, 1993.

[27] K.T. O'Brien and A.M. Mekkaoui. Numerical simulationof the thermal fields occuring in the treatment of malignant tumors by local hyperthermia. *ASME Journal of Biomechanical Engineering*, 115:247–253, August 1993.

[28] S.T. Clegg and R.B. Roemer. Predictions of three-dimensional temperature distributions during hyperthermia experiments. In *Bioheat Transfer - Applications in Hyperthermia, Emerging Horizons in Instrumentation and Modeling*, volume BED-12, pages 37–44. ASME, 1989.

[29] S.T. Clegg and R.B. Roemer. Towards the estimation of three-dimensional temperature fields from noisy temperature measurements during hyperthermia. *International Journal of Hyperthermia*, 5(4):467–484, 1989.

[30] S.T. Clegg and R.B. Roemer. Reconstruction of experimental hyperthermia temperature distributions: applications of state and parameter estimation. *ASME Journal of Biomechanical Engineering*, 115(4A):380–8, November 1993.

[31] C.T. Liauh, R.G. Hills, and R.B. Roemer. Comparison of the adjoint and influence coefficient methods for solving the inverse hyperthermia problem. *ASME Journal of Biomechanical Engineering*, 115:63–71, February 1993.

[32] C.T. Liauh and R.B. Roemer. A semilinear state and parameter estimation algorithm for inverse hyperthermia problems. *ASME Journal of Biomechanical Engineering*, 115:257–246, August 1993.

[33] C.T. Liauh and R.B. Roemer. Multiple minima in inverse hyperthermia temperature estimation problems. *ASME Journal of Biomechanical Engineering*, 115:239–246, August 1993.

[34] J.K. Potocki and H.S. Tharp. Concurrent hyperthermia estimation schemes based on extended Kalman filtering and reduced-order modeling. *International Journal of Hyperthermia*, 9(6):849–865, 1993.

[35] J. Mooibroek and J.J.W. Lagendijik. A fast and simple algorithm for the calculation of convective heat transfer by large vessels in three-dimensional inhomogeneous tissues. *IEEE Transactions on Biomedical Engineering*, 38(5):490–501, 1991.

[36] G. T. Martin, H. F. Bowman, and W. H. Newman. Basis Element Method for computing the temperature field during hyperthermia therapy planning. In *Advances in Biological Heat and Mass Transfer: Proceedings of the ASME Winter Annual Meeting*, volume HTD-Vol. 231, pages 75–80. ASME, November 1992.

[37] G.T. Martin, W.H. Newman, J.J. Breedlove, and H.F. Bowman. Application and optimization of the Basis Element Method for hyperthermia thermal modeling. In *Proceedings of the 42nd Annual Meeting of the Radiation Research Society and the 14th Annual Meeting of the North American Hyperthermia Society*, April 1994.

[38] G.T. Martin, W.H. Newman, and H.F. Bowman. Experimental validation and application of the Basis Element Method. In *Proceedings of the 43rd Annual Meeting of the Radiation Research Society and the 15th Annual Meeting of the North American Hyperthermia Society*, April 1995.

[39] M.J. Pikey-May, A. Taflove, W.C. Lin, D.S. Katz, V. Sathiaseelan, and B.B. Mittal. Initial results for automated computational modeling of patient-specific electromagnetic hyperthermia. *IEEE Transactions on Biomedical Engineering*, 39(3):226–235, March 1992.

[40] B.J. James and D.M. Sullivan. Direct use of CT scans for hyperthermia treatment planning. *IEEE Transactions on Biomedical Engineering*, 39(8):845–851, August 1992.

[41] D.M. Sullivan, R. Ben-Yosef, and D.S. Kapp. Stanford 3D hyperthermia treatment planning system. technical review and clinical summary. *International Journal of Hyperthermia*, 9(5):627–643, 1993.

[42] J.L. Hansen, B.A. Bornstein, G.K. Svensson, W.H. Newman, G.T. Martin, D.A. Sidney, and H.F. Bowman. A quantitative, integrated, clinical focused ultrasound system for deep hyperthermia. In *ASME International Mechanical Engineering Conference and Exhibition*, volume 94-WA/HT-42, 1994.

[43] H.F. Bowman, E.G. Cravalho, and M. Woods. Theory, measurement, and application of thermal properties of biomaterials. *Annual Review of Biophysics and Bioengineering*, 4:43–80, 1975.

[44] J.C. Chato. Selected thermophysical properties of biological materials. In *Heat Transfer in Medicine and Biology*, volume 2, chapter Appendix 2, pages 413–418. Plenum, New York, 1984.

[45] G.J. Smits, R.J. Roman, and J.H. Lombard. Evaluation of laser-doppler flowmetry as a measure of tissue blood flow. *Journal of Applied Physiology*, 86, August 1986.

[46] H.F. Bowman. Estimation of tissue blood flow. In *Heat Transfer in Medicine and Biology*, volume 1, chapter 9, pages 193–230. Plenum, New York, 1984.

[47] H. F. Bowman, G. T. Martin, W. H. Newman, S. Kumar, C. Welch, B. Bornstein, and T. S. Herman. Human tumor perfusion measurements during hyperthermia therapy. In *Hyperthermic Oncology 1992, Volume 1 - Summary Papers Addendum, Proceedings*

of the Sixth International Conference on Hyperthermic Oncology, volume 1, page A17, April 1992.

[48] K.B. Ocheltree and L.A. Frizzell. Sound field calculation for rectangular sources. *IEEE Transactions on Ultrasonics, Ferroelectrics, and Frequency Control*, 36(2):242–248, March 1989.

[49] G.H. Harrison. Ultrasound hyperthermia applicators: intensity distributions and quality assurance. *International Journal of Hyperthermia*, 6(1):169–174, 1990.

[50] J. L. Hansen, D. Delli Carpini, G. T. Martin, and G. K. Svensson. Quality assurance of a spherical, focussed, segmented ultrasound machine. In *Hyperthermic Oncology 1992: Proceedings of the Sixth International Conference on Hyperthermic Oncology (ICHC)*, volume 1 - Summary Papers, April 1992.

[51] X. Fan and K. Hynynen. The effect of wave reflection and refraction at soft tissue interfaces during ultrasound hyperthermia treatments. *Journal of the Acoustical Society of America*, 91(3):1727–1736, March 1992.

[52] X. Fan and K. Hynynen. The effects of curved tissue layers on the power deposition patterns of therapeutic ultrasound beams. *Medical Physics*, 21(1):25–34, January 1994.

[53] B.J. Davis. *A Method of Rapid Hyperthermia for Treatment of Localized Malignancies by Scanned, Focused Ultrasound.* PhD thesis, Massachusetts Institute of Technology, June 1990.

[54] J.J. Breedlove. *The effect of bones on hyperthermia treatment planning*, BS thesis Masschusetts Institute of Technology, 1994.

[55] Wen Xun Zhang. *Engineering Electromagnetism: Functional Methods.* Ellis Horwood, New York, 1991.

[56] W.H. Newman, P.P. Lele, and H. F. Bowman. Limitations and significance of thermal washout data obtained during microwave and ultrasound hyperthermia. *International Journal of Hyperthermia*, 6(4):771–784, 1990.

[57] Bateman Manuscript Project. *Tables of integral transforms.* McGraw-Hill, New York, 1954.

[58] G.N. Watson. *A Treatise on the Theory of Bessel Functions.* Cambridge University Press, London, 1966.

[59] H.S. Carslaw and J.C. Jaeger. *Conduction of Heat in Solids.* Clarendon Press, Oxford, 1959.

[60] M. Abramowitz and L.A. Stegun. *The Handbook of Mathematical Functions with Formulas, Graphs and Mathematical Tables.* NBS Appl. Series 55. U.S. Government Printing Office, Washington, D.C., 1964.

[61] T.F. Higginbotham. The integer square root of N via a binary search. *SIGCSE Bulletin*, 25(4):41–49, December 1993.

[62] T. Barrera and P. Olsson. An integer based square root algorithm. *BIT*, 33:245–261, 1993.

[63] G. Strang and G.J. Fix. *An analysis of the Finite Element Method.* Prentice-Hall, Englewood Cliffs, NJ, 1973.

[64] R.H. MacNeal. *Finite Elements: Their Design and Performance.* Marcel Dekker, New York, 1994.

[65] Nektonics, Inc., Cambridge, MA. *NEKTON Version 2.7 Documentation*, 1991.

[66] G.E. Karniadakis. *The Spectral Element Method Applied to Heat Transport Enhancement by Flow Destabilization.* PhD thesis, Massachusetts Institute of Technology, April 1987.

[67] S. Kumar, G. T. Martin, W. H. Newman, and H. F. Bowman. Thermal model for the hyperthermia treatment of an irregularly shaped tumor. In *Proceedings of the Annual International Conference of the IEEE Engineering in Medicine and Biology Society*, volume 13(2), pages 1038–1039. IEEE, 1991.

[68] J. S. Steinhart and S. R. Hart. Calibration curves for thermistors. *Deep-Sea Research*, 15:497–503, 1968.

[69] D.A. Sidney, W.H. Newman, H.F. Bowman, J.L. Hansen, and G.K. Svensson. Interactive visualization system for hyperthermia planning and evaluation. In *Proceedings of the 42nd Annual Meeting of the Radiation Research Society and the 14th Annual Meeting of the North American Hyperthermia Society*, April 1994.

[70] H.F. Bowman, W.H. Newman, G.T. Martin, M.M. Hsu, S. Ibrahim, M.F. Brodenhofer, J.L. Hansen, G.K Svensson, and B.A. Bornstein. Routine quantification of blood perfusion during clinical hyperthermia. In *Proceedings of the 43rd Annual Meeting of the Radiation Research Society and the 15th Annual Meeting of the North American Hyperthermia Society*, volume 1. RRS/NAHS, April 1995.

[71] M.W. Dewhirst, T.L. Phillips, T.V. Samulski, P. Stauffer, P. Shrivastava, B. Paliwal, T. Pajak, M. Gillim, M. Sapozink, R. Myerson, and *et al.* RTOG quality assurance guidelines for clinical trials using hyperthermia. *International Journal of Radiation Oncology, Biology and Physics*, 5:1249–1259, May 1990.

[72] G.A. Campbell and R.M. Foster. *Fourier Integrals for Practical Application.* Van Nostrand, Princeton, 1948.

About the Author

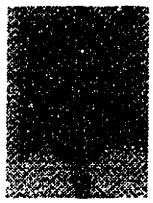

OK, so about me - I was born in Providence, Rhode Island on December 12, 1966 and grew up in the suburb of Warwick where I attended public elementary and junior high school and catholic high school. The earliest recollection I have of receiving advice from my parents (and actually listening to it) was on the importance of getting a good education. Though as a child, I never really understood why one would want this, but since I found learning fun, it was easy to comply with my parents wishes. So I studied - well most of the time. At the tender age of 12 years old, I visited my cousin, Gerry, who was getting his Master's degree in mechanical engineering at M.I.T. Upon return home from my visit, I announced to my parents that I wanted to go to M.I.T. for college. "Oh", was their first response. "Save your money!", was their second. It was at this point apparent to my 12 year-old mind that if I wanted to get there from were I was, I really needed to further my education and excel. So I asked my parents if I could go to a private and catholic high school - Bishop Hendricken. They agreed to pay the tuition if I worked hard and got good marks. I was not the valedictorian or anything, but I did well. At the age of 16, I noticed that I had this ability in mathematics and physics, but that I was really interested in medicine and physiology. Thus, I conceived of reconciling ability with interest through pursuing a career in biomedical engineering. I didn't really know what that was but found out about it when a career counselor at school gave me some literature on the different things that engineers do. Plus, being a biomedical engineering seems like it would beat the hell out of working at Burger King! Six months making burgers was not that bad, but as a career, it would get old - quickly. To this day though, I *never* order the Bacon Double Cheese Burger. OK, so I came to M.I.T. in 1984 - still only 17 years old. Immediately I intended to study mechanical engineering, but as applied to medicine. I finished my Bachelor's degree in 1988. Then I continued on in graduate school and got my Master's in mechanical engineering in 1991. Both theses were conducted at the M.I.T. Biomedical Engineering Center on developing techniques to measure blood flow. And now I'm about to finish my Ph.D. Since you have the thesis in your hand, you know what it's about. Let's see, during graduate school I was married and divorced. I do find it a strange coincidence that my '72 Dodge Dart died on the same day my ex and I split up. That vehicle had a strange connection to the cosmic consciousness the likes of which I will never understand. I still had fun though in graduate school. I spent two summers working in Geneva for the World Health Organization - essentially an all-expense-paid vacation in Switzerland which also allowed me to travel extensively throughout Europe. I never quite mastered French, but I'm still working on Spanish. That's my true, authorized biography, as I would write it. But my professional biography has to be written in the impersonal third person voice to sound objective and it must talk about the number of times I was first author on a publications. So here that is:

Gregory T. Martin received his Bachelor's (1988), Master's (1991) and Doctoral (1995) degrees from M.I.T. all in mechanical engineering. *Dr.* Martin specializes in the application of heat and mass transfer analysis as applied to clinical medicine and physiologic systems. He is the author or co-author of over a dozen publications on topics such as heat transfer, heat conduction, numerical heat transfer, hyperthermia therapy, laser-tissue interaction and computer-aided education. He is an associate member of the American Society of Mechanical Engineering (ASME) and the North American Hyperthermia Society (NAHS) and serves as a consultant to the World Health Organization. His future is uncertain.

THESIS PROCESSING SLIP

FIXED FIELD ill _____ name _____

index _____ biblio _____

▶ COPIES (Archives) Aero Dewey (Eng) Hum

Lindgren Music Rotch Science

TITLE VARIES ▶☐ _____

_____

_____

NAME VARIES ▶☐ _____

_____

IMPRINT (COPYRIGHT) _____

▶ COLLATION 224 p _____

_____

▶ ADD DEGREE _____ ▶ DEPT. _____

SUPERVISORS: _____

_____

_____ _____

_____ _____

_____ _____

_____ _____

_____ _____

_____ _____

_____ _____

NOTES:

cat'r: date:

▶ DEPT: M.E. page: ▶ J137

▶ YEAR: 1995 ▶ DEGREE: Ph.D.

▶ NAME: MARTIN, Gregory Thomas

_____